

**RADIATION SHIELDING CONCRETE FOR SPENT  
NUCLEAR FUEL INTERIM DRY STORAGE**

**RADIATION SHIELDING CONCRETE FOR SPENT NUCLEAR FUEL  
INTERIM DRY STORAGE**

By

Moamen Elsamrah

B.Sc., M.Sc.

A Thesis Submitted to the School of Graduate Studies in Partial Fulfillment of the  
Requirements for the Degree Doctor of Philosophy

McMaster University

Hamilton, Ontario, Canada

July 2021

© Copyright by Moamen Elsamrah, 2021

Doctor of Philosophy (2021)

Department of Civil Engineering

McMaster University, Hamilton, Ontario

TITLE: Radiation Shielding Concrete for Spent Nuclear  
Fuel Interim Dry Storage

AUTHOR: Moamen Elsamrah, M.Sc.

SUPERVISOR: Dr. Samir E. Chidiac, PhD, PEng, FCSCE

NUMBER OF PAGES: 208

## **Lay Summary**

The dire need for radioactive wastes disposal, especially spent nuclear fuel (SNF) being the most hazardous, has increased with the ever-increasing accumulated amount worldwide. This disposal must be safe, efficient, and long-term. Therefore, different techniques have been employed to provide secure storage for these harmful wastes. However, one technique has lately gained notable importance in the absence of a permanent repository until now; which is the interim dry storage technique. This technique guarantees secured long-term storage, with relatively low costs, for all kinds of radioactive wastes.

Concrete, a reasonably cheap construction material, is one of the main components existing in multiple faces of interim dry storage. As a result, continuous research aims to develop concrete mixes with enhanced properties, especially radiation shielding properties. This would lead to a reduction in the needed thickness/area, simplifying the overall design requirements, and saving materials, thus decreasing the total costs.

Accordingly, developing concrete mixes with improved properties, specifically radiation shielding properties, is the pivot of this research.

## Abstract

The demand for nuclear energy, which is marketed as zero-emission clean energy and a secure source of electricity, is continuously rising globally. However, associated radioactive waste such as spent nuclear fuel (SNF) presents a serious health and waste management hurdle. Interim dry storage methods have emerged as a remedial measure for the nuclear industry. This includes the concrete-based dry storage cask which is the focus of this study.

The evolution and design requirements of SNF dry storage casks and interim storage facilities were first reviewed, and the existing design and operation challenges were identified. Accordingly, four comprehensive studies were undertaken: 1) quantify the effects of minerals and other additives added to enhance radiation shielding concrete on the concrete physical and mechanical properties; 2) develop a user-friendly computational software, named MRCsC, for estimating fast neutron macroscopic removal cross-section,  $\Sigma_R$  (in  $\text{cm}^{-1}$ ), for shielding materials; 3) investigate experimentally and analytically the effects of adding powder boron carbide on Portland cement hydration kinetics and concrete compressive strength and radiation shielding properties; 4) study analytically the effectiveness of aggregates such as barite and celestite on concrete radiation shielding properties, and model the feasibility of developed concrete mixes as an overpack in a sandwich-design storage cask using the software OpenMC.

Overall, the results reveal that sandwich-design concrete cask meets all the requirements for SNF dry storage. The addition of powder boron carbide, up to 50% by weight of cement, delayed the cement initial setting time by approximately 6 h, yielded a 15%

increase in cumulative heat of hydration and a 28% increase in concrete compressive strength after 3 days, and increased the thermal neutron absorption ( $\Sigma_{\text{abs}}$ ) close to 62000%. Concrete mixes with barite and celestite, as coarse aggregates replacement, significantly improve concrete radiation shielding efficiency and feasibility of sandwich-design storage cask. The OpenMC model results revealed over 60% decrease in the total dose rate.

## **Acknowledgements**

*All praise and gratitude be to Allah the Most Gracious, the Most Compassionate and the Most Merciful with the blessings of whom the good deeds are fulfilled.*

First, I would like to thank my supervisor, Prof. Dr. S. E. Chidiac, for his unlimited support during my PhD study, and I'm so grateful for his motivation, immense knowledge, and most of all, for being a patient and understanding mentor for me. Also, I would like to thank him for helping me transform into a grown-up researcher. Besides, I greatly appreciate my PhD supervisory committee, Prof. Dr. D. Novog and Prof. Dr. P. Guo, for their helpful comments and valuable guidance since the beginning of the study. My sincere thanks also go to Prof. Dr. S. Razavi, who had the ability to de-stress me with her calm smile and gentle manner through some crucial stages during my study, and Dr. M. A. Zamora, who helped me immensely in doing some critical analytical calculations related to the study.

Also, I would like to thank the Natural Science and Engineering Research Council of Canada, McMaster University Centre for Effective Design of Structures, and Military Technical College in Egypt, for their support, as well as LafargeHolcim Canada and Feldco International USA for providing the needed materials for the experimental part in the study.

My thanks extend to my colleagues, Mouna Reda, Mehdi Shafikhani, Sylvia Mihaljevic, Shannon Guo, and Omar Ashry, and staff at Applied Dynamics Laboratory, especially Mr. Kent Wheeler, for their assistance and encouragement during my study.

Finally, I am indebted to my family: Jana, Youssef, Judy, and my beloved wife, Asmaa, for all the patience, love, and endless support. Also, words cannot express my gratitude to my mother, Zohour, and my father-in-law, Ahmed, for their prayers, love, spiritual support, and encouragement. Last but not least, I dedicate this thesis to my father's soul, who taught me how to be a responsible person ready to face life's difficulties.

## **Publication list**

**This thesis contains the following papers:**

### **Paper I**

El-Samrah, M.G., Tawfic, A.F., and Chidiac, S.E. (2021). Spent nuclear fuel interim dry storage; design requirements, most common methods, and evolution: A review. *Annals of Nuclear Energy*, 160, 108408.

### **Paper II**

Chidiac, S.E., El-Samrah, M.G., and Abdel-Rahman, M.A.E. (2021). Characterization of natural and synthetic aggregates properties and their effect on the physical and mechanical properties of radiation shielding concrete. Submitted to *Physics of Particles and Nuclei Letters*.

### **Paper III**

El-Samrah, M.G., El-Mohandes, A.M., El-Khayatt, A.M., and Chidiac, S.E. (2021). MRCsC: A user-friendly software for predicting shielding effectiveness against fast neutrons. *Radiation Physics and Chemistry*, 182, 109356.

### **Paper IV**

Chidiac, S.E., El-Samrah, M.G., Reda, M.A., and Abdel-Rahman, M.A.E. (2021). Mechanical and radiation shielding properties of concrete containing commercial boron carbide powder. Submitted to *Construction and Building Materials*.

### **Paper V**

El-Samrah, M.G., Zamora, M.A.A., Novog, D.R., and Chidiac, S.E. (2021). Radiation shielding properties of modified concrete mixes and their feasibility in dry storage cask. Submitted to *Progress in Nuclear Energy*.

## **Co-Authorship**

This thesis has been prepared consistent with the regulations for the “Sandwich thesis” format stipulated by the School of Graduate Studies at McMaster University and has comprised of the following research papers that were co-authored as follows:

### **Chapter 2: Spent nuclear fuel interim dry storage; design requirements, most common methods, and evolution: A review**

By M.G. El-Samrah, A.F. Tawfic, and S.E. Chidiac

The idea was proposed by M.G. El-Samrah and refined by Dr. S.E. Chidiac. The Paper was written by M.G. El-Samrah, edited by Dr. S.E. Chidiac, and revised by Dr. A.F. Tawfic.

### **Chapter 3: Characterization of natural and synthetic aggregates properties and their effect on the physical and mechanical properties of radiation shielding concrete**

By S.E. Chidiac, M.G. El-Samrah, and M.A.E. Abdel-Rahman

The idea was proposed by M.G. El-Samrah and refined by Dr. S.E. Chidiac. The paper was written by M.G. El-Samrah and Dr. S.E. Chidiac and revised by Dr. S.E. Chidiac and Dr. M.A.E. Abdel-Rahman.

### **Chapter 4: MRCsC: A user-friendly software for predicting shielding effectiveness against fast neutrons**

By M.G. El-Samrah, A.M. El-Mohandes, A.M. El-Khayatt, and S.E. Chidiac

The idea and the analytical model were proposed by M.G. El-Samrah and refined by Dr. A.M. El-Khayatt. Building the software was made by A.M. El-Mohandes. The paper was written by M.G. El-Samrah and edited by Dr. S.E. Chidiac.

**Chapter 5: Mechanical and radiation shielding properties of concrete containing commercial boron carbide powder**

By S.E. Chidiac, M.G. El-Samrah, M.A. Reda, and M.A.E. Abdel-Rahman

The experimental program was developed by Dr. S.E. Chidiac. Experiments and analytical calculations were conducted by M.G. El-Samrah and M.A. Reda and enhanced by Dr. S.E. Chidiac. The paper was written by M.G. El-Samrah and revised by Dr. S.E. Chidiac.

**Chapter 6: Radiation shielding properties of modified concrete mixes and their feasibility in dry storage cask**

By M.G. El-Samrah, M.A.A. Zamora, D.R. Novog, and S.E. Chidiac

The idea was proposed by M.G. El-Samrah and edited by Dr. D.R. Novog. The analytical calculations and writing the paper were made by M.G. El-Samrah and were edited and revised by Dr. D.R. Novog and Dr. S.E. Chidiac. Conceptualization of the simulated model and providing the needed values/parameters were done by M.G. El-Samrah. The model simulation was conducted by M.A.A. Zamora.

## **Contents**

<b>Lay Summary</b>	<b>II</b>
<b>Abstract</b>	<b>III</b>
<b>Acknowledgements</b>	<b>V</b>
<b>Publication List</b>	<b>VII</b>
<b>Co-Authorship</b>	<b>VIII</b>
<b>Contents</b>	<b>X</b>
<b>List of figures</b>	<b>XV</b>
<b>List of tables</b>	<b>XVIII</b>
<b>1. Thesis Summary</b>	<b>1</b>
1.1 Introduction	1
1.2 Background	3
1.2.1 Design considerations regarding dry storage casks	3
1.2.1.1 Safe enclosure	3
1.2.1.2 Structural integrity	4
1.2.1.3 Adequate radiation shielding	4
1.2.1.4 Subcriticality assurance	5
1.2.1.5 Decay heat dissipation	6
1.2.2 Metal-based and concrete-based casks	7
1.2.3 Radiation shielding analytical calculations	8
1.2.3.1 Mass and linear attenuation coefficients	8
1.2.3.2 Half value layer, tenth value layer, and mean free path	9

---

1.2.3.3	Effective atomic number	10
1.2.3.4	Exposure build-up factors	10
1.2.3.5	Fast neutron macroscopic effective removal cross-section	12
1.2.3.6	Thermal neutron macroscopic absorption cross-section	13
1.3	Impetus of research	14
1.4	Overall objective and scope	14
1.5	Summary of the papers included	15
1.6	Conclusions and recommendations for future work	19
1.6.1	Conclusions	19
1.6.2	Recommendations for future work	23
1.7	References	23
<b>2.</b>	<b>Spent nuclear fuel interim dry storage; design requirements, most common methods, and evolution: A review</b>	<b>29</b>
2.1	Abstract	29
2.2	Introduction	29
2.3	Design requirements	34
2.3.1	Safe enclosure of the contained SNF	34
2.3.2	Structural response and integrity	36
2.3.3	Radiation shielding	39
2.3.4	Subcriticality	43
2.3.5	Heat dissipation	44
2.4	Evolution and trends of SNF interim dry storage	49

---

2.4.1	SNF dry storage casks	49
2.4.2	Pros and cons of full-metal, concrete-steel and sandwich dry storage casks	54
2.4.3	Dry storage facilities	55
2.5	Conclusion	63
2.6	References	66
<b>3.</b>	<b>Characterization of natural and synthetic aggregates properties and their effect on the physical and mechanical properties of radiation shielding concrete</b>	<b>73</b>
3.1	Abstract	73
3.2	Introduction	74
3.3	Concrete properties	75
3.4	Physical and mechanical properties of aggregates possessing radiation atten.	86
3.4.1	Properties	86
3.5	Case studies - RSC containing aggregates possessing radiation attenuation properties	91
3.5.1	Natural aggregates	91
3.5.2	Synthetic aggregates	97
3.6	RSC design methodology	101
3.7	Conclusions	102
3.8	References	103
<b>4.</b>	<b>MRCsC: A user-friendly software for predicting shielding effectiveness against fast neutrons</b>	<b>113</b>
4.1	Abstract	113

---

4.2	Introduction	113
4.3	Theoretical background	116
4.4	Macroscopic Removal Cross-sections Calculator (MRCsC)	119
4.4.1	Program description	119
4.4.2	Analytical model	120
4.4.3	Program testing and validation	123
4.5	Conclusions	129
4.6	Acknowledgments	130
4.7	References	130
<b>5.</b>	<b>Mechanical and radiation shielding properties of concrete containing commercial boron carbide powder</b>	<b>135</b>
5.1	Abstract	135
5.2	Introduction	136
5.3	Materials and methods	140
5.3.1	Materials	141
5.3.2	Samples' preparation and tests protocol	143
5.4	Results and Discussion	147
5.4.1	Powder characterization	147
5.4.2	Isothermal calorimetry	149
5.4.3	Radiation shielding	154
5.5	Conclusions	161
5.6	Acknowledgments	162

5.7	References	163
<b>6.</b>	<b>Radiation shielding properties of modified concrete mixes and their feasibility in dry storage cask</b>	<b>169</b>
6.1	Abstract	169
6.2	Introduction	170
6.3	Materials and Methods	172
6.3.1	Design of experiment	172
6.3.2	Radiation shielding properties	175
6.3.2.1	Mass and Linear attenuation coefficients	175
6.3.2.2	Half value layer, Tenth value layer, and Mean free path	176
6.3.2.3	Effective atomic number	177
6.3.2.4	Exposure build-up factor	177
6.3.2.5	Fast neutron shielding properties	179
6.3.2.6	Thermal neutron shielding properties	180
6.4	Concrete-Based Dry Storage Cask (DSC) Model	181
6.5	Results and discussion	185
6.5.1	Gamma-rays shielding assessment	185
6.5.2	Neutrons shielding assessment	193
6.5.3	Dry Storage Cask model results	197
6.6	Conclusions	201
6.7	Acknowledgments	203
6.8	References	203

## List of Figures

<b>Fig. 2.1</b> Vertical cross-sections of concrete-based cask design with welded lid (on the left) and full-metal cask design with primary and secondary lids using O-ring gaskets (on the right), adapted from (Saegusa et al., 2008; Wimmer et al., 2015) .....	36
<b>Fig. 2.2</b> Considered Scenarios for Aircraft Engine Crash onto a full-metal cask, adapted from (Saegusa et al., 2010).....	38
<b>Fig. 2.3</b> Schematic diagrams for CASTOR V/19 dual purpose cask in transport configuration with impact limiters (on the left) and vertical CONSTOR dry cask (on the right), adapted from (Wimmer et al., 2015).....	42
<b>Fig. 2.4</b> Basket design for CONSTOR V/32 dry storage cask, adapted from (Funke and Diersch, 2004) .....	46
<b>Fig. 2.5</b> Completed MPC-89, Metamic-HT Spent Fuel Storage Basket, adapted from (HOLTEC, 2013) .....	46
<b>Fig. 2.6</b> Half section of a concrete based cask showing air inlet, outlet, thermal shield and fins along with the concrete vessel, adapted from (Saegusa et al., 2008).....	48
<b>Fig. 2.7</b> CASTOR Ic- DIORIT Dry Cask for SNF transport and storage, adapted from (Droste, 2013) .....	51
<b>Fig. 2.8</b> The basic configuration of the TN-24 transportable cask manufactured by Orano (previously Areva), adapted from (Roland et al., 2003).....	52
<b>Fig. 2.9</b> Arranged CASTOR V/21 vertical casks at Surry Nuclear Power Station, Virginia, USA, (Skrzyppek and Kim, 2015) .....	56
<b>Fig. 2.10</b> A site view for Gorleben interim dry storage facility (on the left) and an interior view that shows arranged vertical CASTOR casks stored indoor in the same facility (on the right) (Fraczek, 2013).....	57
<b>Fig. 2.11</b> Interim dry storage sites in Canada (NWMO, 2019) .....	58
<b>Fig. 2.12</b> HI-STORM UMAX design features (on the left) and the site view of Callaway NPP UMAX Facility in the U.S (on the right), adapted from (Woodward, 2015) .....	60

<b>Fig. 2.13</b> The NUHOMS storage system with monolithic one layer structure, adopted from (Orano, 2020) .....	61
<b>Fig. 2.14</b> The NUHOMS Advanced Matrix with its unique two-story structure, adopted from (U.S.NRC, 2018) .....	63
Fig. 3.1 Definition of the cell [20] .....	77
<b>Fig. 3.2</b> Rheological properties versus packing density of 0.4 w/c concrete mixture with a) 14 mm and b) 20 mm max aggregate size.....	79
<b>Fig. 3.3</b> Effects of particle shape and S/A on concrete's yield stress and plastic viscosity [25] ...	80
<b>Fig. 3.4</b> Compressive strength and packing density of aggregate versus packing density of 0.4 w/c concrete mixture with a) 14 mm and b) 20 mm coarse aggregate size .....	82
<b>Fig. 3.5</b> Tortuosity factor versus aggregate volume fraction [24] .....	84
<b>Fig. 3.6</b> Interfacial transition zone factor ( $f_{ITZ}$ ) versus $V_{ITZ}$ [23].....	85
<b>Fig. 3.7</b> Display of RSC aggregates physical and mechanical properties .....	88
<b>Fig. 3.8</b> RSC compressive strength containing dolomite (D), hematite (H), ilmenite (IL) and air-cooled slag (ACS) as coarse (c) and fine (f) aggregates versus curing time [2] .....	92
<b>Fig. 3.9</b> RSC compressive strength versus curing time [36] .....	94
<b>Fig. 3.10</b> Unit weight, compressive strength, and splitting tensile strength of concrete containing colemanite [39] .....	95
<b>Fig. 3.11</b> Hydration reaction of cement containing fine colemanite reported in two different studies; (a) Colemanite percentage relative to the cement weight, (b) Percent of boron relative to cement mass [30, 31] .....	96
<b>Fig. 3.12</b> Slump flow of mortar containing HDPE, PP and UPE [68].....	99
<b>Fig. 3.13</b> Compressive strength of mortar containing HDPE, PP and UPE [68].....	99
<b>Fig. 4.1</b> MRCsC user interface .....	120
<b>Fig. 4.2</b> The Cf-252 neutron energy spectrum derived from measured TOF spectrum, reproduced from (Lee et al., 2016).....	121
<b>Fig. 4.3</b> <sup>241</sup> Am–Be source neutron energy spectrum, reproduced from (Baginova et al., 2018) ..	122

<b>Fig. 4.4</b> $^{239}\text{Pu}$ -Be source neutron energy spectrum, reproduced from (Vega-Carrillo and Torres-Muhech, 2002).....	122
<b>Fig. 4.5</b> The relation between the calculated results obtained from MRCsC program (a), NXCom program (b) and the corresponding measured values.....	129
<b>Fig. 5.1</b> Boron carbide particle size distribution.....	147
<b>Fig. 5.2</b> XRD mineral spectrum of boron carbide powder .....	148
<b>Fig. 5.3</b> Cement pastes' mean heat flow rate curves.....	150
<b>Fig. 5.4</b> Cement pastes' mean cumulative heat curves .....	150
<b>Fig. 5.5</b> Concrete $\mu/\rho$ , $\mu$ , HVL and MFP calculated using WinXCom program .....	156
<b>Fig. 5.6</b> Concrete effective atomic number with photon energy .....	158
<b>Fig. 6.1</b> Model of sandwich-design concrete-based dry storage cask.....	182
<b>Fig. 6.2</b> Flux to dose conversion factors adopted from (McFerran et al., 2020) .....	184
<b>Fig. 6.3</b> Concrete mixes total mass attenuation coefficient and partial contribution of the three main interaction mechanisms .....	186
<b>Fig. 6.4</b> $\mu$ , HVL, TVL, and MFP for the eight concrete mixes .....	188
<b>Fig. 6.5</b> Percent increase in $\mu$ from Mix design no. 2 over $\mu$ from Mix design no. 1 .....	191
<b>Fig. 6.6</b> Concrete mixes effective atomic number ( $Z_{\text{eff}}$ ).....	191
<b>Fig. 6.7</b> EBFs for the mixes prepared using mix design no. 1 (a) and those mixes designed using mix design no. 2 (b) .....	193
<b>Fig. 6.8</b> Fast neutron effective removal cross-sections for the 8 concrete mixes .....	194
<b>Fig. 6.9</b> Thermal neutron macroscopic absorption cross-sections for the 8 concrete mixes .....	196
<b>Fig. 6.10</b> Photon flux variation from the centre of the cask and from the start of the concrete layer .....	198
<b>Fig. 6.11</b> Neutron flux variation from the centre of the cask and from the start of the concrete layer .....	199
<b>Fig. 6.12</b> Photon and neutron flux versus energy at the cask's outer surface.....	200

## List of Tables

<b>Table 2.1</b> Comparison between wet storage and dry storage for SNF .....	31
<b>Table 2.2</b> The main features of the HI-STORM UMAX system .....	60
<b>Table 3.1</b> Aggregates typically used in RSC [9, 10] .....	75
<b>Table 3.2</b> Physical and mechanical properties of aggregates typically used in RSC .....	87
<b>Table 3.3</b> Compressive strength of concrete containing barite and magnetite (MPa) [67].....	97
<b>Table 3.4</b> Physical properties of the used synthetic resins [68] .....	98
<b>Table 4.1</b> Description and density of concrete samples collected from the literature .....	124
<b>Table 4.2</b> Samples elemental composition (w%) .....	125
<b>Table 4.3</b> Measured and calculated effective removal cross-sections of the studied samples .....	126
<b>Table 4.4</b> Theoretically calculated values of effective removal cross-sections $\Sigma_R$ ( $\text{cm}^{-1}$ ) for FCL concrete based on MRCsC and NXCom libraries for $\Sigma_R/\rho$ .....	127
<b>Table 4.5</b> Theoretically calculated values of effective removal cross-sections $\Sigma_R$ ( $\text{cm}^{-1}$ ) for BRS-composite based on MRCsC and NXCom libraries for $\Sigma_R/\rho$ .....	128
<b>Table 4.6</b> Results from the paired samples t-test and the regression analysis.....	129
<b>Table 5.1</b> Cement paste mixtures proportions.....	141
<b>Table 5.2</b> Concrete mixtures proportions .....	141
<b>Table 5.3</b> Concrete elemental analysis, percent weights, and density .....	141
<b>Table 5.4</b> Physical properties and chemical composition of Portland cement type GU .....	142
<b>Table 5.5</b> Physical and mechanical properties of boron carbide powder.....	143
<b>Table 5.6</b> Boron carbide powder mineral composition and corresponding weight percent.....	149
<b>Table 5.7</b> Cement paste $h_{\max}$ , Time of $h_{\max}$ , and H determined by isothermal calorimetry.....	150
<b>Table 5.8</b> Estimated cement paste initial setting time .....	151
<b>Table 5.9</b> Cement paste temporal degree of hydration .....	154

<b>Table 5.10</b> Concrete compressive strength (MPa) .....	154
<b>Table 5.11</b> Concrete mass and linear attenuation coefficients at selected photon energies .....	157
<b>Table 5.12</b> Deduced concrete half-value layer and mean free path at selected photon energies .	157
<b>Table 5.13</b> Concrete mixes calculated $\Sigma_R$ and $HVL_{fn}$ values .....	160
<b>Table 5.14</b> Concrete mixes calculated $\Sigma_a$ and $HVL_{thn}$ values.....	161
<b>Table 6.1</b> Chemical and physical properties of cementing materials and aggregates .....	174
<b>Table 6.2</b> Concrete mix proportions [ $\text{kg}/\text{m}^3$ ] .....	174
<b>Table 6.3</b> Concrete mix elemental composition.....	175
<b>Table 6.4</b> Element's weight percentage and density .....	182
<b>Table 6.5</b> Photon and neutron spectra used to define the radioactive sources .....	184
<b>Table 6.6</b> Values of $\mu$ and HVL for selected photon energy values.....	189
<b>Table 6.7</b> Detailed calculations of the 8 concrete mixes $\Sigma_R$ , $HVL_{fn}$ , and $\lambda_{fn}$ .....	194
<b>Table 6.8</b> Detailed calculations of the 8 concrete mixes $\Sigma_{abs}$ , $HVL_{thn}$ , and $\lambda_{thn}$ .....	197
<b>Table 6.9</b> Neutron, photon, and total dose rates at the cask's outer surface for the 8 concrete mixes .....	200

# 1. Thesis Summary

## 1.1 Introduction

Safe and long-term disposal of radioactive wastes was always crucial and challenging for the nuclear industry. With the increased global use of nuclear technology, a need for a permanent solution is essential for a sustainable industry (Vitkova et al., 2006; Ewing, 2015). Spent nuclear fuel (SNF) discharged from operating reactors is temporarily stored at the reactor secondary pool for a short period before being moved to a storage pool, usually for 5 to 10 years, referred to as a wet storage period. Subsequently, the SNF is transferred to an interim dry storage stage using either above ground or underground dry storage facilities (Fukuda et al., 2003; Haire and Swaney, 2005; Bruno and Ewing, 2006).

Wet storage being a costly process, and with the absence of a permanent geological storage repository for SNF and high-level wastes (HLW), interim dry storage has evolved as a viable alternative. It provides safe long-term storage for SNF, easy transportation when needed, efficient passive decay heat removal process, and high degree of robustness under accidental conditions (Ratiko et al., 2018). Moreover, the phasing out of nuclear power by countries that depended greatly on it as a part of the total energy production has significantly amplified the need for the reliable interim dry storage facilities (Fairlie, 2016).

Nevertheless, dry storage must meet rigid requirements to ensure safe, efficient, and reliable long-term storage for SNF. As such, the research to improve the performance of the dry storage casks is ongoing. This includes coming up with techniques to attain better

containment for this kind of waste and better confrontation with extreme events like tsunamis, tornados, flooding and earthquakes, and terrorist acts. In short, the challenges are multifaceted, social, economic, and technical (Wimmer et al., 2015; Shimizu, 2016; Almomani et al., 2017; Vlček, 2018).

The design and construction requirements of dry casks to store SNF or HLW, include structural capacity and durability, efficient enclosure of the stored SNF, radiation shielding, and heat dissipation (Wimmer et al., 2015; IAEA, 2020).

Each part or component in the dry storage cask has a distinctive role. However, some components can play multiple roles and can describe the overall behavior of the storage cask. One of these components is the concrete layer or overpack, which can help significantly in enhancing the cask's overall durability and heat decay removal, besides its primary function in radiation shielding (Fukuda et al., 2003; Vitkova et al., 2006; Wimmer et al., 2015).

This chapter introduces a background of the performed studies in this thesis along with the impetus that provided the required motivation to conduct this research. Moreover, it presents the overall objective and scope of this study and summarizes the research papers presented in this thesis. Last but not least, it briefs the obtained conclusions and gives some recommendations for future work that can be beneficial for the current research.

## **1.2 Background**

The dry storage cask is the most common shape of SNF interim dry storage. This section deals with the considerations of the design and construction of dry storage cask in brief. The main differences between Steel-based and concrete-based casks are introduced. Furthermore, the required analytical calculations employed to assess various radiation shielding properties of the shielding material are also covered.

### **1.2.1 Design considerations regarding dry storage casks**

#### *1.2.1.1 Safe enclosure*

The cask needs to prevent any possible leakage and protect the spent fuel cladding from any damage or degradation throughout its service life. The loss of fuel integrity during the storage period may cause critical radiological concerns (Droste, 2013; Wimmer et al., 2015). Some of the causes that affect the integrity of the stored SNF and its cladding are; cladding creep under internal gas pressure, stress corrosion cracking, and corrosion of the cladding due to possible fuel oxidation (Vitkova et al., 2006).

The canister steel shell, in canister-based designs, or the outer overpack directly in other designs along with effective decay heat dissipation, and anti-oxidation protecting methods, protect the fuel and its cladding. Also they prevent any possible radioactive material leakage during the cask's service life. Thus, material selection, proper geometrical design, and precise welding for the canister and the surrounding cylindrical shell are essential (Saegusa et al., 2008; Wimmer et al., 2015).

### *1.2.1.2 Structural integrity*

The structural integrity of the cask depends mainly on the overpack, which is a licensing requirement and needs to be evaluated solely before assessing the entire cask. The most common tests for examining the structural integrity are; vertical and horizontal fall from different heights with and without impact limiters, tipping over, seismic analysis, and aircraft or missile horizontal and vertical impacts (Haire, 2006). Some of these tests can be performed using a full-scale cask, while others are conducted either on a reduced scale or through analyzing simulated models using approved software tools (Almomani et al., 2017; Hanifehzadeh et al., 2018; Ratiko et al., 2018).

The obtained results are analyzed to assess the structural integrity of the cask with emphasis on some components that ensure leak tightness and safety of the contained SNF. These components are; the lid(s), the welds, the overpack, whether it is metal or concrete based, and the canister (Saegusa et al., 2010; Almomani et al., 2017).

### *1.2.1.3 Adequate radiation shielding*

The radiation shielding requirements of the SNF dry storage cask are determined from the fuel starting from its fresh state until the complete burnup and the wet storage duration. Thus, the details of the initial loading of each fuel assembly, number of assemblies, fuel type (UO<sub>2</sub> or MOX), burnup value of the fuel, length of the cooling period in wet storage pools, SNF whether it is stored intact or after reprocessing, and the fuel assemblies whether they are stored with or without the structural components, are needed (Ko et al., 2014; Hu et al, 2016).

The main hazardous radiated emissions from the SNF stored during interim dry storage are gamma rays other than relatively little emissions due to fast neutrons (Ko et al., 2014; Hu et al., 2016). Therefore, providing adequate radiation shielding is achieved with the thick shell that encapsulates the canister or the basket. This envelope can be pure metallic using steel or ductile cast iron with a resin layer added on the outer surface, a thick concrete shell with an inner steel liner, or “sandwich” concrete shell with both internal and external steel liners (Droste, 2013; Wimmer et al., 2015; IAEA, 2020).

#### *1.2.1.4 Subcriticality assurance*

Sustained subcriticality should be ensured throughout the entire service life of the cask. To achieve an adequate margin of subcriticality, comprehensive calculations are made to keep the neutron multiplication factor and the reactivity at minimal levels even under extreme events like flooding, earthquakes, or overheating (Ko et al., 2014; Hu et al., 2016). Formerly, SNF was treated as an unirradiated fresh fuel regarding criticality and reactivity calculations which exaggerated the safety limits regarding the basket geometrical dimensions and the required flux traps, thus adding unnecessary costs (Parks, 2000; Fukuda et al., 2003; Clarity et al., 2017). In 2000, a new concept emerged called (burnup credit), which accounts for reducing reactivity due to fuel burnup while in service. Employing this concept led to a reduction in the overall dry cask's size and weight and carrying more SNF assemblies (Parks, 2000; IAEA, 2012; Clarity et al., 2017).

Adopting proper geometrical design, especially for the basket, besides adding neutron absorbers to the design, are responsible for achieving sustained subcriticality. For

instance, borated stainless steel and borated aluminum are used for manufacturing the partitions of the SNF basket (Funke and Diersch, 2004; Vitkova et al., 2006; IAEA, 2012).

#### *1.2.1.5 Decay heat dissipation*

Decay heat removal is essential to protect the integrity of the stored fuel and its cladding. During the first five years, when SNF is usually stored in water pools, the decay heat emission decreases by more than 90% (Hu et al., 2016; Poškas et al., 2019). In SNF dry storage casks, decay heat dissipation depends on conduction, natural convection, and thermal radiation mechanisms. The cask design should assure efficient decay heat dissipation in the long run, and keep on the stored spent fuel and its cladding within the standard safety limits under usual and accidental conditions (Vitkova et al., 2006; Saegusa et al., 2010; IAEA, 2012).

High temperatures, differential pressures, and corresponding stresses on the fuel cladding during the dry storage period can result in permanent creep deformation or even cracking of the fuel cladding (Vitkova et al., 2006; U.S.NRC, 2010). Therefore, it is necessary to keep SNF cladding temperatures below the expected damage threshold in normal operating conditions with a proper margin of safety. The decay heat dissipation in dry storage casks is efficiently achieved through a multi-layered passive process starting with the basket and ending with the overpack or the radially machined fins located on the outer surface of the cask (IAEA, 2012; Vlček, 2018; Wu et al., 2018). Although the primary role of the overpack, whether it is steel or concrete-based, is to provide adequate radiation shielding, some modifications are usually made to enhance the overpack thermal

conductivity to attain a better decay heat removal process (Droste, 2013; Wimmer et al., 2015).

### **1.2.2 Metal-based and concrete-based casks**

There are various classifications of SNF dry storage casks; however, classifying them according to the material and the design of the external overpack is most common (U.S.NRC, 2010; IAEA, 2012). Metal-based cask has a full-metallic cylindrical overpack made of stainless steel or ductile cast iron. The required overpack thickness is smaller than that in the concrete-based cask; thus, the metal-based cask has a smaller diameter and footprint than the concrete-based cask (Roland et al., 2003; Saegusa et al., 2008). Also, metal-based cask is robust and reliable for transporting SNF with shorter cooling periods. However, manufacturing metal-based cask is complicated and expensive. The metallic-overpack thickness is 40 cm or more and needs precise welding using advanced welding techniques like friction stir welding that is not an easy process knowing that the layer to be welded is significantly thick (Droste, 2013; Wimmer et al., 2015). Moreover, although the thick metallic overpack provides adequate shielding against gamma rays, it cannot provide adequate shielding against neutrons. So, special modifications should be made, such as drilling symmetric axial holes into the thick shell and filling them with polyethylene or adding a specific resin layer with a protective steel shell to the outer overpack surface (Roland et al., 2003; Wimmer et al., 2015).

On the other hand, concrete-based casks are much easier to manufacture and much cheaper. The overpack formed of concrete can be designed and poured on-site or offsite and can be modified easily to effectively attenuate gamma rays and neutrons without

needing any additional layers (Roland et al., 2003; Saegusa et al., 2008). Concrete is considered one of the most optimum radiation shielding materials, as it is a proper construction material that can be modified easily using certain additives and aggregates to shield against all harmful kinds of radiation efficiently (Kaplan, 1989; Ouda, 2015). Besides, the contained water alone plays a significant role in moderating energetic neutrons, unlike metallic shields that can protect from energetic photons but cannot provide sufficient protection against neutrons (Roland et al., 2003; Saegusa et al., 2010).

Concrete-based cask that utilizes an inner steel liner alone and has a bare surface, has shown aging and degradation problems, especially when placed in coastal sites (Gray, 2015). As such, the sandwich overpack design, which comprises of a concrete cylindrical layer with both inner and outer steel liners, is considered a robust and reliable alternative. It is comparatively inexpensive and easy to manufacture, and can be used for SNF transportation under specific regulations (Wimmer et al., 2015; Hu et al., 2016; IAEA, 2020).

### **1.2.3 Radiation shielding analytical calculations**

#### *1.2.3.1 Mass and linear attenuation coefficients*

Mass attenuation coefficient ( $\mu/\rho$ ), in  $\text{cm}^2/\text{g}$ , is an essential parameter to assess the radiation shield as it characterizes the resistance of the shield to be penetrated by energetic photons based on the shield constituents only and independent of its density (Gerward et al., 2004). It is calculated as a summation of the cross-sections of photons/matter interaction mechanisms, as shown in Eq. 1.1, especially the three main mechanisms; photoelectric absorption, Compton scattering, and pair production. For

compounds and mixtures,  $(\mu/\rho)$  is calculated employing the corresponding elemental analysis according to Eq. 1.2 (Lamarsh and Baratta, 2001, Gerward et al., 2004):

$$(\mu/\rho) = (\mu/\rho)_{PE} + (\mu/\rho)_{Compton} + (\mu/\rho)_{PP} \quad (1.1)$$

$$(\mu/\rho) = \sum_i w_i (\mu/\rho)_i \quad (1.2)$$

where  $(\mu/\rho)_{PE}$ ,  $(\mu/\rho)_{Compton}$ , and  $(\mu/\rho)_{PP}$  are photoelectric, Compton scattering, and pair production cross-sections, respectively.  $w_i$  and  $(\mu/\rho)_i$  are weight fraction and mass attenuation coefficient of the  $i^{\text{th}}$  element.

Linear attenuation coefficient ( $\mu$ ), in  $\text{cm}^{-1}$ , describes the fraction of attenuated incident photons in a mono-energetic beam per unit thickness of the shield. It depends on both composition and density of the shielding material and can be better used to compare between the studied shields (Huda and Slone, 2003).  $\mu$  is calculated from mass attenuation coefficient  $(\mu/\rho)$  as follows (Lamarsh and Baratta, 2001):

$$\mu = \rho_{mix} (\mu/\rho) \quad (1.3)$$

where  $\rho_{mix}$ , in  $\text{g/cm}^3$ , is the density of the shielding material.

### 1.2.3.2 Half value layer, tenth value layer, and mean free path

Half value layer (*HVL*), tenth value layer (*TVL*), and mean free path (*MFP*), in cm, are all considered necessary parameters that evaluate the radiation shielding efficiency of the studied shield through defining the required thicknesses to attenuate the incident radiation to 50%, 10%, and  $\simeq 37\%$ , respectively (Lamarsh and Baratta, 2001; Oto et al., 2015). The

mentioned parameters are derived from linear attenuation coefficient ( $\mu$ ) using the following equations (Kaplan, 1989; Lamarsh and Baratta, 2001):

$$HVL = \frac{\ln 2}{\mu} \quad (1.4)$$

$$TVL = \frac{\ln 10}{\mu} \quad (1.5)$$

$$MFP = \frac{1}{\mu} \quad (1.6)$$

### 1.2.3.3 Effective atomic number

Effective atomic number ( $Z_{eff}$ ) is an important parameter to assess shielding against energetic photons, as it describes the electronic cloud that controls the photon/atom interaction process (Taylor et al., 2012; Hosamani and Badiger, 2018). In general,  $Z_{eff}$  is calculated using the following equation (Akman et al., 2015):

$$Z_{eff} = \frac{\sigma_a}{\sigma_e} = \frac{\sum f_i A_i (\frac{\mu}{\rho})_i}{\sum f_i \frac{A_i}{Z_i} (\frac{\mu}{\rho})_i} \quad (1.7)$$

where  $\sigma_a$  and  $\sigma_e$  are atomic cross-section and electronic cross-section of the shield,  $A_i$ ,  $Z_i$ ,  $f_i$ , and  $(\mu/\rho)_i$  are atomic mass, atomic number, atomic fraction, and mass attenuation coefficient of the  $i^{\text{th}}$  element.

### 1.2.3.4 Exposure build-up factors

Beer-Lambert law given in Eq. 1.8 (Kaplan, 1989) is only valid with the narrow-beam geometry. However, most real situations depend on the broad-beam geometry that requires an adjustment to be made to the Beer-Lambert law as represented by Eq. 1.9

where  $B$  is called the build-up factor (Kaplan, 1989; Lamarsh and Baratta, 2001). The build-up factor can be represented by exposure build-up factor (EBF) or energy absorption build-up factor (EABF); yet, EBF is most common to use in radiation shielding applications (Singh and Badiger, 2012; Oto et al., 2015; Kaur et al., 2019).

$$I_x = I_0 e^{-\mu x} \quad (1.8)$$

$$I_x = B I_0 e^{-\mu x} \quad (1.9)$$

where ( $I_0$ ) is the intensity of incident beam of photons, ( $I_x$ ) is the photons' intensity after passing a thickness of the shielding material that equals ( $x$ ), in cm.

The calculations take three primary steps in case of dealing with the composite shield. The first step is calculating the equivalent atomic number ( $Z_{eq}$ ) for the shielding material, which depends on the ratio ( $R$ ) between the partial mass attenuation coefficient due to Compton scattering  $(\mu/\rho)_{\text{Compton}}$  and the total mass attenuation coefficient  $(\mu/\rho)_{\text{total}}$ , using the interpolation method indicated by Eq. 1.10 (Harima, 1983).

$$Z_{eq} = \frac{Z_1(\log R_2 - \log R) + Z_2(\log R - \log R_1)}{\log R_2 - \log R_1} \quad (1.10)$$

where  $Z_1$  and  $Z_2$  are the atomic numbers of the two elements corresponding to the ratios  $R_1$  and  $R_2$ , respectively, and  $R$  is the ratio for the composite shield, at specific energy, that lies between  $R_1$  and  $R_2$ .

The second step is to calculate the five G-P fitting parameters ( $a, b, c, d, X_K$ ) using the interpolation method similar to  $Z_{eq}$  but this time based on the calculated  $Z_{eq}$  obtained in the first step as shown in the following equation (Harima, 1983):

$$Y = \frac{Y_1(\log Z_2 - \log Z_{eq}) + Y_2(\log Z_{eq} - \log Z_1)}{\log Z_2 - \log Z_1} \quad (1.11)$$

where  $Y$  represents the fitting parameter ( $a$ ,  $b$ ,  $c$ ,  $d$ , or  $X_K$ ) and  $Y_1$  and  $Y_2$  are the corresponding fitting parameters for the two elements with atomic numbers  $Z_1$  and  $Z_2$ , respectively. The elemental fitting parameters are usually collected from the “ANSI/ANS-6.4.3” standard data set (ANSI/ANS-6.4.3, 1991).

The last step is calculating EBF,  $B(E, X)$ , at the studied energy, employing the G-P fitting parameters obtained using the following equations (Harima et al., 1986):

$$B(E, X) = \begin{cases} 1 + \frac{b-1}{K-1}(K^X - 1) & \text{for } K \neq 1 \\ 1 + (b-1)X & \text{for } K = 1 \end{cases} \quad (1.12)$$

$$K(E, X) = CX^a + d \frac{\tanh\left(\frac{X}{X_K} - 2\right) - \tanh(-2)}{1 - \tanh(-2)} \text{ for penetration depth } (X) \leq 40 \text{ MFP} \quad (1.13)$$

where  $E$  is the energy of the incident photons,  $X$  is the penetration depth measured by  $MFP$ , and  $K$  is the dose multiplicative factor that describes the shape of the curve.

#### 1.2.3.5 Fast neutron macroscopic effective removal cross-section

The shielding effectiveness of the composite shield in attenuating fast neutrons is assessed by computing the macroscopic effective removal cross-section ( $\Sigma_R$ ) (El-Samrah et al., 2021). Elemental composition and the corresponding density of the shield are used to calculate  $\Sigma_R$  based on the following equation (Kaplan, 1989):

$$\Sigma_R = \sum_1^n \rho_s w_i (\Sigma_R / \rho)_i = \sum_1^n \rho_i (\Sigma_R / \rho)_i \quad (1.14)$$

where  $\rho_s$  and  $\rho_i$  are the shield density, in  $\text{g/cm}^3$ , and the partial density of the  $i^{\text{th}}$  element.

To get a better conception, the half value layer that is required to attenuate half of the incident fast neutrons beam ( $HVL_{fn}$ ), in cm, and the relaxation length ( $\lambda_{fn}$ ), in cm, which is the average distance traveled by a fast neutron before interacting with the medium, can be calculated based on  $\Sigma_R$  as follows (Kaplan, 1989; Lamarsh and Baratta, 2001):

$$(1HVL_{fn} = \frac{\ln 2}{\Sigma_R} \quad (1.15)$$

$$\lambda_{fn} = \frac{1}{\Sigma_R} \quad (1.16)$$

#### 1.2.3.6 Thermal neutron macroscopic absorption cross-section

The shield's ability to absorb thermalized neutrons is evaluated by calculating thermal neutron macroscopic absorption cross-section ( $\Sigma_{abs}$ ) (Soppera et al., 2014). Thermal neutron macroscopic absorption cross-section for composite shields,  $\Sigma_{abs}(E_n = 0.025 \text{ eV})$ , in  $\text{cm}^{-1}$ , can be calculated as follows (Madbouly and El-Sawy, 2018):

$$(\Sigma_{abs}/\rho)_i = \frac{N}{\rho_i} (\sigma_a)_i \quad (1.17)$$

$$N = \frac{\rho_i N_A}{M_i} \quad (1.18)$$

$$\Sigma_{abs}(E_n = 0.025 \text{ eV}) = \sum_1^n \rho_s w_i (\Sigma_{abs}/\rho)_i \quad (1.19)$$

where  $(\sigma_a)_i$ ,  $M_i$ ,  $(\Sigma_{abs}/\rho)_i$ ,  $N_A$ , and  $N$  are microscopic absorption cross-section for thermal neutrons, ( $\text{cm}^2/\text{atom}$ ), molar mass, (g/mol), and macroscopic mass absorption cross-section for thermal neutron, ( $\text{cm}^2/\text{g}$ ), Avogadro's constant, (atom/mol), and the atomic density of the element, ( $\text{atom}/\text{cm}^3$ ), respectively.

Like the case with fast neutrons, half value layer ( $HVL_{thn}$ ) and relaxation length ( $\lambda_{thn}$ ), regarding thermal neutrons, can be calculated from ( $\Sigma_{abs}$ ) as follows:

$$HVL_{thn} = \frac{\ln 2}{\Sigma_{abs}} \quad (1.20)$$

$$\lambda_{thn} = \frac{1}{\Sigma_{abs}} \quad (1.21)$$

### 1.3 Impetus of research

Due to the absence of a permanent geological repository until now and as the wet storage technique is impractical for storing radioactive wastes and SNF for long periods, interim dry storage has shown superiority as a reliable long-term storage technique for radioactive wastes, especially SNF, considering concrete-based cask is the most employed all over the world. Based on the former, improvement of the concrete overpack has become a spur for this research. Improving the properties of the concrete layer, especially the radiation shielding properties, leads to a general improvement in the properties of the storage cask. It also leads to a decrease in the required thickness, cross-sectional area, and the needed materials, thus minimizing the total storage area and associated costs.

### 1.4 Overall objective and scope

The intended objective of this study is to develop a concrete mixture for the outer overpack in the concrete-based dry storage cask with enhanced mechanical and radiation attenuation properties. The scope is limited to the concrete overpack and the effects of using certain aggregates on its properties. Detailed mechanical and thermal

characterizations, as well as long-term effects of continuous irradiation and heating on the concrete, are not included in this study.

## **1.5 Summary of the papers included**

This thesis comprises of five research papers that are summarized as follows;

### **Paper I: Spent nuclear fuel interim dry storage; design requirements, most common methods, and evolution: A review**

This study aims to shed light on the importance of the SNF interim dry storage technique and tries to cover, in a detailed fashion, the essential considerations relevant to the design and construction of dry storage casks. These considerations are referred to as follows; ensuring safe and reliable enclosure of the stored SNF assemblies, providing adequate radiation shielding, assurance of sustained subcriticality for the stored SNF throughout the service life of the cask, and achieving efficient and sustainable decay heat dissipation for the entire storage period. The review also captures the ongoing evolution of dry storage casks and facilities, considering the pros and cons of metal-based and concrete-based casks that show the superiority of sandwich-based concrete cask. Furthermore, it discusses two of the most recently launched interim dry storage methods.

### **Paper II: Characterization of natural and synthetic aggregates properties and their effect on the physical and mechanical properties of radiation shielding concrete**

Concrete is considered an effective shield that can be effectively used in attenuating all kinds of harmful radiations. However, to achieve the optimum protection against these harmful radiations and reduce the required shield thickness, which saves time, cost, and area, some modifications regarding the main components of the traditional concrete mix

must be done. This includes replacing the traditional aggregates with specific natural or synthetic aggregates or adding certain additives that possess unique radiation attenuation properties. This study provides a detailed characterization of these aggregates. Also, it investigates the concerns about the physical and mechanical properties of the produced concrete upon conducting these modifications by critically reviewing some reliable studies in preparation and assessment of radiation shielding concrete (RSC). Furthermore, a design methodology is set to get an optimum design for radiation shielding concrete through this critical review.

### **Paper III: MRCsC: A user-friendly software for predicting shielding effectiveness against fast neutrons**

In order to evaluate the fast neutron shielding properties of the proposed mixes during this research and in the absence of a reliable and uncomplicated tool to provide the needed parameters, the idea of this study came to mind. This paper presents developing a new computer program named MRCsC, which is constructed to produce accurate macroscopic effective removal cross-sections,  $\Sigma_R$ , of fast neutrons for different shielding materials. MRCsC program is a user-friendly software that is written and programmed using C-sharp language. Moreover, a modified calculation method is adopted to build up its built-in database based on the most recently updated microscopic total neutron cross-section values provided by the latest version of the Evaluated Nuclear Data Library “ENDF/B-VIII”. The program database contains the mass removal cross-sections,  $\Sigma_R/\rho$ , of all naturally occurring elements, including elements with insignificant natural abundance. For validation, results obtained from the developed program are compared with published

experimental data and other theoretically calculated results from the NXCom program. A good agreement between the MRCsC results and those experimentally measured is observed. Upon comparing the program results with the corresponding NXCom results, the effectiveness and precision of the MRCsC program can be proved. Finally, the MRCsC program can be used as a reliable design/assessment tool for any shielding material dealing with fast neutron attenuation.

#### **Paper IV: Mechanical and radiation shielding properties of concrete containing commercial boron carbide powder**

Boron-containing compounds have a significant role in radiation shielding applications as they own a splendid ability to shield against thermal, epithermal, and slow neutrons. However, most of them show a lack of compatibility when using in cementitious mixtures. In this study, commercial fine-powdered boron carbide ( $B_4C$ ) is investigated to determine its impact on Portland cement hydration reaction and concrete compressive strength upon addition with increasing percentages based on isothermal calorimetry and analytical models. To assess radiation shielding properties, needful shielding parameters concerning photons and neutrons are calculated for concrete mixes containing different percentages of the studied powder. Mass attenuation coefficient,  $\mu/\rho$ , and effective atomic number,  $Z_{\text{eff}}$ , are calculated for the studied mixes for photon energy range; 10 KeV to 10 MeV. Then, linear attenuation coefficient ( $\mu$ ), half-value layer (HVL), and mean free path (MFP) are derived. Moreover, fast neutron macroscopic effective removal cross-section ( $\Sigma_R$ ) and thermal neutron macroscopic absorption cross-section ( $\Sigma_{\text{Abs}}$ ) are calculated for the studied concrete mixes, and the corresponding half-value layers ( $HVL_{\text{fn}}$  and  $HVL_{\text{thn}}$ )

are derived. The obtained results reveal that the studied fine-powdered boron carbide shows a beneficent effect on Portland cement hydration reaction, concrete compressive strength, and a noticeable improvement regarding neutron shielding capabilities upon employing in cementitious composites. However, the existence of soluble boron impurities leads to significant retardation in Portland cement initial setting time that increases with boron content increase in the mix.

#### **Paper V: Radiation shielding properties of modified concrete mixes and their feasibility in dry storage cask**

In this study, eight concrete mixes are prepared using two different cementing material's contents based on four different types of coarse aggregates; dolomite (Do), barite (Ba), ilmenite (Ilm), and celestite (Cel). The main objective is to assess the radiation shielding properties of the prepared concrete mixes in a detailed fashion by obtaining the following radiation shielding parameters; mass attenuation coefficient ( $\mu/\rho$ ), effective atomic number ( $Z_{\text{eff}}$ ), linear attenuation coefficient ( $\mu$ ), half value layer (HVL), tenth value layer (TVL), and mean free path (MFP) for energies ranging from 10 keV to 10 MeV. Exposure build-up factor (EBF) is calculated for the studied concrete mixes using the Geometric Progression (G-P) approximation method up to 40 mean free paths (mfp) for energies range from 15 keV to 10 MeV. Fast neutron macroscopic effective removal cross-section ( $\Sigma_R$ ) and thermal neutron macroscopic absorption cross-section ( $\Sigma_{\text{abs}}$  ( $E_n=0.025\text{eV}$ )) are also calculated to evaluate the mixes' neutron shielding capability. Moreover, the studied mixes are assessed upon employing as a concrete layer in a dry storage cask (DSC) with the help of a (DSC) model developed/simulated using OpenMC

code. All heavy concrete mixes are found to have better radiation shielding properties than that for traditional Do.C mixes especially Ba.C and CeI.C mixes that also show a great reduction in the total dose rate when simulated as an overpack in a sandwich-based storage cask. Furthermore, the differences between the mixes prepared using mix design no. 1 and those mixes employed mix design no. 2 are insignificant.

## **1.6 Conclusions and recommendations for future work**

### **1.6.1 Conclusions**

Critical review and experimental and analytical results presented in this dissertation reveal the importance of the interim dry storage technique and concrete as one of its essential components, especially in sandwich-based concrete dry storage cask. The results also show the improvements that can be achieved when choosing proper materials and reliable mix design for preparing radiation shielding concrete used in SNF interim dry storage. Based on the abovementioned studies that constitute this dissertation, the following conclusions are obtained:

- Interim dry storage for SNF has become very important, as growing amounts of SNF around the world cannot be retained in wet storage over long periods and due to the absence of a permanent storage repository.
- To design and build a reliable dry storage cask that provides efficient storage for these harmful radioactive wastes, some considerations such as safe containment, adequate radiation shielding, subcriticality assurance, and efficient decay heat removal must be achieved in the long range.

- The development in dry storage techniques has not stopped dealing with the conclusions and lessons learned from significant incidents such as Sept. 11<sup>th</sup> and the Fukushima Daiichi disaster. Moreover, adopting modern welding techniques and nano-technology leads to robust casks carrying more heat loads and having a longer service life.
- Through this evolution, developing the concrete layer in concrete-based casks is found to minimize the overpack thickness, the size and weight of the entire cask, and the total storage area thus, saving materials and reducing the total costs.
- Sandwich-design concrete-based cask has shown evident reliability and feasibility as a SNF storage cask that can be used for SNF transportation.
- Radiation shielding concrete usually depends on using specific aggregates to achieve the optimum attenuation capability against the incident radiation and reduce the required thickness, leading to economic benefits due to materials' saving and area reduction.
- Upon employing some of these aggregates, some physic-mechanical considerations are observed for the produced concrete.
- Petrographic analysis and mechanical characterization of the aggregates before use are essential as aggregates' physical and mechanical properties play a notable role in characterizing the final properties of the produced concrete.
- Physical and mechanical properties for the same ore are highly dependent on the mine from where it is extracted.

- Using an optimum aggregates' volume fraction and proper gradation enhances the ratio between packing density and maximum packing density, leading to an overall enhancement in the mechanical properties of the produced radiation shielding concrete.
- Developing a design methodology for radiation shielding concrete helps prepare efficient concrete with optimum physical, mechanical, and radiation shielding properties.
- MRCsC program is a user-friendly software developed through this study and can precisely compute fast neutron macroscopic effective removal cross-section for shielding materials using only the elemental analysis and the density.
- It was found that adding commercial fine-powdered B<sub>4</sub>C with high purity improves Portland cement hydration reaction and concrete compressive strength due to the filler effect.
- The presence of soluble boron compounds as impurities causes a retardation effect on Portland cement hydration reaction.
- The addition of B<sub>4</sub>C, as fine aggregate replacement, to cementitious mixtures has an insignificant effect on  $\gamma$ -rays attenuation properties.
- Adding B<sub>4</sub>C powder to cementitious mixtures in perceptible proportions enhances the fast neutron shielding properties. However, adding it even as a small percent would significantly increase the thermal neutron absorption capacity of the composite shield.

- Obtaining an appreciable linear attenuation coefficient ( $\mu$ ) for the shield is not the only indicator of a shield's effectiveness in attenuating gamma rays as exposure build-up factors have a significant role besides ( $\mu$ ) in evaluating the shielding effectiveness. An obvious example is Cel.C mixes' superiority compared to Ilm.C mixes as elaborated through the study.
- Heavy concrete containing heavy minerals consisting of high-Z elements possesses radiation shielding properties better than that for traditional concrete.
- Ba concrete is the best among the studied concrete mixes in attenuating X-rays and  $\gamma$ -rays for both narrow-beam and broad-beam geometries.
- Cel concrete, which is studied for the first time as radiation shielding concrete, has reliable radiation shielding properties.
- Ilm concrete has good  $\gamma$ -rays shielding capability in addition to the considerable neutron shielding properties.
- SNF storage cask as a nuclear application needs protection against multiple sources of radiation with the override being reliable  $\gamma$ -rays shielding capabilities.
- An overpack slightly thicker than 50 cm of Ba concrete or Cel concrete is potentially feasible to use in SNF concrete-based storage cask as their calculated total dose rates are slightly above the recommended safety limit of 20 - 400 mrem/h.

### **1.6.2 Recommendations for future work**

Considering the research findings reported in this dissertation; this section presents possible research extensions for further improvement and better knowledge regarding the employed concrete in SNF interim dry storage.

- Assessing the physic-mechanical and thermal properties, in detail, for the prepared radiation shielding concrete mixes presented in this study will give a clear image about the overall behavior of these mixes, and their feasibility, in various SNF interim dry storage types.
- Studying the effects of continuous irradiation and heating simultaneously on these proposed mixes can conceptualize the long-term behavior of these mixes if employed as a concrete overpack in a concrete-based dry storage cask.
- Investigating the shielding requirements of the storage cask, considering the proposed concrete mixes, upon increasing the radioactive load i.e., the number of fuel assemblies to be stored.

## **1.7 References**

Akman, F., R. Durak, M. F. Turhan and M. R. Kaçal (2015). "Studies on effective atomic numbers, electron densities from mass attenuation coefficients near the K edge in some samarium compounds." *Applied Radiation and Isotopes* 101: 107-113.

Almomani, B., S. Lee, D. Jang and H. G. Kang (2017). "Probabilistic risk assessment of aircraft impact on a spent nuclear fuel dry storage." *Nuclear Engineering and Design* 311: 104-119.

- ANSI/ANS-6.4.3 (1991). Buildup Factor for Engineering Materials. New York, USA, American National Standards Institute.
- Bruno, J. and R. C. Ewing (2006). "Spent nuclear fuel." *Elements* 2(6): 343-349.
- Clarity, J. B., K. Banerjee, H. K. Liljenfeldt and W. J. Marshall (2017). "As-Loaded Criticality Margin Assessment of Dual-Purpose Canisters Using UNF-ST&DARDS." *Nuclear Technology* 199(3): 245-275.
- Droste, B. (2013). "A survey on 35 years of packaging, transport and storage of radioactive material."
- El-Samrah, M., A. El-Mohandes, A. El-Khayatt and S. Chidiac (2021). "MRCsC: A user-friendly software for predicting shielding effectiveness against fast neutrons." *Radiation Physics and Chemistry* 182: 109356.
- Ewing, R. C. (2015). "Long-term storage of spent nuclear fuel." *Nature Materials* 14(3): 252.
- Fairlie, E. S. a. I. (2016). "Dealing with nuclear waste is so difficult that phasing out nuclear power would be the best option." *Lfpress*.
- Fukuda, K., W. Danker, J. Lee, A. Bonne and M. Crijns (2003). IAEA Overview of global spent fuel storage. *Proceedings of the Storage of Spent Fuel from Power Reactors, 2003, Vienna*.
- Gerward, L., N. Guilbert, K. B. Jensen and H. Leving (2004). "WinXCom—a program for calculating X-ray attenuation coefficients." *Radiation physics and chemistry* 71: 653-654.

- Gray, E. (2015). Coast to coast spent fuel dry storage problems and recommendations. Division of Spent Fuel Management Regulatory Conference.
- Haire, M. J. (2006). "Cask Size and Weight Reduction Through the Use of Depleted Uranium Dioxide (DUO<sub>2</sub>)–Concrete Material."
- Haire, M. J. and P. M. Swaney (2005). "Cask Size and Weight Reduction Through the Use of Depleted uranium Dioxide (DUO<sub>2</sub>)-Steel Cermet Material." Waste Management.
- Hanifehzadeh, M., B. Gencturk and R. Mousavi (2018). "A numerical study of spent nuclear fuel dry storage systems under extreme impact loading." Engineering Structures 161: 68-81.
- Harima, Y. (1983). "An approximation of gamma-ray buildup factors by modified geometrical progression." Nuclear Science and Engineering 83(2): 299-309.
- Harima, Y., Y. Sakamoto, S. Tanaka and M. Kawai (1986). "Validity of the geometric-progression formula in approximating gamma-ray buildup factors." Nuclear Science and Engineering 94(1): 24-35.
- Hosamani, M. and N. Badiger (2018). "Determination of effective atomic number of composite materials using backscattered gamma photons—a novel method." Chemical Physics Letters 695: 94-98.
- Hu, J., J. L. Peterson, I. C. Gauld and S. M. Bowman (2016). US Commercial Spent Nuclear Fuel Assembly Characteristics-1968-2013, Oak Ridge National Lab.(ORNL), Oak Ridge, TN (United States).

- Huda, W. and R. M. Slone (2003). Review of radiologic physics. USA, Lippincott Williams & Wilkins.
- IAEA (2012). Storage of Spent Nuclear Fuel. Vienna, INTERNATIONAL ATOMIC ENERGY AGENCY.
- IAEA (2020). Methodology for a Safety Case of a Dual Purpose Cask for Storage and Transport of Spent Fuel. Vienna, INTERNATIONAL ATOMIC ENERGY AGENCY.
- Kaplan, M. F. (1989). Concrete radiation shielding. NY, USA, John Wiley & Sons.
- Kaur, P., K. Singh, M. Kurudirek and S. Thakur (2019). "Study of environment friendly bismuth incorporated lithium borate glass system for structural, gamma-ray and fast neutron shielding properties." Spectrochimica acta part A: molecular and biomolecular spectroscopy 223: 117309.
- Ko, J.H., J.H. Park, I.S. Jung, G.U. Lee, C.Y. Baeg and T.M. Kim (2014). "Shielding analysis of dual purpose casks for spent nuclear fuel under normal storage conditions." Nuclear engineering and Technology 46(4): 547-556.
- Lamarsh, J. R. and A. J. Baratta (2001). Introduction to nuclear engineering. Prentice hall Upper Saddle River, NJ, USA.
- Madbouly, A. and A. A. El-Sawy (2018). "Calculation of gamma and neutron parameters for some concrete materials as radiation shields for nuclear facilities." International Journal of Emerging Trends in Engineering and Development 3(8): 7-17.
- Oto, B., N. Yıldız, T. Korkut and E. Kavaz (2015). "Neutron shielding qualities and gamma ray buildup factors of concretes containing limonite ore." Nuclear Engineering and Design 293: 166-175.

- Ouda, A. S. (2015). "Development of high-performance heavy density concrete using different aggregates for gamma-ray shielding." *Progress in Nuclear Energy* 79: 48-55.
- Parks, C. V. (2000). *Review and Prioritization of Technical Issues Related to Burnup Credit for LWR Fuel*, ORNL Oak Ridge National Laboratory (United States).
- Poškas, R., V. Šimonis, H. Jouhara and P. Poškas (2019). "Modeling of decay heat removal from CONSTOR RBMK-1500 casks during long-term storage of spent nuclear fuel." *Energy* 170: 978-985.
- Ratiko, R., S. A. Samudera, R. Hindami, A. T. Siahaan, L. Naldi, D. Hapsari, T. Mahlia and N. Nasruddin (2018). "Optimization of dry storage for spent fuel from GA Siwabessy nuclear research reactor." *International Journal of Technology*.
- Roland, V., M. Chiguer and Y. Guenon (2003). "Dry storage technologies: Keys to choosing among metal casks, concrete shielded steel canister modules and vaults." *Storage of Spent Fuel from Power Reactors* 107.
- Saegusa, T., K. Shirai, T. Arai, J. Tani, H. Takeda, M. Wataru, A. Sasahara and P. Winston (2010). "Review and future issues on spent nuclear fuel storage." *Nuclear Engineering and Technology* 42(3): 237-248.
- Saegusa, T., G. Yagawa and M. Aritomi (2008). "Topics of research and development on concrete cask storage of spent nuclear fuel." *Nuclear Engineering and Design* 238(5): 1168-1174.
- Shimizu, Y. (2016). *Lessons Learned from the Fukushima Daiichi Accident, Actions Taken and Challenges Ahead*. International Conference on Effective Nuclear Regulatory Systems.

- Singh, V. P. and N. Badiger (2012). "Comprehensive study of energy absorption and exposure build-up factors for concrete shielding in photon energy range 0.015–15 MeV up to 40 mfp penetration depth: dependency of density, chemical elements, photon energy." *International Journal of Nuclear Energy Science and Technology* 7(1): 75-99.
- Soppera, N., M. Bossant and E. Dupont (2014). "JANIS 4: An improved version of the NEA java-based nuclear data information system." *Nuclear Data Sheets* 120: 294-296.
- Taylor, M., R. Smith, F. Dossing and R. Franich (2012). "Robust calculation of effective atomic numbers: The Auto-Zeff software." *Medical physics* 39(4): 1769-1778.
- U.S.NRC (2010). *Standard review plan for spent fuel dry storage systems at a general license facility*. 1.
- Vitkova, M., I. Gorinov and D. Dacheva (2006). "Safety criteria for wet and dry spent fuel storage."
- Vlček, D. (2018). "Residual heat power removal from spent nuclear fuel during dry and wet storage." *Acta Polytechnica CTU Proceedings* 19: 36-45.
- Wimmer, H., J. Skrzyppek and M. Koebl (2015). "CASTOR® and CONSTOR®. A well established system for the dry storage of spent fuel and high level waste." *VGB PowerTech* 95(5): 52-57.
- Wu, Y., J. Klein, H. Zhou and L. Zuo (2018). "Thermal and fluid analysis of dry cask storage containers over multiple years of service." *Annals of Nuclear Energy* 112: 132-142.

## **2. Spent nuclear fuel interim dry storage; design requirements, most common methods, and evolution: A review**

### **2.1 Abstract**

This review discusses the importance of interim dry storage of spent nuclear fuel. It addresses the requirements to achieve safe and efficient enclosure of spent nuclear fuel assemblies, including providing adequate radiation shielding, maintaining subcriticality, and achieving reliable and efficient decay heat removal process throughout the entire storage period. The review also covers the evolution regarding the dry storage casks and facilities and considers the pros and cons of metal-based and concrete-based casks. Furthermore, two of the most recently deployed techniques for spent nuclear fuel interim dry storage are also addressed.

Keywords: Spent nuclear fuel; Interim dry storage; Dry storage cask; Design requirements

### **2.2 Introduction**

Safe disposal of radioactive wastes remains a critical hurdle for the nuclear industry. The requirements for safe long-term disposal of radioactive wastes represent significant engineering challenges. A demonstrated permanent disposal solution is pivotal for a sustainable industry (Vitkova et al., 2006; Ewing, 2015). Per the US Nuclear Regulatory Commission 10CFR60.2 definition, High-level waste includes (1) Irradiated reactor fuel,

(2) liquid wastes resulting from the operation of the first cycle solvent extraction system, or equivalent, and the concentrated wastes from subsequent extraction cycles, or equivalent, in a facility for reprocessing irradiated reactor fuel, and (3) solids into which such liquid wastes have been converted. The dry cask designs reviewed here only apply to storage of irradiated (spent) nuclear reactor fuel, not liquid first cycle raffinates, concentrated solutions, or solidified HLW (U.S.NRC, 1981; Krause, 1984).

International waste classifications are based on specific values of radioactivity to define low, intermediate and high-level radioactive wastes. Reactor sites may use dry cask storage for non-fuel high activity radioactive waste that must be disposed in a deep geologic repository (U.S.NRC, 1981; Heinonen and Malasek, 1984).

In general, spent nuclear fuel (SNF) that is discharged from operating water-cooled reactors is temporarily stored at the reactor secondary pool, referred to as at-reactor (AR) pool, for a short period before being moved to a storage pool for a period of 5 to 10 years. For commercial power reactors that have a licensed Independent Spent Fuel Storage Facility (ISFSI), the SNF is then transferred to an interim dry storage system (Fukuda et al., 2003; Lewis, 2003).

Wet storage being an active and costly process and with the absence of permanent geological storage repository for SNF, interim dry storage has evolved as a viable alternative given its advantages as listed in Table 2.1 based on (Vitkova et al., 2006; IAEA, 2012; Ratiko et al., 2018).

**Table 2.1** Comparison between wet storage and dry storage for SNF

Wet storage	Dry storage
Water usually contains radioactivity especially due to the formation of tritium	No generation of liquid waste
Water continuously needs to be chemically treated and monitored to adjust the concentration of some ingredients like boric acid	No need for a complex and expensive purification system
Higher corrosion probabilities	Lower corrosion probabilities
Active decay heat removal system based on the continuous circulation of the pool's water on heat exchangers and continuous monitoring to maintain adequate temperatures	Passive decay heat removal system based on natural convection, conduction, and thermal radiation
Wet storage facilities are fixed and fuel assemblies must be removed carefully via transportable shielded systems for further reprocessing or final disposal	Easier to transport if in the future the storage needs to be sent to a permanent repository
Higher risks regarding the release of a greater amount of radioactivity in case of extreme accidents or terroristic events	Release of radioactivity is with lower probability and lower amounts like the case with separate dry casks or underground dry storage facilities

These systems are generally metal dual-purpose casks or two-part systems with metal canisters that contain the radioactive material that are placed in shield structures that are commonly made of concrete. Casks and canisters may be stored in a vertical or horizontal orientation (Haire and Swaney, 2005; Bruno and Ewing, 2006).

The term cask typically refers to packages with thick walls that provide integral radiation shielding for each container. The metal walls may be steel that has been formed into a cylindrical vessel with welded seams and ends with gamma ray shielding using lead, steel

or specialized high-density concrete. Other common designs use thick-wall forged steel rings and heads to form the cask body. In some designs, the body of the cask is fabricated as a single casting of ductile iron. Secondary components are added to provide neutron shielding. Metal-shielded casks are intended to function as dual-purpose designs that meet the requirements for both storage and transportation (IAEA, 2018). In onsite operation, the cask is loaded in the fuel cooling pool and then moved to the storage pad using a heavy transport vehicle (Krause, 1984; Husain and Choi, 2003).

Due to the geometry of the fuel being stored and structural design needs, all of the cask and canister designs reviewed in this document are right circular cylinders of varying lengths and wall thicknesses.

The term canister is usually applied to designs where the majority of the containment package has a thin metal wall that does not provide radiation shielding or impact structure. These designs depend on a secondary structure that is either a reinforced concrete vault or a metal and concrete annulus to provide radiation shielding. Horizontally-loaded systems use a canister with shielding in the ends of the canisters to minimize personnel exposure during loading. Some systems that use the canister-vault approach are deployed with the canister axis in a vertical orientation, while others load the canister into a horizontal vault (Roland et al., 2003; IAEA, 2012; WNN, 2017).

Most recent vertical shield units have metal external and internal shells filled with concrete shield material. Transportation of canisters requires use of a separate metal shielding cask as an overpack that meets the impact criteria for shipping. In general, the concrete-shielded canister systems have lower initial cost because of the reduced cost of

concrete when compared to fabricated metal shield components (Saegusa et al., 2008; Droste, 2013). Onsite handling of the canister involves loading in the pool inside a transfer shield and removing the canister and transfer shield unit from the pool for welding. For horizontal storage systems, a special onsite shielded transfer cask is used to move the canister from the pool to the concrete storage module. For vertical storage systems, the canister is transferred into the shield unit inside the fuel storage building using the transfer shield unit. The vertical storage shield containing the canister is then moved to the outdoor storage pad in the vertical position using a specialized heavy-haul transporter (IAEA, 2000).

In the US, the economics of the concrete-shielded storage has made the various versions of this concept that become the dominant means of storage, with over 1900 canisters containing more than 70,000 fuel assemblies versus 200 metal dual purpose casks containing more than 9000 assemblies as of 2016 (Connolly and Pope, 2016; Hu et al., 2016).

The phasing out of nuclear power by countries that depended on it for energy production has amplified the need for robust, safe and reliable interim long term dry storage facilities. Dry storage must meet rigid requirements to ensure safe, efficient and reliable long-term storage for SNF. As such, storage system vendors continue to improve the performance of dry storage technology against extreme events like tsunamis, tornados, flooding and earthquakes, and terrorist acts (Wimmer et al., 2015; Shimizu, 2016; Almomani et al., 2017; Vlček, 2018).

This paper provides a critical review of the on-going development including the requirements and considerations pertaining to the design and implementation of dry storage casks and some known dry storage facilities.

## **2.3 Design requirements**

The design and construction requirements of dry storage casks to store SNF, which encompass safety and longevity, include reliable containment of the radioactive wastes under any possible mechanical loads, radiation shielding, subcriticality, and heat dissipation (Wimmer et al., 2015; U.S.NRC, 2020).

### **2.3.1 Safe enclosure of the contained SNF**

For SNF, it is assumed that the material being stored is generally intact fuel assemblies. The first requirement of a storage cask or canister is to assure that there is no leakage of any radioactive material during the entire service life of the storage system. Because the fuel structure is expected to provide a first barrier against dispersal, the system should also be designed to protect the spent fuel cladding against damage or degradation during the storage. Some of the possible factors that can affect the integrity of the stored spent fuel and its cladding are; thermal creep, cladding creep under internal gas pressure, stress corrosion cracking, delayed hydride cracking of the cladding, hydride reorientation, corrosion of the cladding due to possible oxidation and defect propagation of the cladding due to oxidation of  $\text{UO}_2$  to  $\text{U}_3\text{O}_8$  in case of defective fuel (IAEA, 1995; Vitkova et al., 2006).

The cask or canister functions as another barrier that prevents radioactive material leakage through a specified lifetime. Thus, material selection, reliable geometrical design and proper manufacturing of the cask or canister are of the utmost importance. Precise fabrication of the cask or canister and use of welded or bolted primary and secondary lids with metallic seals are widely used to ensure leak-tightness (Saegusa et al., 2008; Wimmer et al., 2015).

Integral metal-shielded casks commonly have primary and secondary lids that use O-ring metal seals. Assurance of leak tightness is done by monitoring that the pressure between the lids is higher than the atmospheric pressure. For canisters used with the concrete-shielded storage systems, the canister lids are seal-welded and there is no monitoring of the pressure between the lids. Fig. 2.1 presents vertical cross-sections showing both the metal and the concrete-shielded designs (Saegusa et al., 2008; Wimmer et al., 2015).

To ensure long term integrity of the canisters, many studies investigated the effects of environmental conditions at sites that have high atmospheric chloride concentration (e.g., coastal storage sites). These studies were to evaluate potential for pitting corrosion and Stress Corrosion Cracking (SCC) resistance of the steel canister. For concrete shielded systems, the durability of the concrete layer was evaluated on the basis of chloride diffusion (Saegusa et al., 2008; Gray, 2015).

These studies recommended using SCC-resistant grades of stainless steel like ferritic stainless steel and duplex stainless steel for the casks to be installed in coastal sites. In addition, they emphasized on the importance of the frequent inspection and maintenance.

It has been recommended that concrete shielding structures should be constructed with very low chloride content to reduce the permeability and diffusivity of chloride ions thus, protecting the concrete reinforcement steel and the inner liner (Saegusa et al., 2008; Gray, 2015).

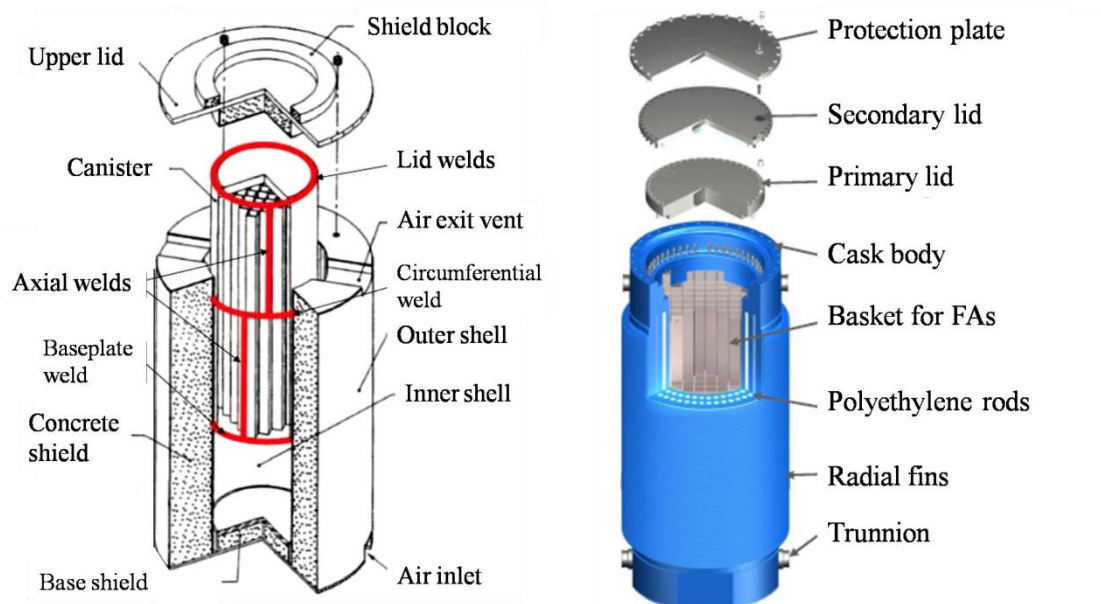


**Fig. 2.1** Vertical cross-sections of concrete-based cask design with welded lid (on the left) and full-metal cask design with primary and secondary lids using O-ring gaskets (on the right), adapted from (Saegusa et al., 2008; Wimmer et al., 2015)

### 2.3.2 Structural response and integrity

Casks and canisters are moved from the fuel storage pool to the interim storage site following being loaded with spent fuel. Eventually the storage packages are intended to be transported to a final disposal site. The casks and canisters must be able to contain the radioactive material in the event of accidents during handling. These accidents range from drops when the loaded package is being removed from the pool to high-speed impact

accidents that could occur in cross country transportation (Stahmer, 2009; Saegusa et al., 2010). Because canisters have minimal shielding, they must be moved using a shielded overpack, whether as part of the storage system or a specifically-designed, shielded transportation package (IAEA, 2018). Transportable packages add impact limiters to absorb kinetic energy to minimize damage to the primary containment component, whether it is a full metal cask or a canister-overpack design. In the event of an impact accident, the cask or canister may be deformed, but must contain its radioactive payload without leaking greater than specified values (Wimmer et al., 2015; Hanifehzadeh et al., 2018; IAEA, 2020).

Analytical models and scale model tests are used to evaluate the structural response and integrity of SNF dry storage casks. Accident analyses address vertical drop from different heights (with and without impact limiters), horizontal drop, tipping over, earthquake testing (or seismic analysis) and aircraft or missile horizontal and vertical impacts (with and without impact limiters) as shown in Fig. 2.2 (Saegusa et al., 2010; Almomani et al., 2017; Hanifehzadeh et al., 2018; IAEA, 2020).

Some of these tests are performed using a full-scale cask. Some other tests that are usually difficult or very expensive to be performed experimentally with the full scale can be performed using reduced scale or can be replaced by well-validated analytical models. Models are commonly used for seismic analysis and aircraft impact simulation scenarios (Saegusa et al., 2010; Almomani et al., 2017; Hanifehzadeh et al., 2018).

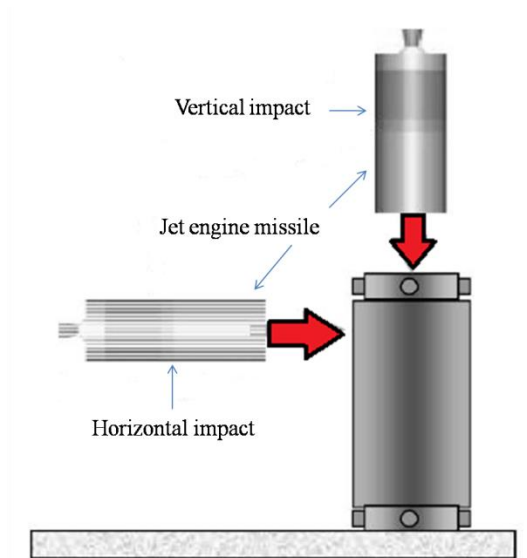


**Fig. 2.2** Considered Scenarios for Aircraft Engine Crash onto a full-metal cask, adapted from (Saegusa et al., 2010)

The mentioned tests are reviewed to assess the structural response and integrity of the cask components that provide leak tightness. These components are; the lid(s), the welds, the transportation overpack, and the contained canister (Saegusa et al., 2010; Almomani et al., 2017; Hanifehzadeh et al., 2018).

Metal based casks usually show higher degree of robustness and reliability under these tests than concrete based casks do. However, cask designs such as the GNS CONSTOR that use specialized concrete shielding encapsulated in structural steel show acceptable response and reliability under these structural evaluations and may be utilized for both SNF storage and transportation (Droste, 2013; Wimmer et al., 2015).

Testing of a metal-based cask without impact limiters against severe horizontal impact of an aircraft engine showed that the leak rate value from the lid immediately increased by 5

orders of magnitude during the impact. However, the measured leak rate was less than  $1.0 \times 10^{-5}$  Pa.m<sup>3</sup>/s. which indicates a high quality of leak-tightness (Saegusa et al., 2010).

### **2.3.3 Radiation shielding**

Radiation shielding requirements of dry storage casks are a function of total number of assemblies, the fuel type (UO<sub>2</sub> or MOX), the length of the cooling period in the storage pools and the burnup value of the spent fuel to be stored (Connolly and Pope, 2016; Hu et al., 2016). The dose rate for each fuel assembly is based on; the amount of fuel fission, activation products, its activated structural components and its time out of reactor. According to US-NRC regulations, the preliminary cooling, and storage period in the auxiliary storage pools should be at least 5 years prior to transfer of intact SNF to dry storage (Connolly and Pope, 2016; Hu et al., 2016). Some recently deployed storage system designs reduce this period to only three years (HOLTEC, 2013). Historically, the preferred period of wet storage is 7 – 10 years before transferring to interim dry storage facilities to be sure that most of the decay heat is released and the short-lived isotopes have decayed (Wegel et al., 2017; U.S.NRC, 2020).

The design life for interim dry storage is projected to be 10 to 50 years. During this period, fission products such as Sr-90, which is a pure beta emitter, ( $t_{1/2}$ = 28.9 years) and Cs-137 (30.2 years) account for the most of decay heat and radiation, respectively. For shielding purposes, Cs-137 is the main gamma emitter for the stored SNF up to 100 years. Other gamma dose contributors include fission products like Cs-134, Eu-154. Co-60 is present as an activation product in the steel structural components of fuel assemblies. It

produces a high energy gamma emission, but only has a 5.27 year half life (Hu et al., 2016; Pořkas et al., 2019).

In practical terms, only neutron and gamma radiation require specific shielding. Alpha and beta particle energy is absorbed within the fuel, and any Brehmstrahlung radiation will be absorbed by the massive gamma shielding (Chilton et al., 1984; Fukuda et al., 2003).

Although the main hazardous doses that need to be shielded are due to gamma radiation, a detectable amount of the total dose is due to fast neutrons. This dose increases with; decreased cooling (wet storage) period, increased burnup value, use of low-enriched fuel and using mixed oxide fuel (MOX) (Hu et al., 2016; Bruno et al., 2020).

The main source of the neutron dose in SNF is due to minor actinides and transuranic isotopes of curium or californium that undergo spontaneous fission. Most curium isotopes have short half-lives (Cm-240 and Cm-242, 26.7 days and 160 days, respectively). Cm-244, however has an 18.1 year half-life and is considered the most important neutron dose contributor in the interim storage stage (Audi et al., 2003; Ewing, 2008). Fissile plutonium isotopes, in case of non-processed fuel, participate in the neutron dose through fission and alpha-neutron reactions, (n, f) and ( $\alpha$ , xn) reactions, but with less degree (Ewing, 2008; Hu et al., 2016; Bruno et al., 2020).

Adequate radiation shielding against gamma rays requires massive shield structure that envelopes the radioactive material with a thickness depends on the density of the material used and its elemental composition and the activity of the radioactive material (Chilton et

al., 1984). This envelope is usually steel or ductile iron for all-metal dual purpose casks. For all-metal designs, neutron shielding in the form of borated polyethylene or another specialized resin layer is added as a component of this envelope (Droste, 2013; Wimmer et al., 2015; IAEA, 2020).

For concrete shielded canister storage systems, the shielding envelope can be concrete with an inner steel liner, reinforced concrete or a steel-concrete-steel annulus with internal and external steel shells. Due to the lower density of concrete, the shield components are thicker than their metal counterparts however, concrete can provide adequate shielding against both gamma rays and neutrons via selecting proper materials/mix design and water content incorporated in it (Kaplan, 1989; Masoud et al., 2020).

These configurations are represented by some well-known storage systems that are already in service. For example, Gesellschaft für Nuclear Service (GNS) produces the widely-used CASTOR dual-purpose full-metal cask and CONSTOR casks that use integral concrete shielding inside a steel shell that are used for open air and indoor storage facilities (Wimmer et al., 2015; Pořkas et al., 2019). Both designs are intended to be used for storage and transportation purposes, although the CASTOR casks are not certified for transportation by the US NRC (Connolly and Pope, 2016; Hu et al., 2016).

For dual-purpose casks (CASTOR V/19 and V/21), the cask generally consists of a thick-walled (about 40 cm) monolithic body made of single ductile iron casting. The cask body and lids provide the desired shielding against gamma-radiation. For neutron moderation, axial bore holes are drilled into the cask walls and filled with polyethylene rods. Neutron

shielding on the ends of the cylinder is present as plates of polyethylene at the bottom end and on the underside of the secondary lid (Funke and Diersch, 2004; Wimmer et al., 2015).

For CONSTOR casks, the cask body composed of a hybrid structure, having an inner liner and an outer liner both made of steel. The space between the liners is filled with CONSTORIT which is heavy concrete based on iron aggregates and copper heat-conducting elements. Other specialized shielding concretes use heavy barite aggregates with dispersed steel granules. Fig. 2.3 shows schematic diagrams for both CASTOR V/19 and CONSTOR casks (Funke and Diersch, 2004; Wimmer et al., 2015).

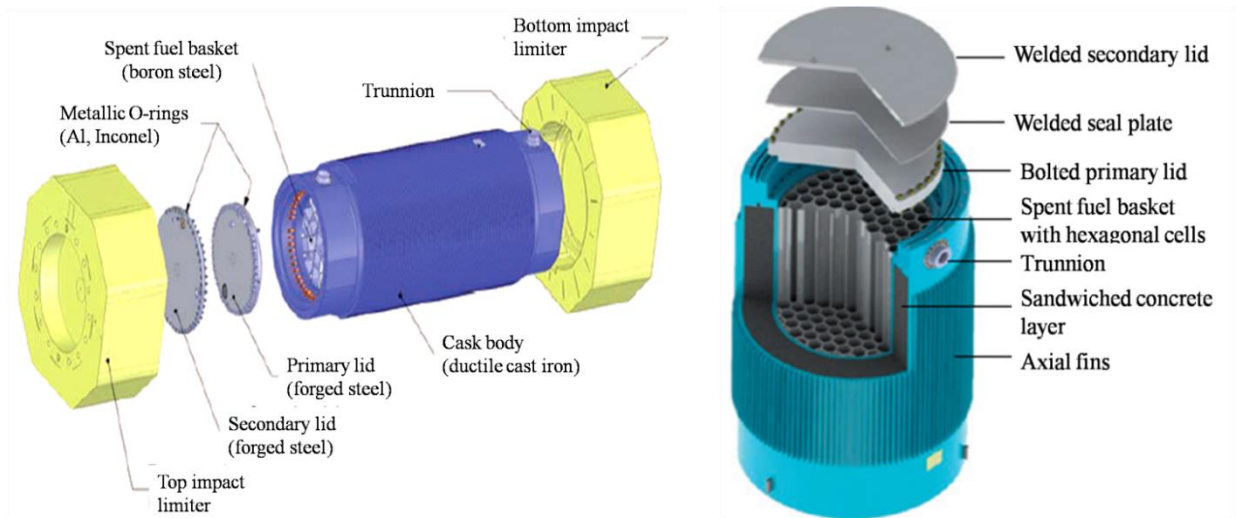


**Fig. 2.3** Schematic diagrams for CASTOR V/19 dual purpose cask in transport configuration with impact limiters (on the left) and vertical CONSTOR dry cask (on the right), adapted from (Wimmer et al., 2015)

Determination of the dose rate limit on the cask surface and at specified distances is used to specify the cask spacing in the storage system. The dose rate affects exposure to

radiation workers during the installation process as well as general maintenance during storage such as visual examination and radiation monitoring. General dose rate limits on the surface of the individual cask and storage systems range from 0.2 to 4 mSv/hr (20 to 400 mrem/hour) under 10CFR Part 72. However, 2 mSv/hr (200 mrem/hour) is common as a specified limit (U.S.NRC, 2010; Ko et al., 2014; IAEA, 2020).

#### **2.3.4 Subcriticality**

Sustained subcriticality must be guaranteed over the entire dry storage period. To achieve an adequate margin of subcriticality, intensive calculations are made to keep the neutron multiplication factor and reactivity at the minimum possible values even under credible accidents like flooding or overheating. As in all cases, criticality is prevented by maintaining the fissionable material in a specific geometry and the presence of neutron moderating and neutron absorbing material (neutron poisons) (Parks, 2000; Clarity et al., 2017).

In earlier designs, the spent fuel was treated as unirradiated fresh fuel regarding criticality and reactivity calculations. This approach exaggerated the required safety limits for basket geometrical dimensions and the needed flux traps thus unnecessary costs were being added (Parks, 2000; Fukuda et al., 2003; Clarity et al., 2017).

The concept of “burnup credit” has been applied since 2000 to take credit for the reduction in reactivity due to fuel burnup during its service history. It has been used to optimize canister size by reducing the intermediate spaces between spent nuclear fuel assemblies in the fuel basket to increase storage system capacity to hold greater number of SNF assemblies (Parks, 2000; IAEA, 2012; Clarity et al., 2017).

Storage geometries and designs for the basket that contains the spent fuel assemblies are limited by the need for heat conduction for decay heat removal. The overall design of the cask assures that subcritical geometry is maintained in normal operating conditions and also in case of accidents (Vitkova et al., 2006; IAEA, 2012; Clarity et al., 2017).

Proper geometrical design to ensure subcriticality is supplemented by considering the use of neutrons moderators and absorbers in the design. Neutron absorbers include boron-10, cadmium and gadolinium. Borated stainless steel and/or borated aluminum are used for manufacturing the fuel baskets. Borated aluminum is typically encapsulated in stainless steel for structural and corrosion protection (Funke and Diersch, 2004; Vitkova et al., 2006; IAEA, 2012; Wimmer et al. 2015).

### **2.3.5 Heat dissipation**

Decay heat removal is essential to protect the integrity of the stored fuel cladding. The typical allowable maximum temperatures for LWR zirconium alloy fuel cladding in dry storage are in the range of 350 to 410°C. CANDU stored spent fuel the licensed temperatures is limited to 160°C (U.S.NRC, 2010; IAEA, 2012; Vlček 2018).

During the first five years of cooling in water pools, decay heat release decreases by greater than 90% (Hu et al., 2016; Poškas et al., 2019). Unlike wet storage which needs an active process for decay heat removal using water circulation and heat exchangers, dry storage systems depend on passive conduction, natural convection, and thermal radiation mechanisms. The design of the dry cask should provide effective decay heat removal to keep on the stored spent fuel cladding within the standard safety limits under normal,

abnormal and accidental conditions (Vitkova et al., 2006; Saegusa et al., 2010; IAEA, 2012).

The relatively high temperatures and differential pressure during storage create stresses on the fuel cladding that can result in permanent creep deformation or cracking of the fuel cladding. Threshold temperature limits have been set for normal operating and accident conditions to protect spent fuel and cladding (Vitkova et al., 2006; U.S.NRC, 2010; IAEA, 2012; Vlček, 2018).

To achieve efficient heat removal, a decay heat must be conducted from the fuel to the basket and backfill gas and be dissipated at the outer surface of the cask. Material selection and geometrical design of the basket affects the heat removal process. In the recent GNS CONSTOR and Holtec HI-STAR licensed designs, baskets constructed of forged steel with borated aluminum plates, using what referred to as an egg-crate configuration where the plates form an array of square cells into which the fuel assemblies are placed, have been used to achieve enhanced thermal properties. This design can be seen in Figs. 2.4 and 2.5 (Funke and Diersch, 2004; HOLTEC, 2013).

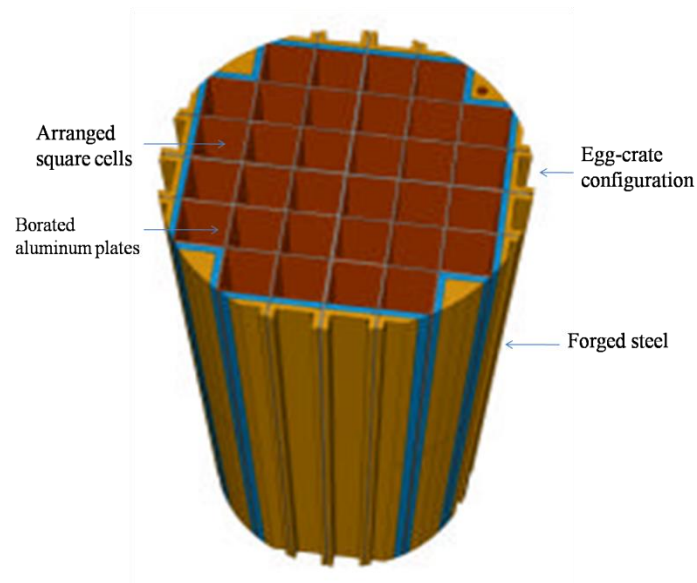


**Fig. 2.4** Basket design for CONSTOR V/32 dry storage cask, adapted from (Funke and Diersch, 2004)

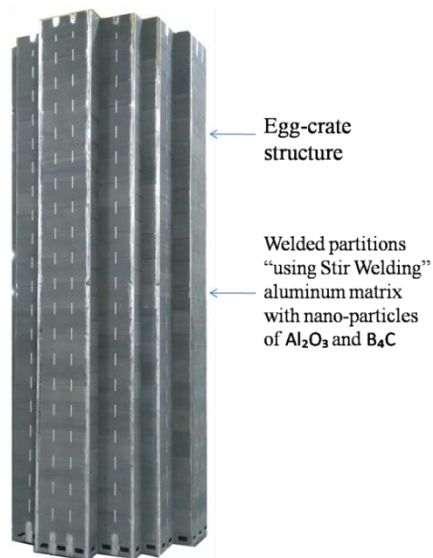


**Fig. 2.5** Completed MPC-89, Metamic-HT Spent Fuel Storage Basket, adapted from (HOLTEC, 2013)

Holtec International (USA) has applied nanotechnology and friction stir welding to produce METAMIC-HT spent fuel storage baskets, shown in Figure 5 (HOLTEC, 2013), that incorporate uniformly dispersed nano-particles of alumina and boron carbide powder in an aluminum matrix to improve thermal conductivity and reduce the basket weight. This improvement allowed development of a cask with increased capacity, 89 storage cells for BWR spent fuel and 37 storage cells in case of PWR spent fuel (HOLTEC, 2013). The improved heat conduction of this design allows safe removal from wet storage to dry storage after only a 3-year cooling period (HOLTEC, 2013; IAEA, 2020).

The internal void volume of the cask or canister is typically filled with an inert gas such as helium. The inertness and the thermal conductivity of the selected gas play an important role in the heat removal process in addition to the protection of the fuel cladding. Helium has excellent heat capacity and is the most common choice. Nitrogen may be used in some applications, but its heat transfer effectiveness is lower than that of helium. Inertness is important to minimize corrosion potential within the storage package (Anderson, 2018; Pořkas et al., 2019; Bruno et al., 2020).

In ventilated steel-concrete canister systems, heat removal is primarily achieved by convective means as air circulates through the gap between the outer surface of the canister and the inner surface of the concrete shield structure. By natural convection, ambient air is drawn through the inlet at the base of the shield structure, absorbs heat from the canister and is ejected from the outlet at the top of the shield structure. To maintain the radiation shielding properties of the structure, the path between the inlet and

the outlet has vertical and horizontal offsets to eliminate any direct radiation shine path (Saegusa et al., 2008; U.S.NRC, 2010; Droste, 2013).

A thermal shield plate may be installed in the annular cooling path between the canister and the concrete shield structure to minimize the transfer of heat to the concrete layer. The cooling path of the air between the inlet and the outlet and the thermal shield is shown via a simple cross-section of a concrete cask in Fig. 2.6 (Saegusa et al., 2008).

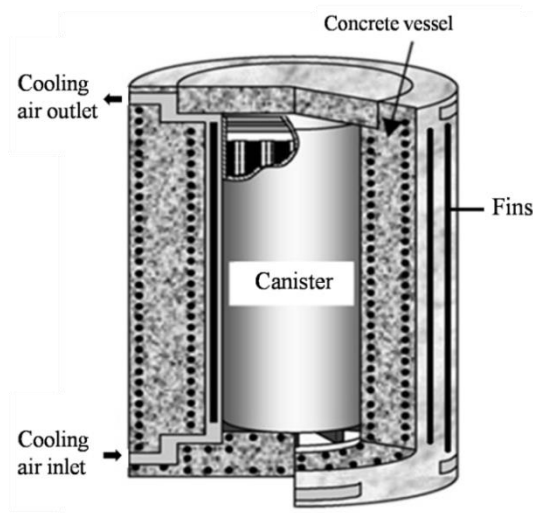


**Fig. 2.6** Half section of a concrete based cask showing air inlet, outlet, thermal shield and fins along with the concrete vessel, adapted from (Saegusa et al., 2008)

The outer surface of the steel overpack or the concrete shield usually has a maximum temperature ranges between 72°C and 78°C with solar insolation. However, some licensing conditions specify that the maximum temperature of the concrete surface should not exceed 110°C and maximum temperature differential through the concrete layer thickness should be less than 60°C to avoid cracking. This is sometimes incorrectly

ignored by some studies (Vitkova et al., 2006; U.S.NRC, 2010; IAEA, 2012; Wang et al., 2014).

The concrete vessel that contains the canister is mainly to achieve the necessary radiation shielding and protection, however, some modifications are usually made to the mix design to enhance its thermal conductivity like impregnation with copper fibers or particulates and using aggregates with higher thermal conductivity (Droste, 2013; Wimmer et al., 2015; El-Samrah et al., 2018; Vlček, 2018).

The last barrier in the multi-layered heat removal process is the machined fins that are radially fixed and homogeneously distributed on the outer surface of the cask. These fins can increase the overall surface area up to 3 times the original one thus, the thermal conductivity and the heat removal depending on thermal radiation and conduction can be greatly enhanced. These fins can be observed in many designs like those used for Westinghouse MC-10, CASTOR and CONSTOR casks (Wimmer et al., 2015; Wu et al., 2018).

## **2.4 Evolution and trends of SNF interim dry storage**

### **2.4.1 SNF dry storage casks**

In the late 1970s and early 1980s, a high interest in dry storage techniques led to research and development of effective and dry storage cask designs.

In one of the earliest designs, concrete was used to completely encapsulate spent nuclear fuel or radioactive wastes while achieving decay heat removal and shielding against neutrons and gamma radiation. In this design, a concrete vessel with steel liner was used

as the container for the contained spent fuel. The concrete mixture contained copper or aluminum fibers to enhance thermal conductivity. Polymers containing boron-based particles were dispersed homogeneously in the mix to provide subcriticality and neutron shielding. The use of fans was also proposed in the design to cool the outer surface of the concrete encapsulation (Fleischer and Gunasekaran, 1981).

In a subsequent design, concrete encapsulation was used for the SNF basket containment but in this design, lateral or radial openings that work as ventilating passages were drilled in the concrete walls. System temperatures in this design were monitored by a plurality of temperature measuring probes installed in the walls of the concrete container (Dyck et al., 1985).

These early designs couldn't provide efficient heat dissipation, which limited their storage capacity for radioactive wastes. Moreover, the expected service life was very limited due to anticipated failures in mechanical and structural properties.

The first cask loading for interim storage was performed in Switzerland in 1983 using one of the first licensed dual-purpose dry casks, CASTOR Ic - DIORIT Cask, which is called the "grandfather" of all dual-purpose casks (Droste, 2013; Wimmer et al., 2015). The design of these DPCs is a monolithic cask body made of ductile iron or forged steel with a double-lid closure system. The over-pressure between the lids is monitored by a pressure switch indicating any possible leak. Cooling fins are machined on the cask's surface as shown in Fig. 2.7 (Droste, 2013).



**Fig. 2.7** CASTOR Ic- DIORIT Dry Cask for SNF transport and storage, adapted from (Droste, 2013)

In the mid 1980s, the Transnuclear Incorporated TN-24 cask design was licensed for storage and transportation of 24 five-year-cooled PWR assemblies. This cask design is a family of casks that includes variations that hold 24, 28, 32, or 40 PWR or up to 68 BWR assemblies. Casks of this design are used at numerous locations internationally (Cagnon and Mason, 1987; Roland et al., 2003).

This design was one of several that were tested for heat transfer performance under a cooperative agreement with the US Department of Energy. Testing was done by the Pacific National Laboratory at the Idaho National Laboratory using fuel supplied by Virginia Electric Power Company (Fukuda et al., 2003; Roland et al., 2003; U.S.NRC, 2010).

The basic structural design for TN-24 cask, as shown in Fig. 2.8, is a thick steel cylindrical forging with a welded forged bottom and one or two bolted forged steel lids

equipped with metallic gaskets. The thick steel cylinder provides the main gamma shielding. The steel cask body is surrounded by a layer of polypropylene resin containing borated polyester encased in a smooth steel outer shell as a neutron shield. A borated aluminum basket is used for supporting the spent fuel assemblies and insuring their subcriticality. The basket consists of mechanically-assembled partitions of boronated aluminum defining an array of cells. Finally, a set of shock-absorbing covers is fitted to the cask for a safe transport operation in addition to lateral impact limiters (Cagnon and Mason, 1987; Roland et al., 2003). These casks are successfully still in service in the US and in Europe (Droste, 2013; Greene et al., 2013; Bruno et al., 2020).

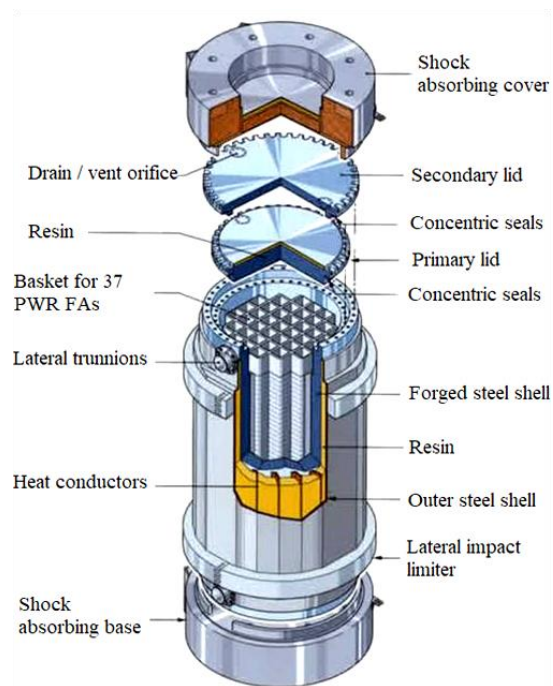


**Fig. 2.8** The basic configuration of the TN-24 transportable cask manufactured by Orano (previously Areva), adapted from (Roland et al., 2003)

Based on the terrorist events of September 2001, additional design requirements for protection of spent nuclear fuel dry storage systems against projectiles were instituted. In 2008, the NRC stated that all dry storage casks used in the USA must be "designed to resist floods, tornadoes, projectiles, temperature extremes, and other unusual scenarios" (U.S.NRC, 2008).

After the Great Sendai Earthquake and resulting tsunami that caused damage to Fukushima Daiichi in 2011, additional requirements for the protection from beyond design basis threats like extreme earthquakes, floods and tsunamis were added to dry storage systems. The significant problems associated with fuel damage in the reactor cooling pools at Fukushima has led to consideration of reducing the wet cooling period to move the fuel to more secure dry storage to minimize risk (Shimizu, 2016). These changes in requirements have led vendors to develop more robust casks that can achieve these considerations (Shimizu, 2016).

Recently, HOLTEC launched HI-STAR dual purpose casks like the HI-STAR-180 that utilize METAMIC-HT spent fuel storage baskets. These casks have higher capacity, 89 BWR spent fuel assemblies or 37 PWR spent fuel assemblies, and have mechanical and structural properties that achieve acceptable leak tightness after a missile strike. Due to the improved heat rejection provided by the basket design and materials, these casks can store spent fuel with a cooling period of 3 years only (HOLTEC, 2013; Stefan and John, 2016).

### **2.4.2 Pros and cons of full-metal, concrete-steel and sandwich dry storage casks**

Full-metal cask designs have a smaller diameter compared to concrete based cask because the density of metal is higher than that of concrete and the needed metal overpack thickness is less than that in case of using concrete, making it more effective to shield against gamma-ray doses. Metal also provides a robust structure that can resist higher mechanical loads, impacts and temperatures. However, metal casks require additional borated resin material to shield for neutrons' doses from high burnup fuel with a short cooling (Roland et al., 2003; Droste, 2013; Wimmer et al., 2015).

Manufacture of thick metal shells (usually around 40 cm) with precise welding is a complex process and the associated price is higher than the concrete based cask (Roland et al., 2003; Saegusa et al., 2008). Concrete-based casks or in another meaning concrete-shielded steel canister systems are less expensive than full-metal casks because the concrete shield requires less technical control and can be either poured on site or fabricated offsite. Concrete also inherently provides neutron absorption. Canister fabrication is less challenging because the canister wall is typically 25 mm (1 inch) or less, resulting in a simpler welding process compared to the case in the full-metal cask (Craig et al., 1989; Saegusa et al., 2008; Chopra et al., 2014).

Another advantage is the great flexibility of the concrete layer to be enhanced or modified to give better functionality regarding radiation protection and/or heat dissipation like the case when using heavy aggregates like barite or magnetite to provide better shielding capabilities or enhancing the thermal properties via adding copper particulates or steel granules (Roland et al., 2003; Saegusa et al., 2008; Droste, 2013).

Aging degradation of the concrete layer in the concrete-shielded canister systems, especially with a bare surface, is a negative aspect when compared to the stainless steel or ductile cast iron full-metal cask. The ability of full-metal cask to carry higher heat loads makes metal casks a preferred choice for storing fuel with short cooling periods. Full-metal designs are more compact, robust, and safer during handling (Roland et al., 2003; U.S.NRC, 2010; Droste, 2013).

Dual purpose casks, based on the sandwich (steel – concrete – steel) structural design such as the GNS CONSTOR have advantages that enable using this type for both storage and transportation. Sandwich design-based casks have less challenging manufacturing compared to the full-metal cask and a higher degree of robustness compared to the concrete-steel cask. The steel external shell protects the concrete layer from many degradation factors which helps greatly in service life extension of the cask (Roland et al., 2003; Hanifehzadeh et al., 2018). However, mechanical loads or impacts in this design are carried by the steel structure only and no credit is taken for the mechanical and structural properties of the concrete layer to simplify the licensing process (Roland et al., 2003; Droste, 2013).

### **2.4.3 Dry storage facilities**

Dry storage site or facility usually can be classified according to the following categories; above the ground or under the ground, at the reactor site (on-site) or away from the reactor in a specified separate site, open-air facility or closed indoor facility and based on arranged vertical casks, vaults or horizontal modules. Each interim storage facility can be

classified according to all the mentioned classifications (Fukuda et al., 2003; Roland et al., 2003; IAEA, 2012; Wimmer et al., 2015; IAEA 2020).

The first dry storage installation in the USA was licensed by the Nuclear Regulatory Commission (NRC) in 1986 at Surry Nuclear Power Plant in Virginia. This interim facility is an open-air above ground on-site dry storage facility utilizes arranged vertical casks (Creer and Schoonen, 1986; Bare et al., 2001; Wimmer et al., 2015). Twenty-five CASTOR V/21 ductile iron casks, each containing 21 PWR are stored at the site as shown in Fig. 2.9 (Skrzyppek and Kim, 2015).



**Fig. 2.9** Arranged CASTOR V/21 vertical casks at Surry Nuclear Power Station, Virginia, USA, (Skrzyppek and Kim, 2015)

Some countries like Germany, Belgium and the Czech Republic utilize closed indoor storage facilities whether on-site or separate. For example, Germany uses GNS vertical dry casks in 16 sites all of these sites are at NPP sites or on-site facilities except only

three separate interim dry storage facilities located in Ahaus, Zwischenlager Nord (ZLN) and Gorleben as shown in Fig. 2.10 (Fraczek, 2013).



**Fig. 2.10** A site view for Gorleben interim dry storage facility (on the left) and an interior view that shows arranged vertical CASTOR casks stored indoors in the same facility (on the right) (Fraczek, 2013)

After 2005 transportation and reprocessing of SNF was prohibited by law in Germany so, SNF is now stored completely on-site and mainly in closed indoor facilities at the German nuclear power plants' sites (Fraczek, 2013; Skrzyppek and Kim, 2015; Wimmer et al., 2015). In addition to the former, Belgium uses TN-24 dual purpose spent fuel storage casks as an onsite facility at DOEL Nuclear Power Plants and Czech Republic depends mainly on CASTOR casks for storing SNF in indoor facilities whether these facilities are onsite or separate like the deployment of CASTOR 1000/19 in the interim storage facility at Temelin (Baroux et al., 2001; Skrzyppek and Kim, 2015).

In Canada, the used nuclear fuel is currently safely managed in facilities licensed for interim storage. Most of these facilities are located at nuclear reactor sites (on-site facilities) in Ontario, Quebec, and New Brunswick, besides the sites belonging to the Atomic Energy of Canada in Manitoba and Chalk River Laboratories in Ontario as shown in Fig. 2.11 (NWMO, 2019).



**Fig. 2.11** Interim dry storage sites in Canada (NWMO, 2019)

Canada utilizes many techniques for storing nuclear spent fuel. For example, at Bruce Nuclear Generating Station, the interim storage facility is a closed indoor facility based on vertical dry casks. In Gentilly nuclear generating station, concrete vaults are used in an outdoor open-air facility and in Point Lepreau generating station, cylindrical reinforced concrete silos are used also as an outdoor open-air facility (Husain and Choi, 2003; NWMO, 2019).

Requirements resulting from natural disasters and political events led to development of highly-secured dry storage facility designs from HOLTEC and ORANO.

HOLTEC launched a high capacity, high heat load underground interim spent fuel storage system named HI-STORM UMAX to be compatible with the above-ground high performance HI-STORM FW system. The HI-STORM UMAX system was licensed by the U.S.NRC in April 2015 in Docket number 72-1040 under Certificate of Compliance (CoC) No. 72-1014 (Woodward, 2015; Diaz-Maurin and Ewing, 2020). The system utilizes buried vertical steel canisters that use METAMIC-HT baskets. Shielding is provided by the surrounding layer of modified concrete or other engineered fillers. A concrete-steel lid is used for the closure and contains openings for both air inlet and exit using a passive decay heat removal system based on natural convection. The top pad ground layer is made of reinforced concrete (HOLTEC, 2013; Woodward, 2015). The system details and properties are shown in Fig. 2.12 and summarized in Table 2.2 for further details (Woodward, 2015).

The HI-STORM UMAX has some advantages over the traditional above-ground facilities. The facility is, largely invulnerable to seismic events. Fuel is virtually inaccessible from impacts by aircraft or airborne missiles from tornados, hurricanes, and tsunamis or terroristic actions. Shielding by the surrounding underground layer provides superior radiation protection for the workers. Combustion of flammable materials inside the cavities cannot be sustained. Inspection of inlet and outlet openings and passages is easier. Finally, the needed area for the facility is smaller and the flexible placement allow for optimum fitting to the available area (Woodward, 2015).

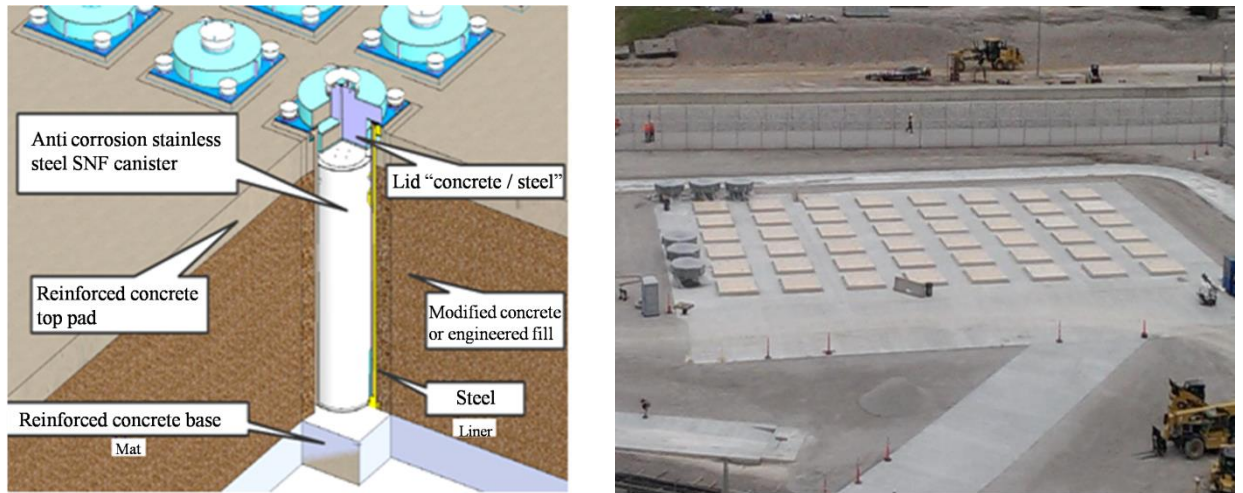


**Fig. 2.12** HI-STORM UMAX design features (on the left) and the site view of Callaway NPP UMAX Facility in the U.S (on the right), adapted from (Woodward, 2015)

**Table 2.2** The main features of the HI-STORM UMAX system

System Property	HI-STORM UMAX System
System Type	Underground storage
System Capacity (PWR/BWR)	37 / 89 SFAs
Damaged Fuel or Fuel Debris Capacity (PWR/BWR)	Up to 12/16
Maximum Heat Load	Up to 37 kW
Maximum Initial Enrichment (PWR/BWR)	5 % / 5 % (wt% U-235)
Minimum Fuel Cooling Time	3 years
Expected Service Life	More than 100 years

HOLTEC has dealt with Eddy Lea Energy Alliance (ELEA) to design and build the proposed largest interim storage facility in New Mexico using HOLTEC's HI-STORM

UMAX spent fuel storage system. An array of 60 by 60 HI-STORM UMAX storage systems can safely store 75,000 metric tons of spent nuclear fuel which is almost the total amount of spent fuel need to be stored in the USA. The size of a consolidated storage site will be only 360 x 360 m which is less than the summed area of four soccer pitches (HOLTEC, 2015; Holtec, 2018).

ORANO (formerly Areva) Company offers the NUtech HORIZONTAL Modular Storage (NUHOMS) storage system which uses steel canisters stored in horizontal alignments in reinforced concrete based parallel cells with monolithic one layer structure as shown in Fig. 2.13 (Orano, 2020).

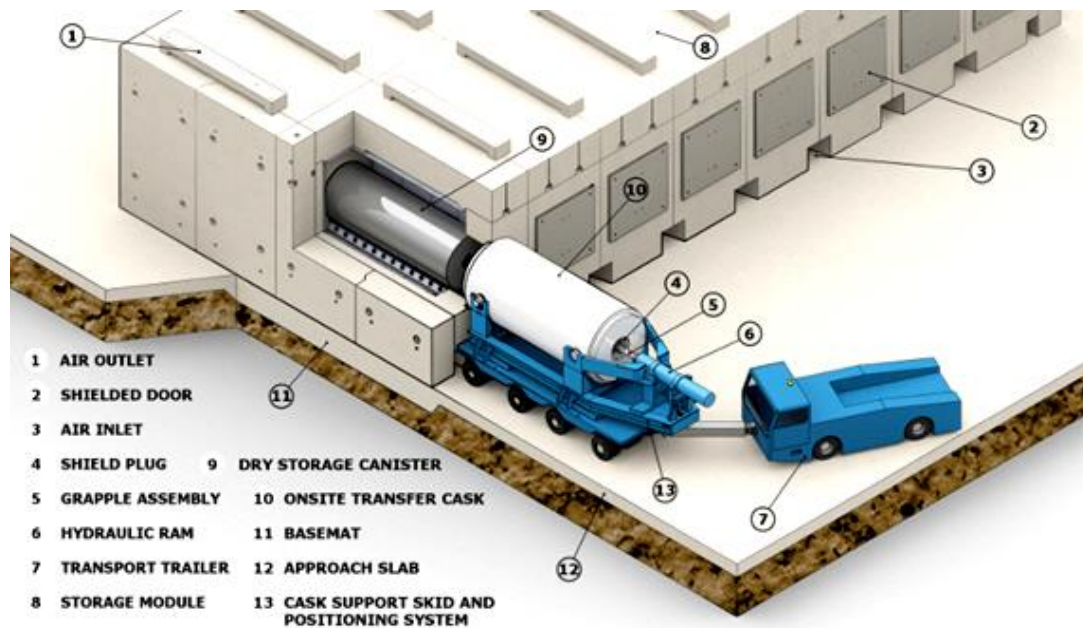


**Fig. 2.13** The NUHOMS storage system with monolithic one layer structure, adopted from (Orano, 2020)

Horizontal modules cannot tip over, and on-site handling using the OS-197 transfer cask is easier and safer in this horizontal position compared to the vertical system. In addition,

the horizontal orientation during storage avoids the significant temperature difference between the two ends of the canister, reducing the possibility of thermally induced stresses in the material, and provides minimal exposure to plant workers (Hanson and Chollet, 2003; Orano, 2020).

In 2017, Orano (formerly Areva) launched the NUHOMS Advanced Matrix design based on a high-density multilayered system for storing multiple spent fuel rods stored in canisters as shown in Fig. 2.14 (U.S.NRC, 2018), which can reportedly “ reduce the footprint of on-site interim fuel storage facilities by almost 50%”. The unique two-level horizontal and modular structure could also save construction costs due to reducing the required area for the concrete base mat. The NUHOMS Advanced Matrix can achieve the smallest storage pad area for the same stored spent fuel capacity in the industry’s international market (WNN, 2017; U.S.NRC, 2018; Orano, 2020).

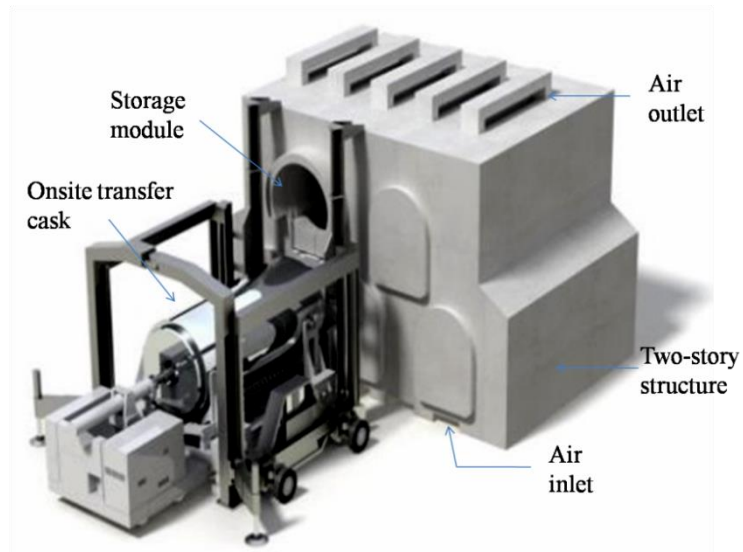


**Fig. 2.14** The NUHOMS Advanced Matrix with its unique two-story structure, adopted from (U.S.NRC, 2018)

## 2.5 Conclusion

Based on the former the following conclusions can be stated as follows;

- The interim dry storage for spent nuclear fuel (SNF) has become very important as growing amounts of SNF round the world cannot be retained in wet storage over long periods and because there is no permanent disposal facility at the present time.
- To design and build a reliable dry storage cask that can provide efficient storage for these radioactive hazardous materials some considerations must be achieved. Safe enclosure of the spent nuclear fuel rods besides adequate radiation shielding and protection against all possible kinds of hazardous radiation must be insured

over long periods. Moreover, subcriticality for the stored used fuel and efficient continuous heat removal should be guaranteed over the entire storage period.

- In the late 1970s and early 1980s, dry storage for SNF became with great importance and continuous evolution has started from this time. This industry started with primitive designs that couldn't provide efficient heat dissipation which led to a confined heat load and the ability to carry only small quantities of radioactive wastes. Moreover, the mechanical properties were unreliable and the expected service life was very limited.
- With time, leading companies like GNS, HOLTEC, and ORANO launched reliable designs and robust casks that are in service till now like CASTOR, CONSTOR, HI-STAR, and TN. However, these casks contained unmodified baskets and canisters especially with the absence of the modern welding techniques and nano-technology which led to limited heat loading and an ability to carry a limited number of SNF assemblies despite the improved shielding and mechanical properties.
- Evolution concerning with dry storage techniques hasn't stopped (till now) in order to cope with the conclusions and the learned lessons from notable accidents like Sept. 11th events or Fukushima Daiichi disaster that needed some modifications regarding the initial design of the cask especially dual-purpose casks.
- Great development was observed especially with the design and material selection of the basket and the concrete layer in the concrete-based casks especially that the

considerably great thickness of the concrete layer upon using conventional concrete was found to be ready to be reduced greatly when using certain heavy aggregates and modified mix designs.

- The main target is always to obtain a robust storage cask that can carry higher heat loads and a greater number of spent fuel assemblies with shorter cooling periods ready for immediate transferring when needed.
- This continuous evolution aims to achieve some other important goals and economic benefits via decreasing the thickness, the size and the weight of dry storage casks. These modifications can be seen for example in HI-STAR casks that utilize high-tech METAMIC-HT spent fuel storage baskets.
- Finally, this evolution has covered not only the design and the technology of dry storage casks but also the techniques related to the entire facility beginning with above-ground facilities that compose of arranged vertical casks and ending with some very recent facilities like the robust underground interim spent fuel storage system (HI-STORM UMAX) by HOLTEC and the economic and area-saving multilayered horizontal system for storing spent nuclear fuel canisters (NUHOMS Advanced Matrix) that launched recently by Orano. These new robust systems have many advantages over the traditionally used vertical above-ground system that make them much safer even under extreme events.

## 2.6 References

- Almomani, B., Lee, S., Jang, D., and Kang H. G., 2017. Probabilistic risk assessment of aircraft impact on a spent nuclear fuel dry storage. *Nuclear Engineering and Design* 311, 104-119.
- Anderson, S. T., 2018. Economics, helium, and the US Federal helium reserve: summary and outlook. *Natural Resources Research* 27(4), 455-477.
- Audi, G., Bersillon, O., Blachot, J., and Wapstra, A., 2003. The NUBASE evaluation of nuclear and decay properties. *Nuclear Physics A* 729(1), 3-128.
- Bare, W. C., Ebner, M. A., and Torgerson, L. D., 2001. Dry cask storage characterization project-Phase 1: CASTOR V/21 cask opening and examination. USDOE Technical Report No. INEEL/EXT-01-00183, USA.
- Baroux, C., Detrilleaux, M., and Demazy, G., 2001. Operational Experience of TN 24 Dual Purpose Spent Fuel Storage Casks at the DOEL Nuclear Power Plants in Belgium. *Proceedings of the ASME 2001 8th International Conference on Radioactive Waste Management and Environmental Remediation*. Bruges, Belgium. September 30–October 4, 2001. 1205-1208. ASME.
- Bruno, J., Duro, L., and Diaz-Maurin, F., 2020. Spent nuclear fuel and disposal. *Advances in Nuclear Fuel Chemistry* 527-553.
- Bruno, J. and Ewing, R. C., 2006. Spent nuclear fuel. *Elements* 2(6), 343-349.
- Cagnon, R. and Mason, M., 1987. Design and demonstration of the TN-24 spent fuel cask for dry storage and transport. *Packaging and transportation of radioactive materials (PATRAM'86)*, IAEA.
- Chilton, A. B., Shultis, J. K., and Faw, R. E., 1984. *Principles of radiation shielding*. United States: Prentice Hall Inc.
- Chopra, O., Diercks, D., Fabian, R., Han, Z., and Liu, Y., 2014. Managing aging effects on dry cask storage systems for extended long-term storage and transportation of used fuel (REV. 2). USDOE Report No. ANL-13/15, Argonne National Lab. (ANL), Argonne, IL, USA.

- Clarity, J. B., Banerjee, K., Liljenfeldt, H. K., and Marshall, W. J., 2017. As-Loaded Criticality Margin Assessment of Dual-Purpose Canisters Using UNF-ST&DARDS. *Nuclear Technology* 199(3), 245-275.
- Connolly, K. J., and Pope, R. B., 2016. A historical review of the safe transport of spent nuclear fuel. Technical Report No. ORNL/TM-2016/390, Oak Ridge National Lab. (ORNL), Oak Ridge, USA.
- Craig, P. A., Haelsig, R. T., Kent, J. D., and Schmoker, D. S., 1989. On-site concrete cask storage system for spent nuclear fuel. U.S. Patent No. 4800062. Google Patents.
- Creer, J.M., & Schoonen, D.H. (1986). CASTOR-V/21 PWR spent fuel storage cask performance test. No. EGG-M--29985. Pacific Northwest Labs, USA.
- Diaz-Maurin, F. and Ewing, R. C., 2020. Socio-technical evaluation of long-term spent nuclear fuel management options: The case of San Onofre, California. *EarthArXiv*.
- Droste, B., 2013. A survey on 35 years of packaging, transport and storage of radioactive material. 17th International Symposium on the Packaging and Transportation of Radioactive Materias (PATRAM 2013), August 18-23, 2013. San Francisco, CA, USA.
- Dyck, H. P., Spilker, H., and Gregor, H. D., 1985. Concrete shielding housing for receiving and storing a nuclear fuel element container, U.S. Patent No. 4532428A. Google Patents.
- El-Samrah, M. G., Abdel-Rahman, M. A., and El Shazly, R., 2018. Effect of heating on physical, mechanical, and nuclear radiation shielding properties of modified concrete mixes. *Radiation Physics and Chemistry* 153, 104-110.
- Ewing, R. C., 2008. Nuclear fuel cycle: environmental impact. *Mrs Bulletin* 33(4), 338-340.
- Ewing, R. C., 2015. Long-term storage of spent nuclear fuel. *Nature Materials* 14(3), 252-257.
- Fleischer, L. R., and Gunasekaran, M., 1981. Concrete encapsulation for spent nuclear fuel storage, U.S. Patent No. 4257912A, Google Patents.

- Fraczek, J., 2013. Commission to determine criteria for final nuclear storage. Deutsche Welle, from <https://www.dw.com/en/commission-to-determine-criteria-for-final-nuclear-storage/a-16698733>.
- Fukuda, K., Danker, W., Lee, J., Bonne, A., and Crijns, M., 2003. IAEA Overview of global spent fuel storage. Proceedings of the Storage of Spent Fuel from Power Reactors, 2003, IAEA, Vienna.
- Funke, T. and Diersch, R., 2004. The use of the CONSTOR cask concept for light water reactor fuel. Proceedings of Packaging and Transportation of Radioactive Materias (PATRAM 2004), September 20-24, 2004. Berlin, Germany.
- Gray, E., 2015. Coast to coast spent fuel dry storage problems and recommendations. Division of Spent Fuel Management Regulatory Conference (DSFM REG CON), November 18-19, 2015. USA.
- Greene, S. R., Medford, J. S., and Macy, S. A., 2013. Storage and Transport Cask Data for Used Commercial Nuclear Fuel - U.S. Edition. USDOE Report No. ATI-TR-13047, USA.
- Haire, M. J., and Swaney, P. M., 2005. Cask size and weight reduction through the use of depleted uranium dioxide (DUO<sub>2</sub>)-Steel Cermet Material. Waste Management.
- Hanifehzadeh, M., Gencturk, B., and Mousavi, R., 2018. A numerical study of spent nuclear fuel dry storage systems under extreme impact loading. Engineering Structures 161, 68-81.
- Hanson, A., and Chollet, P., 2003. International experience of storing spent fuel in NUHOMS® systems. International Conference on Storage of Spent Fuel from Power Reactors, IAEA.
- Heinonen, J., and Malasek, E., 1984. Disposal of low and intermediate-level radioactive wastes in shallow ground and rock cavities. International conference on radioactive waste management, May 16-20, 1983. Seattle, WA, USA.
- HOLTEC, 2013. Completed Metamic-HT Spent Fuel Storage Baskets represent many firsts for the nuclear industry. HOLTEC International News.

- HOLTEC, 2015. Holtec partners with ELEA, LLC in New Mexico to build consolidated interim storage facility. HOLTEC International.
- HOLTEC, 2018. HI-STORE CIS in southeastern New Mexico Edges closer to regulatory approval. HOLTEC International.
- Hu, J., Peterson, J. L., Gauld, I. C., and Bowman, S. M., 2016. US Commercial Spent Nuclear Fuel Assembly Characteristics: 1968-2013. Technical Report No. NUREG/CR-7227, Oak Ridge National Lab. (ORNL), Oak Ridge, USA.
- Husain, A., and Choi, K., 2003. Status of storage, disposal and transportation containers for the management of used nuclear fuel. NWMO Background Papers: Technical Methods.
- IAEA, 1995. Safety and engineering aspects of spent fuel storage. Proceedings of an international symposium held in Vienna, October 10-14, 1994. Vienna, Austria.
- IAEA, 2000. Multi-purpose container technologies for spent fuel management (IAEA-TECDOC-1192). International Atomic Energy Agency (IAEA), Vienna, Austria.
- IAEA, 2012. Storage of spent nuclear fuel: specific safety guide. IAEA Safety Standards Series No. SSG-15. International Atomic Energy Agency (IAEA), Vienna, Austria.
- IAEA, 2018. Regulations for the safe transport of radioactive material – 2018 Edition - Specific Safety Requirements. International Atomic Energy Agency (IAEA), Vienna, Austria.
- IAEA, Waste and Environmental Safety Section, 2020. Methodology for a Safety Case of a Dual Purpose Cask for Storage and Transport of Spent Fuel. Report of a WASSC/TRANSSC Joint Working Group (IAEA-TECDOC-1938). International Atomic Energy Agency (IAEA), Vienna, Austria.
- Kaplan, M. F., 1989. Concrete radiation shielding. John Wiley & Sons, NY, USA.
- Ko, J. H., Park, J. H., Jung, I. S., Lee, G. U., Baeg, C. Y., and Kim, T. M., 2014. Shielding analysis of dual purpose casks for spent nuclear fuel under normal storage conditions. Nuclear Engineering and Technology 46(4), 547-556.

- Krause, H., 1984. Management of radioactive wastes from nuclear power plants. International Conference on Radioactive Waste Management, May 16-20, 1983. Seattle, WA, USA.
- Lewis, D. W., 2003. US Commercial Spent Fuel Storage Facilities: Public Health and Environmental Considerations. ASME 9th International Conference on Radioactive Waste Management and Environmental Remediation, September 21–25, 2003. Oxford, England.
- Masoud, M., Kansouh, W., Shahien, M., Sakr, K., Rashad, A. M., and Zayed, A., 2020. An experimental investigation on the effects of barite/hematite on the radiation shielding properties of serpentine concretes. *Progress in Nuclear Energy* 120, 103220.
- NWMO., 2019. Canada's used nuclear fuel; how is it stored today ? from <https://www.nwmo.ca/en/Canadas-Plan/Canadas-Used-Nuclear-Fuel/How-Is-It-Stored-Today>.
- Orano., 2020. Used Fuel Storage. from <https://www.orano.group/usa/en/our-portfolio-expertise/used-fuel-management/used-fuel-storage>.
- Parks, C. V., 2000. Review and prioritization of technical issues related to burnup credit for LWR fuel. ORNL Oak Ridge National Laboratory (United States). Report No. ORNL/TM-1999/303, Funding organisation: USDOE, USA.
- Poškas, R., Šimonis, V., Jouhara, H., and Poškas, P., 2019. Modeling of decay heat removal from CONSTOR RBMK-1500 casks during long-term storage of spent nuclear fuel. *Energy* 170, 978-985.
- Ratiko, R., Samudera, S. A., Hindami, R., Siahaan, A. T., Naldi, L., Hapsari, D., Mahlia, T., and Nasruddin, N., 2018. Optimization of dry storage for spent fuel from GA Siwabessy nuclear research reactor. *International Journal of Technology* 1, 55-67.
- Roland, V., Chiguer, M., and Guenon, Y., 2003. Dry storage technologies: Keys to choosing among metal casks, concrete shielded steel canister modules and vaults. International conference on radioactive waste and spent fuel management, Nov 6-8, 2003. Plovdiv, Bulgaria.

- Saegusa, T., Shirai, K., Arai, T., Tani, J., Takeda, H., Wataru, M., Sasahara, A., and Winston, P., 2010. Review and future issues on spent nuclear fuel storage. *Nuclear Engineering and Technology* 42(3), 237-248.
- Saegusa, T., Yagawa, G., and Aritomi, M., 2008. Topics of research and development on concrete cask storage of spent nuclear fuel. *Nuclear Engineering and Design* 238(5), 1168-1174.
- Shimizu, Y., 2016. Lessons learned from the Fukushima Daiichi Accident: Actions taken and challenges ahead. *International Conference on Effective Nuclear Regulatory Systems: Sustaining Improvements Globally*, Apr 11-15, 2016. Vienna, Austria.
- Skrzyppek, J., and Kim, J. D., 2015. A well established system for the dry storage of spent fuel. *Transactions of the Korean Nuclear Society Spring Meeting*, May 7-8, 2015. Jeju, Korea.
- Stahmer, U., 2009. Transport of used nuclear fuel – A summary of canadian and international experience. Report No. NWMO TR-2009-14. Nuclear Waste Management Organization (NWMO). Toronto, Canada.
- Stefan, A., and John, Z., 2016. Aircraft impact test on the HI-STAR 180 Dual Purpose Cask. *Proceedings of the 18th International Symposium on the Packaging and Transportation of Radioactive Materials (PATRAM 2016)*, September 18-23, 2016. Kobe, Japan.
- U.S.NRC, 1981. Disposal of high-level radioactive wastes in geologic repositories. Code of Federal Regulations, Title 10. USA.
- U.S.NRC, 2008. Fact sheet on dry cask storage of spent nuclear fuel. Available at: <http://www.nrc.gov/reading-rm/doc-collections/fact-sheets/dry-cask-storage.html>.
- U.S.NRC, 2010. Standard review plan for spent fuel dry storage systems at a general license facility. Report No. NUREG-1536. USA.
- U.S.NRC, 2018. NUHOMS® EOS System Updated Final Safety Analysis Report. Docket Number 72-1042. USA.
- U.S.NRC, 2020. Spent Fuel Storage in Pools and Dry Casks; Key Points and Questions & Answers. from <https://www.nrc.gov/waste/spent-fuel-storage/faqs.html>.

- Vitkova, M., Gorinov, I., and Dacheva, D., 2006. Safety criteria for wet and dry spent fuel storage. International conference on WWER fuel performance, modelling and experimental support, Sep 19-23, 2005. Albena, Bulgaria.
- Vlček, D., 2018. Residual heat power removal from spent nuclear fuel during dry and wet storage. *Acta Polytechnica CTU Proceedings* 19, 36-45.
- Wang, J., Chiang, Y., Li, W., Lin, H., Chen, H., Shih, C., and Chen, S., 2014. TRACE/FRAPTRAN Analysis of Kuosheng Nuclear Power Plant Dry-Storage System. *International Journal of Chemical, Molecular, Nuclear, Materials and Metallurgical Engineering* 8(7), 658-664.
- Wegel, S., Czempinski, V., Hirschhausen, C. V., Oei, P., Rieble, N., Scherwath, T., and Wealer, B., 2017. Processing High-Level Radioactive Waste in the US: A Mathematical Model. 15th IAEE European Conference, september 3-6, 2017. Vienna, Austria.
- Wimmer, H., Skrzyppek, J., and Koebel, M., 2015. CASTOR® and CONSTOR®. A well established system for the dry storage of spent fuel and high level waste." *VGB PowerTech* 95(5), 52-57.
- WNN, 2017. Areva's space-saving solution for used fuel storage. Available at: <https://www.world-nuclear-news.org/WR-Arevas-space-saving-solution-for-used-fuel-storage-2909175.html>.
- Woodward, W. S., 2015. Underground Interim Storage of Spent Nuclear Fuel – HISTORM UMAX. IAEA Conference on Management of Spent Fuel from Nuclear Power Reactors. Vienna, Austria.
- Wu, Y., Klein, J., Zhou, H., and Zuo, L., 2018. Thermal and fluid analysis of dry cask storage containers over multiple years of service. *Annals of Nuclear Energy* 112, 132-142.

### **3. Characterization of natural and synthetic aggregates properties and their effect on the physical and mechanical properties of radiation shielding concrete**

#### **3.1 Abstract**

Concrete is considered an ideal radiation shielding material for its effective capacity to attenuate most harmful radiations. Shielding efficiency against ionizing radiation, specifically neutrons and gamma rays, is achieved by replacing the traditional limestone coarse and siliceous fine aggregates with other natural and/or synthetic aggregates that possess radiation attenuation properties. This study characterizes the mechanical and physical properties of natural and synthetic aggregates and determines the suitability of adding them to radiation shielding concrete as aggregate replacement. The assessment employs analytical models and considers the fresh properties, hardened properties, and durability of concrete. The results were cross-referenced with published experimental studies on radiation shielding concrete (RSC). A design methodology for RSC is proposed that considers the radiation shielding properties, workability, compressive strength, and durability.

Keywords: Radiation shielding concrete; heavyweight aggregates; compressive strength; chloride diffusion coefficient; workability.

### 3.2 Introduction

Concrete, which comprises of cementing material, aggregate, air, water, and admixtures, is the world most used construction material. Its physical, mechanical, and durability properties are well suited for all built infrastructure. Radiation shielding is an additional required concrete property for the nuclear built infrastructure. Traditionally, the effectiveness of radiation shielding concrete (RSC) against X-rays, gamma rays, and neutrons has been addressed by replacing the aggregates with natural and/or synthetic aggregates as those listed in Table 3.1 [1-3]. Micro and nano-scale additives such as ground slag, heavy glass scrap, and heavy metal oxides have been used to enhance the concrete attenuation properties against X-rays and  $\gamma$ -rays [4-6]. Boron carbide powder, ground borosilicate glass, boron frits, and heavy polymers with high hydrogen content and/or elements with high absorption cross-section for thermal neutrons were added to enhance the concrete neutron's attenuation and absorption capabilities [5, 7, 8]. Review of RSC design approach reveals that, for many studies, the aim has been solely on enhancing the shielding properties with little design considerations given to the concrete rheological, physical, mechanical, and durability properties [7, 11-13].

This study examines the effects of adding RSC aggregates on the concrete properties, specifically the rheological, physical, mechanical, and durability properties. This is achieved by collecting and assessing the properties of the aggregates, subsequently the significance of the aggregate properties on the concrete's workability, strength and durability is examined by using analytical models reported in the literature. This is followed by a review of relevant case studies to determine the documented effects of

these aggregates on the properties of concrete. A design methodology is then proposed for developing RSC mixtures that possess the desired radiation shielding, rheological, physical, mechanical, and durability properties.

**Table 3.1** Aggregates typically used in RSC [9, 10]

Predominant constituent	Class of the material	Chemical composition	Specific gravity
Serpentine	Crushed stone, hydrous silicate	$Mg_3Si_2O_5(OH)_4$	2.40 to 2.65
Colemanite	Crushed stone, hydrous boron ore	$Ca_2B_6O_{11}.5H_2O$	2.41 to 2.42
Limonite	Crushed stone, hydrous iron ore	$(HFeO_2).(H_2O)_y$	3.40 to 3.80
Goethite	Crushed stone, hydrous iron ore	$HFeO_2$	3.50 to 4.50
Barite	Gravel or crushed stone	$BaSO_4$	4.00 to 4.40
Ilmenite	Crushed stone, iron ore	$FeTiO_3$	4.20 to 4.80
Hematite	Crushed stone, iron ore	$Fe_2O_3$	4.60 to 5.20
Magnetite	Crushed stone, iron ore	$Fe_3O_4$	4.60 to 5.20
Ferrophosphorus	Synthetic	$Fe_nP$	5.80 to 6.30
Boron Frit	Synthetic	$B_2O_3, Al_2O_3, SiO_2, CaO$	2.60 to 2.80
Boron Carbide	Synthetic	$B_4C$	2.51 to 2.52

### 3.3 Concrete properties

Design and control of concrete mix proportions stipulate workability and curing requirements for when concrete is in a liquid state, and strength and durability requirements for when concrete hardens. Slump, the standard test for workability and consistency of fresh concrete [14], was historically controlled by adding water at the detriment of strength and durability [15, 16]. Advances in concrete technology, through the introduction of chemical and mineral admixtures, has led to the development of ultra-high strength and self-consolidating concrete and exposed the limitations of the slump test [17, 18]. As such, Bingham rheological properties, defined by yield stress and plastic

viscosity, are postulated among others to quantify the flow properties of fresh concrete [17, 19]. Using this scientific premise and analytical tools, predictive models developed for quantifying the concrete's rheological properties using the composition and mix proportion are employed in this study to examine the effects of changing the aggregates properties on the rheological properties of RSC [20, 21]. Additionally, two predictive models for quantifying the concrete compressive strength [22] and chloride diffusion coefficient [23, 24] using the mixture composition and constituents properties, are employed to study the effects of aggregates on the strength and durability of concrete, respectively.

The relationship between concrete composition and rheological properties, specifically plastic viscosity ( $\eta_r$ ) and yield stress ( $\tau_0$ ), has been analytically reproduced in Chidiac and Mahmoodzadeh rheological model [20], where

$$\eta_r \cong \eta_i \lambda; \quad (3.1)$$

$$\lambda = y^3 \frac{4(1-y^7)}{4(1+y^{10})-25y^3(1+y^4)+42y^5}; \quad y(\varphi) = \left(\frac{\varphi}{\varphi_{max}}\right)^{\frac{1}{3}} (1 - K) \quad (3.2)$$

$$K = \begin{cases} 0.006 * \frac{Cement}{Water} & \text{Without HRWRA} \\ 3.8 * \frac{HRWRA}{Cement} * \frac{Water}{Cement+FineSand+Sand} & \text{With HRWRA} \end{cases} \quad (3.3)$$

in which  $\eta_i$  is the intrinsic plastic viscosity,  $\varphi$  is the packing density,  $\varphi_{max}$  is the maximum packing density of the concrete mixture, and *Cement*, *Water*, *HRWRA*, *sand* are mass contents; and

$$\tau_0 \cong \tau_i \lambda \quad (3.4)$$

$$y(\varphi) = \left( \frac{\varphi}{\varphi_{max}} \right)^{\frac{1}{3}} \left( 1 - C_y \frac{m_G}{m_w} \right) \quad (3.5)$$

in which  $\tau_i$  is the intrinsic yield stress,  $m_G$  and  $m_w$  are masses of aggregates and water respectively, and  $C_y$  is a fitting parameter. The models capture geometrically the concrete suspension at the micro-scale,  $y(\varphi)$ , by means of the cell method as shown in Fig. 3.1.

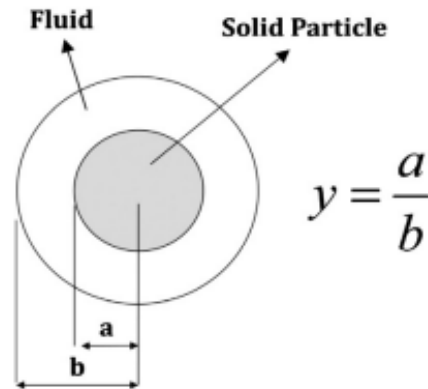
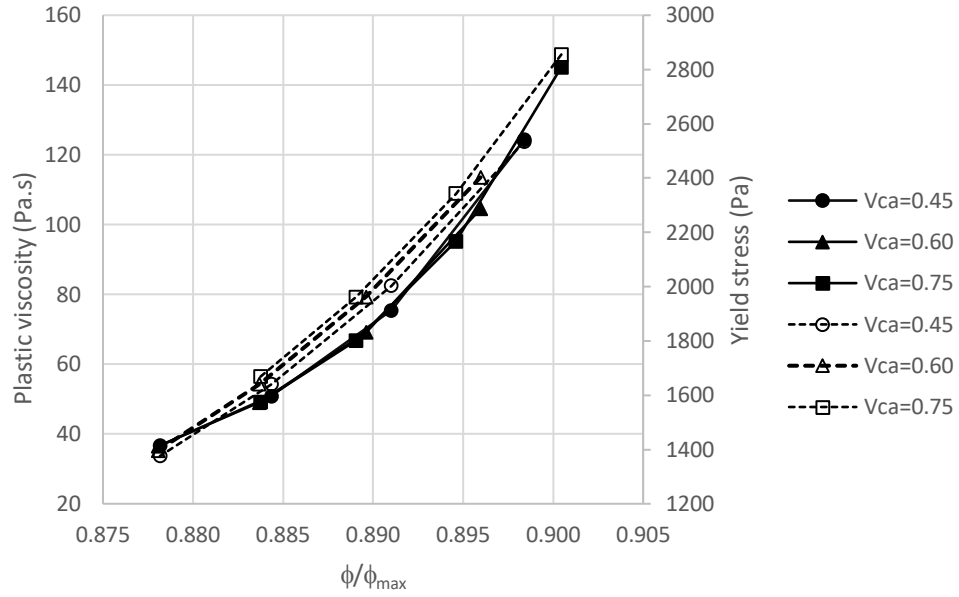


**Fig. 3.1** Definition of the cell [20]

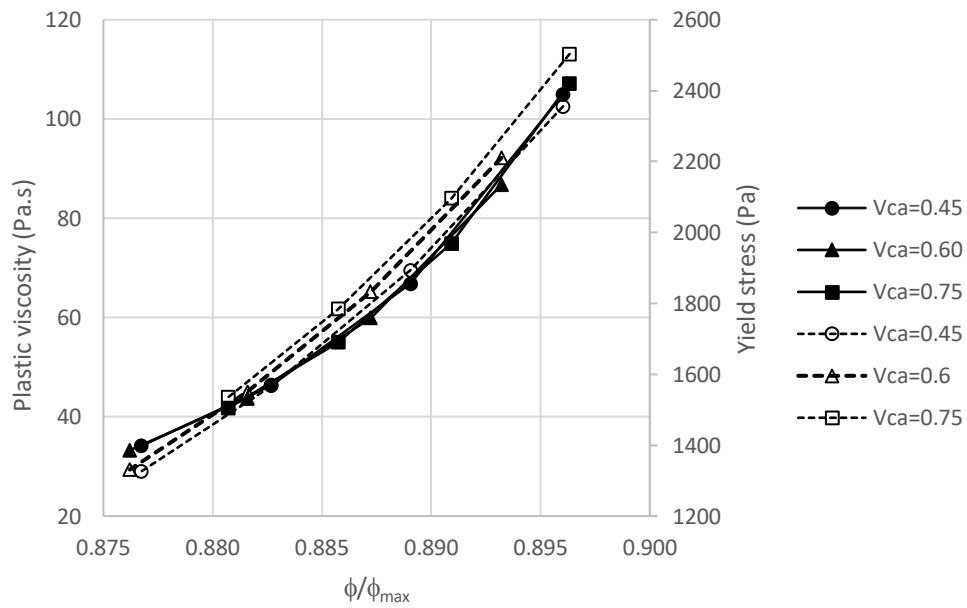
The models uncover the complex relationship between the rheological properties and the mixture composition including the importance of the aggregates. Strong dependency on the ratio of packing density to the maximum packing density is evident. The packing density is affected by the aggregate properties being shape, angularity, surface texture, maximum particle size, and particle size distribution. Studies on binary mixtures revealed that the shape and size of the particles are the main factors affecting the packing density and workability. A linear relationship is observed between the aggregate shape and the packing density and volume fraction, and a convex trend with the aggregate size.

For illustration, the rheological properties of a 0.4 w/c concrete mixture with a maximum aggregate size of 14 and 20 mm and three different volume fractions of coarse aggregates

( $V_{CA}$ ) quantified by the models are plotted in Fig. 3.2. The results show that increasing the maximum aggregate size from 14 mm to 20 mm led to an increase in workability, by decreasing both plastic viscosity and yield stress, which is consistent with other studies whose results have shown that increasing the maximum aggregate size increases the packing density and reduces viscosity [20, 21, 25, 26]. It should be noted that an increase in  $V_{CA}$ , which influences the sand-to aggregate ratio (S/A), can result in either a decrease or an increase in the maximum packing density depending on the total aggregates gradation. The optimum S/A sought corresponds to a mixture with minimum porosity and therefore maximum workability and strength [27]. In addition to the model results, Fig. 3.3, which provides a graphical display of the effect of the particle shape and S/A on the rheological properties, will form part of the criteria adopted to evaluate the effects of adding or replacing aggregates on RSC properties.



a)



b)

**Fig. 3.2** Rheological properties versus packing density of 0.4 w/c concrete mixture with  
 a) 14 mm and b) 20 mm max aggregate size

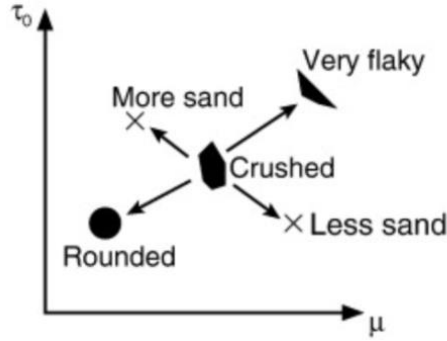


**Fig. 3.3** Effects of particle shape and S/A on concrete's yield stress and plastic viscosity [25]

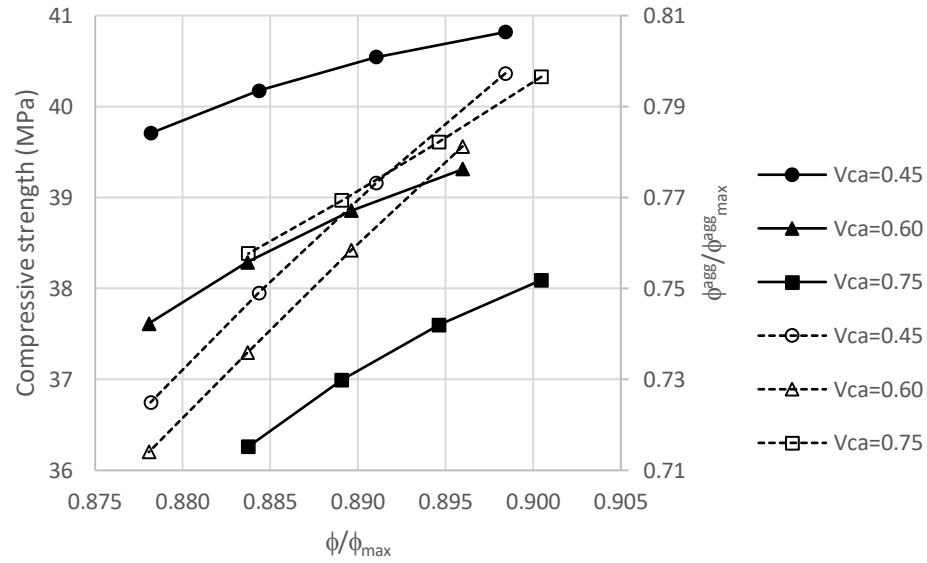
The compressive strength model [22] adopted to evaluate the effects of added aggregates on the strength of RSC accounts for the aggregates type and gradation, in addition to the concrete mix proportions. The model includes a cement hydration model that depends totally on the cement chemical composition and the cement degree of hydration, an APT model which accounts for the concrete mix proportions and the packing density that depends on the aggregate volume fractions and gradation, bond strength model that represents the strength of the bond between the hydrated cement paste and the aggregate, and cement paste strength model at 28 days that depends on the cement type. The model is described by the following equations [22]

$$f_c(t) = \begin{cases} 0, & a(t) \leq a_{cr} \\ KR_{c28} \left(\frac{APT}{D}\right)^A B^{(w+\frac{V_a}{c})} (a(t) - a_{cr}), & a(t) > a_{cr} \end{cases} \quad (3.6)$$

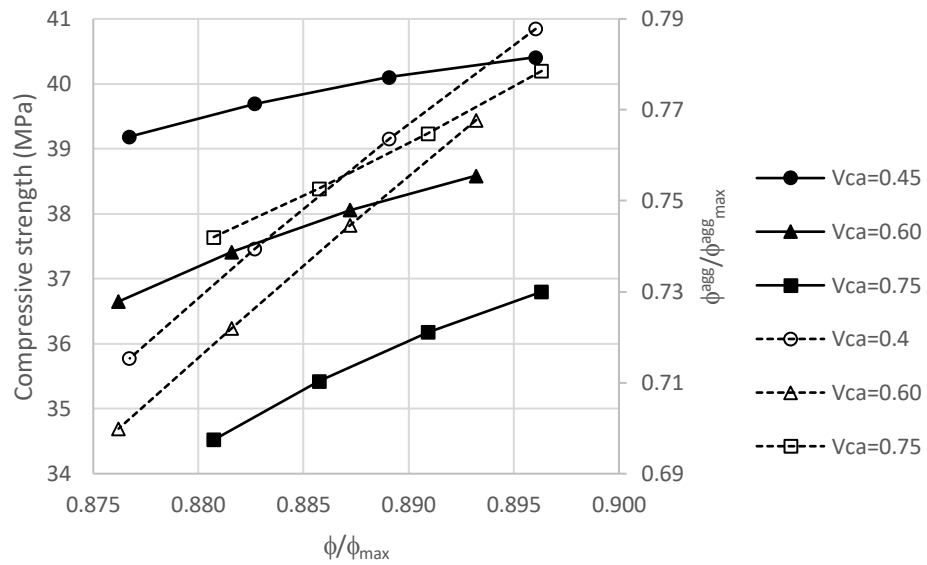
$$APT \approx -0.5 \left( D_s + \frac{\Phi_{ca} D_s^2}{\Phi_s D_{ca}} + \frac{\Phi D_s^2 (1 - \varphi_{max})}{\Phi_s \varphi_{max} D} \right) + 0.5 \sqrt{\left( D_s + \frac{\Phi_{ca} D_s^2}{\Phi_s D_{ca}} + \frac{\Phi D_s^2 (1 - \varphi_{max})}{\Phi_s \varphi_{max} D} \right)^2 + \frac{4(\varphi_{max} - \Phi) D_s^2}{3\varphi_{max} \Phi_s}} \quad (3.7)$$

in which  $f'_c$ ,  $K$ ,  $R_{c28}$ ,  $D$ ,  $D_s$ ,  $D_{ca}$ ,  $A$ ,  $B$ ,  $c$ ,  $w$ ,  $V_a$ ,  $a$ ,  $a_{cr}$ ,  $t$ ,  $\Phi$ ,  $\Phi_s$ ,  $\Phi_{ca}$  are respectively, concrete compressive strength, paste to aggregate bond strength constant, standard cement strength at 28 days, mean diameter of the total aggregate particles gradation, mean diameter of sand particles, mean diameter of coarse aggregate particles, constant that depends on the shape of the aggregate particles, constant that depends on specimen shape and test conditions, cement content, water content, volume fraction of the entrapped and entrained air, degree of cement hydration, critical degree of cement hydration, time, volume fraction of total aggregates, volume fraction of fine aggregates, and volume fraction of coarse aggregates. APT which captures a complex relationship between strength and the properties of aggregates, is inversely proportional to the aggregates volume fraction and consequently to the concrete compressive strength [22].

Figure 3.4 captures the model relationship between the compressive strength and ratio of the mixture packing density to maximum packing density of a 0.4 w/c concrete mixture with 14 mm and 20 mm maximum aggregate size, 5% air entrained, and three different  $V_{CA}$ . The results show that a) an increase in the ratio of packing density to maximum packing density results in an increase in the compressive strength attributed to compaction, b) the increase of compressive strength with packing density ratio is more significant with increased  $V_{CA}$ , and c) an increase in the maximum aggregate size results in a decrease in compressive strength which is attributed to a reduction in the packing density.



a)



b)

**Fig. 3.4** Compressive strength and packing density of aggregate versus packing density of 0.4 w/c concrete mixture with a) 14 mm and b) 20 mm coarse aggregate size

The effects of the aggregates on the cement hydration reaction are equally important. Experimental data and models results reveal that the increase rate and magnitude of concrete compressive strength are directly related to the rate and magnitude of the cement degree of hydration [28, 29]. Accordingly, addition of aggregates that negatively interferes with the rate and/or the magnitude of the cement chemical hydration reaction would be detrimental to the concrete compressive strength. Chemical interference and/or interaction between cement and aggregate will therefore need to be examined as it will have a direct impact on the mechanical and durability properties [30, 31]. Moreover, the bond strength between the hydrated cement paste and the aggregate needs to be examined. The bond consists of a mechanical and chemical bond with the former depends on the aggregate's surface texture and the latter on the aggregate's water absorption.

Concrete chloride diffusion coefficient ( $D_{Cl}^C$ ), which is a measure of durability, is adopted for evaluating the aggregates.  $D_{Cl}^C$  can be estimated using the following equations [23].

$$D_{Cl}^C = f_{\tau} \cdot f_{ITZ} \cdot D_{Cl}^{bcp} \quad (3.8)$$

in which

$$f_{\tau} = \frac{3(1-V_a)^2}{3-V_a} \quad (3.9)$$

$$f_{ITZ} = \frac{12+18 t_{ITZ} S_a}{12-9 t_{ITZ} S_a} \quad (3.10)$$

$$D_{Cl}^{bcp} = \exp\left(a_1 \left(1 - \frac{w+V_{EA}}{cm}\right) (\alpha^* - \alpha)\right) \exp(-a_2 SF - a_3 GGBFS) \quad (3.11)$$

$f_{\tau}$ ,  $f_{ITZ}$ ,  $D_{Cl}^{bcp}$ ,  $V_a$ ,  $t_{ITZ}$ ,  $S_a$ ,  $a_i$ ,  $SF$ ,  $GGBFS$ ,  $w$ ,  $cm$ ,  $V_{EA}$ ,  $\alpha$  are respectively, the tortuosity factor, the ITZ factor, the bulk cement paste chloride diffusion coefficient,

aggregate volume fraction, thickness of the interfacial transition zone (ITZ) layer, aggregate unit surface area, calibration constants, silica fume weight fraction, ground granulated blast furnace slag weight fraction, water content, cementing material content, volume of the entrained air, and degree of hydration.  $D_{cl}^c$  like compressive strength, depends on the properties of the cement paste, properties of the ITZ and the volume fractions and gradation of the aggregates.

It is evident that both  $f_\tau$  and  $f_{ITZ}$  are functions of the aggregate properties. Figures 3.5 and 3.6 are reproduced to illustrate the relationship and significance of the aggregates volume fraction and properties on  $D_{cl}^c$ . Results show an increase in  $V_a$  and a decrease in  $S_a$  result a decrease in  $f_\tau$ ,  $f_{ITZ}$ , and  $D_{cl}^c$ . Moreover, the ITZ thickness and properties are known to depend on aggregate properties like shape, angularity, surface texture, and water absorption [22, 23].

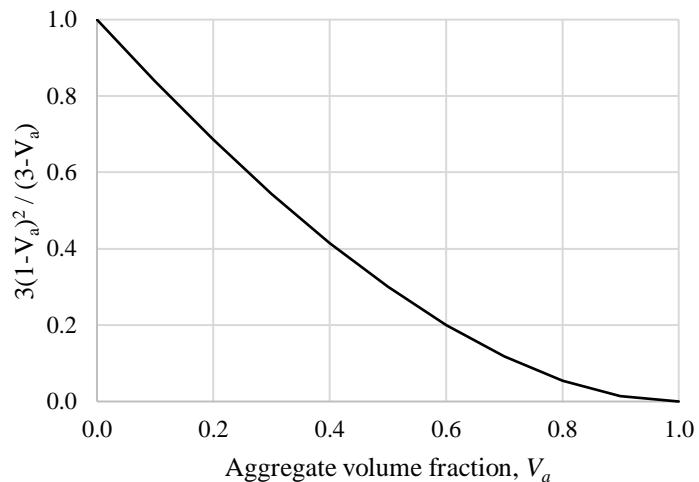


**Fig. 3.5** Tortuosity factor versus aggregate volume fraction [24]

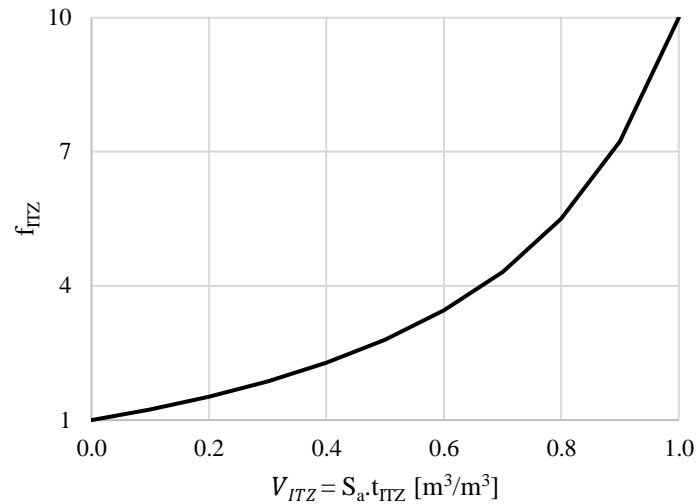


**Fig. 3.6** Interfacial transition zone factor ( $f_{ITZ}$ ) versus  $V_{ITZ}$  [23]

In brief, the physical, mechanical, and chemical properties of the aggregates in addition to their volume fraction are critical to the workability, strength, and durability of concrete. Aggregate and concrete mix packing density, aggregate volume fraction, and aggregate maximum size, although they are very important design parameters for fresh and hardened concrete properties, their values can be specified to meet the design requirement irrespective of the aggregate type. As such, they are not included in this assessment. The density, surface texture, strength, surface water absorption, and reactivity and mineral solubility of the aggregates are examined closely as they impact the mechanical and durability properties of RSC. The assessment provides a comparative analysis of the aggregate properties to those of limestone. The acceptance criteria are deduced from the traditional material used as aggregates, limestone and siliceous sand.

### 3.4 Physical and mechanical properties of aggregates possessing radiation attenuation

#### 3.4.1 Properties

The physical and mechanical properties of the aggregates listed in Table 3.1 are given in Table 3.2. The properties include density, unit weight ( $\gamma$ ), water absorption (WA), crushing value (CV), uniaxial compressive strength (UCS), impact value (IV), Los Angeles abrasion value (LAAV), and modulus of Elasticity ( $E_i$ ).

The values of  $IV$  [56],  $UCS$  [56],  $LAAV$  [56], and  $E_i$  [57] were calculated using the following equations:

$$IV (\%) = 0.99 CV - 0.82 \quad (3.12)$$

$$CV (\%) = 78.82 - 11.73 \ln (UCS) \quad (3.13)$$

$$IV (\%) = 1.92 LAAV - 8.85 \quad (3.14)$$

$$E_i = \left( \frac{\ln UCS^{0.689} \ln \gamma^{4.95}}{16.6} \right)^{2.885} / 10^4 \quad (3.15)$$

Visual comparison of the aggregates' properties, shown in Fig. 3.7, reveals the similarities and differences in their mean values relative to those of a limestone (Li). The corresponding standard deviation shows the variation in the property.

**Table 3.2** Physical and mechanical properties of aggregates typically used in RSC

Aggregate name (label)	Density, g/cm <sup>3</sup>	Avg. unit weight ( $\gamma$ ), kN/m <sup>3</sup>	Water absorption (WA), %	Crushing value (CV), %	Uniaxial compressive strength (UCS)*, MPa	Impact value (IV)*, %	Los Angeles abrasion value (LAAV)*, %	Modulus of elasticity (E <sub>i</sub> )*, GPa
Serpentine (Se)	2.4 - 2.65 [32, 33]	24.75	1.3 - 8.3 [34-36]	23.8 - 37.45 [34-36]	34.02 – 109	22.74 - 35.2	16.45 – 22.94	6.3 – 11.1
Colemanite (Co)	2.41 – 2.42[32, 33]	23.72	1.35 – 4.99 [37-39]	73.74 – 79.5 [38]	0.95 – 1.55	72.19 – 77.89	42.21 – 45.18	≈0.082
Limonite (Lm)	3.4 - 3.8 [32, 33]	35.28	5.1 - 11.42 [40, 41]	22.4 - 31 [41, 42]	58.95 – 122.72	21.35 – 29.87	15.73 – 20.17	37.49 – 52.1
Goethite (Go)	3.5 - 4.5 [32, 33]	39.2	8.07 – 13.5 [36, 43]	20 - 34.3 [36, 43]	44.49 – 150.58	18.98 – 33.14	14.49 – 21.87	49.31 – 85.8
Barite (Ba)	4.0 - 4.4 [32, 33]	41.16	0.6 - 1.5 [36, 43-46]	43 – 63.3 [36, 42, 43, 47]	3.76 – 21.19	41.75 – 61.85	26.35 – 36.82	7.35 – 38.65
Ilmenite (Il)	4.2 - 4.8 [32, 33]	44.1	0.1 - 2.2 [2, 42, 47]	38 - 41.5 [42, 47]	24.08 – 32.46	36.8 - 40.26	24.4 – 26.22	54.54 – 65.18
Hematite (He)	4.6 - 5.2 [32, 33]	48.02	0.8 – 10.4 [2, 41, 48, 49]	12.55 – 59.4 [41, 48, 50]	5.24 – 284.18	11.6 – 57.98	11.15 – 35.55	20.47 - 234.62
Magnetite (Ma)	4.6 - 5.2 [32, 33]	48.02	0.11 – 0.83 [36, 41, 51]	17 – 19.87 [36, 41, 51]	152.26 – 194.46	16.01 – 18.85	13.46 – 14.96	185.92 – 204.34
Limestone (Li)	1.76 – 2.75 [32, 33]	22.15	0.3 – 1.8 [52]	20 – 32 [52]	54.13 – 150.57	18.98 – 30.86	14.49 – 20.68	4.87 – 8.67
Ferro-phosphorus (FP)	5.8 - 6.3 [10, 53]	59.29	0.9 [53]	--	--	--	--	--
Boron Frits (BF)	2.6 - 2.8 [11, 54]	26.46	--	--	--	--	--	--
Boron Carbide (BC)	2.51– 2.52[13, 55]	24.59	Nil [55]	--	--	--	--	--

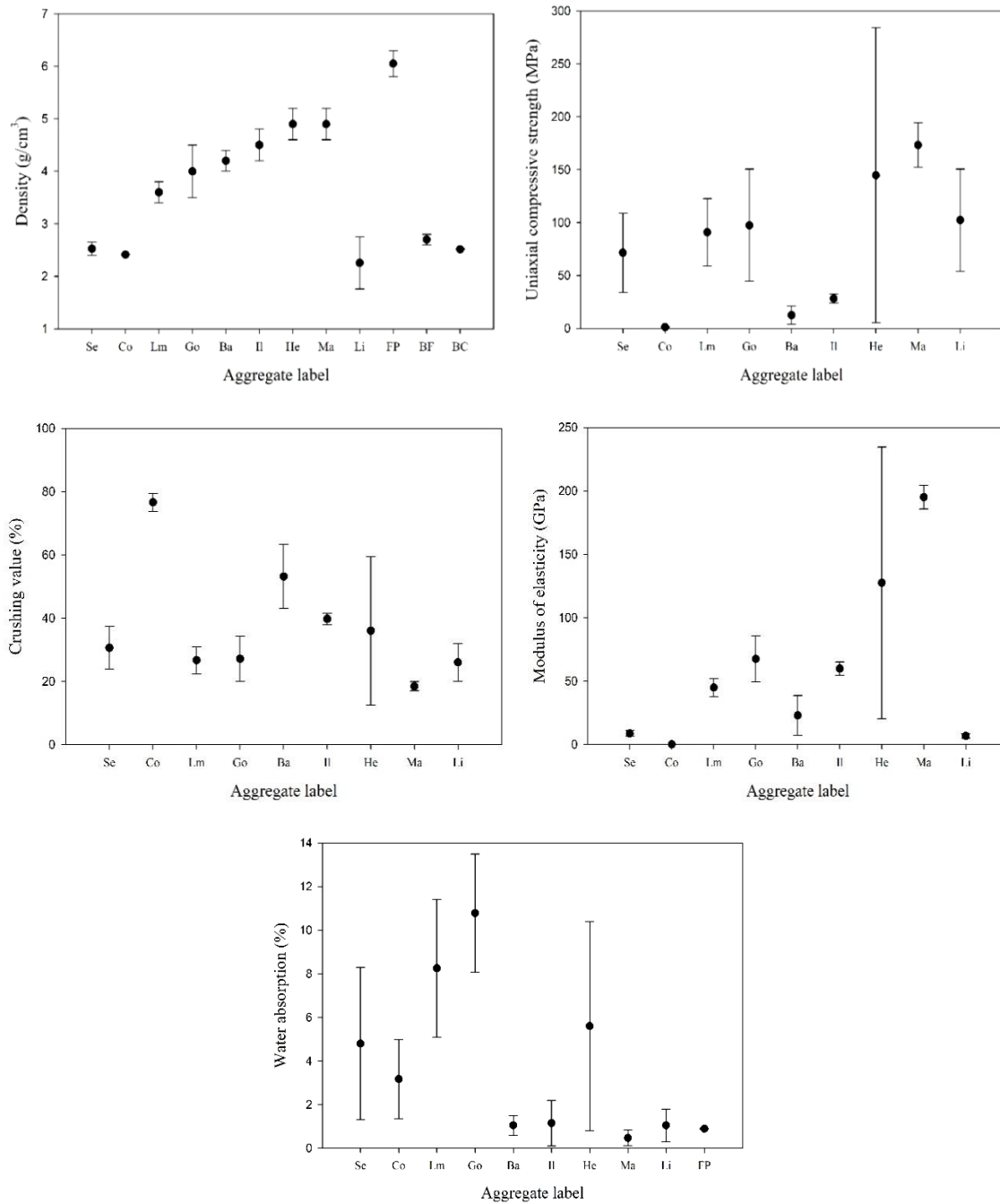


**Fig. 3.7** Display of RSC aggregates physical and mechanical properties

The results show that densities of some aggregates, specifically barite, ilmenite, hematite, magnetite, and ferro-phosphorus, are significantly greater than that of limestone. Denser

aggregates are useful for increasing radiation shielding properties of concrete; however, they can lead to segregation during the mixing and casting process if the concrete mixture is not properly designed [10]. Although the material density is sometimes correlated to its UCS, the results show no apparent correlation. Compared to limestone UCS, most aggregates are statistically equal except for colemanite, barite, and ilmenite, which show lower strength, and magnetite that shows a higher strength. Hematite UCS values indicate that the aggregate can be either very strong or very weak depending on where it is mined. Weak aggregates in concrete will lower its compressive strength.

Aggregate's crushing value is a relative measure of its resistance to crushing under a gradually applied compressive load [58]. Lower aggregate crushing value, which implies lower amount of crushed aggregates, is recommended for use in concrete especially for roads, floors, and pavements, whereas those with values greater than those of limestone should be avoided as they weaken the concrete overall strength [58]. Results show that both colemanite and barite have significantly high crushing values that reduce the concrete strength and wearing resistance [59]. The same deduction on colemanite and barite was made from their UCS values.

Modulus of elasticity, which is a measure of the material stiffness, is an important property for concrete structures [28, 57]. Relative to limestone, aggregate with significantly higher modulus will be stiffer and attract higher load thus making it susceptible to cracking at the interface between the aggregate and cement paste, and the aggregate with lower modulus will be flexible and will not contribute to the composite load sharing thus increasing the stress values in the cement paste. Accordingly, although

most of the aggregates have higher values, they are still considered acceptable. The exception would be colemanite that has a very low modulus of elasticity and magnetite that has a very high value.

The aggregates water absorption is found to range from 0.3% to 13.5%, with limestone values ranging between 0.3 and 1.8%. Except for barite, ilmenite, magnetite, and ferro-phosphorus, the remaining aggregates have high or very high water absorption values that can cause internal bleeding and a weak interfacial transition zone, and weaken the bond between the aggregates' surface and the cement paste. These scenarios will have negative effects on the microstructure, mechanical properties, and durability of the hardened concrete [24, 28]. Aggregate with high water absorption also adversely affects the workability and flow properties of the concrete [17, 27]. Hematite and serpentine show a wide range in their water absorption values, an indicator that the property is not specific to the type of aggregate but more of where the material was mined. Same observation was deduced from hematite UCS values.

Reactivity and water solubility of the aggregates need to be determined before being used in concrete. Most of limestone and traditional aggregates are almost chemically inert and/or chemically compatible with the cementitious material [59]. Some of the aggregates, that are used for radiation shielding concrete, are chemically incompatible or cause a deleterious effect on the chemical reaction when added to cementing materials. For example, colemanite, especially when used as a fine powder, and most of boron compounds like sassolite, ulexite, and borates adversely affect the cement hydration kinetics and significantly retard the reaction rate, weaken the microstructure, and

compromise the concrete mechanical properties and durability [13, 30, 31]. The causes are soluble minerals that react with the dissolved cement constituents and disturb the cement hydration kinetics.

### **3.5 Case studies - RSC containing aggregates possessing radiation attenuation properties**

#### **3.5.1 Natural aggregates**

Properties of high performance concrete mixes with dolomite, hematite, ilmenite, and slag as aggregate replacement were studied by Abo El-Enein et al. [2]. The results reveal differences in slump values that were mainly attributed to the variations in the aggregate water absorption and shape. Specifically, concrete containing hematite produced the lowest slump value as the hematite aggregates had irregular, rough, and porous surface texture, and high water absorption value of 10.4% [2]. Water absorption is necessary for the chemical bond to form; however, a high value implies porous particles that are detrimental to the strength and durability of the concrete as shown in Fig. 3.8. Porous aggregates have been used successfully as reservoir for internal curing to mitigate shrinkage which is not the intended use in this case.

The observed results are consistent with the predictive model results. Specifically, the shape and texture of the aggregate adversely affect the concrete rheological properties. The aggregate's high water absorption and porosity also adversely affect the concrete mechanical and durability properties due to weak ITZ layer that is confirmed by SEM [2], and weak aggregates. For reference, hematite when used as a coarse aggregate replacement yields an efficient radiation shielding concrete for X-rays and  $\gamma$ -rays due to

the increase in the effective atomic number,  $Z_{\text{eff}}$ , and the linear attenuation coefficient,  $\mu$ , of the prepared mix [1-3, 60].

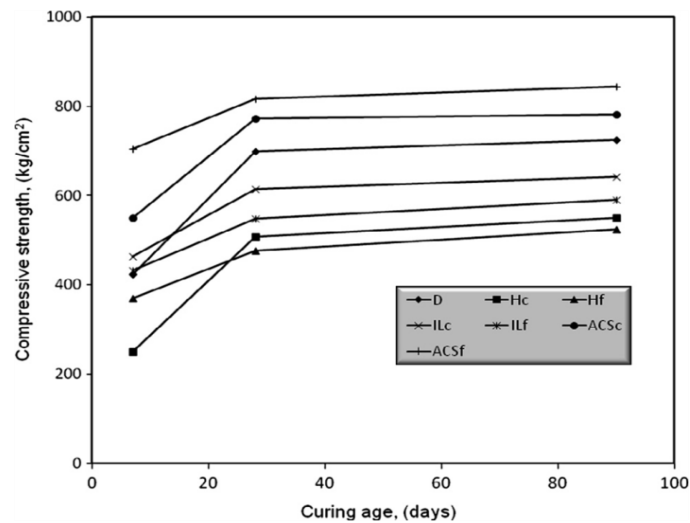


**Fig. 3.8** RSC compressive strength containing dolomite (D), hematite (H), ilmenite (IL) and air-cooled slag (ACS) as coarse (c) and fine (f) aggregates versus curing time [2]

Results of another study that used hematite as coarse aggregate replacement up to 50% by volume showed better physical and mechanical concrete properties [3]. However, the aggregate's water absorption was 1.27%, further confirming the importance of this parameter to RSC mechanical properties and durability. These results also show that the type of aggregate is not the only indicative of its properties as its physical and mechanical properties can differ greatly depending on where it is mined [3].

Barite and goethite, which are also heavy ores, are widely used in RSC. From the perspective of nuclear attenuation properties, barite is a very effective material for attenuating  $\gamma$ -rays especially at low energies because of the high atomic number of barium element,  $Z=56$  [43]. Goethite ore, which is a hydrous iron ore, is very effective in

attenuating X-rays and  $\gamma$ -rays due to the presence of iron, and fast neutrons due to the hydroxyl group contained in the pure molecule ( $\text{FeO}(\text{OH})$ ) [61, 62]. Furthermore, goethite is effective in RSC as it transforms to ferric oxide through a dehydroxylation reaction when the temperature reaches  $385\text{ }^\circ\text{C}$  [61, 63].

Properties of RSC mixes containing magnetite (M), barite (B), goethite (G), or serpentine (S) as coarse aggregate replacement, and 10% silica fume (1), 20% fly ash (2), or 30% ground granulated blast furnace slag (3) added to the cement, were studied [36]. RSC mixes include 0.35 w/c and OPC content of  $450\text{ kg/m}^3$  [36]. The results further confirm the adverse effect of aggregate's high water absorption on workability and compressive strength. Mixes with goethite aggregates, whose water absorption was high at 8.07%, yielded the lowest slump and the lowest compressive strength as shown in Fig. 3.9 [36]. Weak ITZ, bond strength, and aggregates result in a weak concrete.

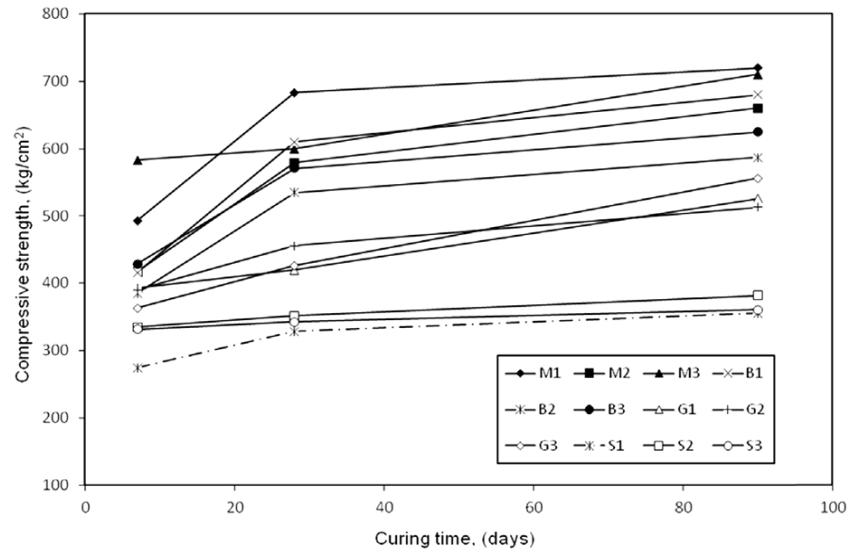


**Fig. 3.9** RSC compressive strength versus curing time [36]

RSC mixes containing barite as coarse aggregate, produced normal workability but low compressive strength values. Barite's low water absorption of 0.6% can adversely affect the chemical bond between the paste and the aggregate. The high crushing value of barite was also reported to contribute to the low strength as it can compromise the particle distribution and the mix packing density. These results correlate with the compressive strength model where the bond strength,  $K$ , decreases. The chloride diffusion coefficient will be high due to the poor bond/pervious interface resulting in poor durability.

The results reported by El-Samrah et al. [43] on concrete mixes containing goethite coarse aggregates with water absorption of 13.5% further confirm the adverse effect of high water absorption on RSC workability and compressive strength. Limonite, which was added as fine aggregates replacement, was studied because of its good neutron shielding properties as it contains a considerable amount of crystallized water. Limonite high water absorption value of 30% was the reason for the low compressive strength in

addition to its clay form as fine aggregates. Colemanite neutrons' attenuation and absorption properties are sought after when preparing neutrons shielding concrete. Colemanite aggregates contain a considerable amount of boron and possesses crystallized water [12, 64-66]. Gencil et al. [39] studied the mechanical properties of concrete containing colemanite as coarse and fine aggregates with an equal ratio and up to 50% by volume with a 10% increment labelled CC10 to CC50. The concrete unit weight, compressive strength, and splitting tensile strength were found to decrease with the increase in colemanite content as reproduced in Fig. 3.10.

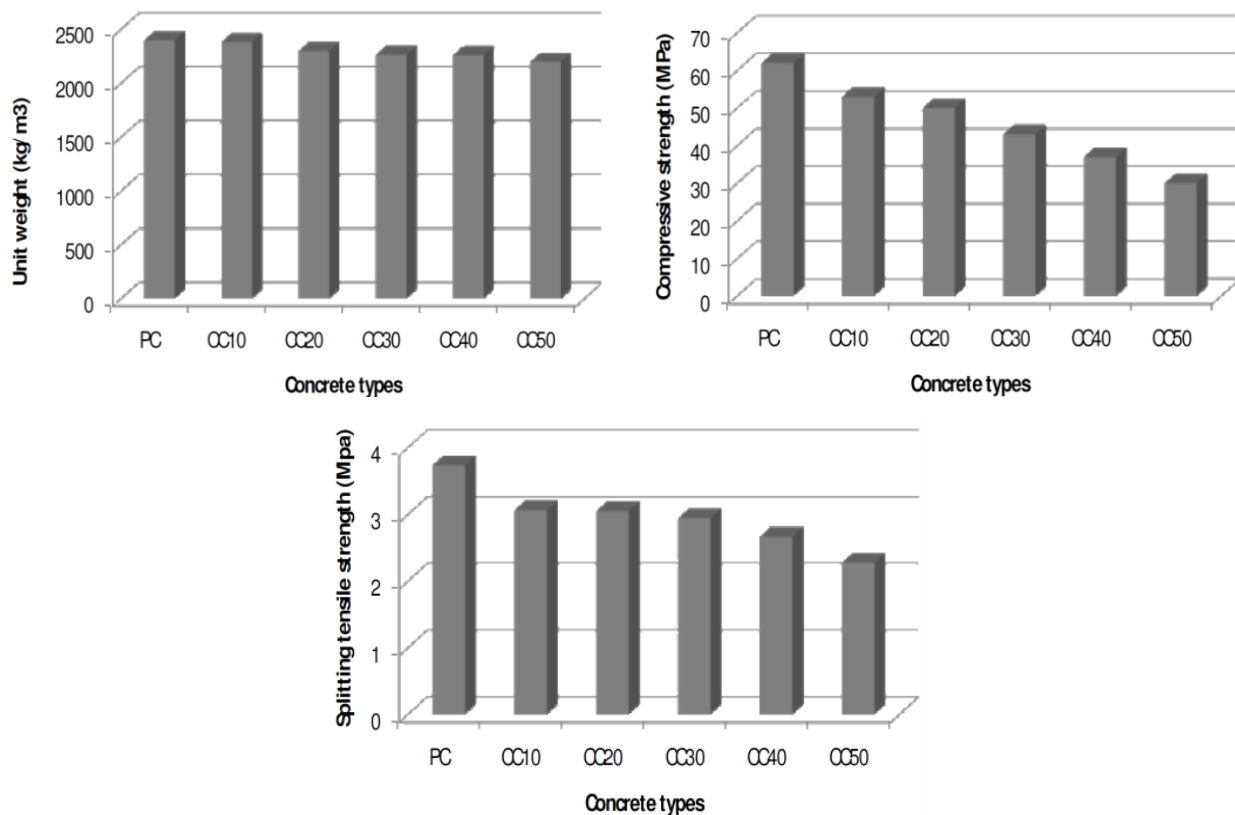


**Fig. 3.10** Unit weight, compressive strength, and splitting tensile strength of concrete containing colemanite [39]

The authors attributed the degradation to the material low specific gravity and a weak ITZ [39]. The observed performance is predictable by the compressive strength model and the chloride diffusion coefficient model, specifically a decrease in the strength due to weakened bond strength and ITZ layer, and an increase in the chloride diffusion coefficient due to an increase in the ITZ factor.

Since the colemanite solubility was not reported, and the cement hydration kinetics were not measured, the authors did not account for the possibility of boron soluble interfering with the hydration kinetics. Colemanite, when added as fine particles to concrete mix, has been reported to retard the hydration reaction and decrease the concrete compressive strength [30, 31]. Figure 3.11 displays the retardation effects of colemanite on the cement hydration captured using isothermal calorimetry [30, 31].

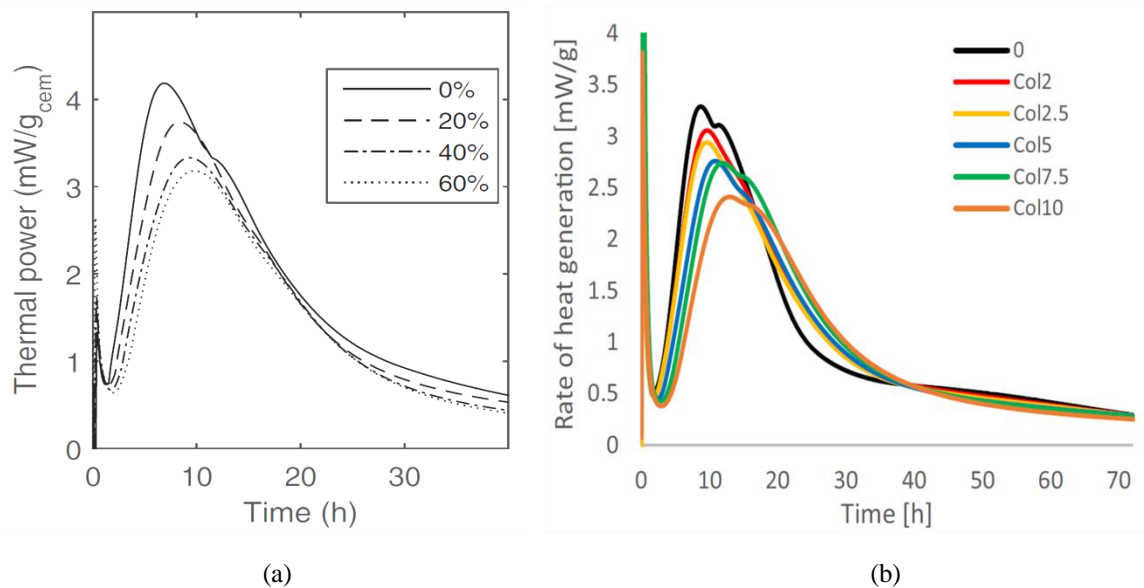


**Fig. 3.11** Hydration reaction of cement containing fine colemanite reported in two different studies; (a) Colemanite percentage relative to the cement weight, (b) Percent of boron relative to cement mass [30, 31]

Kubissa et al. [67] investigated the properties of concrete containing barite and magnetite as coarse aggregates using large scale samples, specifically 4 m high columns and massive blocks. Ready-mix company prepared the concrete and pumped it into the formwork [67]. The concrete compressive strength at 28, 90, and 630 days, given in Table 3.3, show that column A which was filled with concrete contained barite has lower average compressive strength values compared to the magnetite mixes used to fill the blocks, T49, T50 and T51. Dry shrinkage measurements based on ISO 1920-8 up to 90 days revealed that barite concrete (column A) had the largest shrinkage [67]. These results are consistent with the material properties where magnetite has a higher UCS and lower water absorption in comparison to barite.

**Table 3.3** Compressive strength of concrete containing barite and magnetite (MPa) [67]

Age (days)	Concrete mix for column	Concrete mix for large blocks		
	A	T49	T50	T51
28	44.3 ( $\pm$ 2.1)	54.4 ( $\pm$ 1.4)	49.6 ( $\pm$ 1.8)	48.3 ( $\pm$ 1.9)
90	48.6 ( $\pm$ 1.9)	57.1 ( $\pm$ 2.6)	65.0 ( $\pm$ 1.1)	62.6 ( $\pm$ 1.6)
630	–	59.2 ( $\pm$ 1.7)	77.2 ( $\pm$ 2.4)	71.5 ( $\pm$ 2.2)

### 3.5.2 Synthetic aggregates

The use of synthetic and recycled materials with radiation attenuation properties as aggregate replacement for radiation shielding concrete is continuously increasing. Binna et al. [68] studied the use of synthetic resins, due to their high hydrogen and carbon contents, in neutrons shielding mortars. The mortar mixes had a 0.485 w/c, and high density polyethylene (HDPE), polypropylene (PP), or ultra-high molecular weight polyethylene (UPE) as fine aggregates replacement. The properties of the synthetic

polymers are reproduced in Table 3.4 [68]. The slump flow measurements of the mortar, shown in Fig. 3.12, indicate that the flow increased with the increase of HDPE and PP and decreased with the increase of UPE. UPE smaller particle size compared to the replaced sand led to the decrease in the slump flow.

**Table 3.4** Physical properties of the used synthetic resins [68]

Physical property	HDPE	PP	UPE
Particle size, mm	5	5	0.12
Average molecular weight, g/mol	3.5E05	3.5E05	5.0E06
Melting index, g/10 min	0.035	0.5	0.1
Yield stress, MPa	31.4	36	17
Density, g/cm <sup>3</sup>	0.956	0.900	0.930
Flexural modulus, MPa	77	1570	720

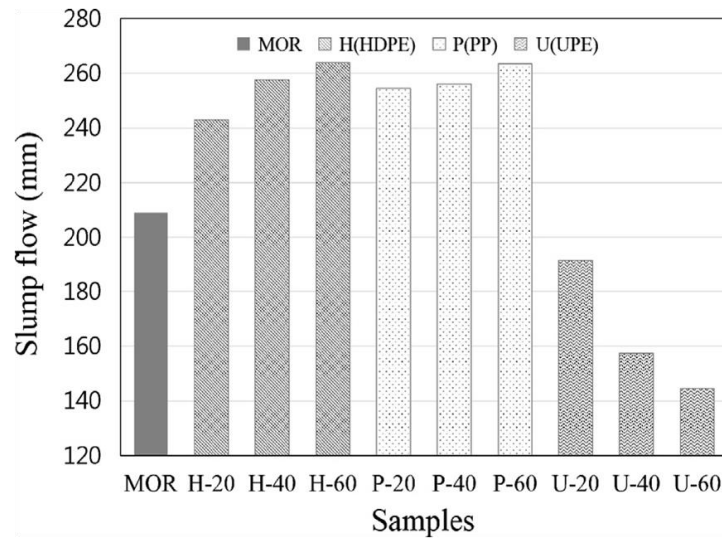


**Fig. 3.12** Slump flow of mortar containing HDPE, PP and UPE [68]

The compressive strength, presented in Fig. 3.13, show a loss in the mortar compressive strength irrespective of the type of synthetic resin used. This loss of strength was attributed to the weak bond between the polymer and the cement matrix due to the hydrophobic properties of synthetic resins and the smooth surface of the aggregates [68].

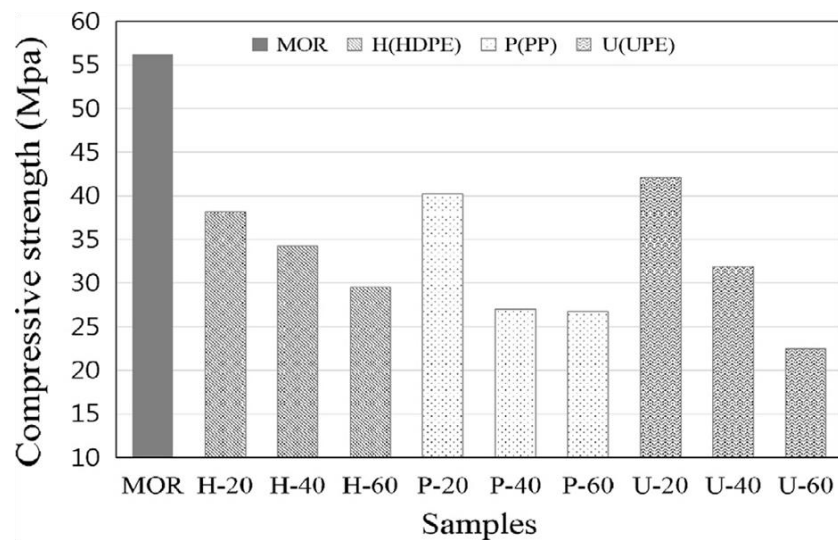


**Fig. 3.13** Compressive strength of mortar containing HDPE, PP and UPE [68]

The effect of using recycled high density polyethylene was studied to produce mortars with enhanced neutrons shielding capabilities by others [69]. The results were like the previous one where the mortars workability increases with increased HDPE, and the compressive strength decreases with increased HDPE. The latter is due to a weak adhesive strength between the polymer particles and the cement paste [69]. Others showed the same results when studying the use of polyethylene, terephthalate, bakelite and polypropylene as coarse or fine aggregates. The workability usually improves when using these polymers provided the particle size is comparable to that of the replaced sand [7, 70, 71].

Heavy weight glass obtained from cathode ray tubes of old TVs and monitors, and borosilicate glass obtained from exhausted thermal resistant cookware and chemical glassware, have been investigated as either aggregate or cement replacement in radiation shielding concrete [4, 6, 72-74]. Kim et al. [6] used cathode ray tube glass (CRTG) to replace 50% and 100% of the fine aggregates. The results show a continuous decrease in flexural and compressive strength with increased CRTG content. The decrease was attributed to the poor bond between the glass and the cement paste and to the inadequate glass particle gradation that adversely affected the packing density. The mixes freeze-thaw resistance, sulfate resistance, and chloride penetration, were also investigated. The results showed improvement in all three properties when CRTG content increased.

Borosilicate glass, which is shown to exhibit pozzolanic properties when used as a very fine powder, has been used as cementing additives to RSC. Lee et al. [72] studied the neutron shielding properties of mortars containing borosilicate glass powder. Although

higher compressive strength values were observed when increasing the borosilicate glass content, the authors reported a significant expansion due to alkali silica reaction (ASR) when borosilicate glass was used as a fine aggregate. By reducing the particle average size to 13  $\mu\text{m}$ , the authors were able to reduce and control the ASR and enhance the pozzolanic reaction [72].

### **3.6 RSC design methodology**

The design of effective RSC requires the addition of aggregates that possess radiation attenuation properties. The physical and mechanical properties of these aggregates were collected and compared to those of limestone. Moreover, predictive models for concrete rheological properties, concrete compressive strength, and concrete chloride diffusion coefficient, were studied to determine the significance of the aggregate physical, mechanical, and chemical properties on the workability, strength, and durability of concrete. It was established that the concrete mix design must specify the following design parameters as they are independent of the type of aggregate; the concrete packing density, the aggregate volume fraction, the aggregate particle distribution, and the aggregate maximum size. And following the review of case studies and accounting for the results obtained from the models and properties' assessment, it is important that the following aggregate properties be measured and controlled to assure a workable, strong, and durable concrete; density, surface texture, physical and mechanical properties, water absorption, strength, crushing value, and reactivity and solubility in water and in alkaline solution. The reference material is limestone.

The use of predictive models is encouraged as they provide quantification of the concrete properties. Last and most important, it is necessary to test the properties of aggregates first to ensure they are suitable for RSC. Moreover, testing the concrete properties is still needed to confirm its acceptance.

It should be noted that some of the aggregates' properties can have an enhancement effect on one of the concrete properties and, at the same time, a decreasing effect on another property. For example, increasing the aggregate maximum size enhances the concrete workability but decreases the strength. Moreover, using aggregates with irregular shape and rough surface texture enhances the concrete strength but at the same time has a negative effect on the workability. As such, optimization between all the mentioned factors should be considered according to the desired application and work environment when designing radiation shielding concrete.

### **3.7 Conclusions**

The effectiveness of concrete to shield against ionizing radiation depends on the aggregates' attenuation properties and the thickness of the concrete. Optimum attenuation capability against incident radiation(s) can lead to a reduction in the required thickness, and a saving in material use and storage area. Based on this study results, the following conclusions that are specific to the aggregate properties for RSC are drawn:

- 1) Aggregates that show high efficiency in attenuating X-rays and gamma rays have higher density that require design considerations to mitigate segregation during the mixing, placement, and consolidation of the concrete.

- 2) Design of concrete mix must specify the concrete packing density, the aggregate volume fraction, the aggregate particle distribution, and the aggregate maximum size.
- 3) Aggregate water absorption should be in the same range as limestone to prevent adverse effects on the workability, strength, and durability of concrete.
- 4) Aggregate smooth surface and water phobic result in a weaker bond, weaker ITZ, and a weaker concrete.
- 5) Aggregate UCS can exceed that of limestone, but it cannot be much lower to prevent adverse effects on the strength and durability of concrete.
- 6) Properties of the naturally occurring aggregates, specifically the density, water absorption, UCS, crushing value, bond strength, and solubility must be measured as they cannot be determined based on the aggregate type and composition.
- 7) Borosilicate glass powder exhibits good pozzolanic activity especially when the average particle size is in the 10  $\mu\text{m}$  range and manifests ASR for larger glass particles.
- 8) Optimum RSC mix design is a balance between the concrete properties and those of the aggregates to meet the performance requirements of the intended application and work environment.

### **3.8 References**

- [1] B. Oto, N. Yildez, F. Akdemir, E. Kavaz, Investigation of gamma radiation shielding properties of various ores. *Progress in Nuclear Energy*, 2015, 85, 391-403.
- [2] S. A. Abo El-Enein, H. A. El-Sayed, A. H. Ali, Y. T. Mohammed, H. M. Khater, A. S. Ouda, Physico-mechanical properties of high performance concrete using

- different aggregates in presence of silica fume. *HBRC Journal*, 2014, 10 (1), 43-48.
- [3] O. Gencel, W. Brostow, C. Ozel, M. Filiz, Concretes containing hematite for use as shielding barriers. *Materials Science (Medziagotyra)*, 2010, 16 (3), 294-256.
- [4] H. Liu, J. Shi, H. Qu, D. Ding, Feasibility of using recycled CRT funnel glass as partial replacement of high density magnetite sand in radiation shielding concrete. *Transactions of Nonferrous Metals Society of China*, 2019, 29 (4), 831-839.
- [5] H. Tekin, M. Sayyed, S. A. Issa, Gamma radiation shielding properties of the hematite-serpentine concrete blended with  $WO_3$  and  $Bi_2O_3$  micro and nano particles using MCNPX code. *Radiation Physics and Chemistry*, 2018, 150, 95-100.
- [6] I. S. Kim, S. Y. Choi, E. I. Yang, Evaluation of durability of concrete substituted heavyweight waste glass as fine aggregate. *Construction and Building Materials*, 2018, 184, 269-277.
- [7] D. DiJulio, C. P. Cooper-Jensen, H. Perrey, K. Fissum, E. Rofors, J. Scherzinger, P. M. Pentley, A polyethylene-B $4C$  based concrete for enhanced neutron shielding at neutron research facilities. *Nuclear Instruments and Methods in Physics Research Section A: Accelerators, Spectrometers, Detectors and Associated Equipment*, 2017, 859, 41-46.
- [8] A. Satish, P. N. Aravind, P. V. Hakesh, D. M. K. Vignesh, Influence of Boron Carbide Addition on Performance and Neutron Shielding Ability of Cement Mortar Mix. *International Journal of Engineering & Technology*, 2018, 7 (4.5), 48-55.
- [9] ASTM C637-09, Standard specification for aggregates for radiation-shielding concrete, 2009, ASTM International, West Conshohocken, PA.
- [10] M. F. Kaplan, *Concrete radiation shielding*, 1989, John Wiley and Sons Inc., United States.

- [11] J. K. Shultis, R.E. Faw, Radiation shielding, 2000, Vol. 555, American Nuclear Society, La Grange Park, Illinois, USA.
- [12] A. Mesbahi, G. Alizadeh, G. Seyed-Oskoe, A. Azarpeyvand, A new barite-colemanite concrete with lower neutron production in radiation therapy bunkers. *Annals of Nuclear Energy*, 2013, 51, 107-111.
- [13] M. Kharita, S. Yousef, M. AlNassar, Review on the addition of boron compounds to radiation shielding concrete. *Progress in Nuclear Energy*, 2011, 53 (2), 207-211.
- [14] ASTM C143 / C143M-12, Standard test method for slump of hydraulic-cement concrete. 2012, ASTM International, West Conshohocken, PA.
- [15] G. H. Tattersall, P. F. Banfill, *The rheology of fresh concrete*, 1983.
- [16] V. Harrison, The science of rheology. *Nature*, 1940, 146 (3705), 580-582.
- [17] S. E. Chidiac, O. Maadani, A. G. Razaqpur, Controlling the quality of fresh concrete - a new approach. *Magazine of Concrete Research*, 2000, 52 (5), 353-363.
- [18] F. De Larrard, *Concrete mixture proportioning: a scientific approach*, 1999, CRC Press.
- [19] C. F. Ferraris, F. De Larrard, *Testing and modeling of fresh concrete rheology*, 1998, NIST, USA.
- [20] S. E. Chidiac, and F. Mahmoodzadeh, Constitutive flow models for characterizing the rheology of fresh mortar and concrete. *Canadian Journal of Civil Engineering*, 2013, 40 (5), 475-482.
- [21] F. Mahmoodzadeh, S. E. Chidiac, Rheological models for predicting plastic viscosity and yield stress of fresh concrete. *Cement and Concrete Research*, 2013, 49, 1-9.

- [22] S. E. Chidiac, F. Moutassem, F. Mahmoodzadeh, Compressive strength model for concrete. *Magazine of concrete research*, 2013, 65 (9), 557-572.
- [23] M. Shafikhani, S. E. Chidiac, A holistic model for cement paste and concrete chloride diffusion coefficient. *Cement and Concrete Research*, 2020, 133, 106049.
- [24] S. E. Chidiac, M. Shafikhani, Phenomenological model for quantifying concrete chloride diffusion coefficient. *Construction and Building Materials*, 2019, 224, 773-784.
- [25] O. H. Wallevik, J. E. Wallevik, Rheology as a tool in concrete science: The use of rheographs and workability boxes. *Cement and concrete research*, 2011, 41 (12), 1279-1288.
- [26] C. Ferraris, F. De Larrard N. Martys, Fresh concrete rheology: recent developments. *Materials Science of Concrete VI*, Amer. Cer. Soc. Ed. S. Mindess, J. Skalny, 2001, 215-241.
- [27] P. N. Quiroga, D. W. Fowler, The effects of the aggregates characteristics on the performance of Portland cement concrete, 2003, The University of Texas at Austin, USA.
- [28] S. H. Kosmatka, B. Kerkhoff, W. C. Panarese, Design and control of concrete mixtures, 2011, Portland Cement Assoc.
- [29] S., Mendez. and Y. J.F., *Concrete*, 1981, Prentice-Hall, New Jersey, USA.
- [30] M. Glinicki, A. Antolik, M. Gawlicki, Evaluation of compatibility of neutron-shielding boron aggregates with Portland cement in mortar. *Construction and Building Materials*, 2018, 164, 731-738.
- [31] L. Wadsö, C. P. Cooper-Jensen, P. M. Bentley, Assessing hydration disturbances from concrete aggregates with radiation shielding properties by isothermal calorimetry. *Physical Review Accelerators and Beams*, 2017, 20 (4), 043502.

- [32] J. C. Ralph, Mindat.org - the mineral and locality database, 1993–2013.
- [33] S. H. Cornellius, Manual of mineralogy, 1985, John Wiley & Son.
- [34] M. Masoud, A. M. Rashad, K. Sakr, M. G. Shahien, A. M. Zayed, Possibility of using different types of Egyptian serpentine as fine and coarse aggregates for concrete production. *Materials and Structures*, 2020, 53 (4), 1-17.
- [35] P. Petrounias, P. P. Giannakopoulou, A. Rogkala, The Effect of petrographic characteristics and physico-mechanical properties of aggregates on the quality of concrete. *Minerals*, 2018, 8 (12), 577.
- [36] A. S. Ouda, Development of high-performance heavy density concrete using different aggregates for gamma-ray shielding. *Progress in Nuclear Energy*, 2015, 79, 48-55.
- [37] N. Morova, S. Terzi, Evaluation of colemanite waste as aggregate hot mix asphalt concrete. *Journal of Natural & Applied Sciences*, 2015, 19 (2), 8-15.
- [38] H. Sarikaya, Specified concrete production containing boron, 2014, Suleyman Demirel, Turkey.
- [39] O. Gencil, W. Brostow, C. Ozel, An investigation on the concrete properties containing colemanite. *International Journal of Physical Sciences*, 2010, 5 (3), 216-225.
- [40] Y. Esen, Z. M. Doğan, Investigation of usability of limonite aggregate in heavy-weight concrete production. *Progress in Nuclear Energy*, 2018, 105, 185-193.
- [41] O. A. Hodhod, M. A. Youssef, S. A. Fouda, Characterization of local Egyptian iron ores for use in radiation shielding concrete. *Health physics*, 2006, 90 (4), 371-376.
- [42] K. Sakr, E. El-Hakim, Effect of high temperature or fire on heavy weight concrete properties. *Cement and concrete research*, 2005, 35 (3), 590-596.

- [43] M. G. El-Samrah, M. A. Abdel-Rahman, A. M. Kany, Study characteristics of new concrete mixes and their mechanical, physical, and gamma radiation attenuation features. *Zeitschrift für anorganische und allgemeine Chemie*, 2018, 644 (2), 92-99.
- [44] I. Ahmad, K. Shahzada, M. I. Ahmad, F. Khan, Y. I. Badrashi, S. W. Khan, H. Ahmad, Densification of concrete using barite as fine aggregate and its effect on concrete mechanical and radiation shielding properties. *Journal of Engineering Research*, 2019, 7 (4), 81-95.
- [45] T. C. Ling, C. S. Poon, High temperatures properties of barite concrete with cathode ray tube funnel glass. *Fire and materials*, 2014, 38 (2), 279-289.
- [46] F. Demir, G. Budak, R. Sahin, A. Karabulut, M. Oltulu, Determination of radiation attenuation coefficients of heavy weight and normal weight concretes containing colemanite and barite for 0.663 MeV  $\gamma$ -rays. *Annals of Nuclear Energy*, 2011, 38 (6), 1274-1278.
- [47] K. Sakr, Effects of silica fume and rice husk ash on the properties of heavy weight concrete. *Journal of materials in civil engineering*, 2006, 18 (3), 367-376.
- [48] B. S. Singh, K. Ramana, Mechanical properties of heavy weight concrete using heavy weight coarse-aggregate as Hematite (Fe-58 High Grade Iron Ore). *PAN*, 2014, 15 (1.5), 100.
- [49] O. Gencil, Physical and mechanical properties of concrete containing hematite as aggregates. *Science and Engineering of Composite Materials*, 2011, 18 (3), 191-199.
- [50] M. Mudgal, R. K. Chouhan, S. Verma, S. S. Amritphale, S. Das, A. Shrivastva, Development of advanced, non-toxic, synthetic radiation shielding aggregate. *Radiochimica Acta*, 2018, 106 (1), 59-68.

- [51] S. Özen, S. Özen, C. Şengül, T. Erenoğlu, Ü. Çolak, İ. A. Reyhancan, M. A. Taşdemir, Properties of heavyweight concrete for structural and radiation shielding purposes. *Arabian Journal for Science and Engineering*, 2016, 41 (4), 1573-1584.
- [52] L. Collis, M.R. Smith, *Aggregates: sand, gravel and crushed rock aggregates for construction purposes*, 2001, Geological Society.
- [53] H. Harlow, P. Matthews, *The use of ferrophosphorus aggregate in making high-density concrete*, 1953, 901, Knolls Atomic Power Laboratory.
- [54] W. Vickery, Borate raw materials for the ceramic frit industry. in *98th Annual Meeting and the Ceramic Manufacturing Council's Workshop and Exposition: Materials & Equipment/Whitewares: Ceramic Engineering and Science Proceedings*, 1997, Wiley Online Library.
- [55] V. Domnich, S. Reynaud, R. A. Haber, Boron carbide: structure, properties, and stability under stress. *Journal of the American Ceramic Society*, 2011, 94 (11), 3605-3628.
- [56] A. A. Al-Harhi, A field index to determine the strength characteristics of crushed aggregate. *Bulletin of Engineering Geology and the Environment*, 2001, 60 (3), 193-200.
- [57] I. Ocak, Estimating the modulus of elasticity of the rock material from compressive strength and unit weight. *Journal of the Southern African Institute of Mining and Metallurgy*, 2008, 108 (10), 621-626.
- [58] B. Standard, *BS 812-110: 1990 Testing Aggregates-Part 110: Methods for Determination of Aggregate Crushing Value (ACV)*, 1990, BSI, UK.
- [59] M. Alexander, S. Mindess, *Aggregates in concrete*, 2010, CRC Press.

- [60] M. A. Abdel-Rahman, M. A. Ali, S. A. El-Mongy, Penetrability of  $\gamma/n$  and static behavior of newly developed concrete using different passive assay techniques. *Nuclear Technology*, 2020, 206 (5), 766-778.
- [61] M. G. El-Samrah, M. A. Abdel-Rahman, R. El Shazly, Effect of heating on physical, mechanical, and nuclear radiation shielding properties of modified concrete mixes. *Radiation Physics and Chemistry*, 2018, 153, 104-110.
- [62] M. A. Abdel-Rahman, A. A. Fouda, S. A. El-Mongy, Study of  $\gamma$ -fast neutron attenuation and mechanical characteristics of modified concretes for shielding and sheltering purposes. *Zeitschrift für anorganische und allgemeine Chemie*, 2019, 645 (8), 649-655.
- [63] B. Rizov, Phase transformations from goethite to hematite and thermal decomposition in various nickeliferous laterite ores. *Journal of the University of Chemical Technology and Metallurgy*, 2012, 47 (2), 207-210.
- [64] A. Yadollahi, E. Nazemi, A. Zolfaghari, A. Ajorloo, Optimization of thermal neutron shield concrete mixture using artificial neural network. *Nuclear Engineering and Design*, 2016, 305, 146-155.
- [65] T. Korkut, A. Ün, F. Demir, A. Karabulut, G. Budak, Neutron dose transmission measurements for several new concrete samples including colemanite. *Annals of Nuclear Energy*, 2010, 37 (7), 996-998.
- [66] B. Oto, Z. Madak, E. Kavaz, N. Yaltay, Nuclear radiation shielding and mechanical properties of colemanite mineral doped concretes. *Radiation Effects and Defects in Solids*, 2019, 174 (9-10), 899-914.
- [67] W. Kubissa, M. A. Glinicki, M. Dąbrowski, Permeability testing of radiation shielding concrete manufactured at industrial scale. *Materials and Structures*, 2018, 51 (4), 83.

- [68] B. Lee, J. S. Lee, J. Min, J. H. Lee, Evaluation of physical characteristics and microscopic structure of mortar containing synthetic resin. *Construction and Building Materials*, 2016, 114, 880-887.
- [69] A. K. Jassim, Recycling of polyethylene waste to produce plastic cement. *Procedia Manufacturing*, 2017, 8, 635-642.
- [70] N. Usahanunth, Study of mechanical properties and recommendations for the application of waste Bakelite Aggregate Concrete. *Case studies in construction materials*, 2018, 8, 299-314.
- [71] M. J. Islam, M. S. Meherier, A. R. Islam, Effects of waste PET as coarse aggregate on the fresh and harden properties of concrete. *Construction and Building materials*, 2016, 125, 946-951.
- [72] J. C. Lee, B. K. Jang, C. S. Shon, J. H. Kim, C. W. Chung, Potential use of borosilicate glass to make neutron shielding mortar: Enhancement of thermal neutron shielding and strength development and mitigation of alkali-silica reaction. *Journal of Cleaner Production*, 2019, 210, 638-645.
- [73] B. K. Jang, J. C. Lee, J. H. Kim, C. W. Chung, Enhancement of thermal neutron shielding of cement mortar by using borosilicate glass powder. *Applied Radiation and Isotopes*, 2017, 123, 1-5.
- [74] S. Y. Choi, Y. S. Choi, E. I. Yang, Effects of heavy weight waste glass recycled as fine aggregate on the mechanical properties of mortar specimens. *Annals of Nuclear Energy*, 2017, 99, 372-382.
- [75] A. Korjakins, G. Shakhmenko, G. Bumanis, Utilisation of borosilicate glass waste as a micro-filler for concrete. *Journal of Civil Engineering and Architecture*, 2012, 6 (7), 876.
- [76] M. K. Moradllo, C. W. Chung, M. H. Keys, A. Choudhary, S. R. Reese, W. J. Weiss, Use of borosilicate glass powder in cementitious materials: Pozzolanic

reactivity and neutron shielding properties. *Cement and Concrete Composites*, 2020, 103640.

## **4. MRCsC: A user-friendly software for predicting shielding effectiveness against fast neutrons**

### **4.1 Abstract**

A user-friendly software called MRCsC was developed to accurately and precisely predict macroscopic effective removal cross-section,  $\Sigma_R$ , (in  $\text{cm}^{-1}$ ) of fast neutrons for different shielding materials. The program includes a revised calculation model and the latest data published by Evaluated Nuclear Data Library “ENDF/B-VIII”. Experimental data and NXCom results were used to comparatively and statistically assess MRCsC predictions. The results reveal that both MRCsC and NXCom programs provide accurate and precise results when compared with the experimental data and that only MRCsC results are statistically equal to the experimental ones to the 95% confidence.

Keywords: Macroscopic effective removal cross-section, NXcom program, MRCsC program, Radiation shielding concrete, Radiation shielding composites.

### **4.2 Introduction**

Protection against fast neutrons by attenuation undertakes two phases: First, the neutrons’ kinetic energy is moderated or slowed down through repeated collisions until thermalizing; Second, the thermalized neutrons are absorbed by elements with considerable absorption cross-sections such as boron and cadmium (Chilton et al., 1984; Kaplan, 1989). Moderation phase accounts for both elastic and inelastic scattering. Elastic scattering is most effective when dealing with intermediate energies and best realized with light elements, especially hydrogen. Inelastic scattering, which has a significant role

in slowing down highly energetic fast neutrons, is most realized with heavy elements (Chilton et al., 1984; Lamarsh and Baratta, 2001). The “un-collided beam” refers to fast neutrons that pass through a shield without colliding with its atoms or nuclei.

The “removal” of these fast neutrons or portion of them occurs when they start colliding or interacting with the shield’s elements (Duderstadt, 1976). Accordingly, the elemental composition of the shield and its density provide a measure of the shield’s fast neutrons removal ability referred to as the macroscopic effective removal cross-section ( $\Sigma_R$ ) (Profio, 1979; Wood, 1982). Further, total removal of fast neutrons from the un-collided beam cannot be realized due to the interactions between incident fast neutrons and shield nuclei as a portion of fast neutrons may undergo either a decrease in their kinetic energy or a small shift in their direction without removing. As such,  $\Sigma_R$  provides a lower bound to the macroscopic total cross-section ( $\Sigma_t$ ) which is the sum of the elastic and inelastic scattering cross-sections, and absorption cross-sections. It should be noted that the portion of the collisions that does not participate in the removal process cannot be accurately identified and therefore obtaining an accurate and precise value for the shield macroscopic effective removal cross-section is difficult to achieve (Profio, 1979; Chilton et al., 1984; Martin, 2006).

In contrast, the microscopic effective removal cross-section,  $\sigma_r$ , (in barns) for most of the elements is almost constant for neutron energies between 2 and 12 MeV which permits the use of simple methodology while quantifying the shield removal cross-section (Kaplan, 1989).

Accordingly, the fast neutrons attenuation efficiency of a shield has been quantified by means of empirical equations that are a function of  $\Sigma_t$  (Wood, 1982; Glasstone, 1986), where

$$\Sigma_R = \frac{2}{3} \bar{\Sigma}_t(E_n) \quad 8 \text{ MeV} \geq E_n \geq 6 \text{ MeV} \quad (4.1a)$$

$$\Sigma_R = \frac{3}{4} \Sigma_t(E_n) \quad E_n = 8 \text{ MeV} \quad (4.1b)$$

in which  $\bar{\Sigma}_t$  and  $E_n$  are the average total macroscopic cross-section for the element between 6 MeV and 8 MeV and is the neutrons' energy in (MeV).

To facilitate the calculations process and mitigate possible round-off errors, some user-friendly computer programs were developed such as MERCSEF-N, NXcom and ParShield (El-Khayatt and Abdo, 2009; El-Khayatt, 2011; Elmahroug et al., 2015). These computer programs employ the same elemental removal cross-section database with a proven reliability in approximating the macroscopic effective removal cross-section for various shields (El-Khayatt, 2010; Yilmaz et al., 2011; Elmahroug et al., 2015; Sayyed, 2016; Lakshminarayana et al., 2020). The shortcoming of these programs is their outdated database that introduces inaccuracies for composites that contain elements such as actinides and lanthanides or composites with high hydrogen content.

The aim of this study is to develop new software that can accurately and precisely predict the fast neutrons attenuation of shields and is user-friendly. To meet this goal, the following tasks were carried out. First, fast neutrons mass removal cross-section values for naturally occurring elements were compiled in a database according to the latest version of the Evaluated Nuclear Data Library "ENDF/B-VIII" released in 2018 by The

Cross-section Evaluation Working Group (CSEWG) (Brown et al., 2018). Second, the empirical model of Eq. 4.1 is revised and enhanced. And third, the new database and the revised empirical model are incorporated into a user-friendly software named Macroscopic Removal Cross-sections Calculator or MRCsC. MRCsC results are then evaluated using experimentally measured values and calculated results reported in the literature. Statistical analyses and experimentally measured values were employed to determine the accuracy and precision of MRCsC results.

### 4.3 Theoretical background

The effective removal cross-section of a given composite or shield is determined experimentally by shining a mono-directional plane source of fission neutrons onto a slab made of shield material with "x" thickness that is immersed in an infinite medium of water. The response of the neutron detector located at a distance (x + z) from the mono-directional source and in the presence of the slab is represented by  $D(x, z)$ , where (Glasstone, 1986):

$$D(x, z) = D_{H_2O}(z)e^{-\Sigma_R x} \quad (4.2)$$

in which  $D_{H_2O}(z)$  is the detector response at distance (z) from the mono-directional plane source in the water medium without the slab.

For most cases, a finite plane source of fission neutrons is used to measure the macroscopic removal cross-sections with the results transformed to represent a point source (Glasstone, 1986), where

$$\Sigma_R = \frac{1}{x} \ln \left[ \frac{(z+x)^2}{z^2} \Phi(z+x) \Phi_{H_2O}(z) \right] \quad (4.3)$$

in which  $\Phi_{H_2O}(z)$  and  $\Phi(z+x)$  are the neutron fluxes at the distances ( $z$ ) in the absence of the slab, and ( $z+x$ ) in the presence of the slab, respectively.

The experimental setup which is based on the narrow beam geometry, includes  $^{239}\text{Pu-Be}$ ,  $^{241}\text{Am-Be}$ , and Cf-252 neutron sources, and stilbene organic scintillation,  $^3\text{He}$ -based fast-neutron detector, and NE-213 organic liquid-scintillation neutron detectors for measuring the liberated counts, count rate, and flux (El-Samrah et al., 2018; Oto et al., 2019; Abdel-Rahman et al., 2020; Lakshminarayana et al., 2020; Levet et al., 2020; Masoud et al., 2020). The Beer-Lambert law is adopted to determine the macroscopic effective removal cross-section (Kaplan, 1989; Lamarsh and Baratta, 2001), where

$$I_x = I_0 e^{-\Sigma_R x} \quad (4.4)$$

in which  $I_x$  and  $I_0$  are respectively, the measured intensity for a material thickness ( $x$ ) and the measured bare intensity in counts/sec. The intensity can be replaced by the total counts or the flux.

The abovementioned experimental setup for measuring the macroscopic effective removal cross-section possesses many challenges such as health and safety risks, availability and cost of the neutron source and detectors, experimental errors, special facility, to name a few. Accordingly, it is not always possible and/or feasible to measure the property of composite shields experimentally, which gave justifications for developing analytical tools such as MCNP and GEANT that are effective and reliable for designing and assessing radiation shields. However, these simulation codes are difficult to

use and require special training (Agostinelli et al., 2003; Pozzi et al., 2003; Allison et al., 2006; Waters et al., 2007).

Empirical models derived from either experimental observation and/or statistics have emerged as alternatives and reliable tools to approximate the macroscopic removal cross-section. In this regard, two approaches have been developed. The first approach approximates the macroscopic effective removal cross-section from the total macroscopic cross-section as presented in Eqs. 4.1a and 4.1b (Wood, 1982; Glasstone, 1986). However, differences have been reported between this first approach and the experimentally measured values for some elements especially hydrogen (El-Khayatt and Abdo, 2009; El-Khayatt, 2011). The second approach postulates that the mass removal coefficient depends on the microscopic nuclear properties of the shield constituent elements. As such, models that are function of the atomic weight and/or the atomic number, given below, have been proposed to approximate the macroscopic effective removal cross-section (Wood, 1982; Chilton et al., 1984).

$$\frac{\Sigma_R}{\rho} = 0.21A^{-0.58} \quad (4.5a)$$

$$\frac{\Sigma_R}{\rho} = 0.00662A^{-0.333} + 0.337 A^{-0.666} - 0.211 A^{-1} \text{ for } A > 12 \quad (4.5b)$$

$$\frac{\Sigma_R}{\rho} = 0.19Z^{-0.743} \quad \text{for } Z \leq 8 \quad (4.5c)$$

$$\frac{\Sigma_R}{\rho} = 0.125Z^{-0.565} \quad \text{for } Z > 8 \quad (4.5d)$$

$$\frac{\Sigma_R}{\rho} = 0.206A^{-0.333}Z^{-0.294} \quad (4.5e)$$

A and Z are the element's atomic mass and atomic number, respectively.

However, these empirical equations are usually valid for elements of A and Z at certain numbers. The effective removal cross-sections for many elements and known shielding materials were approximated using the former empirical equations then reported and compiled in literature (Profio, 1979; Wood, 1982; Kaplan, 1989; Martin, 2006; El-Khayatt, 2010). Moreover, user-friendly computer programs with dataset constructed from these reported values were shown to approximate well the macroscopic removal cross-section for composites and materials.

## **4.4 Macroscopic Removal Cross-sections Calculator (MRCsC)**

### **4.4.1 Program description**

The user-friendly software “MRCsC”, which consists of, a pre- and post-processor, an analytical model, and a built-in database, is an effective tool for radiation shielding design. MRCsC is designed to reliably approximate the fast neutrons macroscopic effective removal cross-section for different materials. The database contains mass removal cross-section values, that can be accessed and updated by the user, for all naturally occurring elements including rare elements located in the earth’s crust with the exception of Astatine and Francium as they are extremely radioactive and very rare elements with half lives of only hours and minutes respectively (Audi et al., 2003).

MRCsC has a user-friendly interface and designed with minimum input requirements from the user. As demonstrated in Fig. 4.1, material density and elements weight fraction are the only input information for determining the macroscopic effective removal cross-section. To obtain a good approximation, the user is reminded that the total sum of the elements must be 1.0 and that the density is a measured value.

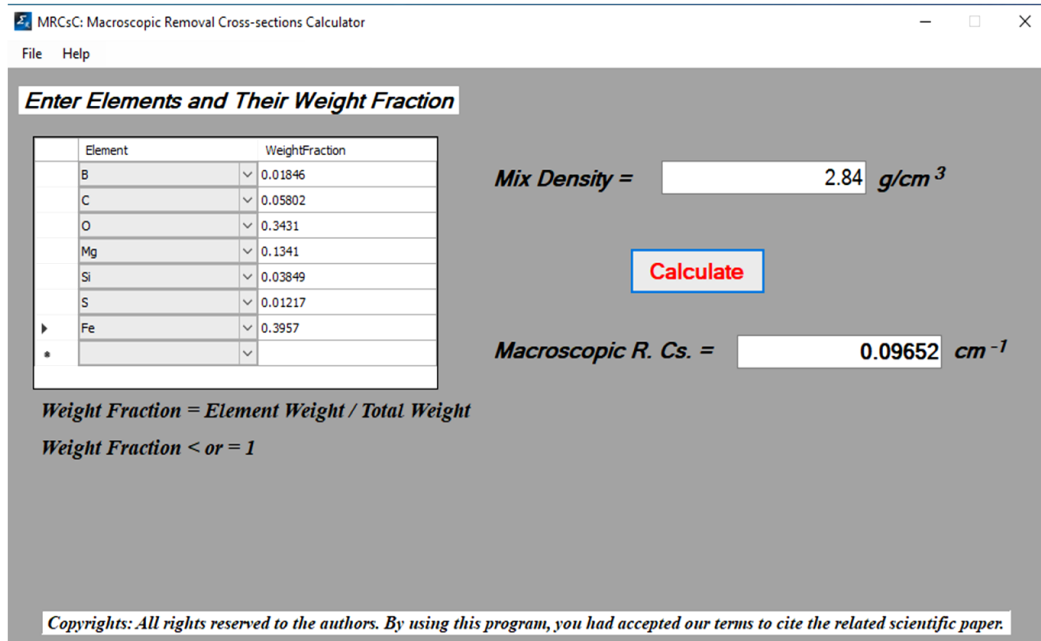


**Fig. 4.1** MRCsC user interface

#### 4.4.2 Analytical model

A priori, the energy range of the liberated fast neutrons from the above-noted neutron sources is mostly between 2 and 10 MeV as reproduced in the spectra of Figs. 4.2 to 4.4 corresponding to Cf-252,  $^{241}\text{Am}$ -Be, and  $^{239}\text{Pu}$ -Be, respectively. The assessment of Eq. 4.1a to approximate  $\Sigma_R / \rho$  in the energy range of 2 to 10 MeV was carried out and the results revealed very good agreement with the experimental data. Accordingly, the average microscopic total cross-sections value,  $\bar{\sigma}_t$ , (in barns) over the energy range of 2 to 10 MeV was calculated using the ENDF/B-VIII neutron database incorporated in JANIS 4.0 software (Soppera et al., 2014) and accounting for the natural abundance as follows,

$$\bar{\sigma}_t(E_n) = \sum_i^n c_i \bar{\sigma}_i(E_n) \quad 2 \leq E_n \leq 10 \text{ MeV} \quad (4.6)$$

in which  $c_i$  and  $\bar{\sigma}_i$  are the natural isotopic abundance and average microscopic total cross-section of the  $i$ th isotope of the element, respectively.

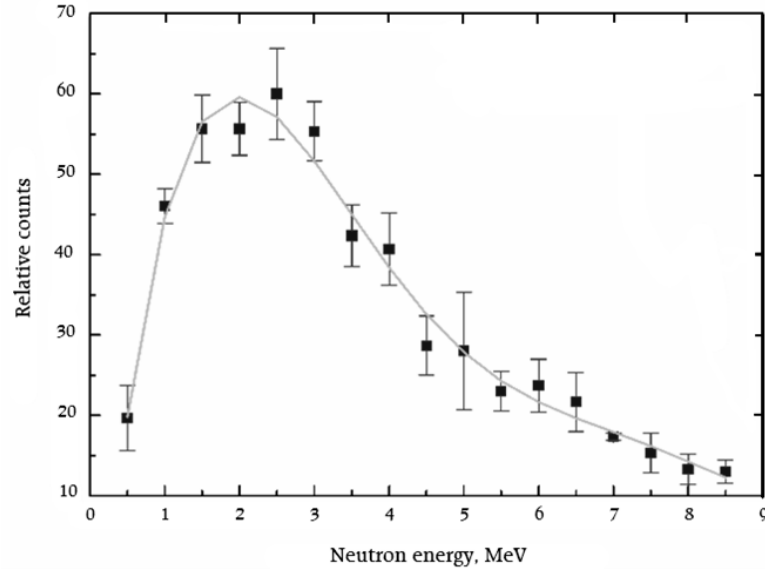


**Fig. 4.2** The Cf-252 neutron energy spectrum derived from measured TOF spectrum, reproduced from (Lee et al., 2016)

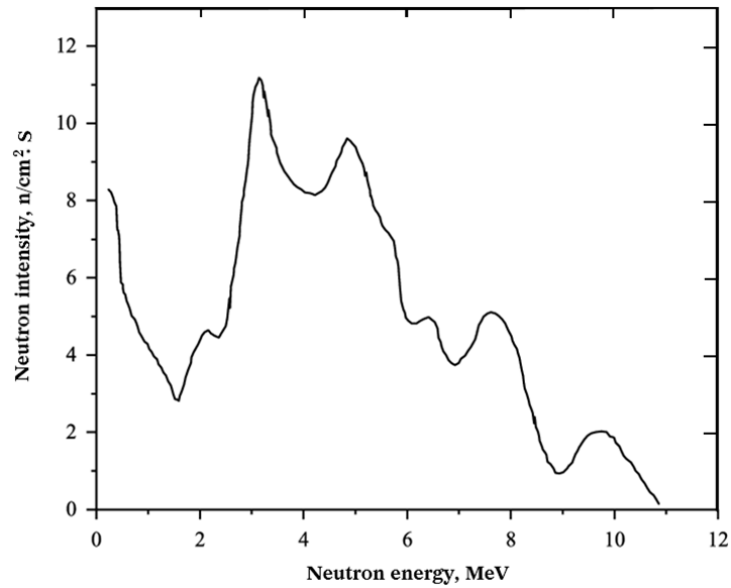


**Fig. 4.3**  $^{241}\text{Am}$ -Be source neutron energy spectrum, reproduced from (Baginova et al., 2018)

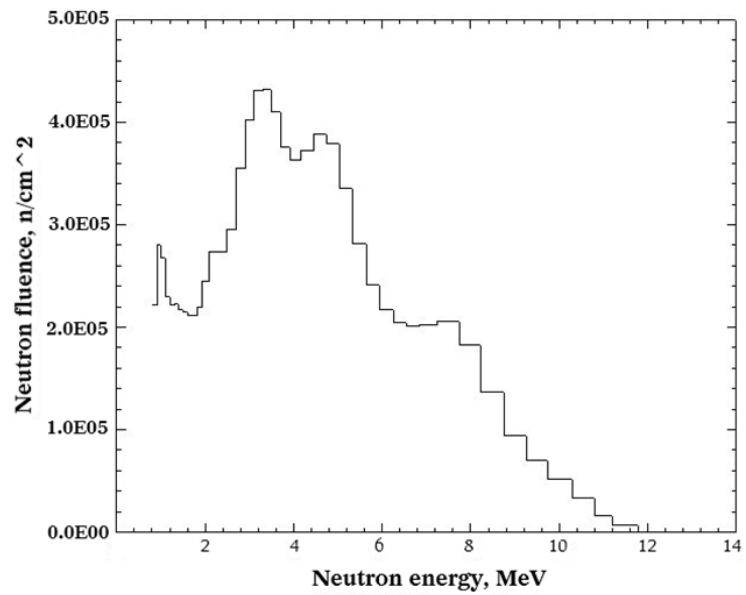


**Fig. 4.4**  $^{239}\text{Pu}$ -Be source neutron energy spectrum, reproduced from (Vega-Carrillo and Torres-Muhech, 2002)

The average total macroscopic cross-section  $\bar{\Sigma}_t$  is related to the average total microscopic cross-section  $\bar{\sigma}_t$  (cm<sup>2</sup>/atom) as follows,

$$\bar{\Sigma}_t/\rho = \frac{N}{\rho} \bar{\sigma}_t \quad (4.7)$$

$$N = \frac{\rho N_A}{A} \quad (4.8)$$

in which  $N$  and  $N_A$  are the number of atoms per cubic cm of the substance and Avogadro constant in (atom/ mol), respectively.

Now, we will consider the empirical model given in Eq. 4.1a after extending the energy range of neutrons to become 2-10 MeV to calculate the mass removal cross-section of each element, where

$$\Sigma_R/\rho = \frac{2}{3} \bar{\Sigma}_t/\rho \quad (4.9)$$

The material macroscopic effective removal cross-section is then calculated using the following relationship

$$\Sigma_R = \sum_1^n \rho_s w_i (\Sigma_R/\rho)_i = \sum_1^n \rho_i (\Sigma_R/\rho)_i \quad (4.10)$$

in which  $\rho_s$ ,  $\rho_i$  are, respectively, the sample density (g/cm<sup>3</sup>), and the density of the  $i^{\text{th}}$  element as it appears in the mixture ( $\rho_i = \rho_s w_i$ ).  $w_i$  is the weight fraction of the  $i^{\text{th}}$  element.

#### 4.4.3 Program testing and validation

The program results were compared numerically and statistically with experimentally measured values and NXCom (El-Khayatt, 2011) predictions to assess its precision and accuracy. The statistical analyses include paired samples t-test to evaluate the statistical

difference between the means and linear regression to determine the variability captured by the model. Fourteen samples were collected from the literature whose description, density and elemental composition are given in Tables 4.1 and 4.2. The experimental macroscopic removal cross-sections, the corresponding computed values according to MRCsC and NXCom programs, and their percent differences with the experimental values are given in Table 4.3.

**Table 4.1** Description and density of concrete samples collected from the literature

Sample code	Density, g/cm <sup>3</sup>	Description
FL1 (Oto et al., 2015)	2.610	Concrete with limonite as a portion of the fine aggregates
FL3 (Oto et al., 2015)	2.760	Concrete with limonite fine aggregates
FCL (Oto et al., 2015)	2.890	Concrete with limonite fine and coarse aggregates
OC (Zalegowski et al., 2020)	2.251	Concrete with crushed granite coarse aggregates
M (Zalegowski et al., 2020)	3.014	Concrete with magnetite coarse aggregates
MF2 (Zalegowski et al., 2020)	3.164	Concrete with magnetite coarse aggregates and PP microfibers
IC (Abdo, 2002)	3.690	Concrete with ilmenite fine and coarse aggregates
BLC (El-Samrah et al., 2018)	2.963	Concrete with barite coarse aggregates and limonite fine aggregates
BCIOC (Li et al., 2013)	2.840	Composite of boron containing ore and epoxy
BRS (Li et al., 2013)	2.370	Composite of high percent of boron containing ore and epoxy
C6 (Elwahab et al., 2019)	2.060	Composite of cement, sand, HDPE, and borax
C7 (Elwahab et al., 2019)	2.080	Composite of cement, sand, lower percent of HDPE, and borax
Terphenyl (Perlini et al., 1970)	1.106	Commercial terphenyl (OM2), a mixture of ortho and meta-terphenyls
CFM (Abdo et al., 2003)	2.858	Cement fiber magnetite composite

**Table 4.2** Samples elemental composition (w%)

Element	Concrete					Composites and organic mixtures								
	FL1	FL3	FCL	OC	M	MF2	IC	BLC	BCIOC	BRS	C6	C7	Terph-enyl	CFM
H	1.014	1.318	2.094	0.330	0.260	0.270	0.640	0.918	-	-	6.080	5.990	6.130	1.780
B	-	-	-	-	-	-	-	-	1.846	3.650	7.580	7.720	-	9.200
C	-	-	-	-	-	0.090	-	0.113	5.802	7.364	14.20	7.110	93.87	9.456
O	46.43	45.25	42.37	49.58	36.59	36.55	38.41	32.17	34.31	42.10	53.00	54.40	-	32.72
Na	0.346	0.722	1.667	1.480	0.180	0.180	0.694	-	-	-	9.530	15.90	-	-
Mg	6.230	4.815	1.232	0.610	0.300	0.300	0.172	0.860	13.41	21.07	0.914	0.913	-	0.500
Al	2.184	1.921	1.252	4.570	0.570	0.570	0.372	0.833	-	3.727	1.740	1.730	-	0.610
Si	19.76	14.62	1.625	33.55	13.20	13.19	1.561	7.818	3.849	10.76	1.060	1.060	-	2.580
P	0.010	0.039	0.113	0.030	0.390	0.390	0.078	-	-	-	0.281	0.281	-	-
S	0.338	0.337	0.336	0.150	0.130	0.130	0.086	1.260	1.217	-	0.234	0.234	-	0.170
Cl	0.016	0.017	0.017	0.010	0.010	0.010	-	-	-	-	-	-	-	-
K	0.151	0.277	0.596	1.890	0.180	0.180	0.223	-	-	-	1.510	1.510	-	-
Ca	16.33	14.66	10.44	6.370	5.570	5.570	5.330	6.478	-	10.54	1.210	1.210	-	12.63
Ti	0.012	0.047	0.136	0.090	-	-	24.30	0.051	-	-	0.424	0.424	-	2.870
Cr	-	-	-	-	-	-	-	-	-	-	-	-	-	0.164
Mn	0.145	0.121	0.061	0.020	-	-	0.155	0.508	-	-	-	-	-	-
Fe	7.035	15.84	38.04	1.310	42.63	42.59	28.00	12.69	39.57	0.790	2.950	2.950	-	27.32
Cu	0.006	0.009	0.018	-	-	-	-	-	-	-	-	-	-	-
Sr	-	0.001	0.003	-	-	-	-	-	-	-	-	-	-	-
Ba	-	-	-	-	-	-	-	36.29	-	-	-	-	-	-

**Table 4.3** Measured and calculated effective removal cross-sections of the studied samples

Sample category	Sample	$\Sigma_R, \text{cm}^{-1}$				
		Exp.	MRCsC	% diff.	NXcom	% diff.
Concrete	FL1	0.1081	0.1101	1.79	0.1022	5.61
	FL3	0.1289	0.1194	7.62	0.1107	15.2
	FCL	0.1481	0.1334	10.4	0.1229	18.6
	OC	0.0913	0.0866	5.26	0.0818	11.0
	M	0.0996	0.1006	1.04	0.0942	5.57
	MF2	0.1000	0.1059	5.77	0.0992	0.80
	IC	0.1240	0.1337	7.50	0.1204	2.95
	BLC	0.1051	0.0981	6.89	0.0914	13.9
Composites and organic mixtures	BCIOC	0.0996	0.0965	3.14	0.0916	8.37
	BRS	0.0940	0.0925	1.58	0.0873	7.39
	C6	0.1690	0.1698	0.48	0.1550	8.64
	C7	0.1570	0.1677	6.59	0.1538	2.06
	Terphenyl	0.1026	0.1092	6.25	0.0926	10.3
	CFM	0.1410	0.1414	0.25	0.1275	10.1

The results reveal a maximum difference of 10.4% and 18.6% for MRCsC and NXCom, respectively. The corresponding average percent difference is 4.6% and 8.6% for MRCsC and NXCom. These results indicate that MRCsC approximations of the macroscopic effective removal cross-section of shielding materials are accurate and precise when compared to the experimental data and more consistent and accurate when compared to NXCom results. This is attributed in part to the adoption of the latest data published by Evaluated Nuclear Data Library “ENDF/B-VIII” and to the revised empirical model by suggesting a new energy range for the included fast neutrons.

For a closer examination of the computed results, the elemental values of  $\Sigma_R/\rho$  and  $\Sigma_R$  corresponding to FCL and BRS are reproduced in Tables 4.4 and 4.5, respectively.

MRCsC results reveal a significant increase in the mass removal cross-section for the moderator elements H (13.9%), B (7.29%), and C (18.3%), and a considerable increase for intermediate and heavy elements such as Ti (35.8%), Mn (22.4%), Fe (13.8%), Cu (13.5%), and Sr (12.7%). A modest decrease for O (4.78%) was also noticed. These results clearly show that the database used by each program yields different elemental results. Therefore, it can be stated that the adoption of the latest data released by Evaluated Nuclear Data Library has provided MRCsC with a better approximation of the macroscopic effective removal cross-section of shielding materials.

**Table 4.4** Theoretically calculated values of effective removal cross-sections  $\Sigma_R$  ( $\text{cm}^{-1}$ ) for FCL concrete based on MRCsC and NXCom libraries for  $\Sigma_R/\rho$

Element	$w$	$\rho.w.$	$(\Sigma_R/\rho), \text{cm}^2/\text{g}$			$\Sigma_R, \text{cm}^{-1}$	
	%	$\text{g}/\text{cm}^3$	MRCsC	NXCom	% diff	MRCsC	NXCom
H	2.094	0.0605	0.68736	0.5980	13.9	4.17E-02	3.63E-02
O	42.37	1.2245	0.03861	0.0405	-4.78	4.73E-02	4.96E-02
Na	1.667	0.0482	0.03861	0.0341	12.4	1.86E-03	1.64E-03
Mg	1.232	0.0356	0.03475	0.0333	4.26	1.24E-03	1.19E-03
Al	1.252	0.0362	0.03622	0.0293	21.1	1.31E-03	1.06E-03
Si	1.625	0.0470	0.03404	0.0295	14.3	1.60E-03	1.39E-03
P	0.113	0.0033	0.03604	0.0283	24.1	1.19E-04	9.34E-05
S	0.336	0.0097	0.03336	0.0277	18.5	3.24E-04	2.69E-04
Cl	0.017	0.0005	0.03437	0.0252	30.8	1.72E-05	1.26E-05
K	0.596	0.0172	0.03395	0.0247	31.5	5.84E-04	4.25E-04
Ca	10.44	0.3017	0.03379	0.0243	32.7	1.02E-02	7.33E-03
Ti	0.136	0.0039	0.02943	0.0205	35.8	1.15E-04	8.00E-05
Mn	0.061	0.0018	0.02543	0.0203	22.4	4.58E-05	3.65E-05
Fe	38.04	1.0993	0.02457	0.0214	13.8	2.70E-02	2.35E-02
Cu	0.018	0.0005	0.02129	0.0186	13.5	1.06E-05	9.30E-06
Sr	0.003	0.0001	0.01816	0.0160	12.7	1.82E-06	1.60E-06
$\Sigma_R$						0.13342	0.1229

**Table 4.5** Theoretically calculated values of effective removal cross-sections  $\Sigma_R$  ( $\text{cm}^{-1}$ ) for BRS- composite based on MRCsC and NXCom libraries for  $\Sigma_R/\rho$

Element	$w$	$\rho.w.$	$(\Sigma_R/\rho), \text{cm}^2/\text{g}$		% diff.	$\Sigma_R, \text{cm}^{-1}$	
	%	$\text{g}/\text{cm}^3$	MRCsC	NXCom		MRCsC	NXCom
B	3.650	0.0865	0.06185	0.0575	7.29	5.35E-03	4.97E-03
C	7.364	0.1745	0.06032	0.0502	18.3	1.05E-02	8.76E-03
O	42.10	0.9978	0.03861	0.0405	-4.78	3.85E-02	4.04E-02
Mg	21.07	0.4994	0.03475	0.0333	4.26	1.74E-02	1.66E-02
Al	3.727	0.0883	0.03622	0.0293	21.1	3.20E-03	2.59E-03
Si	10.76	0.2550	0.03404	0.0295	14.3	8.68E-03	7.52E-03
Ca	10.54	0.2498	0.03379	0.0243	32.7	8.44E-03	6.07E-03
Fe	0.790	0.0187	0.02457	0.0214	13.8	4.60E-04	4.00E-04
$\Sigma_R$						0.09253	0.0873

The statistical analyses of MRCsC and NXCom results were carried out using the statistical program SPSS v23 (Statistics, 2015). The results from the linear regression analysis (no y-intercept model) show that both programs provide good estimates as shown by Fig. 4.5. Although the coefficient of determination is found to be the same for both results, the regression equations show that MRCsC values, at most, are very close to the experimental values whereas NXCom are slightly lower. These results correlate with the results shown in Tables 4.4 and 4.5. The results from the t-test, given in Table 4.6, reveal that the difference between the experimental values and MRCsC results are not statistically significant to the 95% confidence whereas the difference between the experimental values and NXCom results are statistically significant to the 95% confidence. Moreover, the standard error of estimate of about 0.007 and the residual sum of squares of 0.001 for both programs indicate that their estimated values are both accurate and precise.

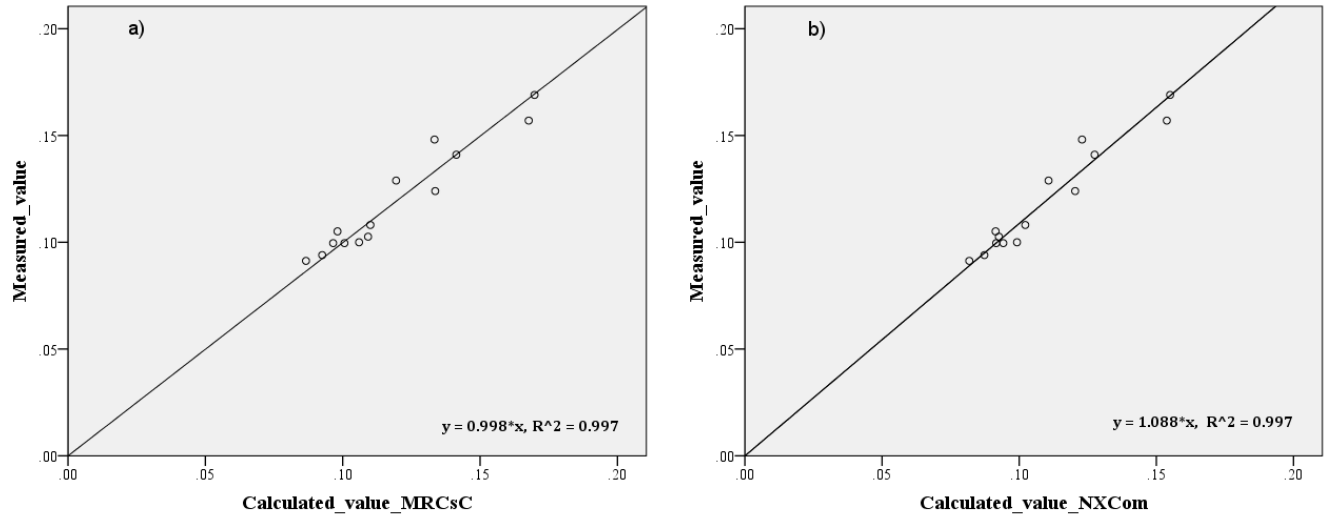


**Fig. 4.5** The relation between the calculated results obtained from MRCsC program (a), NXCom program (b) and the corresponding measured values

**Table 4.6** Results from the paired samples t-test and the regression analysis

Used program	Paired samples t-test			Regression analysis			
	df	t	P-value	Resid. Sum-of Squares	$R^2$	Adj. $R^2$	Std. Error of the estimate
MRCsC	13	0.12	0.904	0.001	0.997	0.996	0.0072
NXCom	13	5.58	0.000	0.001	0.997	0.997	0.0066

## 4.5 Conclusions

MRCsC has been developed and shown to reliably predict the macroscopic effective removal cross-section,  $\Sigma_R$ , of fast neutrons for any shielding material used as an attenuating medium for fast neutrons. According to the results from the comparative and statistical analyses, the following conclusions are drawn:

1. MRCsC results are as accurate as NXCom but more consistent.
2. MRCsC mean values are statistically equal to the experimental ones to the 95% confidence.
3. In general, MRCsC results are very close to the corresponding experimental values whereas NXCom predictions are slightly lower.
4. MRCsC improvements in computing the macroscopic removal cross-sections are due to the revised empirical model, by considering a new energy range for the included fast neutrons, and the adoption of the latest version of the Evaluated Nuclear Data Library "ENDF/B-VIII".
5. MRCsC program is freely available upon request via contacting the authors.

#### **4.6 Acknowledgments**

This research was funded and supported by the Natural Sciences and Engineering Research Council of Canada, McMaster University Centre for Effective Design of Structures, and Military Technical College in Egypt.

#### **4.7 References**

- Abdel-Rahman, M.A., Ali, M.A., and El-Mongy, S.A., 2020. Penetrability of  $\gamma/n$  and static behavior of newly developed concrete using different passive assay techniques. *Nuclear Technology* 206 (5), 766-778.
- Abdo, A.E.S. 2002. Calculation of the cross-sections for fast neutrons and gamma-rays in concrete shields. *Annals of Nuclear Energy* 29 (16), 1977-1988.
- Abdo, A.E.S., Ali, M., and Ismail, M., 2003. Influence of magnetite and boron carbide on radiation attenuation of cement-fiber/composite. *Annals of Nuclear Energy* 30 (4), 391-403.

- Agostinelli, S., Allison, J., Amako, K.A., Apostolakis, J., Araujo, H., Arce, P., Asai, M., Axen, D., Banerjee, S., and Barrand, G., 2003. GEANT4—a simulation toolkit. *Nuclear instruments and methods in physics research section A: Accelerators, Spectrometers, Detectors and Associated Equipment* 506 (3), 250-303.
- Allison, J., Amako, K., Apostolakis, J., Araujo, H., Dubois, P.A., Asai, M., Barrand, G., Capra, R., Chauvie, S., and Chytracsek, R., 2006. Geant4 developments and applications. *IEEE Transactions on nuclear science* 53 (1), 270-278.
- Audi, G., Bersillon, O., Blachot, J., and Wapstra, A.H., 2003. The NUBASE evaluation of nuclear and decay properties. *Nuclear Physics A* 624, 1-124.
- Baginova, M., Vojtyla, P., and Povinec, P.P., 2018. Investigation of neutron interactions with Ge detectors. *Nuclear Instruments and Methods in Physics Research Section A: Accelerators, Spectrometers, Detectors and Associated Equipment* 897, 22-31.
- Brown, D.A., Chadwick, M., Capote, R., Kahler, A., Trkov, A., Herman, M., Sonzogni, A., Danon, Y., Carlson, A., and Dunn, M., 2018. ENDF/B-VIII. 0: The 8th major release of the nuclear reaction data library with CIELO-project cross sections, new standards and thermal scattering data. *Nuclear Data Sheets* 148, 1-142.
- Chilton, A.B., Shultis, J.K., and Faw, R.E., 1984. *Principles of radiation shielding*. Prentice Hall Inc, NJ, USA.
- Duderstadt, J.J., 1976. *Nuclear reactor analysis*. John Wiley & Sons, NY, USA.
- El-Khayatt, A., 2010. Calculation of fast neutron removal cross-sections for some compounds and materials. *Annals of Nuclear Energy* 37 (2), 218-222.
- El-Khayatt, A., 2010. Radiation shielding of concretes containing different lime/silica ratios. *Annals of Nuclear Energy* 37 (7), 991-995.
- El-Khayatt, A., 2011. NXcom—A program for calculating attenuation coefficients of fast neutrons and gamma-rays. *Annals of Nuclear Energy* 38 (1), 128-132.
- El-Khayatt, A., and Abdo, A.E.S., 2009. MERCFSF-N: A program for the calculation of fast neutron removal cross sections in composite shields. *Annals of Nuclear Energy* 36 (6), 832-836.

- El-Samrah, M.G., Abdel-Rahman, M.A., and El Shazly, R., 2018. Effect of heating on physical, mechanical, and nuclear radiation shielding properties of modified concrete mixes. *Radiation Physics and Chemistry* 153, 104-110.
- Elmahroug, Y., Tellili, B., Souga, C., and Manai, K., 2015. ParShield: a computer program for calculating attenuation parameters of the gamma rays and the fast neutrons. *Annals of Nuclear Energy* 76, 94-99.
- Elwahab, N.R.A., Helal, N., Mohamed, T., Shahin, F., and Ali, F.M., 2019. New shielding composite paste for mixed fields of fast neutrons and gamma rays. *Materials Chemistry and Physics* 233, 249-253.
- Glasstone, S., Sesonske, A., 1986. *Nuclear reactor engineering*. CBS Publishers & Distributors, Delhi, India.
- Kaplan, M.F., 1989. *Concrete radiation shielding*. John Wiley & Sons, NY, USA.
- Lakshminarayana, G., Elmahroug, Y., Kumar, A., Dong, M., Lee, D.E., Yoon, J., and Park, T., 2020. Li<sub>2</sub>O–B<sub>2</sub>O<sub>3</sub>–Bi<sub>2</sub>O<sub>3</sub> glasses: gamma-rays and neutrons attenuation study using ParShield/WinXCOM program and Geant4 and Penelope codes. *Applied Physics A* 126 (4), 1-16.
- Lamarsh, J.R., and Baratta, A.J., 2001. *Introduction to nuclear engineering*. Prentice hall, Upper Saddle River, NJ, USA.
- Lee, C.H., Son, J., Kim, T.H., Lee, S., and Kim, Y.K., 2016. Measurement of neutron energy spectrum emitted by Cf-252 source using time-of-flight method. *Transactions of the Korean Nuclear Society Autumn Meeting*.
- Levet, A., Kavaz, E., and Özdemir, Y., 2020. An experimental study on the investigation of nuclear radiation shielding characteristics in iron-boron alloys. *Journal of Alloys and Compounds* 819, 152946.
- Li, Z.F., Xue, X.X., Duan, P.N., Tian, A., Li, S.X., and Yin, Z.S., 2013. Preparation and thermal/fast neutron shielding properties of novel boron containing ore composites. *Materials Science Forum*, 743-744, 613-622.
- Martin, J. E., 2006. *Physics for radiation protection: a handbook*. 2nd ed. John Wiley & Sons, NY, USA.

- Masoud, M., Kansouh, W., Shahien, M., Sakr, K., Rashad, A.M., and Zayed, A., 2020. An experimental investigation on the effects of barite/hematite on the radiation shielding properties of serpentine concretes. *Progress in Nuclear Energy* 120, 103220.
- Oto, B., Madak, Z., Kavaz, E., and Yaltay, N., 2019. Nuclear radiation shielding and mechanical properties of colemanite mineral doped concretes. *Radiation Effects and Defects in Solids* 174 (9-10), 899-914.
- Oto, B., Yıldız, N., Korkut, T., and Kavaz, E., 2015. Neutron shielding qualities and gamma ray buildup factors of concretes containing limonite ore. *Nuclear Engineering and Design* 293, 166-175.
- Perlini, G., Nicks, R., Penkuhn, H., Ponti, C., Manduchi, C., Moschini, G., and Zago, G., 1970. Attenuation of monoenergetic source neutrons in different shielding materials. *Nuclear Engineering and Design* 13 (3), 377-389.
- Pozzi, S.A., Padovani, E., and Marseguerra, M., 2003. MCNP-PoliMi: a Monte-Carlo code for correlation measurements. *Nuclear Instruments and Methods in Physics Research Section A: Accelerators, Spectrometers, Detectors and Associated Equipment* 513 (3), 550-558.
- Profio, A.E., 1979. *Radiation shielding and dosimetry*. Wiley & Sons Inc., NewYork, USA.
- Sayyed, M., 2016. Investigation of shielding parameters for smart polymers. *Chinese journal of physics* 54 (3), 408-415.
- Soppera, N., Bossant, M., and Dupont, E., 2014. JANIS 4: An improved version of the NEA java-based nuclear data information system. *Nuclear Data Sheets* 120, 294-296.
- Statistics, SPSS. V23, 2015. IBM Corporation, North Castle, NY, USA.
- Vega-Carrillo, H.R., and Torres-Muhech, C., 2002. Low energy neutrons from a  $^{239}\text{PuBe}$  isotopic neutron source inserted in moderating media. *Revista mexicana de física* 48 (5), 405-412.

- Waters, L.S., McKinney, G.W., Durkee, J.W., Fensin, M.L., Hendricks, J.S., James, M.R., Johns, R.C., and Pelowitz, D.B., 2007. The MCNPX Monte Carlo radiation transport code. AIP conference Proceedings, 896.
- Wood, J., 1982. Computational methods in reactor shielding. Pergamon Press, NY, USA.
- Yilmaz, E., Baltas, H., Kırıs, E., Ustabas, I., Cevik, U., and El-Khayatt, A., 2011. Gamma ray and neutron shielding properties of some concrete materials. Annals of Nuclear Energy 38 (10), 2204-2212.
- Zalegowski, K., Piotrowski, T., Garbacz, A., and Adamczewski, G., 2020. Relation between microstructure, technical properties and neutron radiation shielding efficiency of concrete. Construction and Building Materials 235, 117389.

## **5. Mechanical and Radiation Shielding Properties of Concrete Containing Commercial Boron Carbide Powder**

### **5.1 Abstract**

Boron-containing compounds have an excellent radiation shielding capability against slow neutrons. Moreover, sassolite in boron-containing compounds adversely affects cement hydration by retarding cement setting times. Accordingly, experimental and analytical investigations were carried out to examine the filler effect of commercial boron carbide ( $B_4C$ ) fine powder with a mean particle diameter of  $2.64 \mu m$  on Portland cement hydration reaction, and concrete mechanical and radiation shielding properties. Isothermal calorimetry method was used to study the heat evolution and the cement degree of hydration of mixes containing 0, 25, 50 and 75% of  $B_4C$  to cement by weight. Effects of adding  $B_4C$  on concrete compressive strength were then investigated. Analytical investigations, specifically mass attenuation coefficient using WinXcom program and effective atomic number using Auto- $Z_{eff}$ , were carried out to evaluate the radiation shielding of the corresponding concrete mixes for photon energies range from 10 keV to 10 MeV. Moreover, macroscopic effective removal cross-sections for fast neutrons and thermal neutron macroscopic absorption cross-sections were calculated using MRCsC program and JANIS-4 software, respectively. The results confirm that the presence of sassolite in the studied  $B_4C$  powder retards the hydration reaction for the first 24h, and reveal significant improvements in concrete strength thereafter with the increase

of boron carbide due to the filler effect. Furthermore, the addition of boron carbide yielded measurable improvement in neutron shielding capabilities of concrete mixes.

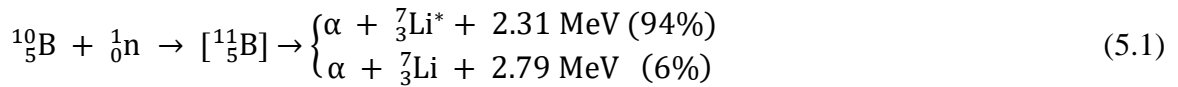
Keywords: Boron carbide powder; Cement degree of hydration; Compressive strength; Heat of hydration; Isothermal calorimetry; Radiation shielding.

## 5.2 Introduction

Concrete, being the most economical and malleable construction material, is used to build all types of civil infrastructure including nuclear power plants and spent nuclear fuel storage facilities [1]. Coarse and fine aggregates, which comprise up to 80% of concrete mixes, typically are added to provide bulk to concrete, as well as strength, stiffness, and durability. For concrete used in nuclear applications, the chemical and physical properties of the aggregates are pivotal as they must possess effective shielding properties against ionizing radiation like gamma rays and neutrons. Such aggregates include heavy natural minerals, synthetic aggregates, and/or certain micro and nano additives [2-6]. Of significance to this study is boron carbide ( $B_4C$ ) which is a hard-ceramic covalent material with a Vickers hardness greater than 30 GPa and considered an effective shield against harmful radiation especially neutrons being thermal, slow, and fast [2, 7, 8].

Boron's thermal and slow neutrons absorption capabilities stem from two primary isotopes,  $^{10}B$  and  $^{11}B$ , in which  $^{10}B$  has high absorption cross-section ( $\sigma_a$ ) equals to 3837 barn at  $E_n = 0.025$  eV [9, 10]. Natural boron that contains approximately 19.6%  $^{10}B$  has a thermal neutron absorption cross-section of 752 barn [9, 11]. For neutrons with high energy, boron's absorption cross-section decreases gradually with increased neutron

energy and still considered sufficiently high and efficient when compared to other neutron absorbers such as cadmium and gadolinium whose cross-sections become abruptly very small [12]. For reference, boron microscopic absorption cross-section is slightly below 1 barn at 1 MeV neutron energy, and boron total microscopic cross-section ranges between 1 to 3 barn for energies from 1 to 20 MeV [13]. Moreover, boron's reaction products upon absorbing thermal and slow neutrons, i.e. the alpha particle,  $\alpha$ , which turns to neutral helium, and lithium, Li, pose minimal hazard as demonstrated in Eq. (5.1) [14, 15],



The excited lithium ( ${}^7_3\text{Li}^*$ ) in Eq. (5.1) emits soft captured gamma rays with energy of about 0.478 MeV that is easily absorbed within the radiation shield [11, 14]. In comparison, cadmium and gadolinium which also possess a high cross-section for absorbing thermal and slow neutrons, are expensive, poisonous, and emit extremely high-energetic secondary gamma rays that need additional shielding considerations [14, 16]. Similarly, hydrogen, whether in hydrogen-rich polymers or water, is very efficient in attenuating fast neutrons but also has a great tendency for liberating high-energetic capture gamma rays "2.22 MeV" upon absorbing thermal neutrons [6, 17]. As such, boron-containing compounds are suited for applications such as transportation and storage of spent nuclear fuel and high-level wastes where mixed radiations exist [18, 19]. Boron which does not occur naturally in a pure state, is extremely difficult to prepare and use in its elemental form [7, 16]. As such, boron compounds have been added to concrete

mixes as aggregate replacements with varying composition and particle sizes [7]. Boron compounds, specifically borax and boric acid, are known to cause retardation in Portland cement setting even when added in small percentage [7, 8, 10, 16, 20]. Boron aggregates; colemanite, ulexite, borax, and boron carbide, when added to concrete as a coarse aggregate, fine aggregate, or in powder form, the concrete physical and mechanical properties were adversely affected [8, 9, 21]. Using isothermal calorimetry method, Glinicki et al. [15] studied the effects of adding colemanite, ulexite, borax, and synthetic boron carbide as a partial replacement of sand on the cement hydration kinetics and the setting time, and tested the corresponding mortar compressive strength at 3 and 28 days.

The results confirmed the adverse effects of ulexite, borax, and colemanite on the cement hydration and setting time even with small boron content of 0.3%, 1.8%, and 10%, respectively. The effects were correlated with soluble minerals in the boron aggregates. However, mortar containing up to 40% synthetic B<sub>4</sub>C powder with a 90 – 125 μm particle size showed no delay in setting time and a very slight increase in the cement total heat generated. This can only be attributed to zero soluble minerals in the synthetic B<sub>4</sub>C powder as no leaching test was performed or other tests showing its mineral composition. Unfortunately, most if not all high grade commercially available B<sub>4</sub>C powder contains a small percentage of boron soluble, as such, the use of these results may be limited. Of interest was the addition of 1 to 2% nanosilica by cement weight to colemanite and ulexite, which acts as nucleation sites, was reported to significantly accelerate the hydration process, and eliminate, to huge extent, the delay caused by the small amount of boron soluble. On the other hand, regarding neutron shielding, others have reported that

around 22% replacement of limestone with boron carbide was sufficient to effectively attenuate poly-energetic neutrons [9, 22, 23].

Borosilicate glass which is a type of glass that contains over 80% silica and a maximum of 15% boron trioxide, is commercially produced for its thermal shock resistance. Given its high amorphous silica content and considerable boron content, the pozzolanic reactivity and neutron shielding properties of the borosilicate glass powder (BSGP) with a mean particle size of 13  $\mu\text{m}$  was evaluated [24]. The maximum pozzolanic reactivity was estimated to be 55%, which is between a typical class F fly ash ( $\approx 30\%$ ) and silica fume ( $\approx 80\%$ ). The results showed an 8% increase in the mortar compressive strength with the addition of 25% BSGP as cement replacement, and a 10 to 40% increase in the mortar neutron attenuation coefficient depending on BSGP replacement levels and curing time. However, the results revealed that the mortar attenuation coefficient plateaus at 25% BSGP replacement level which was attributed to reduction in hydration and pozzolanic reaction.

The above noted findings are significant for shielding concrete as 1) cement setting retardation adversely impacts the microstructural evolution of cement, 2) pozzolanic reactivity enhances the microstructure, 3) nanosilica accelerates cement hydration, and 4) boron increases neutron attenuation coefficient. Moreover, the use of high-purity synthetic  $\text{B}_4\text{C}$  with zero soluble minerals or BSGP is neither economically feasible nor practical given the discussed limitations and considering the need for mass production.

This study aims to investigate the effects of adding a high percentage of commercially inexpensive available  $\text{B}_4\text{C}$  fine powder on the cement hydration kinetics and concrete

compressive strength and radiation shielding specifically, to study the benefits of adding the fine boron carbide powder which serves as nucleation sites and the detriments of adding boron soluble minerals which retard cement hydration. The purpose is to determine the feasibility of commercially available B<sub>4</sub>C powder as a radiation shielding additive to structural concrete. Experimental and analytical programs were developed to measure the effects of B<sub>4</sub>C content on cement hydration kinetics, cement setting time, concrete compressive strength, and concrete radiation shielding properties against harmful radiation that includes X-ray,  $\gamma$ -ray, thermal neutrons, and fast neutrons.

### **5.3 Materials and methods**

Four cement paste mixes, designed to account for the boron carbide powder additions, are summarized in Table 5.1. A 0.6 water to cement ratio (w/c) was selected to facilitate the mixing process without the need to add chemical admixtures, to ensure sufficient water content for the chemical reaction, and to eliminate any external effects on the cement hydration reaction from chemical admixtures. Three samples were cast and tested per mix. The concrete mixtures were designed using the same proportions, namely a constant w/c and same varying cement to boron carbide ratio. The boron carbide was added as a fine aggregate replacement. The concrete mixtures proportions are summarized in Table 5.2. The corresponding elemental analyses along with the measured densities are presented in Table 5.3.

**Table 5.1** Cement paste mixtures proportions

Paste ID	Cement (g)	Water (g)	w/c	B <sub>4</sub> C powder (g)
Mix (0)	24	14.4	0.6	0
Mix (1)	24	14.4	0.6	6
Mix (2)	24	14.4	0.6	12
Mix (3)	24	14.4	0.6	18

**Table 5.2** Concrete mixtures proportions

Concrete ID	Cement (kg/m <sup>3</sup> )	Water (kg/m <sup>3</sup> )	CA (kg/m <sup>3</sup> )	Sand (kg/m <sup>3</sup> )	B <sub>4</sub> C powder (kg/m <sup>3</sup> )
Conc (0)	360	216	971	787	0
Conc (1)	360	216	971	690	90
Conc (2)	360	216	971	593	180
Conc (3)	360	216	971	495	270

**Table 5.3** Concrete elemental analysis, percent weights, and density

Element	Conc (0)	Conc (1)	Conc (2)	Conc (3)
H	1.036	1.040	1.045	1.051
B	0.000	3.218	6.455	9.716
C	5.085	5.686	6.291	6.902
O	51.87	49.83	47.78	45.71
Na	0.073	0.073	0.074	0.074
Mg	0.251	0.252	0.253	0.254
Al	0.399	0.401	0.402	0.404
Si	17.17	15.31	13.44	11.55
S	0.241	0.242	0.243	0.243
Ca	23.49	23.57	23.64	23.72
Fe	0.372	0.373	0.374	0.375
Density (g/cm <sup>3</sup> )	2.334	2.327	2.320	2.232

### 5.3.1 Materials

Portland cement CSA type GU manufactured by Lafarge-Holcim in Canada meeting CAN/CSA A3001 specifications [25] was used in this study. Table 5.4 summarizes the cement chemical and physical properties. The boron carbide powder, which was obtained from Feldco International located in Ladera Ranch, CA, USA, possesses the physical and mechanical properties presented in Table 5.5. Crushed limestone CA with 14 mm

nominal maximum aggregate size was used. The aggregates were obtained from Lafarge, North America's Dundas quarry located in Dundas, Ontario, Canada. The specific gravities, absorption values, and bulk density for the 14 mm CA are 2.74, 0.88%, and 1576 kg/m<sup>3</sup>, respectively. The siliceous sand with SiO<sub>2</sub> greater than 99%, and a maximum and mean particle sizes of 5.00 mm and 0.94 mm, respectively, was obtained from Lafarge North America's West Paris plant. The fineness modulus, specific gravity, bulk density, and absorption value of the used sand are 2.88, 2.71, 1756 kg/m<sup>3</sup>, and 1.28%, respectively. The bulk density, specific gravity, and absorption value of sand and CA were determined in accordance with ASTM C127-15 [26] and ASTM C128-15 [27], respectively. The particle size distribution was evaluated and found to comply with CSA A23.2 specifications [28].

**Table 5.4** Physical properties and chemical composition of Portland cement type GU

Physical/Mechanical property	Value	Spec. limit [25]
Blaine Fineness (m <sup>2</sup> .kg <sup>-1</sup> )	363	-
Percent passing 325 mesh (45 µm) (%)	96	≥72
Autoclave expansion (%)	0.08	≤1
Compressive strength (MPa)		
3 days	26.1	≥14.5
7 days	32.7	≥20.0
28 days	40.7	≥26.5
Time of setting-initial (min)	103	45 – 375
Chemical composition	Value	Spec. limit
SiO <sub>2</sub> (%)	19.5	-
Al <sub>2</sub> O <sub>3</sub> (%)	4.9	-
Fe <sub>2</sub> O <sub>3</sub> (%)	3.1	-
CaO (%)	61.6	-
MgO (%)	2.7	≤5
SO <sub>3</sub> (%)	3.9	≤3
Loss on ignition at 950°C (%)	2.3	≤3
Insoluble residue (%)	0.52	≤1.5
Equivalent Alkalis (%) (as Na Oxide)	0.64	-

**Table 5.5** Physical and mechanical properties of boron carbide powder

Water Solubility	Insoluble
Odor	Odorless
Form	Fine powder
Color	Black
Specific gravity	2.51
Particle size	<6 $\mu$ m
Chemical stability	Stable
Flexural strength (MPa)	408
Elastic modulus (GPa)	452
Hardness (kg.mm <sup>-2</sup> )	3200
Poisson's ratio	0.16

### 5.3.2 Samples' preparation and tests protocol

The experimental procedure for mixing and placing was the same for all the cement mixes. The mixing water was placed in the calorimeter to reach the temperature of 21 °C, while the cement and boron carbide were kept in the laboratory at 21±2 °C for at least 24h prior to mixing. The mixture's constituents were weighed and mixed using the external mixing method outlined in ASTM C1702 - Method B [29] with a time gap between the start of mixing and logging initiation for the samples inside the calorimeter kept at 10 min for all the mixes. The measurement of isothermal heat was done on the cement paste mixes in triplicate at 21°C for 72 h, using I-Cal 8000 HPC isothermal calorimeter with CalCommander software. The measurements were recorded every 1 min.

Concrete mixing procedure was as follows: a) Mix water and AEA for 30 s; b) Place CA, sand, cement, 1/3 of the mixed fluid into the pan mixer; c) Mix the content for 2 min; d) Add the remaining fluid while the mixer is still running; e) Mix the content for an additional 2 min; f) Stop the mixer for 1 min; g) Mix the content for 1 min. Subsequently, the slump and air content of two samples were measured according to CSA

test method A23.2-5C [28] and CSA test method A23.3-4C [28], respectively. Three 100 mm by 200 mm standard cylinders were cast, consolidated by rodding, and finished in accordance with ASTM C192-02 [30]. The cylinders were sealed for 24 h then demoulded and placed in a moist curing room, where the relative humidity was greater than 95% and a constant temperature of 24°C. The concrete compressive strength was evaluated after 3 and 28 days in accordance with ASTM C39-12 [31]. Reported results represent the average and one standard deviation of three cylinders.

The physical and chemical characterization of boron carbide were carried out using the Multisizer 3 Coulter Counter particle size analyzer [32] and D8 Discover X-ray diffractometer from Bruker with cobalt X-ray source at 60 kV [33], respectively. Boron carbide particle size distribution was measured using a sample volume of 67.09  $\mu\text{m}^3$  and a particle size analysis ranging from 0.6 to 18  $\mu\text{m}$ . The X-ray diffraction (XRD) analysis was performed based on Bragg's law [34]. The reflection peaks, corresponding spacing distances, and intensities were obtained for  $2\theta$  ranging between 16 and 94 at 298 k. The International Center for Diffraction Data (ICDD) files [35] were used to identify the mineralogy of the boron carbide powder.

Multiple analytical tools were used for evaluating the radiation shielding properties of concrete containing boron carbide. Concrete mass attenuation coefficients ( $\mu/\rho$ ) were calculated using WinXcom program [36] for photons' energies from 10 keV to 10 MeV. WinXcom was used to compute the mass attenuation coefficient for X-rays and  $\gamma$ -rays up to 100 GeV for elements, chemical compounds, and composites. Using the elemental

analysis of the mixture, the mass attenuation coefficients were calculated according to [36, 37]

$$\frac{\mu}{\rho} = \sum_i w_i \left( \frac{\mu}{\rho} \right)_i \quad (5.2)$$

in which  $w$  and  $i$  are, respectively, the weight fraction and  $i^{\text{th}}$  element. The corresponding linear attenuation coefficient ( $\mu$ ) in  $\text{cm}^{-1}$ , half-value layer ( $HVL$ ) in cm, and mean free path ( $MFP$ ) in cm, were also calculated to assess their photons attenuation capabilities using the following equations [22, 37]:

$$\mu = \frac{\mu}{\rho} \rho \quad (5.3)$$

$$HVL = \frac{\ln 2}{\mu} \quad (5.4)$$

$$MFP = \frac{1}{\mu} \quad (5.5)$$

in which  $\rho$  is the mixture density.

The effective atomic number ( $Z_{\text{eff}}$ ), needed to assess the mixture shielding against X-rays and  $\gamma$ -rays, was calculated using the computer program Auto- $Z_{\text{eff}}$  version 1.7 [38]. The program has a matrix of cross-sections at photon energies starting from 10 keV to 1 GeV and atomic numbers from  $Z = 1$  to 100. The calculated cross-sections for the mixture, using its elemental weight fractions by linear summation, are compared to the built-in matrix as a function of  $Z$ , and then  $Z_{\text{eff}}$  is computed at each energy by interpolation (b-spline) of  $Z$  values between the adjacent cross-section data. The program was used to compute the concrete mixture  $Z_{\text{eff}}$  for photon energy ranging from 10 keV to 10 MeV.

The concrete mix shielding capabilities against fast neutrons is assessed by calculating its macroscopic effective removal cross-section ( $\Sigma_R$ ) using MRCsC software [39]. MRCsC,

which has a built-in database of mass removal cross-section values for all naturally occurring elements [39], employs the weight fractions and density of the mixture to predict the corresponding  $\Sigma_R$  as per the following equation,

$$\Sigma_R = \sum_1^n \rho_s w_i (\Sigma_R / \rho)_i = \sum_1^n \rho_i (\Sigma_R / \rho)_i \quad (5.6)$$

in which  $\rho_s$  and  $\rho_i$  are the mixture density in  $\text{g/cm}^3$  and density of the  $i$ th element.

The efficiency of the concrete mixes in absorbing and eliminating thermalized neutrons was evaluated by calculating the macroscopic absorption cross-section ( $\Sigma_a$ ) at  $E_n = 0.025$  eV using the computer program JANIS-4, which is an improved version of the NEA Java-based Nuclear Data Information System that provides access to nuclear evaluated certified libraries such as EXFOR, CINDA, EAF, ENDF and others [40]. For precise and up-to-date calculations, the ENDF/ B-VIII library which is the most recently updated version of the ENDF database, that was released in 2018, was selected for the calculations [13]. Thermal neutron macroscopic absorption cross-section,  $\Sigma_a(E_n = 0.025 \text{ eV})$ ,  $\text{cm}^{-1}$ , for each mortar mix was calculated as follows,

$$(\Sigma_a / \rho)_i = \frac{N}{\rho_i} (\sigma_a)_i \quad (5.7)$$

$$N = \frac{\rho_i N_A}{M_i} \quad (5.8)$$

$$\Sigma_a(E_n = 0.025 \text{ eV}) = \sum_1^n \rho_s w_i (\Sigma_a / \rho)_i \quad (5.9)$$

in which  $(\sigma_a)_i$ ,  $M_i$ ,  $(\Sigma_a / \rho)_i$ ,  $N_A$ , and  $N$  are the thermal neutron microscopic absorption cross section ( $\text{cm}^2/\text{atom}$ ), molar mass ( $\text{g/mol}$ ), macroscopic thermal neutron mass absorption cross-section ( $\text{cm}^2/\text{g}$ ), Avogadro's constant ( $\text{atom/mol}$ ), and the atomic density of the element ( $\text{atom/cm}^3$ ), respectively. The required thicknesses to remove half of the

initial fast neutrons intensity ( $HVL_{fn}$ ) and to fully absorb half of the initial thermal neutrons intensity ( $HVL_{thn}$ ) were calculated using Eq. (4) and replacing  $\mu$  with  $\Sigma_R$  and  $\Sigma_a$ , respectively, as given below [22, 37].

$$\begin{aligned} HVL_{fn} &= \frac{\ln 2}{\Sigma_R}, \\ HVL_{thn} &= \frac{\ln 2}{\Sigma_a} \end{aligned} \quad (5.10)$$

## 5.4 Results and Discussion

### 5.4.1 Powder characterization

Boron carbide particle size distribution, shown in Fig. 5.1, reveals that the powder has a maximum particle size less than 6  $\mu\text{m}$  and a mean diameter of 2.643  $\mu\text{m}$ . The distribution also shows that 91% of the particles' diameter ranges between 1.175 and 4.575  $\mu\text{m}$ , and about 4% are in the nanoscale. Accordingly, boron carbide particles are finer than those of the Portland cement and can provide nucleation sites for the cement.

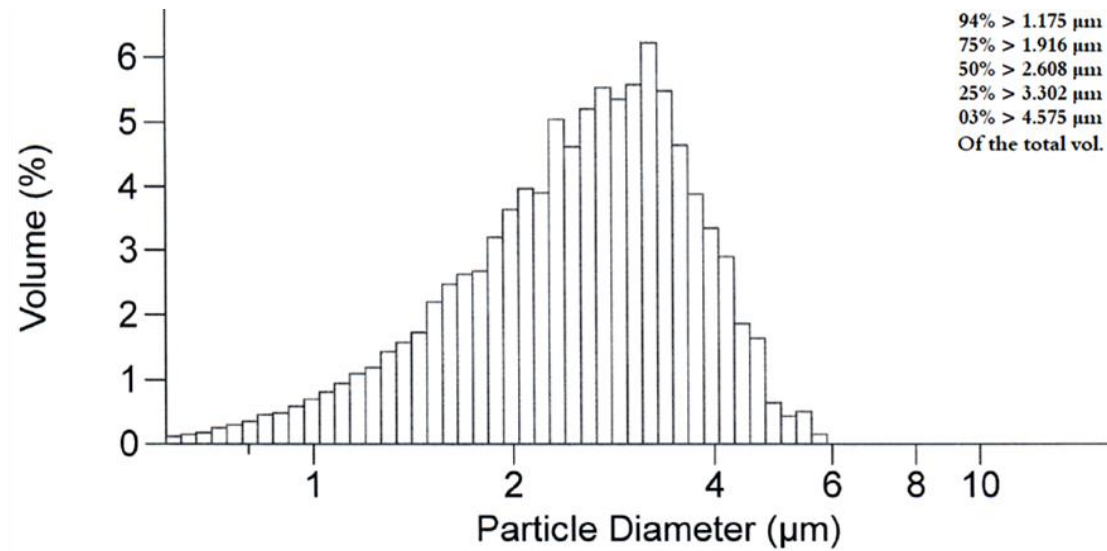


**Fig. 5.1** Boron carbide particle size distribution

Results of the boron carbide powder XRD analysis, shown in Fig. 5.2, reveal that the powder consists of 4 minerals; boron carbide ( $C_{1.7}B_{13.3}$ ), graphite (C), silicon carbide (SiC), and sassolite with the latter being the mineral form of boric acid ( $H_3BO_3$ ). The percent weights of the boron carbide powder constituents are presented in Table 5.6. The associated Rietveld refinement analysis results show that the purity of the boron carbide powder exceeds 97% by weight.

Reported studies on the use of boron carbide in cement have revealed that sassolite (boric acid) and borax retard the setting time of cement even in small percentage [7, 8, 16]. As noted in Table 5.6, boron carbide was found to contain 0.9% sassolite by weight. The effects of sassolite on the kinetics of cement chemical reactions are presented next using isothermal calorimetric test results.

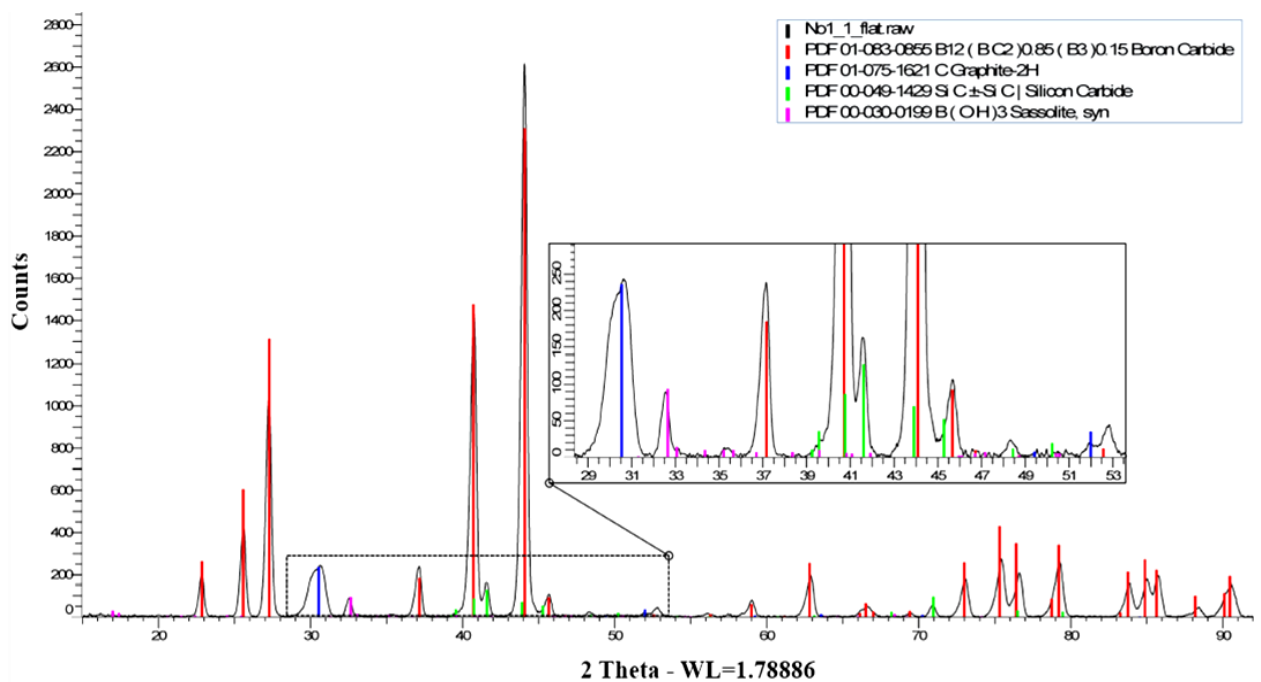


**Fig. 5.2** XRD mineral spectrum of boron carbide powder

**Table 5.6** Boron carbide powder mineral composition and corresponding weight percent

ICDD reference code	Mineral name	Chemical formula	Weight (%) [Std]
01-083-0855	Boron carbide	$C_{1.7}B_{13.3}$	97.23 [0.115]
01-075-1621	Graphite – 2H	C	0.567 [0.057]
00-049-1429	Silicon carbide	SiC	1.267 [0.058]
00-030-0199	Sassolite	$H_3BO_3 [B(OH)_3]$	0.933 [0.152]

#### 5.4.2 Isothermal calorimetry

The isothermal calorimetry test results, in triplicate for the cement paste mixes containing boron carbide and sextuplet for the control mix, in the form of heat flow rate are shown in Fig. 5.3. The corresponding mean and coefficient of variance (COV) of the peak heat flow rate value ( $h_{max}$ ), time of the peak heat flow rate occurs, and cumulative heat released, summarized in Table 5.7, reveal the accuracy and repeatability of the measurements. Results show that the addition of 25% and 50% of  $B_4C$  per cement by weight resulted a 7% and 13% increase in  $h_{max}$ , a 5.0h and 7.5h shift or delay in the occurrence of  $h_{max}$ , and a 12% and 15% increase in the cumulative heat released after 72h, respectively, when compared to Mix (0) that contains no  $B_4C$ . Moreover, the addition of 75%  $B_4C$  per cement has resulted in a 5% decrease in  $h_{max}$ , a 15.4h delay in the occurrence of  $h_{max}$ , and a 35% increase in cumulative heat released after 72h in comparison to Mix (0). In brief, the results confirm the retardation effect of the studied boron carbide powder on the cement hydration reaction, but also show that the overall cement hydration improved almost exponentially as  $B_4C$  per cement ratio increased from 0 to 75%. These results are evident in Fig. 5.4.

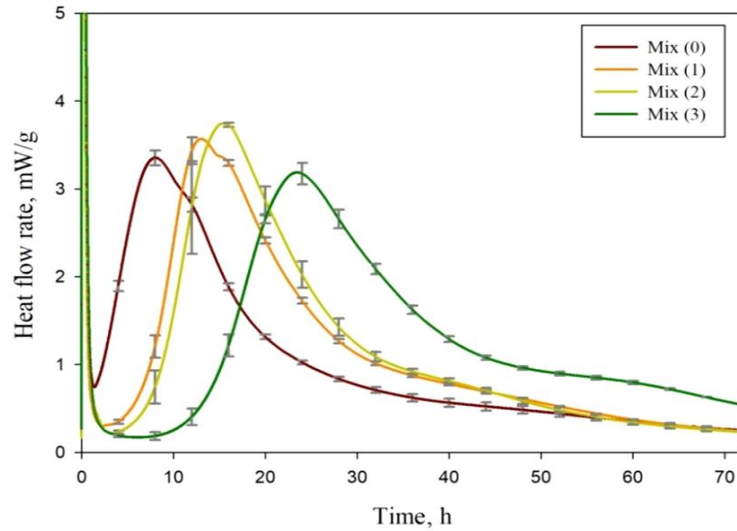


**Fig. 5.3** Cement pastes' mean heat flow rate curves

**Table 5.7** Cement paste  $h_{\max}$ , Time of  $h_{\max}$ , and H determined by isothermal calorimetry

Mix	$h_{\max}$		Time of $h_{\max}$		H @ 72 h	
	Mean (mW/g)	COV (%)	Mean(h)	COV (%)	Mean (J/g)	COV (%)
Mix (0)	3.352	2.6	8.0	0.9	277	2.1
Mix (1)	3.573	2.2	13.0	2.2	311	1.0
Mix (2)	3.799	2.3	15.5	5.1	319	1.5
Mix (3)	3.187	3.6	23.4	1.1	367	2.0

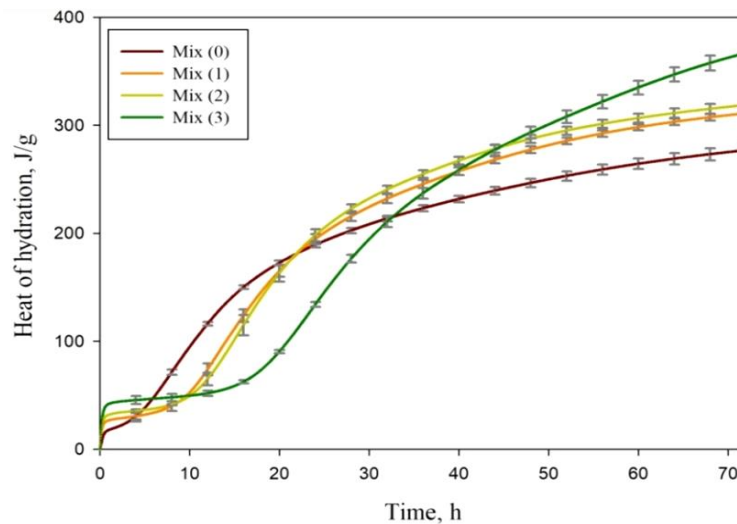


**Fig. 5.4** Cement pastes' mean cumulative heat curves

The cement initial setting time was estimated using the calorimetry test results and the tangents intersection method proposed by Bobrowicz [41]. The results, in the form of mean values and COV, given in Table 5.8, indicate that the initial setting was delayed 4.9h, 5.8h and 11.4h with the addition of 25%, 50% and 75% of B<sub>4</sub>C per cement weight, respectively. The observed retardation values in initial setting time, albeit they are not negligible, they are still manageable even with the 75% addition of B<sub>4</sub>C.

**Table 5.8** Estimated cement paste initial setting time

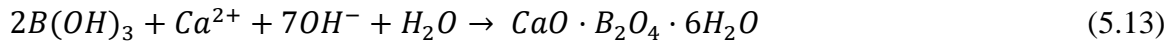
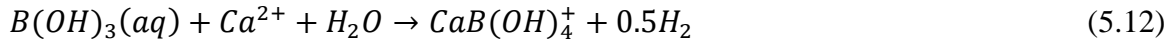
Mix	Initial setting time	
	Mean (h)	COV (%)
Mix (0)	1.9	5.1
Mix (1)	6.8	2.9
Mix (2)	7.7	7.1
Mix (3)	13.3	4.0

The results have so far quantified the effects of adding boron carbide powder to cement on the chemical reaction kinetics but not the causes and consequences. Previous studies have concluded that sassolite (boric acid) acts as a cement retarder even in very small percentages [2, 7, 8, 16, 42]. Boric acid (H<sub>3</sub>BO<sub>3</sub> or B(OH)<sub>3</sub>) which is a weak acidic hydrate of boric oxide, is partially soluble in cold water and its solubility increases with temperature and alkaline media. Boric acid forms soluble salts with monovalent cations like Na<sup>+</sup> however, it forms insoluble salts with divalent cations such as Ca<sup>+2</sup> [43, 44]. First, it partially dissolves in water liberating H<sup>+</sup>, as given in Eq. (5.11) [42].



It also has great tendency to form complexes and insoluble compounds with the dissolved ions in the pore solution, especially Ca<sup>+2</sup> and OH<sup>-</sup>, forming insoluble precipitate such as

calcium borate hydrate (CBH,  $\text{CaB}(\text{OH})_4^+$ ) and calcium diborate hexahydrate ( $\text{CBH}_6$ ,  $\text{CaO} \cdot \text{B}_2\text{O}_4 \cdot 6\text{H}_2\text{O}$ ) as given in Eqs. (5.12 and 5.13) [2, 42, 45].



During the reactions, the alkalinity of the pore solution decreases due to the liberated hydrogen ions ( $\text{H}^+$ ) and consumption of hydroxyl anions ( $\text{OH}^-$ ). The consumption of the dissolved ions especially  $\text{Ca}^{+2}$  and  $\text{OH}^-$  reduces their concentration and retards the occurrence of the saturation level needed for the formation and precipitation of cement hydration products that trigger the “nucleation and rapid growth” stage. Additionally, the meta stable layer of the above mentioned borates (CBH) can form on the un-hydrated cement and encapsulate them, thus inhibiting the dissolution of more ions and diffusion of solution to the grains’ surface [2, 20, 42]. These chemical reactions triggered by the presence of boric acid prolong the dormant stage [2, 20, 46]. By using the solubility curves of boric acid at 21°C, an estimate of 2.708 g of solute per 100 g of sat. solution is deduced [47]. Accordingly, the soluble boric acid for Mix (1), Mix (2), and Mix (3) is estimated at 0.417, 0.833, and 1.25 g per 100 g of saturated solution, respectively. The estimated solutes in Mix (1) to Mix (3) and results of Eqs. 5.11 to 5.13 explain the prolongation in the dormant period upon increasing the amount of  $\text{B}_4\text{C}$ .

After 24 h, the total cement reactivity are found to increase for Mix (1) and Mix (2) according to their total heat released compared to Mix (0), and for Mix (3) after 48h. This increase in cement reactivity is attributed to the filler effect of the  $\text{B}_4\text{C}$  fine powder, which provides nucleation sites that enhance the nucleation and growth of CSH [48, 49].

The retardation effect of boric acid and the benefit of B<sub>4</sub>C filler effect are evident in Mix (3), see Fig. 5.4 [50].

The consequences of adding B<sub>4</sub>C to cement are assessed by means of cement degree of hydration and compressive strength. The hydration kinetics of the Portland cement were assessed using the mixes heat release rate measurements and the following relationship [51, 52],

$$\alpha_C = \frac{H(t)}{H_u} \quad (5.14)$$

in which  $\alpha_C$ ,  $H(t)$  and  $H_u$  are the cement degree of hydration, heat released up to time  $t$ , and the ultimate heat obtainable from the reaction, respectively. Riding et al. [51] has provided a complete model that accounts for the cement chemistry as given below.

$$H_u = H_c = 500 p_{C3S} + 260 p_{C2S} + 866 p_{C3A} + 420 p_{C4AF} + 624 p_{SO3} + 1186 p_{Free-CaO} + 850 p_{MgO} \quad (5.15)$$

in which  $p_{C3S}$ ,  $p_{C2S}$ ,  $p_{C3A}$ , and  $p_{C4AF}$  are respectively, the mass fractions of tricalcium silicate, dicalcium silicate, tricalcium aluminate, and tetracalciumaluminoferrite phases in Portland cement, and  $p_{SO3}$ ,  $p_{Free-CaO}$ , and  $p_{MgO}$  are mass fractions of SO<sub>3</sub>, free CaO and MgO in Portland cement, respectively. The temporal degree of hydration determined using the isothermal calorimetry measurements and Eq. (5.14) are summarized in Table 5.9. The results show that the overall effects of B<sub>4</sub>C on the chemical reaction have no notable consequences on the structure development after 24h for the mixes containing up to 50% addition of B<sub>4</sub>C per cement and 48h for Mix (3) with 75% addition of B<sub>4</sub>C per cement. Moreover, the improvement in the cement degree of hydration upon adding B<sub>4</sub>C powder is evident after 72h [53, 54].

**Table 5.9** Cement paste temporal degree of hydration

Mix	$\alpha_c$							
	12h		24h		48h		72h	
	Mean	COV (%)	Mean	COV (%)	Mean	COV (%)	Mean	COV (%)
Mix (0)	0.24	1.5	0.40	1.2	0.52	1.6	0.58	2.1
Mix (1)	0.16	7.4	0.41	2.5	0.58	1.1	0.65	1.0
Mix (2)	0.14	8.8	0.42	2.8	0.60	1.3	0.67	1.5
Mix (3)	0.11	4.9	0.28	1.7	0.62	1.9	0.77	2.0

The concrete compressive strength at 3 and 28 days was measured for Conc (0) and estimated at 1, 3, and 28 days using the measured cement degree of hydration and compressive strength prediction model [54]. The model results are found to be within 6% of the measured compressive strength. The results also show that a considerable increase in Conc (3) strength at 3 days and a measurable improvement in Conc (1) and Conc (2) strength which is attributed to the filler effect. These results demonstrate that the concrete mixes except for Conc (3) are suitable for demolding after 24 to 48h, and Conc (3) between 48 to 72h. For reference, concrete forms are removed for walls and columns 1 to 2 days after casting and about 3 to 4 days for slabs [55, 56].

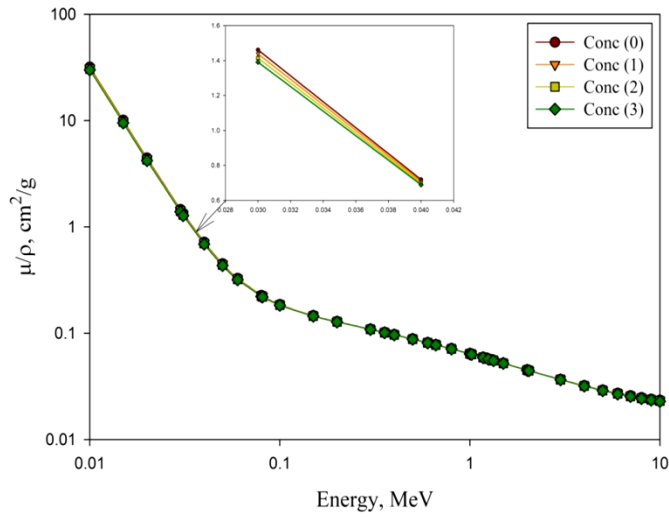
**Table 5.10** Concrete compressive strength (MPa)

Concrete ID	1-day	3-days	3-day Exp.	28-day	28-day Exp.
Conc (0)	7.8	21.8	21.1±0.8	33.0	31.0±0.3
Conc (1)	8.5	26.6			
Conc (2)	9.1	27.9			
Conc (3)	0.5	34.3			

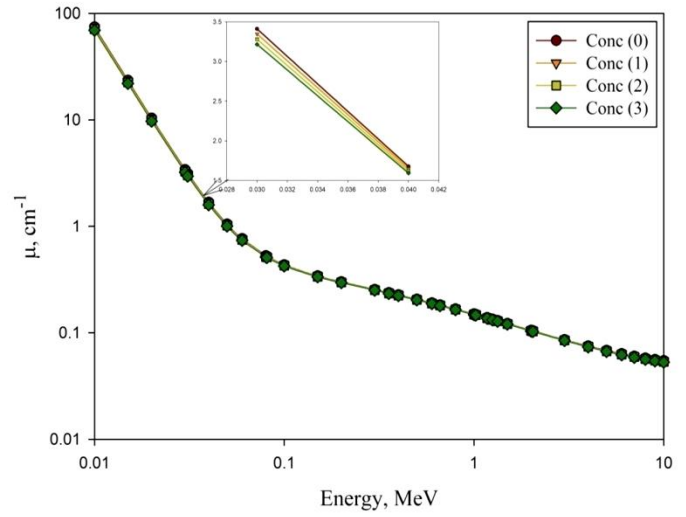
### 5.4.3 Radiation shielding

The concrete mass attenuation coefficient ( $\mu/\rho$ ), linear attenuation coefficient ( $\mu$ ), half-value layer (HVL), and mean free path (MFP), calculated using WinXCom program [36],

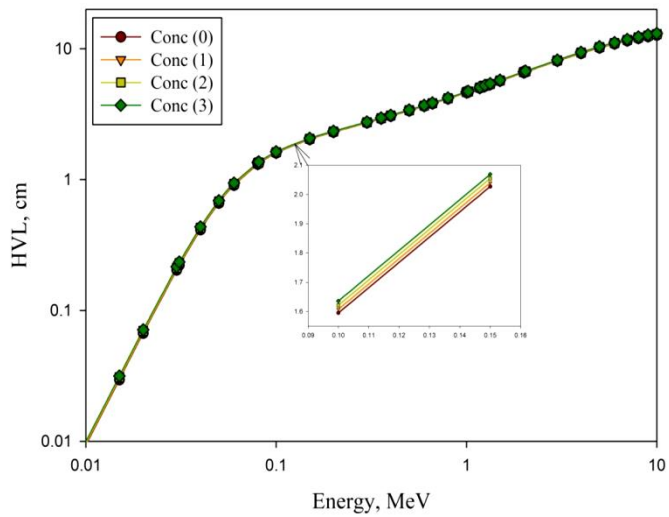
are shown in Fig. 5.5. To get a clear image, the values at known representative energy lines, namely the photon categories such as intermediate and high-energy X-rays that also stand for low-energy gamma rays, and intermediate and high-energy gamma rays, are reproduced in Tables 5.11 and 5.12. The results show that mass and linear attenuation coefficients have the same decreasing pattern as photon energy increases for all 4 concrete mixes. This behavior indicates that the total interaction cross-section of the transmitted photons within the shield atoms and their corresponding electronic clouds decreases with increasing photon energy [22, 37]. However, the corresponding HVL, which corresponds to the required shield thickness to eliminate half of the initial photons' intensity, flux, or dose, and MFP, which is the average distance a photon should travel in the shield before interacting, increase as photon energy increases for all 4 concrete mixes. The results show that the addition of boron carbide powder even at a high percentage has a minor decreasing effect on the gamma rays' attenuation efficiency. The percent decrease in the concrete mixes mass and linear attenuation coefficients and percent increase in HVL and MFP are recorded to be less than 6% at low, intermediate, and high-energy gamma rays for the concrete mix with the highest B<sub>4</sub>C content, Conc (3), in comparison to the reference mix, Conc (0).



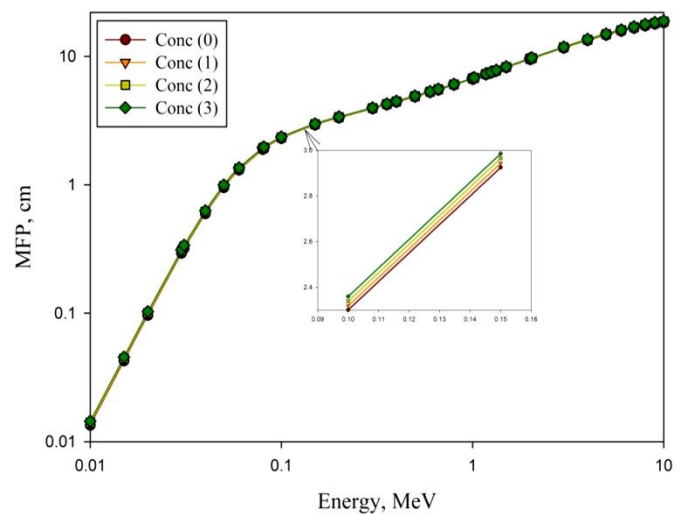
a)



b)



c)



d)

**Fig. 5.5** Concrete  $\mu/\rho$ ,  $\mu$ , HVL and MFP calculated using WinXCom program

**Table 5.11** Concrete mass and linear attenuation coefficients at selected photon energies

Property	$E_\gamma$ (MeV)	Conc (0)	Conc (1)	Conc (2)	Conc (3)	Conc(3)/Conc(0) % Decrease
$\mu/\rho$ (cm <sup>2</sup> /g)	0.031	1.341	1.320	1.299	1.278	4.70
	0.081	0.224	0.223	0.221	0.219	2.23
	0.356	0.102	0.102	0.101	0.101	0.98
	0.662	0.078	0.078	0.078	0.078	0.64
	1.173	0.059	0.059	0.059	0.059	0.67
	1.332	0.056	0.056	0.055	0.055	1.79
$\mu$ (cm <sup>-1</sup> )	0.031	3.130	3.072	3.014	2.955	5.59
	0.081	0.523	0.518	0.512	0.507	3.05
	0.356	0.238	0.237	0.235	0.234	1.68
	0.662	0.182	0.181	0.180	0.179	1.65
	1.173	0.139	0.138	0.137	0.136	2.16
	1.332	0.130	0.129	0.129	0.128	1.54

**Table 5.12** Deduced concrete half-value layer and mean free path at selected photon energies

Property	$E_\gamma$ (MeV)	Conc (0)	Conc (1)	Conc (2)	Conc (3)	Conc(3)/Conc(0) % Increase
HVL (cm)	0.031	0.221	0.226	0.230	0.234	5.88
	0.081	1.326	1.339	1.353	1.366	3.02
	0.356	2.912	2.929	2.946	2.962	1.72
	0.662	3.800	3.820	3.841	3.863	1.66
	1.173	4.997	5.024	5.051	5.081	1.68
	1.332	5.332	5.361	5.390	5.421	1.67
MFP (cm)	0.031	0.319	0.326	0.332	0.338	5.95
	0.081	1.913	1.931	1.951	1.971	3.03
	0.356	4.200	4.226	4.251	4.274	1.76
	0.662	5.482	5.512	5.541	5.574	1.68
	1.173	7.209	7.248	7.287	7.330	1.68
	1.332	7.692	7.735	7.776	7.821	1.68

When adding B<sub>4</sub>C powder, a minor degradation effect is observed at very low photon energies, as the predominant interaction mechanism is the photoelectric effect, which is directly proportional to  $Z^4$  and inversely proportional to  $E^{3.5}$  [37]. For higher energies,

this degradation becomes insignificant. At intermediate and high-energy gamma rays, namely energies of 0.356, 0.662, 1.173, and 1.332 MeV, the predominant mechanisms are Compton scattering and pair production mechanisms that have lower sensitivity to both atomic number and photon energy variations in comparison to the photoelectric mechanism. As such, these two mechanisms are less dependent on E besides, Compton scattering is linearly proportional to Z and pair production varies with  $Z^2$  [5, 22, 37]. Regarding the obtained  $Z_{\text{eff}}$  values using Auto-Zeff program, Fig. 5.6. shows that the values slightly decrease for concrete mixes as  $B_4C$  per cement increases over the studied energy range.

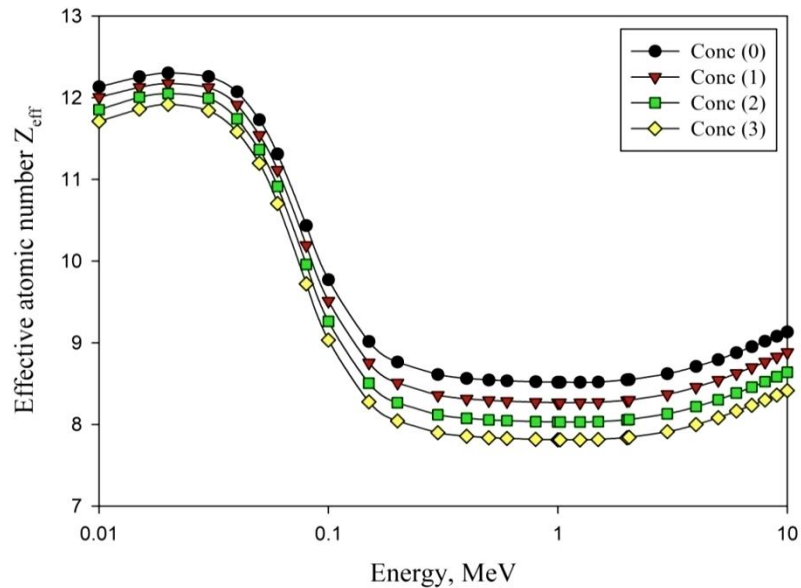


**Fig. 5.6** Concrete effective atomic number with photon energy

As  $Z_{\text{eff}}$  is fundamentally attributed to the interaction mechanisms of the photons with the attenuating medium, its value notably varies with the photon energy. As a result, higher values are seen at lower energies due to the dominance of the photoelectric mechanism which greatly depends on the atomic number as denoted earlier. However, for the energy

range from 0.1 MeV up to about 2 MeV, the lowest  $Z_{\text{eff}}$  values are in this range and, almost, independent on the incident photon energy, which can be attributed to the dominance of Compton scattering mechanism. A regain in the increasing slope can be observed for all the concrete mixes after 2 MeV and up to 10 MeV, as the pair production mechanism that depends on the squared value of the atomic number becomes a major interaction mechanism.

The macroscopic fast neutron removal cross-section values,  $\Sigma_R$ , calculated using the MRCsC program, are presented in Table 5.13. The results show that the addition of boron carbide has a slight positive effect on fast neutron attenuation efficiency, resulting in a decrease in the required half-value layer. The calculated percent change in concrete's  $\Sigma_R$  and  $\text{HVL}_{\text{fn}}$  ranged from approximately 2% to 6% as  $\text{B}_4\text{C}$  per cement content increases from 25% to 75%.

**Table 5.13** Concrete mixes calculated  $\Sigma_R$  and  $HVL_{fn}$  values

	Conc (0)		Conc (1)		Conc (2)		Conc (3)	
	Partial density	Partial $\Sigma_R$ ( $cm^{-1}$ )	Partial density	Partial $\Sigma_R$ ( $cm^{-1}$ )	Partial density	Partial $\Sigma_R$ ( $cm^{-1}$ )	Partial density	Partial $\Sigma_R$ ( $cm^{-1}$ )
H	2.42E-02	1.66E-02	2.42E-02	1.66E-02	2.43E-02	1.67E-02	2.43E-02	1.67E-02
B	0.00E+00	0.00E+00	7.49E-02	4.63E-03	1.50E-01	9.26E-03	2.25E-01	1.39E-02
C	1.19E-01	7.16E-03	1.32E-01	7.98E-03	1.46E-01	8.80E-03	1.60E-01	9.63E-03
O	1.21E+00	4.67E-02	1.16E+00	4.48E-02	1.11E+00	4.28E-02	1.06E+00	4.08E-02
Na	1.71E-03	6.60E-05	1.71E-03	6.60E-05	1.71E-03	6.60E-05	1.71E-03	6.60E-05
Mg	5.86E-03	2.04E-04	5.86E-03	2.04E-04	5.86E-03	2.04E-04	5.86E-03	2.04E-04
Al	9.34E-03	3.38E-04	9.34E-03	3.38E-04	9.34E-03	3.38E-04	9.34E-03	3.38E-04
Si	4.01E-01	1.36E-02	3.56E-01	1.21E-02	3.12E-01	1.06E-02	2.67E-01	9.09E-03
S	5.63E-03	1.88E-04	5.63E-03	1.88E-04	5.63E-03	1.88E-04	5.63E-03	1.88E-04
Ca	5.48E-01	1.85E-02	5.48E-01	1.85E-02	5.48E-01	1.85E-02	5.48E-01	1.85E-02
Fe	8.67E-03	2.13E-04	8.67E-03	2.13E-04	8.67E-03	2.13E-04	8.67E-03	2.13E-04
$\Sigma_R$ ( $cm^{-1}$ )	0.1037		0.1057		0.1077		0.1097	
% Inc. $\Sigma_R$	-		1.9		3.9		5.8	
$HVL_{fn}$ (cm)	6.684		6.558		6.436		6.318	
% Dec. $HVL_{fn}$	-		1.9		3.7		5.5	

The calculated macroscopic absorption cross-section ( $\Sigma_a$ ) values for thermal neutrons obtained using ENDF/ B-VIII library [13] and JANIS-4 software [40] are presented in Table 5.14. The results show that the addition of boron carbide has a significant positive effect on absorbing thermal neutrons. This benefit is attributed to the boron element as it is known to be a strong thermal and slow neutron absorber [37, 57]. Accordingly, the increase in thermal neutron macroscopic absorption cross-section ( $\Sigma_a$ ) and the decrease in the required half-value layer with the increase in  $B_4C$  per cement are very large when compared to Conc (0).

**Table 5.14** Concrete mixes calculated  $\Sigma_a$  and  $HVL_{thn}$  values

	Conc (0)		Conc (1)		Conc (2)		Conc (3)	
	Partial density	Partial $\Sigma_a$ (cm <sup>-1</sup> )	Partial density	Partial $\Sigma_a$ (cm <sup>-1</sup> )	Partial density	Partial $\Sigma_a$ (cm <sup>-1</sup> )	Partial density	Partial $\Sigma_a$ (cm <sup>-1</sup> )
H	2.42E-02	4.84E-03	2.42E-02	4.85E-03	2.43E-02	4.86E-03	2.43E-02	4.87E-03
B	0.00E+00	0.00E+00	7.49E-02	3.21E+00	1.50E-01	6.42E+00	2.25E-01	9.64E+00
C	1.19E-01	2.29E-05	1.32E-01	2.55E-05	1.46E-01	2.81E-05	1.60E-01	3.07E-05
O	1.21E+00	7.74E-06	1.16E+00	7.41E-06	1.11E+00	7.09E-06	1.06E+00	6.76E-06
Na	1.71E-03	2.36E-05	1.71E-03	2.36E-05	1.71E-03	2.36E-05	1.71E-03	2.36E-05
Mg	5.86E-03	9.17E-06	5.86E-03	9.17E-06	5.86E-03	9.17E-06	5.86E-03	9.17E-06
Al	9.34E-03	4.86E-05	9.34E-03	4.86E-05	9.34E-03	4.86E-05	9.34E-03	4.86E-05
Si	4.01E-01	1.42E-03	3.56E-01	1.26E-03	3.12E-01	1.10E-03	2.67E-01	9.45E-04
S	5.63E-03	5.51E-05	5.63E-03	5.52E-05	5.63E-03	5.51E-05	5.63E-03	5.51E-05
Ca	5.48E-01	3.63E-03	5.48E-01	3.63E-03	5.48E-01	3.63E-03	5.48E-01	3.63E-03
Fe	8.67E-03	2.41E-04	8.67E-03	2.41E-04	8.67E-03	2.41E-04	8.67E-03	2.41E-04
$\Sigma_a$ (cm <sup>-1</sup> )	0.0103		3.222		6.434		9.646	
% Inc. $\Sigma_a$	-		3.1E+04		6.2E+04		9.4E+04	
$HVL_{thn}$ (cm)	67.31		0.215		0.108		0.072	
% Dec. $HVL_{th}$	-		99.7		99.8		99.9	

## 5.5 Conclusions

Based on the experimental and analytical results carried out on the cement paste and concrete mixes with varying B<sub>4</sub>C powder content, the following conclusions were achieved:

1. The studied commercial boron carbide powder is a fine powder with a 2.643  $\mu\text{m}$  mean particle size and a 97% purity.
2. The presence of 0.9% sassolite in the boron carbide powder retarded the cement paste initial setting time by 4.9h, 5.8h and 11.4h with the addition of 25%, 50% and 75% of B<sub>4</sub>C per cement, respectively, however, the cement hydration reaction was significantly enhanced thereafter by B<sub>4</sub>C fine particle size due to the filler effect.

3. Cement paste mixes from 0 to 50% B<sub>4</sub>C per cement yielded statistically equal cement degree of hydration at 24h, while the paste with 75% B<sub>4</sub>C per cement yielded a 30% decrease.
4. After 48h and 72h, the cement degree of hydration values for the mixes containing 25%, 50% and 75% B<sub>4</sub>C per cement were 12%, 15% and 19%, and 12%, 16% and 33% greater than the mix with no B<sub>4</sub>C, respectively.
5. The compressive strength of concrete containing up to 50% B<sub>4</sub>C per cement is greater than the mix with no B<sub>4</sub>C after 24 h, and the mix with 75% B<sub>4</sub>C per cement is the largest after 3 days.
6. The addition of boron carbide to concrete as fine aggregate replacement has an insignificant effect on  $\gamma$ -rays attenuation properties.
7. High percent addition of B<sub>4</sub>C powder to concrete slightly enhanced its fast neutrons shielding properties.
8. The addition of B<sub>4</sub>C powder to concrete, even in small percentages, led to a significant increase in the thermal neutrons' absorption capability of the composite shield.
9. Concrete mix containing up to 50% B<sub>4</sub>C per cement is found beneficial to the development of concrete early age properties and achieving effective neutron shielding.

## 5.6 Acknowledgments

This research was funded and supported by the Natural Sciences and Engineering Research Council of Canada, McMaster University Centre for Effective Design of Structures, and Military Technical College in Egypt.

## 5.7 References

- [1] M.G. El-Samrah, A. Tawfic, and S.E. Chidiac, Spent nuclear fuel interim dry storage; Design requirements, most common methods, and evolution: A review, *Annals of Nuclear Energy*. 160 (2021) 108408.
- [2] A.M. Zayed, M.A. Masoud, M.G. Shahien, H.S. Gökçe, K. Sakr, W.A. Kansouh, and A.M. El-Khayatt, Physical, mechanical, and radiation attenuation properties of serpentine concrete containing boric acid, *Construction and Building Materials*. (2020) 121641.
- [3] M.A. Masoud, W.A. Kansouh, M.G. Shahien, K. Sakr, A.M. Rashad, and A.M. Zayed, An experimental investigation on the effects of barite/hematite on the radiation shielding properties of serpentine concretes, *Progress in Nuclear Energy*. 120 (2020) 103220.
- [4] B. Oto, Z. Madak, E. Kavaz, and N. Yaltay, Nuclear radiation shielding and mechanical properties of colemanite mineral doped concretes, *Radiation Effects and Defects in Solids*. 174 (9-10) (2019) 899-914.
- [5] M.G. El-Samrah, M.A. Abdel-Rahman, and A.M. Kany, Study Characteristics of New Concrete Mixes and their Mechanical, Physical, and Gamma Radiation Attenuation Features, *Zeitschrift für anorganische und allgemeine Chemie*. 644 (2) (2018) 92-99.
- [6] M.G. El-Samrah, M.A. Abdel-Rahman, and R. El Shazly, Effect of heating on physical, mechanical, and nuclear radiation shielding properties of modified concrete mixes, *Radiation Physics and Chemistry*. 153 (2018) 104-110.
- [7] R. Adeli, S. Shirmardi, and R. Bagheri, Theory and Simulation Investigation of Low-Energy Neutron Shielding for Different Boron Compounds, *Journal of Testing and Evaluation*. 45 (5) (2017) 1570-1576.
- [8] D. Sarıyer, R. Küçer, and N. Küçer, Neutron shielding properties of concretes containing boron carbide and ferro–boron, *Procedia-Social and Behavioral Sciences*. 195 (2015) 1752-1756.

- [9] M. Kharita, S. Yousef, and M. AlNassar, Review on the addition of boron compounds to radiation shielding concrete, *Progress in Nuclear Energy*. 53 (2) (2011) 207-211.
- [10] M. Glinicki, A. Antolik, and M. Gawlicki, Evaluation of compatibility of neutron-shielding boron aggregates with Portland cement in mortar, *Construction and Building Materials*. 164 (2018) 731-738.
- [11] J. Kratochvíl, T. Opravil, and P. Diviš, The effect of boron and its compounds on setting of Portland cement, *Advanced Materials Research*. 1000 (2014) 16-19.
- [12] B. Bayanov, et al., Readiness for boron neutron capture therapy, *International Conference on Biomedical Engineering and Computational Technologies (SIBIRCON)*. IEEE. (2015) 27-32.
- [13] D.A. Brown, et al., ENDF/B-VIII. 0: The 8th major release of the nuclear reaction data library with CIELO-project cross sections, new standards and thermal scattering data, *Nuclear Data Sheets*, 148 (2018) 1-142.
- [14] G.H. Lee, and J.T. Kim, *Ultrasmall lanthanide oxide nanoparticles for biomedical imaging and therapy*, Woodhead Publishing, 2014.
- [15] G. Gambarini, C. Birattari, C. Colombi, L. Pirola, and G. Rosi, Fricke gel dosimetry in boron neutron capture therapy, *Radiation protection dosimetry*. 101 (1-4) (2002) 419-422.
- [16] L. Wadsö, C.P. Cooper-Jensen, and P.M. Bentley, Assessing hydration disturbances from concrete aggregates with radiation shielding properties by isothermal calorimetry, *Physical Review Accelerators and Beams*, 20 (4) (2017) 043502.
- [17] V. Ryzhikov, L. Nagornaya, V. Volkov, V. Chernikov, and O. Zelenskaya, Thermal neutron detectors based on complex oxide crystals. *Nuclear Instruments and Methods in Physics Research Section A: Accelerators, Spectrometers, Detectors and Associated Equipment*, 486 (1-2) (2002) 156-159.
- [18] T. Saegusa, K. Shirai, T. Arai, J. Tani, H. Takeda, M. Wataru, A. Sasahara and P.L. Winston, Review and future issues on spent nuclear fuel storage, *Nuclear Engineering and Technology*. 42 (3) (2010) 237-248.

- [19] J. Bruno, and R.C. Ewing, Spent nuclear fuel, *Elements*. 2 (6) (2006) 343-349.
- [20] Q. Zhao, J. Tu, W. Han, X. Wang, and Y. Chen, Hydration properties of Portland cement paste with boron gangue, *Advances in Materials Science and Engineering*. 2020 (2020).
- [21] O. Gencil, W. Brostow, C. Ozel, and M. Filiz, An investigation on the concrete properties containing colemanite, *International Journal of Physical Sciences*. 5 (3) (2010) 216-225.
- [22] M.F. Kaplan, *Concrete Radiation Shielding: Nuclear Physics, Concrete Properties, Design and Construction*, Longman Scientific & Technical, Harlow, England, 1989.
- [23] S. Ebrahimi, M.S. Heydari, H.R. Baharvandi, and N. Ehsani, Effect of iron on the wetting, sintering ability, and the physical and mechanical properties of boron carbide composites: A review, *International Journal of Refractory Metals and Hard Materials*. 57 (2016) 78-92.
- [24] M.K. Moradillo, C. Chung, M.H. Keys, A. Shoudhary, S.R. Reese, and W.J. Weiss, Use of borosilicate glass powder in cementitious materials: Pozzolanic reactivity and neutron shielding properties, *Cement and Concrete Composites*. (2020) 103640.
- [25] CSA A3001-18, *Cementitious materials for use in concrete*, Canadian Standards Association, Canada, 2018.
- [26] ASTM C127-15, *Standard test method for relative density (specific gravity) and absorption of coarse aggregate*, ASTM International, West Conshohocken, PA, 2015.
- [27] ASTM C128-15, *Standard test method for relative density (Specific Gravity) and absorption of fine aggregate*, ASTM International, West Conshohocken, PA, 2015.
- [28] CSA A23.1:19/CSA A23.2:19, *Concrete materials and methods of concrete construction/Test methods and standard practices for concrete*. CSA Group, Mississauga, Ontario, Canada, 2019.
- [29] ASTM C1702-09, *Standard test method for measurement of heat of hydration of hydraulic cementitious materials using isothermal conduction calorimetry*, ASTM International, West Conshohocken, PA, USA, 2009.

- [30] ASTM C192 / C192M-02, Standard practice for making and curing concrete test specimens in the laboratory, ASTM International, West Conshohocken, PA, USA, 2002.
- [31] ASTM C39/C39M-12, Standard test method for compressive strength of cylindrical concrete specimens, ASTM International, West Conshohocken, PA, USA, 2012.
- [32] Beckman Coulter™, Multisizer 3 COULTER COUNTER®, 2009.
- [33] K. Leuven, X-ray diffraction– bruker D8 discover, KU Leuven Institute for Nuclear and Radiation Physics, 2013.
- [34] H. Meyers, and H. Myers, Introductory solid state physics, CRC press, 1997.
- [35] PD File, International Centre for Diffraction Data (ICDD). Newtown Square, PA, 2004.
- [36] L. Gerward, N. Guilbert, K.B. Jensen, and H. Leving, WinXCom—a program for calculating X-ray attenuation coefficients. Radiation physics and chemistry, 71 (2004) 653-654.
- [37] J.R. Lamarsh, and A.J. Baratta, Introduction to nuclear engineering, Vol. 3, Prentice hall Upper Saddle River, NJ, USA, 2001.
- [38] M. Taylor, R.L. Smith, F. Dossing, and R.D. Franich, Robust calculation of effective atomic numbers: The Auto-Zeff software, Medical physics. 39 (4) (2012) 1769-1778.
- [39] M.G. El-Samrah, A.M. Elmohandes, A.M. El-Khayatt, and S.E. Chidiac, MRCsC: A computer program for predicting fast neutron shielding, submitted to Radiation Physics and Chemistry. 182 (2020) 109356.
- [40] N. Soppera, M. Bossant, and E. Dupont, JANIS 4: An improved version of the NEA java-based nuclear data information system, Nuclear Data Sheets. 120 (2014) 294-296.
- [41] J. Bobrowicz, Study of cements initial setting time determination using curves of hydration rate evolution, measured by isometric calorimetry, Cement Wapno Beton. 20 (2015) 401-410.

- [42] M. Davraz, The effect of boron compound to cement hydration and controllability of this effect, *Acta Physica Polonica*, A. 128 (2015).
- [43] National Toxicology Program, Institute of Environmental Health Sciences, National Institutes of Health (NTP), National Toxicology Program Chemical Repository Data Base, Research Triangle Park, North Carolina, 1992.
- [44] I.A. Khan, and E.A. Abourashed, *Leung's encyclopedia of common natural ingredients: used in food, drugs and cosmetics*, John Wiley & Sons, 2011.
- [45] D.M. Schubert, Method for producing calcium borate, U.S. Patent No. 5,688,481. 18 Nov. 1997.
- [46] K.L. Scrivener, P. Juilland, and P.J. Monteiro, Advances in understanding hydration of Portland cement, *Cement and Concrete Research*. 78 (2015) 38-56.
- [47] W.C. Blasdale, and C.M. Slansky, The solubility curves of boric acid and the borates of sodium, *Journal of the American Chemical Society*. 61 (4) (1939) 917-920.
- [48] T. Oey, A. Kumar, J.W. Bullard, N. Neithalath, and G. Sant, The filler effect: the influence of filler content and surface area on cementitious reaction rates, *Journal of the American Ceramic Society*. 96 (6) (2013) 1978-1990.
- [49] J.J. Thomas, H.M. Jennings, and J.J. Chen, Influence of nucleation seeding on the hydration mechanisms of tricalcium silicate and cement, *The Journal of Physical Chemistry C*. 113 (11) (2009) 4327-4334.
- [50] E. Berodier, and K. Scrivener, Understanding the filler effect on the nucleation and growth of C-S-H, *Journal of the American Ceramic Society*. 97 (12) (2014) 3764-3773.
- [51] K.A. Riding, J.L. Poole, K.J. Folliard, M. Juenger, A.K. Schindler, Modeling hydration of cementitious systems, *ACI Materials Journal*. 109 (2) (2012) 225-234.
- [52] S.E. Chidiac, and M. Shafikhani, Cement degree of hydration in mortar and concrete, *Journal of Thermal Analysis and Calorimetry*. 138 (3) (2019) 2305-2313.

- [53] K. Zalewski, T. Piotrowski, A. Garbacz, and G. Adamczewski, Relation between microstructure, technical properties and neutron radiation shielding efficiency of concrete, *Construction and Building Materials*. 235 (2020) 117389.
- [54] S.E. Chidiac, F. Moutassem, and F. Mahmoodzadeh, Compressive strength model for concrete, *Magazine of concrete research*. 65 (9) (2013) 557-572.
- [55] P.K. Mehta, and P.J. Monteiro, *Concrete microstructure, properties and materials*, 2017.
- [56] E.G. Nawy, *Concrete construction engineering handbook*, CRC press, 2008.
- [57] R. Barth, D. Carpenter, and A. Soloway, *Advances in neutron capture therapy*, Springer Science & Business Media, 2012.

## **6. Radiation shielding properties of modified concrete mixes and their feasibility in dry storage cask**

### **6.1 Abstract**

The radiation shielding properties of 8 concrete mixes were studied in detail. The concrete mixes included 4 coarse aggregate types; dolomite, barite, ilmenite, and celestite, and 2 cementing material content. Important radiation shielding parameters accounted for in this study include: Mass attenuation coefficient for energy ranging from 10 keV to 10 MeV was calculated using the WinXCom program then linear attenuation coefficient, half value layer, tenth value layer, and mean free path were deduced; Effective atomic number was calculated for the same energy range using *Auto-Z<sub>eff</sub>* software; Exposure build-up factor was calculated using the Geometric Progression approximation method up to 40 mean free path using *Phy-X/PSD* Software for energy ranging from 15 keV to 10 MeV; Fast neutrons macroscopic effective removal cross-section ( $\Sigma_R$ ) and thermal neutron macroscopic absorption cross-section ( $\Sigma_{\text{abs}}(E_n=0.025\text{eV})$ ) were calculated using *MRCsC* and *JANIS-4* programs, respectively. Subsequently, the 8 concrete mixes were assessed for use in a dry storage cask using *OpenMC* code. The results confirmed that heavy concrete mixes have better radiation shielding properties than that of traditional mixes. Concrete mixes containing barite and celestite were the best in attenuating gamma rays emitted in a broad beam situation. The contribution from neutronic dose in the calculation of the total dose rate at the cask's outer surface is very small compared to that of gamma rays or photons.

Keywords; Concrete; Gamma rays; Neutrons; OpenMC; Radiation shielding; Storage cask.

## **6.2 Introduction**

With the misconception of zero-emission green energy source, nuclear energy has emerged as one of the most popular and effective ways for generating electricity around the globe. However, nuclear energy produces radioactive material which subsequently becomes radioactive waste. Therefore, materials that effectively reduce the exposure to hazardous indirect ionizing radiation like gamma rays and neutrons are essential for the sustainability of the nuclear industry. Accordingly, radiation shielding materials have been developed and documented in literature such as modified heavy glass systems doped with heavy metals and rare earth elements' oxides (Kaur et al., 2019; Tekin et al., 2019; Lakshminarayana et al., 2020; Mahmoud and Rammah, 2020), polymeric composites (Shin et al., 2014; Sayyed, 2016; Elwahab et al., 2019), modified alloys (Tellili et al., 2017; Levet et al., 2020; Alshahrani et al., 2021), and modified radiation shielding concretes that utilize heavy natural minerals, synthetic aggregates, and/or certain micro and nano additives (El-Samrah et al., 2018; El-Samrah et al., 2018; Oto et al., 2019; Masoud et al., 2020; Zayed et al., 2020). Notwithstanding, radiation shielding concrete remains the most widely used shielding material due to its high strength, durability, malleability, versatility, relatively inexpensive, availability, and suitability for small and large rigid shielding components and installations (Kaplan, 1989; Zayed et al., 2020).

Assessment of a material effectiveness to radiation shielding is often carried out analytically and/or through numerical modeling prior to conducting any experimental investigation (El-Khayatt, 2010; Oto et al., 2019; Tekin et al., 2019; Lakshminarayana et al., 2020; Mahmoud and Rammah, 2020). The material radiation shielding parameters are first analyzed to evaluate its capabilities in attenuating photons and neutrons at different energies such as mass attenuation coefficient ( $\mu/\rho$ ), linear attenuation coefficient ( $\mu$ ), half value layer (HVL), tenth value layer (TVL), mean free path (MFP), effective atomic number ( $Z_{\text{eff}}$ ), exposure build-up factors (EBF), fast neutrons macroscopic effective removal cross-section ( $\Sigma_R$ ), and thermal neutron macroscopic absorption cross-section ( $\Sigma_{\text{abs}}(E_n = 0.025 \text{ eV})$ ) (Kaplan, 1989; Lamarsh and Baratta, 2001; Bethge et al., 2004). Additionally, Monte Carlo methods such as GEANT4 (Allison et al., 2006), MCNPX (Waters et al., 2007), SuperMC (Wu et al., 2015), and OpenMC (Romano et al., 2014) can provide reliable simulations for real and complex radiological applications. It is critical to simulate the shielding components, in addition to the integral parameters such as ( $\mu/\rho$ ) and TVL, for realistic geometries to assess overall suitability of the shielding material (Waters et al., 2007; Tekin et al., 2019; Azreen et al., 2020).

This study examines the effectiveness of radiation shielding concrete mixes prepared using natural heavy minerals including celestite, which is used for the first time in this study as a coarse aggregate in radiation shielding concrete. The radiation shielding properties of the concrete mixes were first investigated for both photons and neutrons. Subsequently, the feasibility of radiation shielding concrete-based dry storage cask was

assessed by means of a 1-D axisymmetric model representing the geometry of the cask and the simulation software OpenMC (Romano et al., 2014).

### **6.3 Materials and Methods**

Experimental and analytical programs were developed to study the effects of cementing content and aggregates on the radiation shielding concrete (Kaplan, 1989; Abo-El-Enein et al., 2014; Ouda, 2015; El-Samrah et al., 2018; Masoud et al., 2020). Accordingly, eight concrete mixes with varying density and composition were designed using the absolute volume method (ACI, 1996) to meet a target slump of  $100 \pm 15$  mm without any signs of segregation and bleeding, and a minimum compressive strength of 45 MPa. The experimental and analytical programs include respectively, the design of the experiment, the quantification of the concrete mixture chemical composition, physical properties, and elemental composition, and the estimation of concrete's mass and linear attenuation coefficients, half value and tenth value layer, mean free path, effective atomic number, exposure build-up factors, and the fast neutron and thermal neutron shielding properties.

#### **6.3.1 Design of experiment**

The experimental variables considered in this study are coarse aggregate and cementing material content. Specifically, four aggregate types are studied; dolomite which is composed of calcium magnesium carbonate,  $\text{CaMg}(\text{CO}_3)_2$ , quarried from Helwan region in Egypt; barite which consists of barium sulfate,  $\text{BaSO}_4$ , extracted from El-Bahariya Oasis of the Western Desert in Egypt; ilmenite which is a titanium-iron oxide mineral,  $\text{FeTiO}_3$ , supplied by El-Nasr Phosphate Company in Egypt; and celestite which is a mineral consisting of strontium sulfate,  $\text{SrSO}_4$ , mined from Wadi-Essel in Egypt. The

aggregates chemical and physical properties are given in Table 6.1. The cementing material includes ordinary Portland cement (OPC) Type I, silica fume (SF), and ground granulated blast-furnace slag (GGBFS). The cementing materials composition and properties are also given in Table 6.1. OPC and GGBFS were produced by Egypt's Tourah Portland Cement Company and conform to ASTM C-150 (ASTM-C150, 2012) and ASTM C-989 (ASTM-C989, 2006), respectively. SF was supplied by Egypt Geos Company and conforms to ASTM 1240 (ASTM-C1240, 2006). Sikament® NN, which is a high range liquid water reducer that is produced by Sika in compliance with ASTM C494 type G (ASTM-C494, 2011), was added as needed to achieve the target slump without segregation and bleeding.

The eight concrete mixes, given in Table 6.2, were proportioned to have a 0.4 water to cementing ratio, a 20 mm nominal maximum coarse aggregate size, a 2 to 1 ratio of coarse aggregate to fine aggregate by volume, and 7% SF and 20% GGBFS as OPC replacement by weight. The total aggregate volume fraction is 0.56 and 0.64 for the mixes with 600 and 500 kg/m<sup>3</sup> cementing content, respectively. The coarse and fine aggregates particle distribution conforms to ASTM C637 (ASTM-C637, 2009). The fine aggregate, which was obtained from Helwan region in Egypt, is siliceous sand with a fineness modulus of 2.88 and a maximum particle size of 4.75 mm.

**Table 6.1** Chemical and physical properties of cementing materials and aggregates

Oxides/ Compounds	Composition [weight, %]							
	OPC	SF	GGBFS	Sand	Dolomite	Barite	Ilmenite	Celestite
SiO <sub>2</sub>	2.28E+01	9.71E+01	2.45E+01	9.58E+01	2.24E+00	2.03E+00	3.66E+00	2.05E+00
Al <sub>2</sub> O <sub>3</sub>	5.57E+00	1.00E-02	7.46E+00	1.12E+00	9.50E-01	6.40E-01	7.10E-01	4.40E-01
Fe <sub>2</sub> O <sub>3</sub>	3.92E+00	1.09E+00	3.42E+00	8.20E-01	6.10E-01	6.79E+00	2.84E+01	2.70E-01
FeO	-	-	-	-	-	-	2.58E+01	-
CaO	6.13E+01	2.00E-02	5.56E+01	5.20E-01	3.79E+01	6.60E-01	2.00E-01	1.98E+01
MgO	1.57E+00	1.00E-02	3.36E+00	1.00E-01	1.50E+01	3.80E-01	2.35E+00	1.45E+00
SO <sub>3</sub> <sup>2-</sup>	1.52E+00	1.00E-02	2.45E+00	1.10E-01	3.90E-01	2.96E+01	2.00E-02	2.34E+01
Na <sub>2</sub> O	1.40E-01	2.00E-01	4.10E-01	2.70E-01	2.50E-01	4.20E-01	9.00E-02	1.19E+00
K <sub>2</sub> O	9.00E-02	7.00E-02	2.40E-01	6.90E-01	7.00E-02	2.00E-02	4.00E-02	-
MnO	-	-	-	-	-	2.00E-01	-	-
Cl <sup>-</sup>	-	-	4.00E-02	6.00E-02	1.30E-01	6.10E-02	2.00E-02	-
TiO <sub>2</sub>	-	-	5.20E-01	1.20E-01	1.30E-01	-	3.77E+01	5.10E-02
BaO	-	-	8.00E-02	-	-	5.79E+01	-	1.10E-01
SrO	-	-	-	-	-	-	-	3.77E+01
P <sub>2</sub> O <sub>5</sub>	-	-	4.00E-02	-	-	3.00E-02	-	-
H <sub>2</sub> O	-	-	-	-	-	-	1.50E-01	-
CO <sub>2</sub>	2.45E+00	1.36E+00	1.39E+00	2.20E-01	4.23E+01	1.10E+00	8.10E-01	1.35E+01
Total	9.93E+01	9.99E+01	9.95E+01	9.99E+01	1.00E+02	9.98E+01	9.99E+01	1.00E+02
Blaine [cm <sup>2</sup> /g]	2850	-	-	-	-	-	-	-
Specific gravity	3.15	2.26	2.90	2.65	2.68	4.30	4.00	3.95

**Table 6.2** Concrete mix proportions [kg/m<sup>3</sup>]

Mix label	OPC	SF	GGBFS	Sand	Dolomite	Barite	Ilmenite	Celestite
Do_1	471	34	95	497	1005	-	-	-
Ba_1	471	34	95	497	-	1612	-	-
Ilm_1	471	34	95	497	-	-	1500	-
Cel_1	471	34	95	497	-	-	-	1481
Do_2	393	28	79	561	1136	-	-	-
Ba_2	393	28	79	561	-	1822	-	-
Ilm_2	393	28	79	561	-	-	1695	-
Cel_2	393	28	79	561	-	-	-	1674

For reference, the concrete mixes were labelled based on the coarse aggregate type and cementing material content, i.e., Do, Ba, Ilm, and Cel corresponding to dolomite, barite, ilmenite, and celestite mixes, respectively, and 1 and 2 corresponding to the mixes

containing 600 and 500 kg/m<sup>3</sup> cementing content. The concrete mixes elemental compositions were calculated and given in Table 6.3.

**Table 6.3** Concrete mix elemental composition

Element	Weight fraction							
	Do_1	Ba_1	Ilm_1	Cel_1	Do_2	Ba_2	Ilm_2	Cel_2
H	1.15E-02	9.11E-03	9.55E-03	9.53E-03	9.34E-03	7.26E-03	7.67E-03	7.62E-03
C	5.00E-02	2.87E-03	2.45E-03	2.06E-02	5.50E-02	2.76E-03	2.29E-03	2.20E-02
O	5.17E-01	3.98E-01	4.27E-01	4.50E-01	5.16E-01	3.87E-01	4.19E-01	4.43E-01
Na	9.41E-04	1.82E-03	4.73E-04	4.76E-03	9.97E-04	1.93E-03	4.78E-04	5.13E-03
Mg	4.16E-02	3.42E-03	9.74E-03	6.86E-03	4.52E-02	3.08E-03	9.93E-03	6.80E-03
Al	9.69E-03	7.83E-03	8.20E-03	7.48E-03	8.52E-03	6.77E-03	7.13E-03	6.34E-03
Si	1.36E-01	1.10E-01	1.18E-01	1.15E-01	1.41E-01	1.12E-01	1.20E-01	1.16E-01
P	1.62E-05	8.44E-05	1.33E-05	1.34E-05	1.31E-05	8.76E-05	1.07E-05	1.08E-05
S	2.29E-03	6.60E-02	1.38E-03	5.06E-02	2.06E-03	7.10E-02	1.12E-03	5.46E-02
Cl	5.74E-04	3.41E-04	1.19E-04	1.35E-05	6.29E-04	3.65E-04	1.25E-04	1.08E-05
K	3.39E-04	1.62E-04	2.49E-04	7.42E-05	3.48E-04	1.54E-04	2.49E-04	5.92E-05
Ca	2.20E-01	8.53E-02	8.67E-02	1.61E-01	2.13E-01	6.88E-02	6.96E-02	1.50E-01
Ti	4.61E-04	1.00E-04	1.20E-01	2.66E-04	4.72E-04	7.99E-05	1.30E-01	2.58E-04
Mn	-	8.47E-04	-	-	-	9.15E-04	-	-
Fe	8.43E-03	3.12E-02	2.16E-01	6.48E-03	7.40E-03	3.22E-02	2.33E-01	5.47E-03
Sr	-	-	-	1.68E-01	-	-	-	1.82E-01
Ba	2.91E-05	2.83E-01	2.40E-05	5.42E-04	2.36E-05	3.06E-01	1.91E-05	5.81E-04
Total	1.000	1.000	1.000	1.000	1.000	1.000	1.000	1.000
Density (g/cm <sup>3</sup> )	2.342	2.949	2.837	2.818	2.397	3.083	2.956	2.935

### 6.3.2 Radiation shielding properties

The methods and models employed for estimating the concrete's mass and linear attenuation coefficients, half value and tenth value layers, mean free path, effective atomic number, exposure build-up factors, and the fast neutron and thermal neutron shielding properties are presented.

#### 6.3.2.1 Mass and Linear attenuation coefficients

The concrete mass attenuation coefficient ( $\mu/\rho$ ), in cm<sup>2</sup>/g, was calculated for photon energies ranging from 10 keV to 10 MeV using the computer program WinXCom

(Gerward et al., 2004). The X-rays and  $\gamma$ -rays mass attenuation coefficients are computed based on the mixtures elemental composition and in accordance with the following equation (Lamarsh and Baratta, 2001; Gerward et al., 2004):

$$(\mu/\rho) = \sum_i w_i (\mu/\rho)_i \quad (6.1)$$

in which  $w_i$  and  $(\mu/\rho)_i$  are the weight fraction and mass attenuation coefficient of the  $i^{\text{th}}$  element, respectively. The effects of the coarse aggregates on  $\mu/\rho$  were studied by investigating the partial contribution of the photoelectric absorption, incoherent (Compton) scattering, and pair production. For comparative analysis, the mixture linear attenuation coefficient ( $\mu$ ), in  $\text{cm}^{-1}$ , which depends on the elemental composition and density of the concrete mix ( $\rho_{\text{mix}}$ ), was calculated using the following equation (Lamarsh and Baratta, 2001),

$$\mu = \rho_{\text{mix}}(\mu/\rho) \quad (6.2)$$

### 6.3.2.2 Half value layer, Tenth value layer, and Mean free path

The concrete radiation shielding efficiency was assessed by calculating the required thickness to attenuate the incoming incident radiation to 50%, 10%, and  $\approx 37\%$  referred to as half value layer (HVL), tenth value layer (TVL), and mean free path (MFP), respectively (Lamarsh and Baratta, 2001; Oto et al., 2015). The equations to calculate the corresponding thicknesses, in cm, are (Kaplan, 1989; Lamarsh and Baratta, 2001)

$$HVL = \frac{\ln 2}{\mu} \quad (6.3)$$

$$TVL = \frac{\ln 10}{\mu} \quad (6.4)$$

$$MFP = \frac{1}{\mu} \quad (6.5)$$

### 6.3.2.3 Effective atomic number

Effective atomic number ( $Z_{\text{eff}}$ ), which is used to assess shielding against X-rays and  $\gamma$ -rays as it characterizes the electronic cloud that participates in the photon/atom interaction process (Taylor et al., 2012; Hosamani and Badiger, 2018), was evaluated in this study.  $Z_{\text{eff}}$  was calculated using the computer program Auto- $Z_{\text{eff}}$  version 1.7 (Taylor et al., 2012). The program has a matrix of cross-sections at photon energies ranging from 10 keV to 1 GeV and atomic numbers ( $Z$ ) going from 1 to 100. The calculated cross-sections for the mixture, using its elemental weight fractions by linear summation, are compared to the built-in matrix as a function of  $Z$ , and then  $Z_{\text{eff}}$  is computed by interpolation (b-spline) of the  $Z$  values between the adjacent cross-section data at the specified energies (Taylor et al., 2012).

### 6.3.2.4 Exposure build-up factor

The Beer Lambert law, given by Eq. (6.6) (Kaplan, 1989), is valid for narrow-beam geometry, where

$$I_x = I_0 e^{-\mu x} \quad (6.6)$$

and  $I_0$  and  $I_x$  are, respectively, the initial photon intensity and the photon intensity after passing an  $x$ , in cm, thickness of the shield. However, for radiation shielding applications, broad-beam geometry is most common. Accordingly, the Beer Lambert law is modified as follows,

$$I_x = BI_0 e^{-\mu x} \quad (6.7)$$

where  $B$  is the build-up factor (Kaplan, 1989; Lamarsh and Baratta, 2001). There are two approaches for determining the build-up factor, the exposure build-up factor (EBF) and energy absorption build-up factor (EABF), with the former commonly employed in radiation shielding calculations (Singh and Badiger, 2012; Oto et al., 2015; Kaur et al., 2019). EBF was calculated using Phy-X/PSD program for photon energies ranging from 15 keV to 10 MeV (Şakar et al., 2020). Phy-X/PSD was developed for calculating the shielding and dosimetry parameters concerning X-rays and  $\gamma$ -rays (Şakar et al., 2020).

The procedure adopted to calculate  $B$  is as follows. First, the concrete mix's equivalent atomic number  $Z_{eq}$ , which depends on the ratio ( $R$ ) between the mass attenuation coefficient due to Compton scattering  $(\mu/\rho)_{\text{Compton}}$  and the total mass attenuation coefficient  $(\mu/\rho)_{\text{total}}$ , is calculated for each energy in the specified energy range using the following interpolation method (Harima, 1983)

$$Z_{eq} = \frac{Z_1(\log R_2 - \log R) + Z_2(\log R - \log R_1)}{\log R_2 - \log R_1} \quad (6.8)$$

in which  $Z_1$  and  $Z_2$  are the atomic numbers of the two elements corresponding to the ratios  $R_1$  and  $R_2$ , respectively.  $R$  is the ratio for the concrete mix at a specific energy that is located between  $R_1$  and  $R_2$ . The geometric progression (G-P) fitting parameters ( $a$ ,  $b$ ,  $c$ ,  $d$ ,  $X_K$ ) are then calculated using the same interpolation method adopted for  $Z_{eq}$ , i.e.,

$$Y = \frac{Y_1(\log Z_2 - \log Z_{eq}) + Y_2(\log Z_{eq} - \log Z_1)}{\log Z_2 - \log Z_1} \quad (6.9)$$

in which  $Y$  represents the fitting parameter  $a$ ,  $b$ ,  $c$ ,  $d$ , and  $X_K$ , and  $Y_1$  and  $Y_2$  correspond to the fitting parameters for the two elements with atomic numbers  $Z_1$  and  $Z_2$ , respectively. The elemental fitting parameters are collected from the “ANSI/ANS-6.4.3” standard data set (ANSI/ANS-6.4.3, 1991). Subsequently,  $B(E,X)$  is calculated for all energies that lie in the specified energy range by employing the calculated G-P fitting parameters and using the following equations (Harima et al., 1986)

$$B(E, X) = \begin{cases} 1 + \frac{b-1}{K-1}(K^X - 1) & \text{for } K \neq 1 \\ 1 + (b-1)X & \text{for } K = 1 \end{cases} \quad (6.10)$$

$$K(E, X) = CX^a + d \frac{\tanh\left(\frac{X}{X_K} - 2\right) - \tanh(-2)}{1 - \tanh(-2)} \text{ for penetration depth } (X) \leq 40 \text{ MFP} \quad (6.11)$$

where  $E$ ,  $X$ , and  $K$  are the energy of the incident photons, the penetration depth measured by MFP, and the dose multiplicative factor that also defines the shape of the curve, respectively.

#### 6.3.2.5 Fast neutron shielding properties

The concrete fast neutrons' shielding effectiveness was evaluated by first computing the macroscopic fast neutron effective removal cross-section ( $\Sigma_R$ ) by using the computer program MRCsC (El-Samrah et al., 2021). MRCsC has a built-in database of microscopic mass removal cross-sections for all naturally occurring elements and therefore only requires the weight fractions and corresponding density of the mixture to calculate  $\Sigma_R$  (Kaplan, 1989), as per the following equation;

$$\Sigma_R = \sum_1^n \rho_s w_i (\Sigma_R / \rho)_i = \sum_1^n \rho_i (\Sigma_R / \rho)_i \quad (6.12)$$

where  $\rho_s$  and  $\rho_i$  are respectively, the mix density, in  $\text{g/cm}^3$ , and the density of the  $i^{\text{th}}$  element. The half value layer ( $HVL_{fn}$ ), in cm, which is the required thickness to attenuate half of the incident fast neutrons beam, and the relaxation length ( $\lambda_{fn}$ ), in cm, the average distance traveled by a fast neutron before interacting with the medium, are then calculated based on  $\Sigma_R$  as follows (Kaplan, 1989; Lamarsh and Baratta, 2001):

$$HVL_{fn} = \frac{\ln 2}{\Sigma_R} \text{ and } \lambda_{fn} = \frac{1}{\Sigma_R} \quad (6.13)$$

### 6.3.2.6 Thermal neutron shielding properties

Concrete's capability to absorb thermalized neutrons was assessed by calculating the macroscopic absorption cross-section ( $\Sigma_{\text{abs}}$ ) at  $E_n = 0.025$  eV using JANIS-4 software (Soppera et al., 2014). JANIS-4 is an improved version of the NEA Java-based Nuclear Data Information System that allows direct access to nuclear evaluated certified libraries such as EXFOR, CINDA, EAF, ENDF (Soppera et al., 2014). ENDF/ B-VIII library which is the most recently updated version of the ENDF database was selected for the calculations (Brown et al., 2018). Thermal neutron macroscopic absorption cross-section,  $\Sigma_{\text{abs}}(E_n = 0.025 \text{ eV})$ , in  $\text{cm}^{-1}$ , was calculated using the followings

$$(\Sigma_{\text{abs}}/\rho)_i = \frac{N}{\rho_i} (\sigma_a)_i \quad (6.14)$$

$$N = \frac{\rho_i N_A}{M_i} \quad (6.15)$$

$$\Sigma_{\text{abs}}(E_n = 0.025 \text{ eV}) = \sum_1^n \rho_s w_i (\Sigma_{\text{abs}}/\rho)_i \quad (6.16)$$

in which  $(\sigma_a)_i$ ,  $M_i$ ,  $(\Sigma_{\text{abs}}/\rho)_i$ ,  $N_A$ , and  $N$  are the microscopic absorption cross-section for thermal neutrons ( $\text{cm}^2/\text{atom}$ ), the molar mass ( $\text{g/mol}$ ), the macroscopic mass absorption

cross-section for thermal neutron ( $\text{cm}^2/\text{g}$ ), Avogadro's constant ( $\text{atom}/\text{mol}$ ), and the atomic density of the element ( $\text{atom}/\text{cm}^3$ ), respectively.

Analogous to fast neutrons, the half value layer ( $HVL_{thn}$ ) and relaxation length ( $\lambda_{thn}$ ) for thermal neutrons are deduced from ( $\Sigma_{abs}$ ) as follows,

$$HVL_{thn} = \frac{\ln 2}{\Sigma_{abs}} \text{ and } \lambda_{thn} = \frac{1}{\Sigma_{abs}} \quad (6.17)$$

#### 6.4 Concrete-Based Dry Storage Cask (DSC) Model

An axisymmetric 1-D model of a sandwich-design concrete-based dry storage cask was constructed to study the effects of the coarse aggregate type and cementing material content on the radiation shielding properties of the concrete overpack in a dry storage cask. The simulations were carried out using the computer program OpenMC version 0.12.0 (Romano et al., 2014). The cask was divided into seven layers as shown in Figure 6.1. Starting from the centre of the cask, the layers composition and thickness are as follows: Layer 1 is the interior of the canister that is filled with helium gas with a density of  $0.178\text{E-}03 \text{ g}/\text{cm}^3$  and a radial thickness of 88 cm; Layer 2 which represents the canister shell, is made up of boron steel with a thickness of 1 cm; Layer 3 is a 4.45 cm thick air gap; Layers 4 and 6 represent the steel liner that frames the concrete with a thickness of 2.54 cm; Layer 5 is a 50 cm thick concrete; Layer 7 is air representing the surrounding environment. The weight percentages and densities of the elements used in the model, except for the concrete layer, are given in Table 6.4.

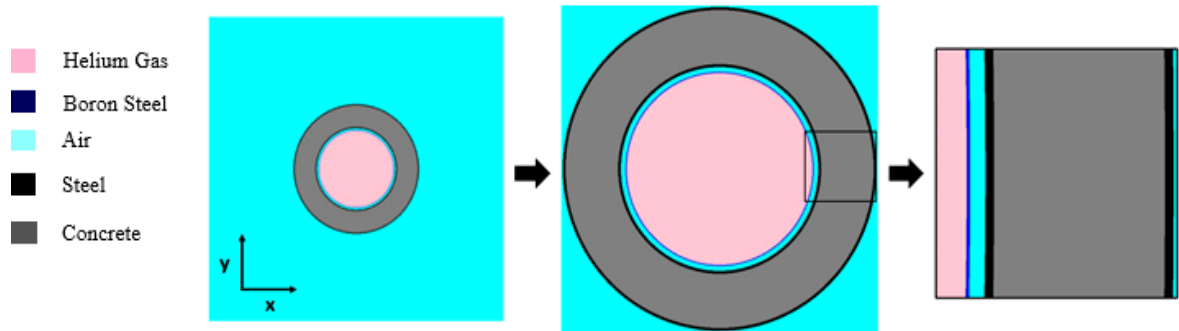


**Fig. 6.1** Model of sandwich-design concrete-based dry storage cask

**Table 6.4** Element's weight percentage and density

Element	Boron Steel	Air	Steel
Si	0.22E-01	-	7.50E-01
Al	-	-	-
Fe	9.80E+01	-	6.65E+01
Ca	-	-	-
Mg	-	-	-
S	-	-	3.00E-02
K	-	-	-
Na	-	-	-
O	-	2.10E+01	-
H	-	-	-
C	2.90E-01	-	8.00E-02
B	3.00E-03	-	-
Mn	1.23E+00	-	2.00E+00
P	-	-	4.50E-02
Ti	-	-	-
N	-	7.90E+01	1.00E-01
U	-	-	-
Cr	3.10E-01	-	1.75E+01
Ni	-	-	1.10E+01
Mo	-	-	2.00E+00
Density (g/cm <sup>3</sup> )	7.90E+00	1.23E-03	7.85E+00

The considered stored fuel in the dry cask was Westinghouse 17x17 assemblies with an active fuel length of 365 cm, and a total neutron and photon emissions of  $8.26\text{E}+09$  n/sec and  $3.52\text{E}+12$  photons/sec, respectively. For the simulations, the stored fuel was modelled as two isotropic point sources, representing neutrons and photons, placed at the centre of the cask. The proposed isotropic point source model for the stored fuel

assemblies is expected to slightly underestimate the fluxes at the inner surface of the cask; however, this effect is partially counteracted by the shielding caused by the assemblies and the basket. The corresponding neutron and photon spectra adopted for the model point source are given in Table 6.5 (Ko et al., 2014).

The Monte Carlo simulations, which consisted of 300 batches, were carried out using the ENDF/B-VII.1 library, and a half million particles point source. Hence, the neutrons and photons attenuations were evaluated. The neutron and photon fluxes at the surface of the cask were calculated using the mesh and particle filters. Moreover, the neutron and photon fluxes with energy were computed at the cask's outer surface by employing particle, mesh, and energy filters, and by increasing the particle number to 10M. This was carried out to evaluate the total dose rate using ANSI 1991 conversion factors reproduced in Fig. 6.2 (ANSI, 1991).

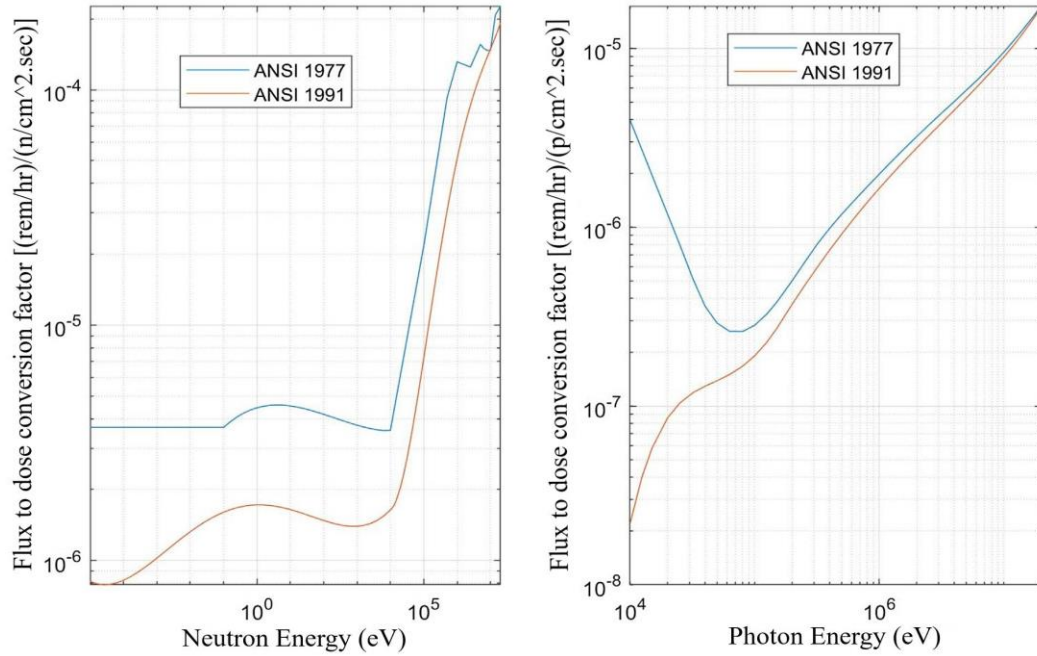


**Fig. 6.2** Flux to dose conversion factors adopted from (McFerran et al., 2020)

**Table 6.5** Photon and neutron spectra used to define the radioactive sources

Photon energy (MeV)	Fraction	Neutron energy (MeV)	Fraction
0.01~0.05	2.72E-01	1.00E-08~1.00E-07	3.37E-02
0.05~0.10	7.59E-02	1.00E-07~1.00E-06	5.14E-02
0.10~0.20	5.50E-02	1.00E-06~1.00E-05	7.25E-02
0.20~0.30	1.62E-02	1.00E-05~1.00E-04	9.35E-02
0.30~0.40	1.06E-02	1.00E-04~1.00E-03	1.13E-01
0.40~0.60	4.34E-02	1.00E-03~1.00E-02	1.33E-01
0.60~0.80	4.90E-01	1.00E-02~1.00E-01	1.53E-01
0.80~1.00	2.26E-02	1.00E-01~1.00E+00	1.70E-01
1.00~1.33	1.31E-02	1.00E+00~3.00E+00	8.25E-02
1.33~1.66	1.75E-03	3.00E+00~5.00E+00	3.57E-02
1.66~2.00	3.59E-05	5.00E+00~8.00E+00	3.57E-02
2.00~2.50	1.32E-05	8.00E+00~1.10E+01	2.63E-02
2.50~3.00	8.04E-07		
3.00~4.00	7.62E-08		
4.00~5.00	2.06E-09		
5.00~6.50	8.28E-10		
6.50~8.00	1.62E-10		
8.00~10.00	3.45E-11		
Total	1.00E+00	Total	1.00E+00

## 6.5 Results and discussion

### 6.5.1 Gamma-rays shielding assessment

The effects of the coarse aggregate composition on  $(\mu/\rho)$  was examined in detail by calculating the total mass attenuation coefficient and the partial contribution of the three main interaction mechanisms for energy ranging from 10 keV to 10 MeV. The corresponding results for the 4 concrete mixes, shown in Fig. 6.3, reveal that the greatest contribution of Compton scattering in the total mass attenuation coefficient corresponds to Dolomite concrete as it becomes the major contributor starting from 60 keV till the end of the studied energy range of 10 MeV. For Ilmenite concrete, the dominance of Compton scattering mechanism starts after 80 keV and remains the major mechanism till the end of the energy range even though the contribution of the pair production mechanism becomes significant at the end. Regarding Celestite concrete, the Compton scattering mechanism becomes dominant after 100 keV. For Barite concrete, the dominance of the Compton scattering mechanism is the lowest among the concrete mixes with the major interaction mechanism starting at 200 keV, and at 10 MeV the contribution of the pair production mechanism becomes almost equivalent to the Compton scattering mechanism.

The difference in the observed mass attenuation coefficient of the concrete mixes is attributed to the composition of the coarse aggregates. The photoelectric interaction mechanism, which is proportional to  $Z^{4.5}$ , becomes a major contributor in the total attenuation than Compton scattering mechanism with the increase of heavy elements' content and atomic number in the concrete mix. For example, Barite concrete contains a considerable amount of barium (Ba) that has an atomic number ( $Z$ ) of 56 shows a higher

contribution of photoelectric interaction mechanism in comparison to Celestite concrete that has a significant amount of strontium (Sr) with Z equals 38 and Celestite concrete has higher contribution of photoelectric interaction mechanism in comparison to Ilmenite concrete that contains iron (Fe) and titanium (Ti) with Z equals 26 and 22, respectively.

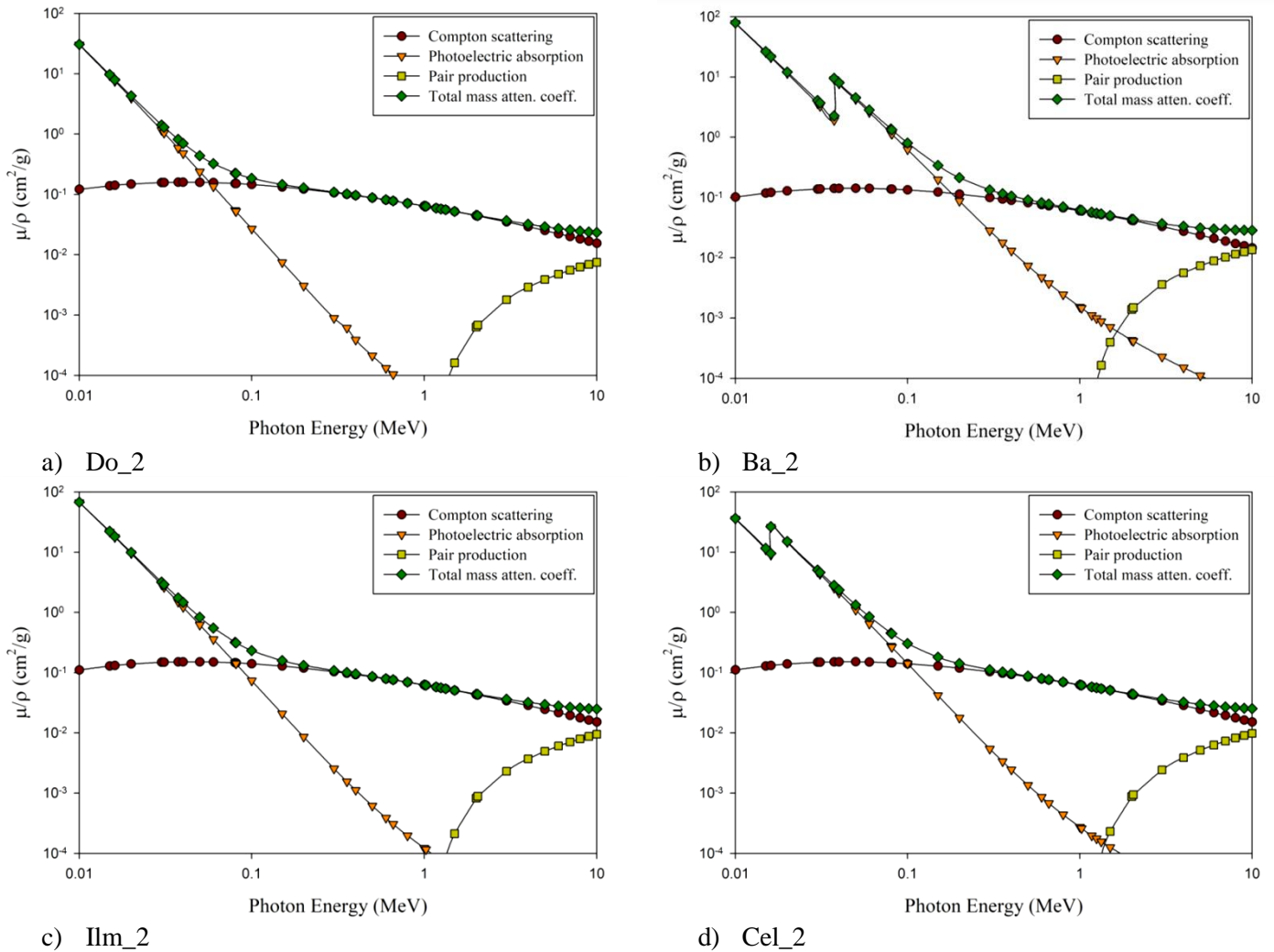


**Fig. 6.3** Concrete mixes total mass attenuation coefficient and partial contribution of the three main interaction mechanisms

At high energy, the pair production mechanism that is proportional to  $Z^2$  and  $\log(E)$  becomes more significant. As such, Dolomite concrete which contains negligible amounts of heavy elements has Compton scattering mechanism which is the least dependent on  $Z$  as the major interacting mechanism of photons with the shield constituents along with a limited dominance of the photoelectric mechanism at very low energy.

A comparison of the concrete's photon shielding potential must account for the mix's composition and density. As such, their respective values of linear attenuation coefficient ( $\mu$ ) along with the derived half value layer (HVL), tenth value layer (TVL), and mean free path (MFP), shown in Fig. 6.4, were examined for the suggested energy range. The values of  $\mu$  and HVL for selected energy values, which represent the ranges dominated by the three interaction mechanisms discussed previously, are reproduced in Table 6.6.

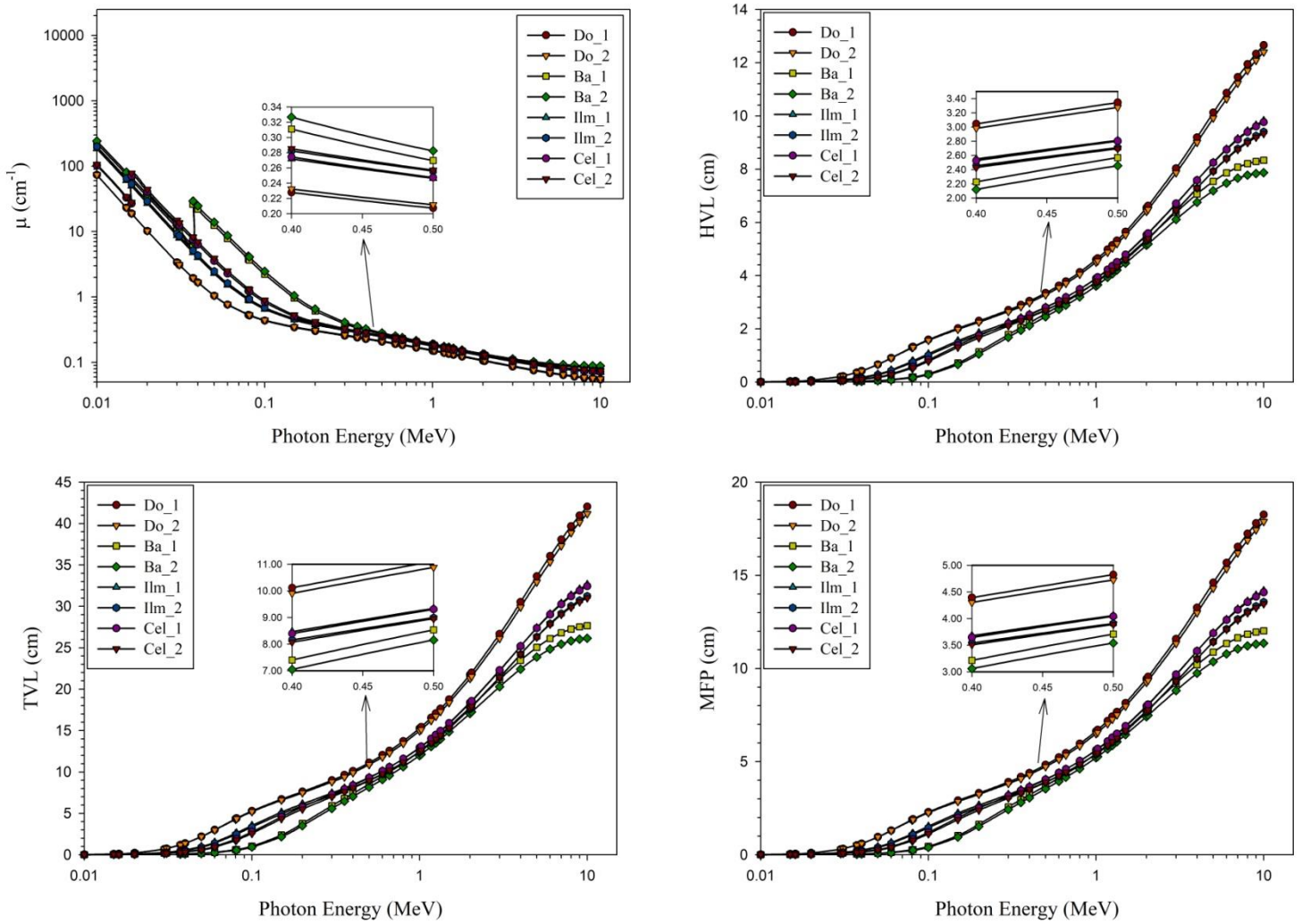


**Fig. 6.4**  $\mu$ , HVL, TVL, and MFP for the eight concrete mixes

**Table 6.6** Values of  $\mu$  and HVL for selected photon energy values

Property	$E_\gamma$ (MeV)	Mix design no. 1				Mix design no. 2			
		Do_1	Ba_1	Ilm_1	Cel_1	Do_2	Ba_2	Ilm_2	Cel_2
$\mu$ , $\text{cm}^{-1}$ (% Increase)	0.031	3.101	10.48	7.969	12.39	3.111	11.47	8.608	13.59
		(-)	(238)	(157)	(300)	(-)	(269)	(177)	(337)
	0.081	0.523	3.680	0.875	1.204	0.531	4.103	0.928	1.300
		(-)	(604)	(67.3)	(130)	(-)	(673)	(74.8)	(145)
	0.356	0.239	0.338	0.286	0.290	0.247	0.356	0.297	0.302
		(-)	(41.4)	(19.7)	(21.3)	(-)	(44.1)	(20.2)	(22.2)
	0.662	0.183	0.230	0.217	0.217	0.187	0.240	0.226	0.226
		(-)	(25.7)	(18.6)	(18.6)	(-)	(28.3)	(20.9)	(20.9)
	1.173	0.139	0.169	0.165	0.164	0.142	0.176	0.171	0.170
		(-)	(21.6)	(18.7)	(18.0)	(-)	(23.9)	(20.4)	(19.7)
1.332	0.130	0.158	0.154	0.154	0.133	0.165	0.160	0.160	
	(-)	(21.5)	(18.5)	(18.5)	(-)	(24.1)	(20.3)	(20.3)	
5	0.068	0.092	0.084	0.084	0.070	0.096	0.087	0.088	
	(-)	(35.3)	(23.5)	(23.7)	(-)	(37.1)	(24.3)	(25.7)	
10	0.055	0.083	0.071	0.071	0.056	0.088	0.074	0.074	
	(-)	(50.9)	(28.2)	(29.1)	(-)	(57.1)	(32.1)	(32.5)	
$HVL$ , cm (% Decrease)	0.031	0.224	0.066	0.087	0.056	0.223	0.060	0.081	0.051
		(-)	(70.5)	(61.2)	(75.0)	(-)	(73.1)	(63.7)	(77.1)
	0.081	1.326	0.188	0.792	0.576	1.306	0.169	0.747	0.533
		(-)	(85.8)	(40.3)	(56.6)	(-)	(87.1)	(42.8)	(59.2)
	0.356	2.902	2.049	2.424	2.390	2.806	1.945	2.331	2.297
		(-)	(29.4)	(16.5)	(17.6)	(-)	(30.7)	(16.9)	(18.1)
	0.662	3.785	3.013	3.190	3.190	3.704	2.886	3.072	3.071
		(-)	(20.4)	(15.7)	(15.7)	(-)	(22.1)	(17.1)	(17.1)
	1.173	4.983	4.095	4.205	4.219	4.876	3.933	4.054	4.067
		(-)	(17.8)	(15.6)	(15.3)	(-)	(19.3)	(16.9)	(16.6)
1.332	5.314	4.377	4.491	4.505	5.202	4.205	4.325	4.340	
	(-)	(17.6)	(15.5)	(15.2)	(-)	(19.2)	(16.9)	(16.6)	
5	10.12	7.538	8.251	8.240	9.913	7.185	7.925	7.914	
	(-)	(25.5)	(18.5)	(18.6)	(-)	(27.5)	(20.1)	(20.2)	
10	12.65	8.329	9.828	9.765	12.39	7.869	9.406	9.338	
	(-)	(34.2)	(22.3)	(22.8)	(-)	(36.5)	(24.1)	(24.7)	

The results show the same general trend for all mixes with  $\mu$  values decreasing as photon energy increases and HVL, TVL, and MFP values increasing. Noticeably are the observed sharp peaks in the low energy region for Ba and Cel mixes indicating the K-shell absorption edges for the heavy elements contained in these mixes. The peaks occurred at 0.0374 MeV for barium and 0.0161 MeV for strontium.

The photon shielding superiority of the concrete mixes containing heavy elements, especially Ba, is noticeable from low energy up to 200 keV due to the photoelectric absorption mechanism contributions. Moreover, all mixes show a significant decrease with energy in the noted range due to the photoelectric mechanism being inversely correlated with  $E^{3.5}$ . From intermediate to high energy, the decrease in attenuation coefficient with energy is gradual as expected.

The superiority of heavy concrete mixes to shield photons in comparison to traditional concrete mix that includes Dolomite is demonstrated by calculating their respective percent increase for  $\mu$  and percent decrease for HVL at the selected energy values. The results, given in Table 6.6, reveal the improvement in photon shielding efficiency achieved by the heavy mixes at low energy, especially for Ba mix then Cel mix, to a lesser degree at high energy, and minor at intermediate energy. When comparing the results of mix design 1 and 2, the improvement is slightly better for mix design no. 2. The improvement in the heavy concrete mixes especially Ba mixes is attributed to the relatively greater aggregate content in mix design no. 2 that leads to greater heavy elements content in the mix, greater effective atomic number, and relatively higher density. To visualize the difference between the two mix designs, a plot of the percent increase for linear attenuation coefficient at the selected energy values is shown in Fig. 6.5. Except for Do mix, the results show the same general trend, i.e., a noticeable improvement in photon shielding at very low energy, minor improvement at intermediate energy, and moderate improvement at higher energy. Although some improvements

appear small, they may still be significant in dry storage cask application as the difference represents a reduction in concrete materials of approximately the same percentage.

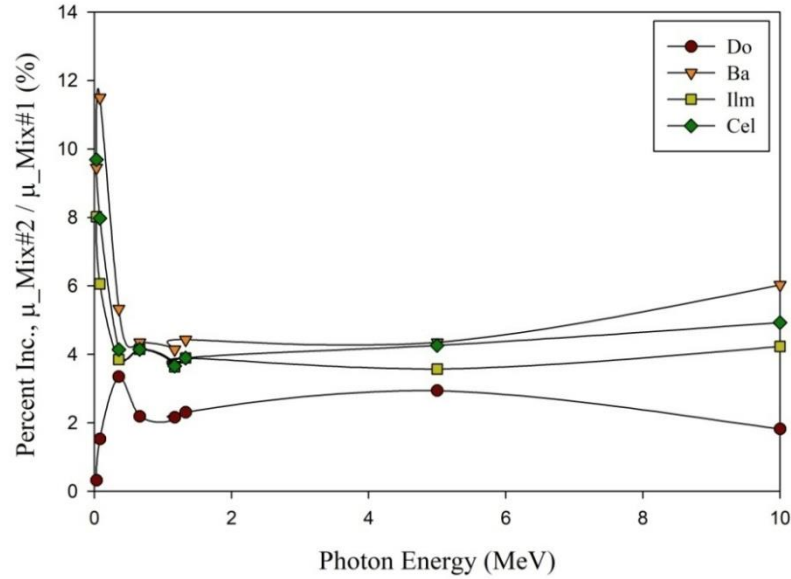


**Fig. 6.5** Percent increase in  $\mu$  from Mix design no. 2 over  $\mu$  from Mix design no. 1

The computed effective atomic numbers ( $Z_{\text{eff}}$ ) corresponding to the 8 concrete mixes for the selected energy range are presented in Fig. 6.6.

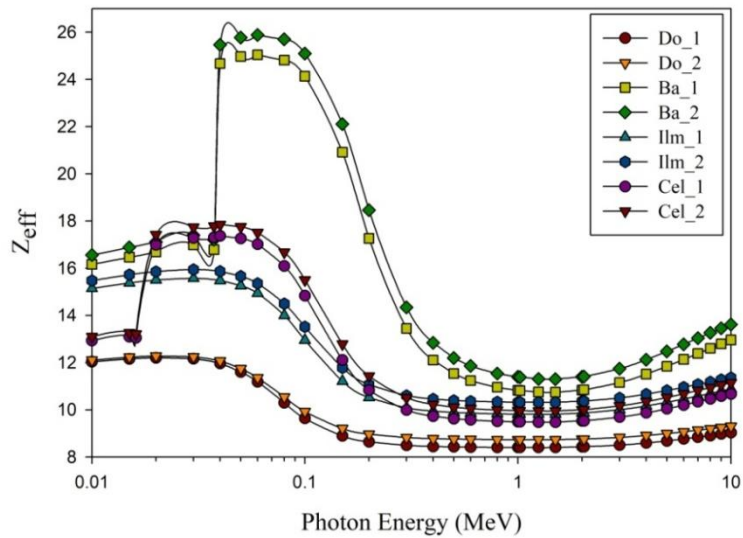


**Fig. 6.6** Concrete mixes effective atomic number ( $Z_{\text{eff}}$ )

Recognizing that  $Z_{\text{eff}}$  is associated with the main photon interaction mechanisms, its value is expected to vary with photon energy similar to the attenuation coefficient. Accordingly, the same trend is observed with Do mixes have the lowest effective atomic numbers and Ba mixes have the highest  $Z_{\text{eff}}$  values for almost the entire energy range. Similar to the attenuation coefficient, a discontinuity is observed in both Ba mixes and Cel mixes caused by Ba and Sr K-edge absorption peaks.

EBF values corresponding to concrete mix design no. 1 and mix design no. 2 are shown in Fig. 6.7. The results reveal that the EBF values for all mixes are low in the low-energy region, relatively high in the high-energy range, and significantly high in the intermediate-energy range. The observed trend is attributed to the weight of photoelectric absorption, pair production, and Compton scattering interaction mechanisms in these regions. EBF values are small in the low energy region because photons are completely absorbed by the photoelectric absorption mechanism or completely removed, the values then gradually increase with photon energy due to multiple scattering of photons by Compton scattering in the intermediate energy range, and then the values decrease again in the high energy range due to the pair-production mechanism. The EBF values are higher in the high energy range than those in the low energy region because of the secondary photons that may emit due to the annihilation process. Moreover, the concrete mixes EBF values are expected to increase with the thickness of the shield represented by MFP due to the buildup increase of the secondary and scattered photons.

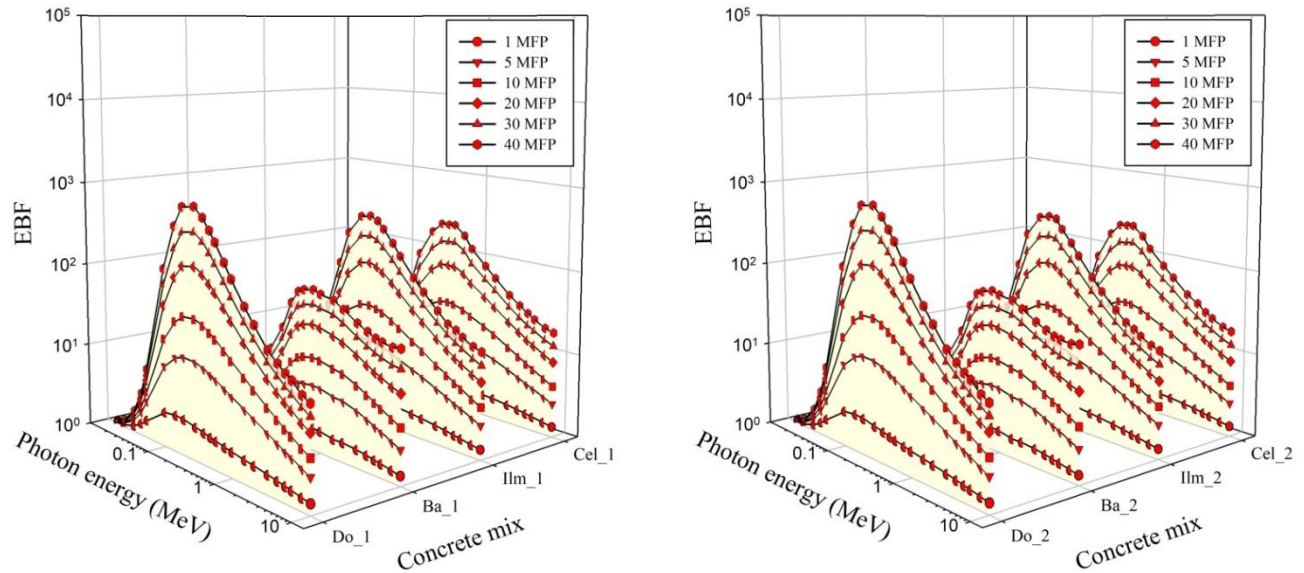


**Fig. 6.7** EBFs for the mixes prepared using mix design no. 1 and those mixes designed using mix design no. 2

Closer examination of the results indicates a negligible difference in the calculated EBF values for concrete mix design no. 1 and mix design no. 2. The EBF calculation method, which is an interpolation method, could not discriminate between the two mix designs well, as it accounts only for the mix composition and not the density. Results show that Do mixes have the largest EBF values, followed by Ilm mixes, Cel mixes, and then Ba mixes have the smallest values. These results indicate the superiority of Ba mixes followed by Cel mixes for the selected energy range.

### 6.5.2 Neutrons shielding assessment

The concrete mixes fast neutrons effective macroscopic removal cross-sections ( $\Sigma_R$ ) are shown in Fig. 6.8, and the corresponding detailed calculations, and values of  $HVL_{fn}$  and  $\lambda_{fn}$  are given in Table 6.8.  $\Sigma_R$  percent increase, and  $HVL_{fn}$  and  $\lambda_{fn}$  percent decrease of the heavy concrete mixes relative to the traditional Do mix are also given in Table 6.8.

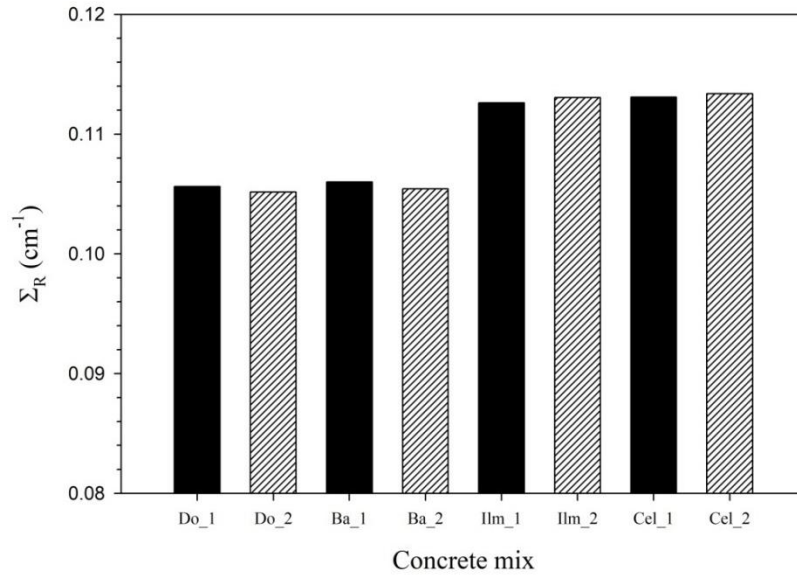


**Fig. 6.8** Fast neutron effective removal cross-sections for the 8 concrete mixes

**Table 6.7** Detailed calculations of the 8 concrete mixes  $\Sigma_R$ ,  $HVL_{fn}$ , and  $\lambda_{fn}$

Ele.	$\Sigma_R/\rho$ (cm <sup>2</sup> /g)	Partial $\Sigma_R$ (cm <sup>-1</sup> )							
		Do_1	Do_2	Ba_1	Ba_2	Ilm_1	Ilm_2	Cel_1	Cel_2
H	0.6874	1.85E-02	1.54E-02	1.84E-02	1.54E-02	1.86E-02	1.56E-02	1.85E-02	1.54E-02
C	0.0603	7.06E-03	7.95E-03	5.16E-04	5.13E-04	4.19E-04	4.09E-04	3.50E-03	3.90E-03
O	0.0386	4.67E-02	4.77E-02	4.53E-02	4.60E-02	4.68E-02	4.78E-02	4.90E-02	5.02E-02
Na	0.0386	8.51E-05	9.22E-05	2.05E-04	2.30E-04	5.18E-05	5.46E-05	5.18E-04	5.81E-04
Mg	0.0348	3.39E-03	3.76E-03	3.48E-04	3.30E-04	9.60E-04	1.02E-03	6.72E-04	6.94E-04
Al	0.0362	8.22E-04	7.40E-04	8.33E-04	7.56E-04	8.43E-04	7.63E-04	7.63E-04	6.74E-04
Si	0.0340	1.09E-02	1.15E-02	1.10E-02	1.17E-02	1.14E-02	1.21E-02	1.10E-02	1.16E-02
P	0.0353	1.34E-06	1.11E-06	8.78E-06	9.53E-06	1.33E-06	1.12E-06	1.33E-06	1.12E-06
S	0.0334	1.79E-04	1.65E-04	6.49E-03	7.30E-03	1.31E-04	1.10E-04	4.70E-03	5.34E-03
Cl	0.0344	4.62E-05	5.18E-05	3.46E-05	3.87E-05	1.16E-05	1.27E-05	1.31E-06	1.09E-06
K	0.0340	2.70E-05	2.83E-05	1.62E-05	1.62E-05	2.40E-05	2.50E-05	7.10E-06	5.90E-06
Ca	0.0338	1.74E-02	1.73E-02	8.50E-03	7.16E-03	8.31E-03	6.96E-03	1.52E-02	1.49E-02
Ti	0.0294	3.18E-05	3.33E-05	8.68E-06	7.25E-06	1.00E-02	1.13E-02	2.21E-05	2.23E-05
Mn	0.0254	0.00E+00	0.00E+00	6.35E-05	7.18E-05	0.00E+00	0.00E+00	0.00E+00	0.00E+00
Fe	0.0246	4.85E-04	4.36E-04	2.26E-03	2.44E-03	1.51E-02	1.69E-02	4.49E-04	3.94E-04
Sr	0.0182	0.00E+00	0.00E+00	0.00E+00	0.00E+00	0.00E+00	0.00E+00	8.61E-03	9.69E-03
Ba	0.0143	9.72E-07	8.07E-07	1.19E-02	1.35E-02	9.71E-07	8.07E-07	2.74E-05	2.43E-05
Tot. $\Sigma_R$ (cm <sup>-1</sup> )		0.1056	0.1052	0.1060	0.1055	0.1126	0.1130	0.1130	0.1134
%Inc.		-	-	0.341	0.295	6.617	7.445	6.939	7.845
$HVL_{fn}$ (cm)		6.562	6.591	6.540	6.571	6.155	6.134	6.136	6.112
%Dec.		-	-	0.335	0.303	6.202	6.934	6.492	7.267
$\lambda_{fn}$ (cm)		9.467	9.509	9.435	9.481	8.879	8.850	8.853	8.817
%Dec.		-	-	0.338	0.294	6.211	6.930	6.486	7.277

The results show that Cel mixes is the best with respect to fast neutron attenuation parameters as they have the largest  $\Sigma_R$  and the smallest  $HVL_{fn}$  and  $\lambda_{fn}$  values when compared to the other concrete mixes. Relative to the traditional concrete mix, an improvement of about 8%, 7%, and 7% with respect to  $\Sigma_R$ ,  $HVL_{fn}$ , and  $\lambda_{fn}$ , respectively, is achieved. For the effective removal cross-section, oxygen (O), silicon (Si), and calcium (Ca), beside hydrogen (H) whose contribution is almost the same for all 8 concrete mixes, are the major contributors. Although Cel mixes contain a significant amount of Sr, the latter has a small contribution reflected by its small mass removal cross-section of 0.0182  $\text{cm}^2/\text{g}$  at high neutron energy.

In contrast, Do mixes contain more moderators (H, C, and O) in comparison to the other concrete mixes, however having a lower density diminished this advantage and led to the weakest performance. Ba mixes did slightly better than Do mixes despite having the highest density among all 8 concrete mixes. Although Ba mixes have considerable amounts of barium, which is found beneficial for photon shielding, this heavy element has a low mass removal cross-section of 0.0143  $\text{cm}^2/\text{g}$  which offsets any advantage from the higher density. The case is different with iron (Fe) and titanium (Ti) contained in Ilm mixes. Their respective mass removal cross-sections of 0.0246 and 0.0294  $\text{cm}^2/\text{g}$  are significant and contributed to Ilm mixes having the largest total  $\Sigma_R$ . Among the two mix designs, the difference is negligible. Nonetheless, both Do and Ba mixes show a slightly lower total  $\Sigma_R$  values for mix design no.2, and slightly higher for Ilm and Cel mixes.

The calculated thermal neutron macroscopic absorption cross-section ( $\Sigma_{abs}$ ) for the 8 concrete mixes is shown in Fig 6.9.  $\Sigma_{abs}$  detailed calculation,  $HVL_{thn}$ , and  $\lambda_{thn}$  values

pertaining to absorption of thermal neutrons of the 8 concrete mixes are given in Table 6.9. The results show that all the mixes except Ilm mixes are inefficient in absorbing and eliminating thermal neutrons. This is attributed to the total absence of the known neutron absorbers “Neutron Poisons” such as boron (B), cadmium (Cd), and gadolinium (Gd). Despite the notable percent increase in  $\Sigma_{\text{abs}}$  and percent decrease in  $\text{HVL}_{\text{thn}}$  and  $\lambda_{\text{thn}}$  achieved by Ba mixes and Cel mixes over the traditional Do mixes, these mixes capabilities are still inadequate in removing thermal neutron. In contrast, thermal neutron absorption capability of Ilm mixes increased due to the increased content of Fe and Ti.

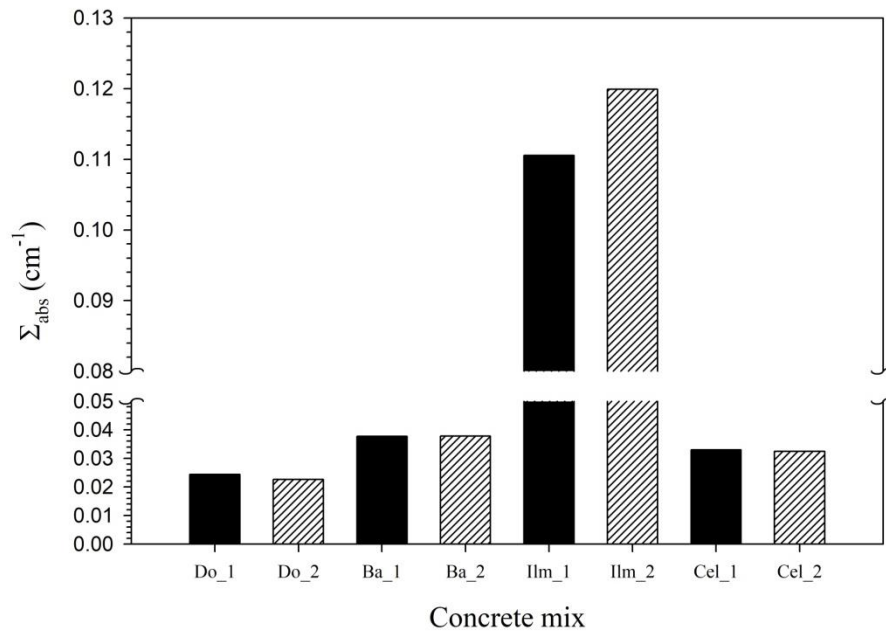


**Fig. 6.9** Thermal neutron macroscopic absorption cross-sections for the 8 concrete mixes

**Table 6.8** Detailed calculations of the 8 concrete mixes  $\Sigma_{abs}$ ,  $HVL_{thn}$ , and  $\lambda_{thn}$ 

Ele.	$\Sigma_{abs}/\rho$ ( $cm^2/g$ )	Partial $\Sigma_{abs}$ ( $cm^{-1}$ )							
		Do_1	Do_2	Ba_1	Ba_2	Ilm_1	Ilm_2	Cel_1	Cel_2
H	2.0E-01	1.12E-02	9.33E-03	1.12E-02	9.33E-03	1.13E-02	9.45E-03	1.12E-02	9.33E-03
C	1.9E-04	4.69E-05	5.28E-05	3.39E-06	3.40E-06	2.78E-06	2.71E-06	2.32E-05	2.59E-05
O	6.4E-06	1.61E-05	1.65E-05	1.56E-05	1.59E-05	1.61E-05	1.65E-05	1.69E-05	1.73E-05
Na	1.4E-02	6.34E-05	6.87E-05	1.54E-04	1.71E-04	3.86E-05	4.07E-05	3.86E-04	4.33E-04
Mg	1.6E-03	3.17E-04	3.52E-04	3.28E-05	3.09E-05	8.99E-05	9.55E-05	6.29E-05	6.49E-05
Al	5.2E-03	2.46E-04	2.21E-04	2.50E-04	2.26E-04	2.52E-04	2.28E-04	2.28E-04	2.02E-04
Si	3.5E-03	2.35E-03	2.49E-03	2.39E-03	2.53E-03	2.47E-03	2.61E-03	2.38E-03	2.52E-03
P	3.3E-03	2.60E-07	2.15E-07	1.70E-06	1.85E-06	2.58E-07	2.17E-07	2.59E-07	2.17E-07
S	9.8E-03	1.09E-04	1.01E-04	3.97E-03	4.46E-03	7.98E-05	6.74E-05	2.91E-03	3.27E-03
Cl	5.7E-01	1.60E-03	1.79E-03	1.19E-03	1.34E-03	4.01E-04	4.40E-04	4.52E-05	3.75E-05
K	3.2E-02	5.31E-05	5.58E-05	3.20E-05	3.19E-05	4.73E-05	4.93E-05	1.40E-05	1.16E-05
Ca	6.6E-03	7.09E-03	7.03E-03	3.46E-03	2.92E-03	3.38E-03	2.83E-03	6.20E-03	6.06E-03
Ti	8.1E-02	1.81E-04	1.90E-04	4.94E-05	4.13E-05	5.71E-02	6.43E-02	1.26E-04	1.27E-04
Mn	1.5E-01	0.00E+00	0.00E+00	7.56E-04	8.54E-04	0.00E+00	0.00E+00	0.00E+00	0.00E+00
Fe	2.8E-02	1.14E-03	1.02E-03	5.32E-03	5.74E-03	3.54E-02	3.98E-02	1.06E-03	9.27E-04
Sr	8.5E-03	0.00E+00	0.00E+00	0.00E+00	0.00E+00	0.00E+00	0.00E+00	8.33E-03	9.39E-03
Ba	5.1E-03	7.27E-07	6.04E-07	8.91E-03	1.01E-02	7.27E-07	6.04E-07	1.63E-05	1.82E-05
Tot. $\Sigma_{abs}$ ( $cm^{-1}$ )		0.0244	0.0227	0.0377	0.0378	0.1105	0.1199	0.0330	0.0324
%Inc.		-	-	54.51	66.52	352.9	428.2	35.25	42.73
$HVL_{thn}$ (cm)		28.41	30.53	18.37	18.35	6.270	5.781	21.01	21.38
%Dec.		-	-	35.34	39.90	77.93	81.06	26.05	29.97
$\lambda_{thn}$ (cm)		40.98	44.05	26.53	26.46	9.050	8.340	30.30	30.85
%Dec.		-	-	35.26	39.93	77.92	81.07	26.06	29.96

### 6.5.3 Dry Storage Cask model results

The OpenMC dry storage cask (DSC) model results in the form of photon flux and neutron flux along the thickness of the cask are shown in Fig. 6.10 and Fig. 6.11, respectively.

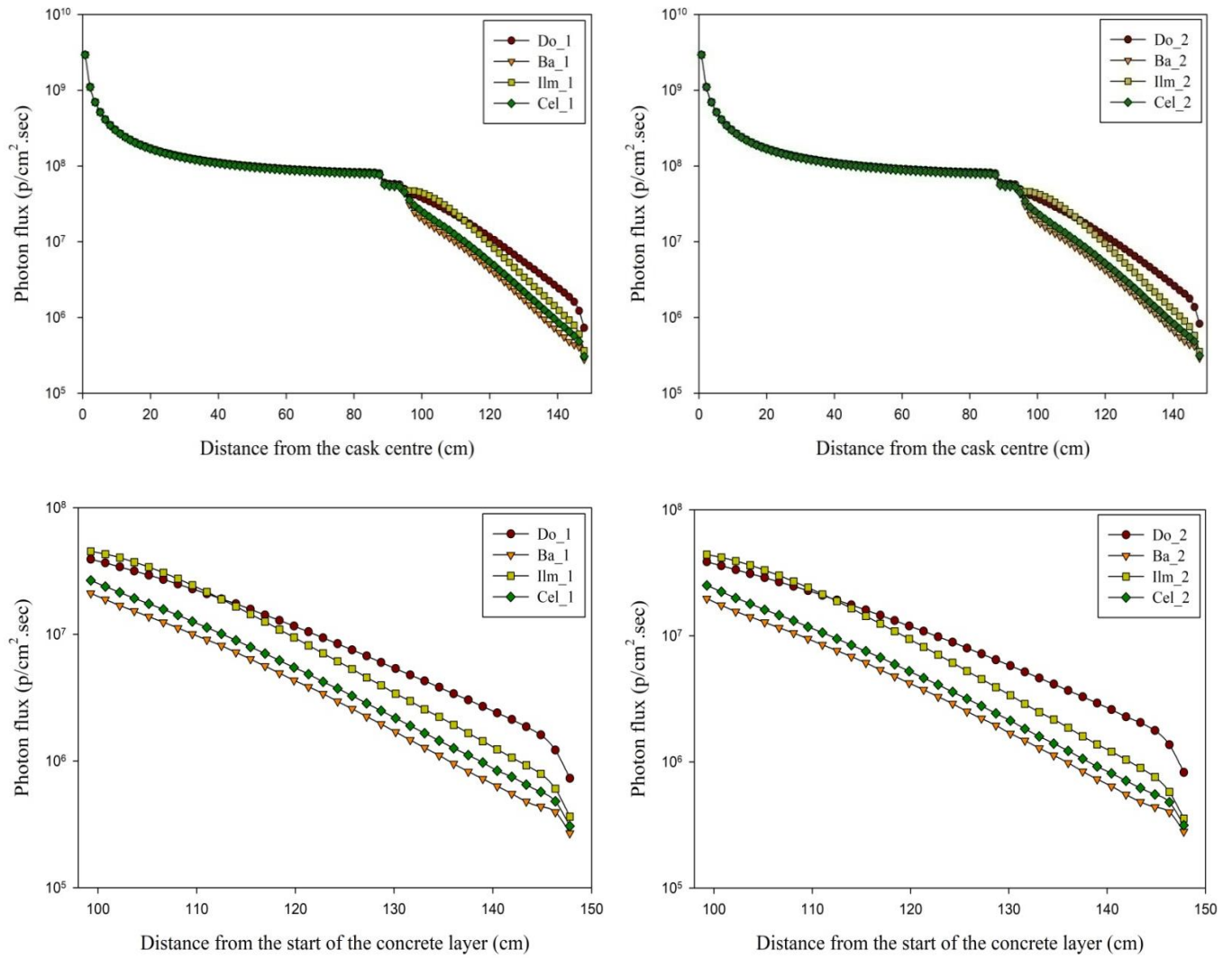


**Fig. 6.10** Photon flux variation from the centre of the cask and from the start of the concrete layer

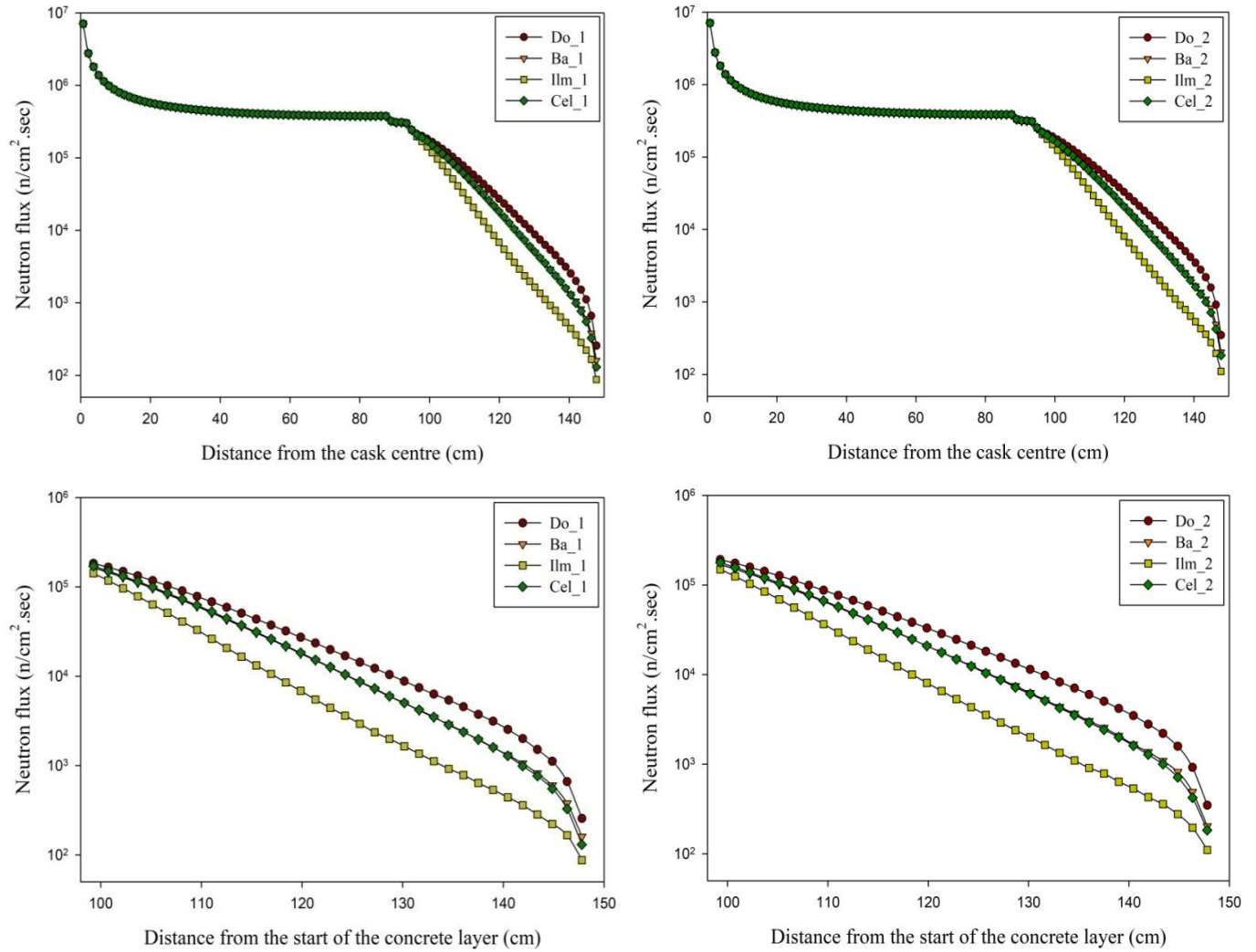


**Fig. 6.11** Neutron flux variation from the centre of the cask and from the start of the concrete layer

The variation of photon flux and neutron flux as a function of energy at the cask’s outer surface is shown in Fig. 6.12. Moreover, the calculated neutron, photon, and total dose rates at the cask’s outer surface are given in Table 6.10.

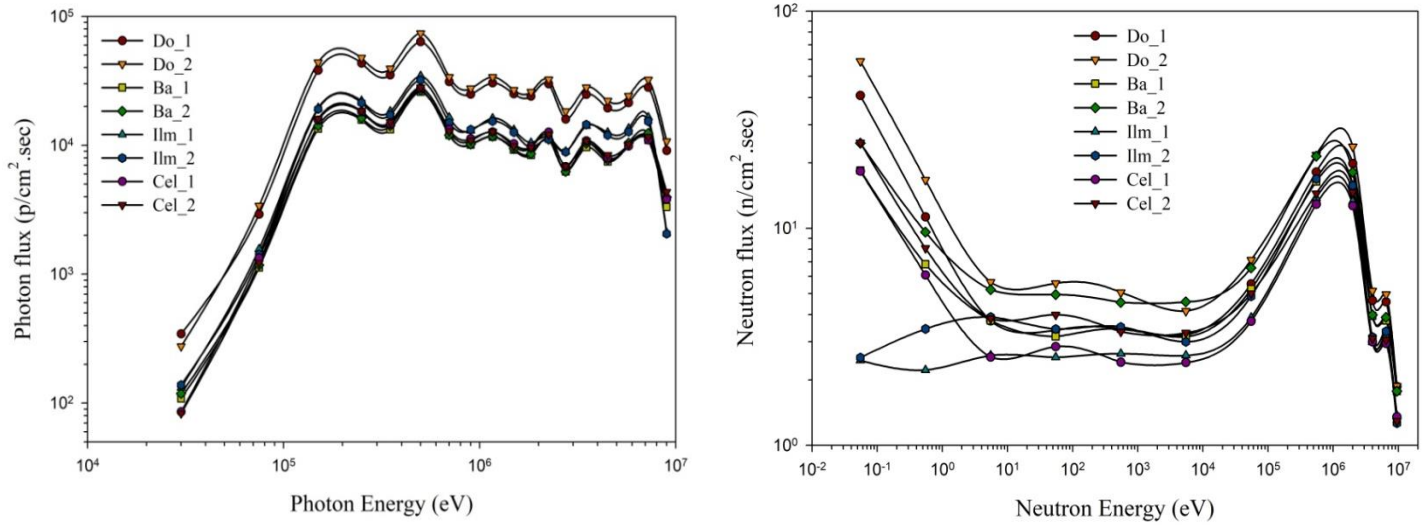


**Fig. 6.12** Photon and neutron flux versus energy at the cask’s outer surface

**Table 6.9** Neutron, photon, and total dose rates at the cask’s outer surface for the 8 concrete mixes

	Mix design no. 1				Mix design no. 2			
	Do_1	Ba_1	Ilm_1	Cel_1	Do_2	Ba_2	Ilm_2	Cel_2
Neutron dose rate (mrem/h)	2.78	2.30	1.88	1.82	3.22	2.60	2.11	2.01
Photon dose rate (mrem/h)	1035	406	549	436	1167	428	524	445
Total dose rate (mrem/h)	1038	408	551	438	1170	431	526	447
%Dec. (Tot. dose rate)	-	61	47	58	-	63	55	62

The results from the neutron flux and photon flux show that decreasing the cementing content from 600 to 500 kg/m<sup>3</sup> and increasing the aggregate content of the mix accordingly did not have a significant effect. This observation is further confirmed by the calculated total dose rates at the outer surface of the cask that yielded a percent difference of 6%, 5%, and 2% for the Ba mixes, Ilm mixes, and Cel mixes, respectively. Off

significance, is the slight total dose rate increase observed on the surface of Ba and Cel concrete-based casks for mix design no. 2, whereas the opposite is observed for Ilm concrete-based casks. The difference can be attributed to the higher pair production contribution that led to greater secondary gamma rays.

The values of the neutron flux, photon flux, and the calculated total dose rate at the cask's outer surface reveal that Do concrete-based cask has the highest photon/neutron flux and total dose rate and that Ba then Cel concrete-based casks have the least photon flux and total dose rate. These results are consistent with the results and discussions presented in the previous sections. Ba mixes are noticeably the best in attenuating gamma rays that are emitted in a broad beam situation like the simple dry cask model currently being investigated. Cel mixes are also highly acceptable.

Regarding neutrons' attenuation, both Cel and Ilm mixes were found to have the best performance and the least neutronic doses. However, the results show that the contribution from the neutronic dose in the calculated total dose rate at the cask's outer surface is very small compared to that due to gamma rays or photons.

## **6.6 Conclusions**

Radiation shielding concrete which employs heavy minerals was shown to have efficient radiation shielding properties for use in nuclear industry and radiation shielding applications. According to the results obtained from this experimental and analytical study, and the analysis presented, the following conclusions have been drawn:

1. Linear attenuation coefficient ( $\mu$ ) is a necessary but not a sufficient indicator of the effectiveness of a shield against  $\gamma$ -rays.
2. Exposure build-up factor needs to be considered in addition to ( $\mu$ ) when evaluating the shield effectiveness against  $\gamma$ -rays.
3. Exposure build-up factor significantly decrease when increasing the shield effective atomic number which increases when increasing the shield content of high ( $Z$ ) elements.
4. Heavy concrete with high ( $Z$ ) elements possesses better radiation shielding properties compared to traditional concrete.
5. Ba mix is the best among the studied concrete mixes in attenuating X-rays and  $\gamma$ -rays for both narrow-beam and broad-beam geometries.
6. Cel concrete, which is studied for the first time as radiation shielding concrete, has reliable radiation shielding properties.
7. Ilm concrete has good  $\gamma$ -rays shielding capability in addition to the considerable neutron shielding properties.
8. SNF storage cask as a nuclear application needs protection against multiple sources of radiation with the override being reliable  $\gamma$ -rays shielding capabilities.
9. An overpack slightly thicker than 50 cm of Ba concrete or Cel concrete is potentially feasible to use in SNF concrete-based storage cask as their calculated total dose rates are slightly above the recommended safety limit of 20 - 400 mrem/h.

The conclusions and observations made in this paper are specific to the composition of the aggregates and cement, the radiation sources, and the model and tools employed in this study.

## **6.7 Acknowledgments**

This research was supported by the Natural Sciences and Engineering Research Council of Canada, McMaster University Centre for Effective Design of Structures, Compute Ontario (<https://computeontario.ca/>), Compute Canada ([www.computecanada.ca](http://www.computecanada.ca)), and Military Technical College in Egypt. The authors also want to thank Dr. Moustafa A. Masoud, Geology department, Faculty of science, Beni-Suef University, Egypt, for his efforts to provide most of the aggregates used in the study.

## **6.8 References**

- Abo El-Enein, S.A., El-Sayed, H.A., Ali, A.H., Mohammed, Y.T., Khater, H.M., Ouda, A.S., 2014. Physico-mechanical properties of high performance concrete using different aggregates in presence of silica fume. *HBRC Journal* 10 (1), 43-48.
- American Concrete Institute (ACI) Standard, 1996. Standard practice for selecting proportions for normal, heavyweight, and mass concrete. *ACI Man. Concr. Pract*, 1-38.
- Allison, J., Amako, K., Apostolakis, J., Araujo, H., Dubois, P.A., Asai, M., Barrand, G., Capra, R., Chauvie, S., Chytracsek, R., 2006. Geant4 developments and applications. *IEEE Transactions on nuclear science* 53 (1), 270-278.
- Alshahrani, B., Olarinoye, I., Mutuwong, C., Sriwunkum, C., Yakout, H., Tekin, H., Al-Buriahi, M., 2021. Amorphous alloys with high Fe content for radiation shielding applications. *Radiation Physics and Chemistry* 183, 109386.
- American National Standard, 1991. Neutron and gamma-ray fluence-to-dose factors, ANSI/ANS-6.1.1-1991, American Nuclear Society, La Grange Park, IL, USA.

- American National Standard, 1991. Buildup Factor for Engineering Materials. ANSI/ANS-6.4.3, American National Standards Institute, New York, USA.
- ASTM-C150, 2012. Standard specification for Portland cement. ASTM International, West Conshohocken, PA, USA.
- ASTM-C494, 2011. Standard specification for chemical admixtures for concrete. ASTM, West Conshohocken, PA, USA.
- ASTM-C637, 2009. Standard specification for aggregates for radiation-shielding concrete. ASTM, West Conshohocken, PA, USA.
- ASTM-C989, 2006. Standard specification for ground granulated blast furnace slag for use in concrete and mortars. ASTM, West Conshohocken, PA, USA.
- ASTM-C1240, 2006. Specification for silica fume used in cementitious mixtures. ASTM, West Conshohocken, PA, USA.
- Azreen, N., Rashid, R. S., Amran, Y. M., Voo, Y., Haniza, M., Hairie, M., Alyousef, R., Alabduljabbar, H., 2020. Simulation of ultra-high-performance concrete mixed with hematite and barite aggregates using Monte Carlo for dry cask storage. *Construction and Building Materials* 263, 120161.
- Bethge, K., Kraft, G., Kreisler, P., Walter, G., 2004. *Medical applications of nuclear physics*. Springer-Verlag, Springer Science & Business Media, Berlin, Germany.
- Brown, D. A., Chadwick, M., Capote, R., Kahler, A., Trkov, A., Herman, M., Sonzogni, A., Danon, Y., Carlson, A., Dunn, M., 2018. ENDF/B-VIII. 0: The 8th major release of the nuclear reaction data library with CIELO-project cross sections, new standards and thermal scattering data. *Nuclear Data Sheets* 148, 1-142.
- El-Khayatt, A. 2010. Calculation of fast neutron removal cross-sections for some compounds and materials. *Annals of Nuclear Energy* 37 (2), 218-222.
- El-Samrah, M., El-Mohandes, A., El-Khayatt, A., Chidiac, S., 2021. MRCsC: A user-friendly software for predicting shielding effectiveness against fast neutrons. *Radiation Physics and Chemistry* 182, 109356.

- El-Samrah, M. G., Abdel-Rahman, M. A., El Shazly, R., 2018. Effect of heating on physical, mechanical, and nuclear radiation shielding properties of modified concrete mixes. *Radiation Physics and Chemistry* 153, 104-110.
- El-Samrah, M. G., Abdel-Rahman, M. A., Kany, A. M., 2018. Study Characteristics of New Concrete Mixes and their Mechanical, Physical, and Gamma Radiation Attenuation Features. *Zeitschrift für anorganische und allgemeine Chemie* 644 (2), 92-99.
- Elwahab, N. R. A., Helal, N., Mohamed, T., Shahin, F., Ali, F. M., 2019. New shielding composite paste for mixed fields of fast neutrons and gamma rays. *Materials Chemistry and Physics* 233, 249-253.
- Gerward, L., Guilbert, N., Jensen, K. B., Leving, H., 2004. WinXCom—a program for calculating X-ray attenuation coefficients. *Radiation physics and chemistry* 71, 653-654.
- Harima, Y. 1983. An approximation of gamma-ray buildup factors by modified geometrical progression. *Nuclear Science and Engineering* 83 (2), 299-309.
- Harima, Y., Sakamoto, Y., Tanaka, S., Kawai, M., 1986. Validity of the geometric-progression formula in approximating gamma-ray buildup factors. *Nuclear Science and Engineering* 94 (1), 24-35.
- Hosamani, M. Badiger, N., 2018. Determination of effective atomic number of composite materials using backscattered gamma photons—a novel method. *Chemical Physics Letters* 695, 94-98.
- Kaplan, M. F., 1989. *Concrete radiation shielding*. John Wiley & Sons, NY, USA.
- Kaur, P., Singh, K., Kurudirek, M., Thakur, S., 2019. Study of environment friendly bismuth incorporated lithium borate glass system for structural, gamma-ray and fast neutron shielding properties. *Spectrochimica acta part A: molecular and biomolecular spectroscopy* 223, 117309.
- Ko, J. H., Park, J. H., Jung, I. S., Lee, G. U., Baeg, C. Y., Kim, T. M., 2014. Shielding analysis of dual purpose casks for spent nuclear fuel under normal storage conditions. *Nuclear engineering and Technology* 46 (4), 547-556.

- Lakshminarayana, G., Elmahroug, Y., Kumar, A., Dong, M., Lee, D. E., Yoon, J., Park, T., 2020.  $\text{Li}_2\text{O}-\text{B}_2\text{O}_3-\text{Bi}_2\text{O}_3$  glasses: gamma-rays and neutrons attenuation study using ParShield/WinXCOM program and Geant4 and Penelope codes. *Applied Physics A* 126 (4), 1-16.
- Lamarsh, J. R., Baratta, A. J., 2001. *Introduction to nuclear engineering*. Prentice hall, Upper Saddle River, NJ, USA.
- Levet, A., Kavaz, E., Özdemir, Y., 2020. An experimental study on the investigation of nuclear radiation shielding characteristics in iron-boron alloys. *Journal of Alloys and Compounds* 819, 152946.
- Mahmoud, K., Rammah, Y., 2020. Investigation of gamma-ray shielding capability of glasses doped with Y, Gd, Nd, Pr and Dy rare earth using MCNP-5 code. *Physica B: Condensed Matter* 577, 411756.
- Masoud, M., Kansouh, W., Shahien, M., Sakr, K., Rashad, A. M., Zayed, A., 2020. An experimental investigation on the effects of barite/hematite on the radiation shielding properties of serpentine concretes. *Progress in Nuclear Energy* 120, 103220.
- McFerran, N. J., Gao, Y., Enqvist, A., Tulenko, J. E., Baciak, J. E., 2020. Dry cask radiation shielding validation and estimation of cask surface dose rate with MAVRIC during long-term storage. *Annals of Nuclear Energy* 140, 107145.
- Oto, B., Madak, Z., Kavaz, E., Yaltay, N., 2019. Nuclear radiation shielding and mechanical properties of colemanite mineral doped concretes. *Radiation Effects and Defects in Solids* 174 (9-10), 899-914.
- Oto, B., Yıldız, N., Korkut, T., Kavaz, E., 2015. Neutron shielding qualities and gamma ray buildup factors of concretes containing limonite ore. *Nuclear Engineering and Design* 293, 166-175.
- Ouda, A. S., 2015. Development of high-performance heavy density concrete using different aggregates for gamma-ray shielding. *Progress in Nuclear Energy* 79, 48-55.
- Romano, P. K., Horelik, N. E., Herman, B. R., Nelson, A. G., Forget, B., Smith, K., 2015. OpenMC: A state-of-the-art Monte Carlo code for research and development. *Annals of Nuclear Engineering* 82 (2015), 90-97.

- Şakar, E., Özpolat, Ö. F., Alım, B., Sayyed, M., Kurudirek, M., 2020. Phy-X/PSD: development of a user friendly online software for calculation of parameters relevant to radiation shielding and dosimetry. *Radiation Physics and Chemistry* 166, 108496.
- Sayyed, M. 2016. Investigation of shielding parameters for smart polymers. *Chinese journal of physics* 54 (3), 408-415.
- Shin, J. W., Lee, J. W., Yu, S., Baek, B. K., Hong, J. P., Seo, Y., Kim, W. N., Hong, S. M., Koo, C. M., 2014. Polyethylene/boron-containing composites for radiation shielding. *Thermochemica Acta* 585, 5-9.
- Singh, V. P., Badiger, N., 2012. Comprehensive study of energy absorption and exposure build-up factors for concrete shielding in photon energy range 0.015–15 MeV up to 40 mfp penetration depth: dependency of density, chemical elements, photon energy. *International Journal of Nuclear Energy Science and Technology* 7 (1), 75-99.
- Soppera, N., Bossant, M., Dupont, E., 2014. JANIS 4: An improved version of the NEA java-based nuclear data information system." *Nuclear Data Sheets* 120: 294-296.
- Taylor, M., Smith, R., Dossing, F., Franich, R., 2012. Robust calculation of effective atomic numbers: The Auto-Zeff software. *Medical physics* 39 (4), 1769-1778.
- Tekin, H., Altunsoy, E., Kavaz, E., Sayyed, M., Agar, O., Kamislioglu, M., 2019. Photon and neutron shielding performance of boron phosphate glasses for diagnostic radiology facilities. *Results in Physics* 12, 1457-1464.
- Tellili, B., Elmahroug, Y., Souga, C., 2017. Investigation on radiation shielding parameters of cerrobend alloys. *Nuclear Engineering and Technology* 49 (8), 1758-1771.
- Waters, L. S., McKinney, G. W., Durkee, J. W., Fensin, M. L., Hendricks, J. S., James, M. R., Johns, R. C., Pelowitz, D. B., 2007. The MCNPX Monte Carlo radiation transport code. *AIP conference Proceedings*, American Institute of Physics, 896, 81-90.
- Wu, Y., Song, J., Zheng, H., Sun, G., Hao, L., Long, P., Hu, L., Team, FDS., 2015. CAD-based Monte Carlo program for integrated simulation of nuclear system SuperMC. *Annals of Nuclear Energy* 82, 161-168.

Zayed, A., Masoud, M., Shahien, M., Gökçe, H., Sakr, K., Kansouh, W., El-Khayatt, A., 2020. Physical, mechanical, and radiation attenuation properties of serpentine concrete containing boric acid. *Construction and Building Materials* 272 (2021), 121641.